

1-1-2013

Structural and Photoluminescent Characterization of Substituted A_3MO_4F ($A = Sr, Ba, Ca; M = Al, Ga, In, Si$ and Ge)

Robert Lenwood Green
University of South Carolina - Columbia

Follow this and additional works at: <https://scholarcommons.sc.edu/etd>

 Part of the [Chemistry Commons](#)

Recommended Citation

Green, R. L. (2013). *Structural and Photoluminescent Characterization of Substituted A_3MO_4F ($A = Sr, Ba, Ca; M = Al, Ga, In, Si$ and Ge)*. (Doctoral dissertation). Retrieved from <https://scholarcommons.sc.edu/etd/2529>

This Open Access Dissertation is brought to you by Scholar Commons. It has been accepted for inclusion in Theses and Dissertations by an authorized administrator of Scholar Commons. For more information, please contact dillarda@mailbox.sc.edu.

STRUCTURAL AND PHOTOLUMINESCENT CHARACTERIZATION OF SUBSTITUTED
 A_3MO_4F ($A = \text{Sr, Ba, Ca}$; $M = \text{Al, Ga, In, Si, and Ge}$)

by

Robert Lenwood Green

Bachelor of Science
Morehouse College, 2002

Master of Science
Purdue University, 2005

Submitted in Partial Fulfillment of the Requirements

For the Degree of Doctor of Philosophy in

Chemistry

College of Arts and Sciences

University of South Carolina

2013

Accepted by:

Thomas Vogt, Major Professor

Richard Adams, Committee Member

Brian Benicewicz, Committee Member

Xiao-Dong Zhou, Committee Member

Lacy Ford, Vice Provost and Dean of Graduate Studies

© Copyright by Robert Lenwood Green, 2013
All Rights Reserved.

DEDICATION

This dissertation is dedicated to the people who believe in me...I love you all!

ACKNOWLEDGEMENTS

I first want to thank God for guiding my path in pursuing a doctorate in chemistry. He has led me to be taught by a most remarkable advisor in Dr. Thomas Vogt. Although the road has not been easy to achieve such a degree, it has definitely been the most gratifying and rewarding educational endeavor that I have experienced. I thank you, Dr. Vogt, for allowing me to stumble at times in order to teach me to become a more independent thinker, and more importantly that there is always something that you could learn...even when you are an expert. For an expert is someone who makes every mistake and learns from it!

I would also like to thank Dr. Eirin Sullivan for giving me lots of moral support and being a true leader. I wish you well in your future endeavors and I know that you will be an excellent professor and PI. I would also like to thank the other graduate student in the Vogt Research Group, Dr. Sonali Mitra. It has been a pleasure working with you to navigate through lots of diffraction data and trying to understand the wonders of Rietveld refinement and crystallography. I would also like to thank Dr. Maxim Avdeev for assisting me by collecting neutron data. May God bless each of you in your future endeavors. I would like to acknowledge the Department of Energy for providing support through grant DE-FG02-09ER46617 for this project.

A special thank you goes to my lovely wife Chasity and my son RJ for enduring this process with me. Thank you for being there to encourage me through the sleepless

nights and long days. Your patience and understanding will always be appreciated and I hope that I can finally get some sleep. We have lots of “catching up” to do.

I would also like to thank my entire family (near and far) for continued love and support through this journey. You all played a very important role in shaping me into the person I am today. Whether providing an occasional meal, providing a word of encouragement, or allowing me to sleep at your residence when I was too tired to drive, I want to say thank you from the bottom of my heart.

Thanks to my parents Leon and Winnie Green, my brother Zan and my sister Leondra for providing me guidance from birth. The lessons learned from being the youngest in the house will never be forgotten. I hope that I have made you proud. Finally, I would like to thank my in-laws Derrick, Glendia, and Courtney Cole. You have always treated me like family and have always supported me as if I were your own. Thank you for all that you have done for me.

ABSTRACT

In this dissertation, the structure and photoluminescent properties of A_3MO_4F -type materials ($A = \text{Sr, Ba, Ca}$; $M = \text{Al, Ga, In, Si, and Ge}$) are studied as potential phosphors for compact fluorescent lamps (CFLs) and phosphor converted light emitting diode (pc-LED) lights. Chapter 1 outlines background information of the evolution of lighting technology as well as detailing the synthesis, structural characterization and photoluminescence measurements. Chapter 2 focuses on the changes that the $\text{Sr}_3\text{AlO}_4\text{F}$ structure undergoes as a result of exposure to a 5% $\text{H}_2/95\%$ Ar atmosphere. High-resolution neutron powder diffraction is used to probe for minute structural changes. Chapter 3 is a detailed study of the isovalent substitution of Sr^{2+} by Ba^{2+} and Ca^{2+} at the A-site in $\text{Sr}_{3-x}\text{A}_x\text{GaO}_4\text{F}$. In this study, changes in bond valence sums, global instability indices, and photoluminescent properties are related as a result of these substitutions. As the Ba^{2+} content increases in $\text{Sr}_{3-x}\text{A}_x\text{GaO}_4\text{F}$, the global instability indices decrease. Conversely, Ca^{2+} substitution in these materials causes the global instability indices to increase. Chapter 4 focuses on substitutions at the M -site of the host structure, where the M -site contains Al^{3+} , Ga^{3+} , and In^{3+} . These substitutions at the M site allow us to tailor the photoluminescence of A_3MO_4F -type materials for potential use in UV-LED lights. In chapter 5, $\text{Sr}_3\text{GaO}_4\text{F}$ is doped with Ce^{3+} and Na^+ to determine the critical concentration with respect to quenching. After identifying the critical concentration for radiationless quenching, aliovalent substitutions of Ga^{3+} by Si^{4+} and Ge^{4+} are made at the M site and their effect on the PL emission is studied. Significant photoluminescence intensity is

seen when $\lambda_{\text{ex}} = 450 \text{ nm}$ in the Ce^{3+} substituted $\text{Sr}_3\text{GaO}_4\text{F}$ structure, which allows for these materials to become potential LED phosphors.

TABLE OF CONTENTS

DEDICATION	iii
ACKNOWLEDGEMENTS.....	iv
ABSTRACT	vi
LIST OF TABLES	x
LIST OF FIGURES	xii
LIST OF ABBREVIATIONS.....	xvi
CHAPTER 1: INTRODUCTION.....	1
The Physics of Photoluminescence	4
Diffraction and Crystallographic Techniques	13
Calculating Bond Valence Sums of Sr_3MO_4F	20
A_3MO_4F Synthesis and Structure.....	22
CHAPTER 2: PHOTOLUMINESCENCE AND STRUCTURAL STUDY OF AIR-ANNEALED AND REDUCED Sr_3AlO_4F USING HIGH RESOLUTION NEUTRON POWDER DIFFRACTION.....	29
INTRODUCTION	29
EXPERIMENTAL	31
RESULTS AND DISCUSSION	32
CONCLUSIONS	45
REFERENCES.....	46
CHAPTER 3: STRUCTURES AND SELF-ACTIVATING PHOTOLUMINESCENT PROPERTIES OF $Sr_{3-x}A_xGaO_4F$ ($A = Ca, Ba$).....	48
INTRODUCTION	49

EXPERIMENTAL	53
RESULTS AND DISCUSSION	54
CONCLUSIONS	83
REFERENCES.....	85
CHAPTER 4: STRUCTURES AND SELF-ACTIVATING PHOTOLUMINESCENT PROPERTIES OF A_3MO_4F ($A = Sr, Ba; M = Al, Ga, In$).....	87
INTRODUCTION	87
EXPERIMENTAL	89
RESULTS AND DISCUSSION	90
CONCLUSIONS	127
REFERENCES.....	129
CHAPTER 5: SYNTHESIS AND CHARACTERIZATION OF STRUCTURAL AND PHOTOLUMINESCENT PROPERTIES OF $Sr_{2.98-x/2}Na_{0.01}Ce_{0.01}Ga_{1-x}M_xO_4F$ MATERIALS	131
INTRODUCTION	131
EXPERIMENTAL	135
RESULTS AND DISCUSSION	136
CONCLUSIONS	157
REFERENCES.....	158
CHAPTER 6: CONCLUSIONS AND FUTURE WORK.....	160
APPENDIX A: COPYRIGHT PERMISSION	163

LIST OF TABLES

Table 2.1: Refined lattice parameters and atomic positions for $\text{Sr}_3\text{AlO}_4\text{F}_{(\text{air})}$	42
Table 2.2: Refined lattice parameters and atomic positions for $\text{Sr}_3\text{AlO}_4\text{F}_{(\text{r})}$	42
Table 2.3: Changes in distances and angles between $\text{Sr}_3\text{AlO}_4\text{F}_{(\text{air})}$ and $\text{Sr}_3\text{AlO}_4\text{F}_{(\text{r})}$	43
Table 2.4: Bond valence sums (BVS) of ions in $\text{Sr}_3\text{AlO}_4\text{F}_{(\text{air})}$ and $\text{Sr}_3\text{AlO}_4\text{F}_{(\text{r})}$	44
Table 2.5: Discrepancy factors (d_i) of ions and global instability indices (G) of $\text{Sr}_3\text{AlO}_4\text{F}_{(\text{air})}$ and $\text{Sr}_3\text{AlO}_4\text{F}_{(\text{r})}$	44
Table 3.1: Structural Parameters of $\text{Sr}_{3-x}\text{A}_x\text{GaO}_4\text{F}$ obtained by Rietveld analysis of X-ray diffraction patterns	58
Table 3.2: Selected Atomic Distances (Å) and Angles (deg) of $\text{Sr}_{3-x}\text{A}_x\text{GaO}_4\text{F}$	60
Table 3.3: Tilt angles of $\text{Sr}_{3-x}\text{A}_x\text{GaO}_4\text{F}$ and $\text{Sr}_{3-x}\text{A}_x\text{AlO}_4\text{F}$ materials from the $a^0a^0c^-$ tilt system of $I4/mcm$. Data in set 1 and set 2 were produced by the authors and data from set 3 from Prodjosantoso <i>et al.</i> 2	62
Table 3.4: Bond Valence Sums of Ba and Ca substituted $\text{Sr}_{3-x}\text{A}_x\text{GaO}_4\text{F}$ and $\text{Sr}_{3-x}\text{A}_x\text{AlO}_4\text{F}$. Data in Set 1 and set 2 were produced by the author and data from set 3 from Prodjosantoso <i>et al.</i>	64
Table 3.5: d_i values for cations in $\text{Sr}_{3-x}\text{A}_x\text{MO}_4\text{F}$ materials, where data in set 1 and set 2 were produced by the author and data from set 3 were calculated from data published by Prodjosantoso <i>et al.</i>	67
Table 3.6: Chromaticity coordinates of Selected $\text{Sr}_{3-x}\text{A}_x\text{MO}_4\text{F}$ phosphors	78
Table 4.1: Structural Parameters and tilt angles obtained by Rietveld analysis of X-ray diffraction patterns for $\text{Sr}_{3-x}\text{Ba}_x\text{Al}_y\text{Ga}_{1-y}\text{O}_4\text{F}$	92
Table 4.2: Chromaticity coordinates of Selected $\text{Sr}_{3-x}\text{Ba}_x\text{MO}_4\text{F}$ phosphors.....	95
Table 4.3: Structural Parameters and tilt angles obtained by Rietveld analysis of X-ray diffraction patterns for $\text{Sr}_{2.4}\text{Ba}_{0.6}\text{Al}_{0.1}\text{Ga}_{0.9-x}\text{In}_x\text{O}_4\text{F}$	99

Table 4.4: CIE chromaticity coordinates for reduced $\text{Sr}_{2.4}\text{Ba}_{0.6}\text{Al}_y\text{Ga}_{1-y-z}\text{In}_z\text{O}_4\text{F}$ materials. Samples 1-6 are tempered in a 5% H_2 /95% Ar atmosphere at 1050°C. Samples 7-10 and 15-18 are tempered in a 5% H_2 /95% Ar atmosphere at 900°C. Samples 11-14 and 19-22 are tempered in a 5% H_2 /95% Ar atmosphere at 800°C	123
Table 5.1: Lattice Parameters of Substituted $\text{Sr}_{3-x/2}\text{Na}_{0.01}\text{Ce}_{0.01}\text{Ga}_{1-x}\text{M}_x\text{O}_4\text{F}$. All materials are refined using the <i>I4/mcm</i> space group.....	144
Table 5.2: Bond distances and angles for $\text{Sr}_{3-x/2}\text{Na}_{0.01}\text{Ce}_{0.01}\text{Ga}_{1-x}\text{M}_x\text{O}_4\text{F}$ materials	145
Table 5.3: Bond Valence Sums (BVS) of ions in $\text{Sr}_{3-x/2}\text{Na}_{0.01}\text{Ce}_{0.01}\text{Ga}_{1-x}\text{Si}_x\text{O}_4\text{F}$	147
Table 5.4: Discrepancy factors and Global Instability Indices in $\text{Sr}_{3-x/2}\text{Na}_{0.01}\text{Ce}_{0.01}\text{Ga}_{1-x}\text{Si}_x\text{O}_4\text{F}$	148
Table 5.5: Bond Valence Sums (BVS) of ions in $\text{Sr}_{3-x/2}\text{Na}_{0.01}\text{Ce}_{0.01}\text{Ga}_{1-x}\text{Ge}_x\text{O}_4\text{F}$	148
Table 5.6: Discrepancy factors and Global Instability Indices in $\text{Sr}_{3-x/2}\text{Na}_{0.01}\text{Ce}_{0.01}\text{Ga}_{1-x}\text{Ge}_x\text{O}_4\text{F}$	148
Table 5.7: CIE Chromaticity Coordinates (415nm excitation).....	155

LIST OF FIGURES

Figure 1.1: Diagram of PC-LED lighting assemblies, (a) blue semiconductor chip with yellow phosphor, (b) blue semiconductor chip with yellow and red phosphor, and (c) blue semiconductor chip with red and green phosphor.	4
Figure 1.2: The configurational coordinate diagram for luminescence of phosphor materials.	7
Figure 1.3: Diagram of the Perkin Elmer LS55 spectrofluorometer	12
Figure 1.4: CIE chromaticity diagram	13
Figure 1.5: Diffraction of x-rays in accordance with Bragg's law	14
Figure 1.6: Diagram of the Rigaku Miniflex X-ray diffractometer	15
Figure 1.7: Oxygen nearest neighbors in Sr_3AlO_4F	21
Figure 1.8: Tube furnace setup for reduction of materials.....	23
Figure 1.9: Structure of A_3MO_4F	24
Figure 1.10: Comparison of Perovskite structure of (a) $SrTiO_3$ and distorted anti-Perovskite (b) Sr_3MO_4F in the 001 direction.	25
Figure 2.1: Images of (a) $Sr_3AlO_4F_{(r)}$, (b) $Sr_3AlO_4F_{(air)}$, and (c) SrF_2 . ($\lambda_{ex} = 254nm$)	33
Figure 2.2: Emission and excitation spectra of $Sr_3AlO_4F_{(air)}$ and $Sr_3AlO_4F_{(r)}$ samples....	35
Figure 2.3: Photoluminescence of $Sr_3AlO_4F_{(air)}$ and SrF_2 , where $\lambda_{ex} = 254nm$	35
Figure 2.4: Plot of CIE chromaticity coordinates, (1) denotes $Sr_3AlO_4F_{(r)}$, (2) denotes $Sr_3AlO_4F_{(air)}$ and (3) is SrF_2 ($\lambda_{ex} = 254nm$).....	36

Figure 2.5: Rietveld refinement plot of neutron diffraction data of $\text{Sr}_3\text{AlO}_4\text{F}_{(\text{air})}$. The red green and pink profiles represent the observed, calculated and difference plots, respectively. The black vertical lines represent the peaks in the $\text{Sr}_3\text{AlO}_4\text{F}$ phase, while the red vertical lines represent the peaks in the SrF_2 phase.39

Figure 2.6: Rietveld refinement plot of neutron diffraction data of $\text{Sr}_3\text{AlO}_4\text{F}_{(\text{r})}$. The red green and pink profiles represent the observed, calculated and difference plots, respectively. The black vertical lines represent the peaks in the $\text{Sr}_3\text{AlO}_4\text{F}$ phase, while the red vertical lines represent the peaks in the SrF_2 phase.40

Figure 2.7: Plot of Δ_{esd} values for (a) FSr_6 octahedra, (b) a -parameter, and (c) Al-Sr(1) distance.41

Figure 3.1: Structure of $\text{Sr}_3\text{MO}_4\text{F}$ where the yellow atoms are F, the purple atoms are Sr, and the blue tetrahedrons represent the MO_4 : a) Unit cell viewed along the 101 plane, while b) $\text{Sr}_{3-x}\text{MO}_4\text{F}$ viewed down the 001 direction.50

Figure 3.2 $\text{Sr}_{3-x}\text{Ba}_x\text{GaO}_4\text{F}$ powder diffraction pattern, where (a) $x = 0.1$, (b) $x = 0.2$, (c) $x = 0.4$, (d) $x = 0.5$, (e) $x = 0.8$, (f) $x = 1.0$, and (g) $x = 1.2$55

Figure 3.3 Diffraction patterns of $\text{Sr}_{3-x}\text{Ca}_x\text{GaO}_4\text{F}$: where (a) $x = 0.0$, (b) $x = 0.2$, (c) $x = 0.3$, (d) $x = 0.4$, (e) $x = 0.6$, (f) $x = 0.8$, and (g) $x = 1.0$. The hkl values along pattern (g) indicate $\text{Sr}_3\text{GaO}_4\text{F}$ phase, while the hkl values along pattern (e) indicate the CaO phase. The star along diffraction pattern (e) represents an impurity peak appearing at approximately $2\theta = 43^\circ$56

Figure 3.4 Rietveld refinement plots of selected powder diffraction patterns using the space group $I4/mcm$ a) $\text{Sr}_3\text{GaO}_4\text{F}$ b) $\text{Sr}_2\text{BaGaO}_4\text{F}$ and c) $\text{Sr}_{2.8}\text{Ca}_{0.2}\text{GaO}_4\text{F}$. The red plot denotes observed data, green pattern indicates calculated pattern, and purple line indicates the difference between observed and calculated patterns.57

Figure 3.5 Composition dependence of the tetragonal lattice parameters in $\text{Sr}_{3-x}\text{A}_x\text{AlO}_4\text{F}$ and $\text{Sr}_{3-x}\text{A}_x\text{GaO}_4\text{F}$, where a) plots the a -parameter as x increases and b) plots the c -parameter. (* indicates data plotted from Prodjosantoso *et al.* ²)59

Figure 3.6: The structure of $\text{Sr}_3\text{MO}_4\text{F}$, where all the atoms in the A(1) layer are shown in yellow and the atoms in the A(2) layer are shown in green. Elongation is evidenced by positive d_i values, while compression is determined by negative d_i values for the A(1) and A(2) layers, respectively.69

Figure 3.7: Global instability index plots of $\text{Sr}_{3-x}\text{A}_x\text{MO}_4\text{F}$, where a) $\text{Sr}_{3-x}\text{Ba}_x\text{GaO}_4\text{F}$ b) $\text{Sr}_{3-x}\text{Ca}_x\text{GaO}_4\text{F}$ c) $\text{Sr}_{3-x}\text{Ba}_x\text{AlO}_4\text{F}$ d) $\text{Sr}_{3-x}\text{Ca}_x\text{AlO}_4\text{F}$ e) $\text{Sr}_{3-x}\text{Ba}_x\text{AlO}_4\text{F}^*$ and f) $\text{Sr}_{3-x}\text{Ca}_x\text{AlO}_4\text{F}^*$. (*indicates data calculated from Prodjosantoso *et al.* ²)71

Figure 3.8: Images of Ba substituted $\text{Sr}_{3-x}\text{A}_x\text{AlO}_4\text{F}$ and $\text{Sr}_{3-x}\text{A}_x\text{GaO}_4\text{F}$ host structures reduced in 5% $\text{H}_2/95\%$ Ar excited under 254 nm lamp a) $\text{Sr}_{2.6}\text{Ba}_{0.4}\text{AlO}_4\text{F}$ b) $\text{Sr}_{2.5}\text{Ba}_{0.5}\text{GaO}_4\text{F}$77

Figure 3.9 Emission and Excitation spectra of $\text{Sr}_{3-x}\text{Ba}_x\text{GaO}_4\text{F}$ where a) $x = 0.1$ b) $x = 0.2$ c) $x = 0.4$ d) $x = 0.5$ and e) $x = 0.8$ 79

Figure 3.10: CIE chromaticity diagram of $\text{Sr}_{3-x}\text{A}_x\text{GaO}_4\text{F}$ materials with $\lambda_{\text{ex}} = 254$ nm where (1) $\text{Sr}_3\text{GaO}_4\text{F}$ (2) $\text{Sr}_{2.9}\text{Ba}_{0.1}\text{GaO}_4\text{F}$ (3) $\text{Sr}_{2.6}\text{Ba}_{0.4}\text{GaO}_4\text{F}$ (4) $\text{Sr}_{2.2}\text{Ba}_{0.8}\text{GaO}_4\text{F}$ (5) $\text{Sr}_{2.8}\text{Ca}_{0.2}\text{GaO}_4\text{F}$ and (6) $\text{Sr}_{2.6}\text{Ca}_{0.3}\text{GaO}_4\text{F}$. Black dots indicate Ba^{2+} substitutions and white dots indicate Ca^{2+} substitutions.....80

Figure 3.11 Emission and excitation spectra of $\text{Sr}_{3-x}\text{A}_x\text{AlO}_4\text{F}$, where a) $\text{Sr}_{2.8}\text{Ca}_{0.2}\text{AlO}_4\text{F}$ b) $\text{Sr}_{2.6}\text{Ca}_{0.4}\text{AlO}_4\text{F}$ c) $\text{Sr}_{2.8}\text{Ba}_{0.2}\text{AlO}_4\text{F}$ and d) $\text{Sr}_{2.6}\text{Ba}_{0.4}\text{AlO}_4\text{F}$ 81

Figure 3.12: CIE chromaticity diagram of $\text{Sr}_{3-x}\text{A}_x\text{AlO}_4\text{F}$ excited by 254 nm light, where 1) $\text{Sr}_{2.8}\text{Ca}_{0.2}\text{AlO}_4\text{F}$ 2) $\text{Sr}_{2.6}\text{Ca}_{0.4}\text{AlO}_4\text{F}$ 3) $\text{Sr}_{2.8}\text{Ba}_{0.2}\text{AlO}_4\text{F}$ and 4) $\text{Sr}_{2.6}\text{Ba}_{0.4}\text{AlO}_4\text{F}$ 82

Figure 4.1: Structure of $\text{Sr}_3\text{MO}_4\text{F}$, where F is represented by green spheres, Sr is represented by blue spheres and MO_4 is represented by yellow tetrahedra with a centered red sphere.88

Figure 4.2: Rietveld refinement plots of $\text{Sr}_{2.2}\text{Ba}_{0.8}\text{Al}_{0.25}\text{Ga}_{0.75}\text{O}_4\text{F}$ using the space group $I4/mcm$. The red diffraction pattern denotes observed data, the green line pattern indicates the calculated pattern, and the difference between observed and calculated patterns is shown below.91

Figure 4.3: Plot of PL excitation and emission spectra of (a) $\text{Sr}_{3-x}\text{Ba}_x\text{Al}_{0.25}\text{Ga}_{0.75}\text{O}_4\text{F}$, (b) $\text{Sr}_{3-x}\text{Ba}_x\text{Al}_{0.5}\text{Ga}_{0.5}\text{O}_4\text{F}$, and (c) $\text{Sr}_{3-x}\text{Ba}_x\text{Al}_{0.75}\text{Ga}_{0.25}\text{O}_4\text{F}$ ($\lambda_{\text{ex}} = 254\text{nm}$). Emission spectra of $\text{Sr}_3\text{MO}_4\text{F}$ type materials under $\lambda_{\text{ex}} = 254$ nm where (d) $\text{Sr}_{3-x}\text{Ba}_x\text{AlO}_4\text{F}$ taken from Park and Vogt⁷ and (e) $\text{Sr}_{3-x}\text{Ba}_x\text{GaO}_4\text{F}$ ⁸94

Figure 4.4: CIE chromaticity diagram of $\text{Sr}_{3-x}\text{Ba}_x\text{Al}_y\text{Ga}_{1-y}\text{O}_4\text{F}$ $\lambda_{\text{ex}} = 254$ nm. The black dots indicate $x = 0.8$, red dots indicate $x = 0.6$, blue dots indicate $x = 0.4$, and orange dots represent $x = 0.2$ in $\text{Sr}_{3-x}\text{Ba}_x\text{Al}_y\text{Ga}_{1-y}\text{O}_4\text{F}$ 95

Figure 4.5: Diffraction patterns of $\text{Sr}_{2.4}\text{Ba}_{0.6}\text{Al}_{0.1}\text{Ga}_{0.9-z}\text{In}_z\text{O}_4\text{F}$ materials, where a) $\text{Sr}_{2.4}\text{Ba}_{0.6}\text{Al}_{0.1}\text{Ga}_{0.875}\text{In}_{0.025}\text{O}_4\text{F}$, b) $\text{Sr}_{2.4}\text{Ba}_{0.6}\text{Al}_{0.1}\text{Ga}_{0.8625}\text{In}_{0.0375}\text{O}_4\text{F}$, c) $\text{Sr}_{2.4}\text{Ba}_{0.6}\text{Al}_{0.1}\text{Ga}_{0.85}\text{In}_{0.05}\text{O}_4\text{F}$, d) $\text{Sr}_{2.4}\text{Ba}_{0.6}\text{Al}_{0.1}\text{Ga}_{0.8375}\text{In}_{0.0625}\text{O}_4\text{F}$, e) $\text{Sr}_{2.4}\text{Ba}_{0.6}\text{Al}_{0.1}\text{Ga}_{0.825}\text{In}_{0.075}\text{O}_4\text{F}$, f) $\text{Sr}_{2.4}\text{Ba}_{0.6}\text{Al}_{0.2}\text{Ga}_{0.775}\text{In}_{0.025}\text{O}_4\text{F}$, g) $\text{Sr}_{2.4}\text{Ba}_{0.6}\text{Al}_{0.2}\text{Ga}_{0.7625}\text{In}_{0.0375}\text{O}_4\text{F}$, h) $\text{Sr}_{2.4}\text{Ba}_{0.6}\text{Al}_{0.2}\text{Ga}_{0.75}\text{In}_{0.05}\text{O}_4\text{F}$, i) $\text{Sr}_{2.4}\text{Ba}_{0.6}\text{Al}_{0.2}\text{Ga}_{0.7375}\text{In}_{0.0625}\text{O}_4\text{F}$, and j) $\text{Sr}_{2.4}\text{Ba}_{0.6}\text{Al}_{0.2}\text{Ga}_{0.725}\text{In}_{0.075}\text{O}_4\text{F}$98

Figure 4.6: Images of $\text{Sr}_{2.4}\text{Ba}_{0.6}\text{Al}_{0.2}\text{Ga}_{0.775}\text{In}_{0.025}\text{O}_4\text{F}$ (a) before and (b) after reduction in 5% H_2 /95%Ar atmosphere $\lambda_{\text{ex}} = 254\text{nm}$101

Figure 4.7: Photoluminescence emission spectra of $\text{Sr}_{2.4}\text{Ba}_{0.6}\text{Al}_{0.2}\text{Ga}_{0.775}\text{In}_{0.025}\text{O}_4\text{F}$ under $\lambda_{\text{ex}} = 254\text{nm}$, where (a) is the PL emission spectrum before reduction in 5% H_2 /95%Ar atmosphere and (b) is the PL emission spectrum after reduction.101

Figure 4.8: Emission and excitation spectra of $\text{Sr}_{2.4}\text{Ba}_{0.6}\text{Al}_y\text{Ga}_{1-y-z}\text{In}_z\text{O}_4\text{F}$, where a) $\text{Sr}_{2.4}\text{Ba}_{0.6}\text{Al}_{0.10}\text{Ga}_{0.875}\text{In}_{0.025}\text{O}_4\text{F}$ b) $\text{Sr}_{2.4}\text{Ba}_{0.6}\text{Al}_{0.10}\text{Ga}_{0.85}\text{In}_{0.05}\text{O}_4\text{F}$, c) $\text{Sr}_{2.4}\text{Ba}_{0.6}\text{Al}_{0.10}\text{Ga}_{0.825}\text{In}_{0.075}\text{O}_4\text{F}$, d) $\text{Sr}_{2.4}\text{Ba}_{0.6}\text{Al}_{0.20}\text{Ga}_{0.775}\text{In}_{0.025}\text{O}_4\text{F}$, e) $\text{Sr}_{2.4}\text{Ba}_{0.6}\text{Al}_{0.20}\text{Ga}_{0.75}\text{In}_{0.05}\text{O}_4\text{F}$, and f) $\text{Sr}_{2.4}\text{Ba}_{0.6}\text{Al}_{0.20}\text{Ga}_{0.725}\text{In}_{0.075}\text{O}_4\text{F}$ at 1050°C. Other samples include g) $\text{Sr}_{2.4}\text{Ba}_{0.6}\text{Al}_{0.10}\text{Ga}_{0.875}\text{In}_{0.025}\text{O}_4\text{F}$, h) $\text{Sr}_{2.4}\text{Ba}_{0.6}\text{Al}_{0.10}\text{Ga}_{0.8625}\text{In}_{0.0375}\text{O}_4\text{F}$, i) $\text{Sr}_{2.4}\text{Ba}_{0.6}\text{Al}_{0.10}\text{Ga}_{0.8375}\text{In}_{0.0625}\text{O}_4\text{F}$ j) $\text{Sr}_{2.4}\text{Ba}_{0.6}\text{Al}_{0.10}\text{Ga}_{0.825}\text{In}_{0.075}\text{O}_4\text{F}$, k) $\text{Sr}_{2.4}\text{Ba}_{0.6}\text{Al}_{0.20}\text{Ga}_{0.775}\text{In}_{0.025}\text{O}_4\text{F}$, l) $\text{Sr}_{2.4}\text{Ba}_{0.6}\text{Al}_{0.20}\text{Ga}_{0.7625}\text{In}_{0.0375}\text{O}_4\text{F}$, m) $\text{Sr}_{2.4}\text{Ba}_{0.6}\text{Al}_{0.20}\text{Ga}_{0.7375}\text{In}_{0.0625}\text{O}_4\text{F}$, and n) $\text{Sr}_{2.4}\text{Ba}_{0.6}\text{Al}_{0.20}\text{Ga}_{0.725}\text{In}_{0.075}\text{O}_4\text{F}$ measured at 900°C and 800°C. Plot (A) represents the excitation spectrum, plot (B) is the emission spectrum (254nm), and plot (C) is the emission spectra (365nm).....104

Figure 4.9: CIE chromaticity diagram for $\text{Sr}_{2.4}\text{Ba}_{0.6}\text{Al}_y\text{Ga}_{1-y-z}\text{In}_z\text{O}_4\text{F}$ materials. The arrows indicate shifts in CIE coordinates from 254nm (black dots) to 365nm excitation (red dots).124

Figure 5.1: Structure of $\text{Sr}_3\text{MO}_4\text{F}$ (left) and Sr_3SiO_5 (right) viewed along the 001 axis. The blue spheres represent Sr, while the red spheres represent O. The yellow and teal octahedral represent AlO_4 and SiO_4 , respectively.135

Figure 5.2: X-ray diffraction patterns of $\text{Sr}_{3-2x}\text{Na}_x\text{Ce}_x\text{GaO}_4\text{F}$, where $x = 0.01, 0.015, 0.02,$ and 0.025138

Figure 5.3: Photoluminescence emission and excitation spectra of $\text{Sr}_{3-2x}\text{Na}_x\text{Ce}_x\text{GaO}_4\text{F}$, where $x = 0.01, 0.015, 0.02,$ and 0.025139

Figure 5.4: XRD patterns of Ge substituted $\text{Sr}_{2.98-x/2}\text{Na}_{0.01}\text{Ce}_{0.01}\text{Ga}_{1-x}\text{Si}_x\text{O}_4\text{F}$, where $0 \leq x \leq 0.20$141

Figure 5.5: XRD patterns of Ge substituted $\text{Sr}_{2.98-x/2}\text{Na}_{0.01}\text{Ce}_{0.01}\text{Ga}_{1-x}\text{Ge}_x\text{O}_4\text{F}$, where $0 \leq x \leq 0.20$142

Figure 5.6: Photoluminescence spectra of $\text{Sr}_{3-x/2}\text{Na}_{0.01}\text{Ce}_{0.01}\text{Ga}_{1-x}\text{Si}_x\text{O}_4\text{F}$ with a post-synthesis reduction temperature of 800°C, 900°C and 1050°C.....150

Figure 5.7: Photoluminescence spectra of $\text{Sr}_{3-x/2}\text{Na}_{0.01}\text{Ce}_{0.01}\text{Ga}_{1-x}\text{Ge}_x\text{O}_4\text{F}$ with a post-synthesis reduction temperature of 800°C, 900°C and 1050°C.....151

Figure 5.8: Comparison of the photoluminescence intensities of $\text{Sr}_{2.93}\text{Na}_{0.01}\text{Ce}_{0.01}\text{Ga}_{0.90}\text{Si}_{0.10}\text{O}_4\text{F}$ reduced at 1050°C under $\lambda_{\text{ex}} = 427\text{nm}$ and $\lambda_{\text{ex}} = 450\text{nm}$, where 450nm indicates blue excitation for LED devices153

Figure 5.9: Comparison of the maximum photoluminescence intensities at 800°C, 900°C and 1050°C of $\text{Sr}_{3-x/2}\text{Na}_{0.01}\text{Ce}_{0.01}\text{Ga}_{1-x}\text{Si}_x\text{O}_4\text{F}$ and $\text{Sr}_{3-x/2}\text{Na}_{0.01}\text{Ce}_{0.01}\text{Ga}_{1-x}\text{Ge}_x\text{O}_4\text{F}$154

Figure 5.10: Dependence of Si^{4+} and Ge^{4+} substituted $\text{Sr}_{3-x/2}\text{Na}_{0.01}\text{Ce}_{0.01}\text{Ga}_{1-x}\text{M}_x\text{O}_4\text{F}$ on chromaticity coordinates. The red, black and blue dots represent the reducing156

LIST OF ABBREVIATIONS

BVS.....	Bond Valence Sum
CCT.....	Correlated Color Temperature
CFL.....	Compact Fluorescent Lamp
IR.....	Infrared
LED.....	Light Emitting Diode
NPD.....	Neutron Powder Diffraction
PL.....	Photoluminescence
RE.....	Rare Earth
UV.....	Ultraviolet
YAG.....	Yttrium Aluminum Garnet ($Y_3Al_5O_{12}$)

CHAPTER 1

INTRODUCTION

Recently, we have witnessed substantial changes in the lighting industry resulting in the availability of compact fluorescent lamps (CFL) and light emitting diode (LED) lights. These represent more energy efficient alternatives to the incandescent light bulb and have already reduced lighting costs. The development of CFLs has been going on for decades involving the early use of naturally fluorescing minerals such as willimite ($\text{Zn}_2\text{SiO}_4: \text{Mn}^{2+}$)¹ in 1935. Halophosphate phosphors were developed in the 1940s with $\text{Ca}_5(\text{PO}_4)_3(\text{Cl},\text{F})$, which has an apatite structure, activated by Sb^{3+} and Mn^{2+} ions being the most prominent one¹. The use of halophosphate phosphors for general home lighting was not appealing to consumers due to its low color rendering index. This sparked the development of rare-earth activated triphosphor materials for fluorescent lamps in the 1970s. Triphosphor materials used in fluorescent lighting include the red emitting $\text{Y}_2\text{O}_3:\text{Eu}^{3+}$, green emitting $\text{CeMgAl}_{11}\text{O}_{19}:\text{Tb}^{3+}$, and blue emitting $\text{BaMgAl}_{10}\text{O}_{17}:\text{Eu}^{2+}$ phosphors²⁻³. In the mid-1990s, Ce^{3+} activated $\text{Y}_3\text{Al}_5\text{O}_{12}$ used in white light LEDs was introduced and is currently being used for home and industrial lighting needs⁴.

Phosphors are materials that exhibit luminescence when activated by radiation. These materials are often doped with transition metal or rare earth ions called activators. The activator ions have excited state electronic levels that are occupied either by direct

excitation or by energy transfer from sensitizer ions, which transfer energy via dipole-dipole or multipolar interactions⁵⁻⁷.

While many advances were made in lighting technology over time, the continued production of solid-state lighting materials containing rare earths is in jeopardy. It is projected that rare-earth oxide demand will surpass the supply of rare-earth oxide materials. Furthermore, China controls approximately 97% of the global market. The export of these materials will also decrease due to China's own growing demand. This supply and demand situation for rare-earth materials may eventually cause lighting research to focus more and more on the development of rare-earth free lighting materials and/or organic light emitting devices (OLEDs)⁶. A 2011 report by Philips Lighting Company, showed the critical need for rare-earths oxides to sustain the global demand for lighting materials. The main rare earth ions needed for phosphor materials are Lanthanum (La), Europium (Eu), Cerium (Ce), Terbium (Tb), Erbium (Er), and Yttrium (Y). Shortages of rare-earth materials impact not only the production of phosphors, but also magnets, medical imaging units, metallic alloys and catalysts used in petroleum refining⁸.

While incandescent bulbs have been the most commonly used form of lighting, focus has shifted towards the production of compact fluorescent lamps (CFLs) and light emitting diode (LED) lamps. This is due to the incandescent lamp's low efficiency, where only about 5% of the energy is converted to visible light. CFLs and LEDs have greater efficiencies near 20% and 50%, respectively⁹. Of the lamps that use phosphor materials, CFLs have been available in retail stores for years. While the availability is currently greater than for LED lamps, there is an environmental risk associated with the

disposal of this lamp due to its mercury content. The implementation of LED lamps allow for a more safe and efficient means of lighting with longer lifetimes.

Fluorescent lamps are based on low-pressure gas (Hg) discharge lamps. The fluorescent lamp is a sealed glass tube that contains a small amount of mercury and an inert gas. The tube also contains a phosphor powder coating on the inside of the glass. Electrons and ions created in the tube interact with the mercury atoms at low pressures *via* collisions causing UV emissions at 185 nm and 254 nm. The emission at these wavelengths by mercury is the excitation energy for the coated phosphors and subsequently causes a visible PL emission ¹⁰.

There are three main methods of producing high intensity white light LEDs. One method is to rely on individual LEDs that emit red, green, and blue light. These are known as primary colors to produce white light. An alternative method of producing white light LEDs involves coating a blue light emitting semiconductor chip, such as $\text{In}_x\text{Ga}_{1-x}\text{N}$, with red and green emitting phosphors to produce “warm” white light or by coating it with a yellow emitting phosphor to create “cool” white light LED assemblies. The latter was used in the first commercially available white light emitting LED made by the Nichia Corporation, where the emission from the $\text{In}_x\text{Ga}_{1-x}\text{N}$ semiconductor chip ($x = 0.3$) is combined with the yellow emission of Ce^{3+} doped $\text{Y}_3\text{Al}_5\text{O}_{12}$ (YAG: Ce^{3+}) phosphor by coating the luminescent phosphor materials onto the blue emitting semiconductor chips ¹¹. Such a lamp has poor color rendering. This led to a different approach for white light emitting LEDs, where a blue emitting semiconductor chip can be coated by both the yellow emitting YAG: Ce^{3+} phosphor and a red emitting phosphor. Examples of these LED types are shown in Figure 1.1.

Light can be characterized as “warm” or “cool” based on the correlated color temperature (CCT), which is based on the spectrum of light emitted from heating a blackbody. As the temperature increases, the color of light emitting from a blackbody ranges from red and orange at lower temperatures to blue at higher temperatures. Although red, orange and yellow colors emit at lower temperatures, the colors themselves are generally perceived as warm. Incandescent bulbs have color temperatures values ranging from 2700K-3000K. Cool white CCT values are around 5000K, which correspond to a bluish-white color.

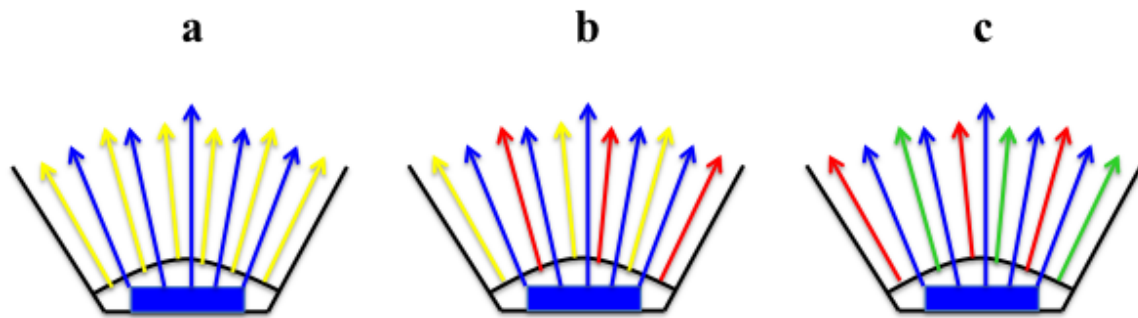


Figure 1.1: Diagram of PC-LED lighting assemblies, (a) blue semiconductor chip with yellow phosphor, (b) blue semiconductor chip with yellow and red phosphor, and (c) blue semiconductor chip with red and green phosphor.

The Physics of Photoluminescence

Photoluminescence is a process involving the absorption of light energy, which excites electrons in a material and their subsequent de-excitation causes light to be emitted. The remaining energy not used to produce light appears as vibrational energy or heat. The time in which the decay process can occur ranges from 10^{-9} s to 10^{-3} s in fluorescence and from 10^{-3} s to 100 sec in phosphorescence⁷. The emission of light may

be more or less energetic than the excitation energy. A Stokes shift occurs when materials absorb higher energy radiation, and emit lower energy light. Anti-Stokes shifts occur by the absorption of lower energy radiation (i.e in the IR region) and the subsequent emission of higher energy light (i.e in the visible region). Similarly, Stokes and anti-Stokes shifts can be referred to as down- and up-conversion, respectively. In this dissertation photoluminescent materials were explored with respect to their Stokes shift or down-conversion of near and far UV to produce light in the visible region.

The Configurational Coordinate Model for Photoluminescence

The configurational coordinate model uses potential energy curves of electronic states as a function of a configurational coordinate. This coordinate can be, for instance, one of the vibrational modes of an atom involved such in a symmetrical stretch where the central atom, i.e. of an octahedron is at rest, and the ligands are oscillating around the center. In this model the lower parabola represents the ground state. Its shape is parabolic having a minimum at R_0 , which corresponds to an equilibrium distance in the ground state. This is due to the underlying assumption of a harmonic oscillator⁵. In the excited electronic state there can be a different minimum configurational coordinate. These differences are due to the fact that in the excited state the chemical bond is weaker than in the ground state⁵. This is caused by electrons being promoted to non-or antibonding orbitals which cause the bond length to increase and the bond strength to weaken.

In the absorption processes described in the configurational coordinate model, the transitions between the ground state and excited state parabolas are electronic transitions, which also involve interactions between the electrons and the vibrations of

the optical centers. In the case of a weak vibrational coupling, the electron is promoted from the ground state to an excited state, with little or no change of the configurational coordinate since the electrons move much faster than the nuclei. This is based on the Born and Oppenheimer approximation¹⁰. As a result of the near static nature of the atoms compared to the electrons, the absorption of energy is represented as a vertical electronic transition in the configurational coordinate diagram. This is also known as the Frank Condon principle¹⁰.

The photoluminescence of materials is illustrated in Figure 1.2. The electronic transition starts from the lowest vibrational level $\nu = 0$ in the electronic ground state. The most probable transition occurs at R_0 where the vibrational wave function has its maximum value. The transition will end at the edge of the excited electronic state parabola, since it is there that the vibrational levels of the excited state have their highest amplitude. This transition corresponds to the maximum of the absorption band. Once the excited state is reached, a rapid relaxation process to the lowest vibrational state in the excited state occurs, and heat is generated. The electron subsequently returns to the ground state and a photon is emitted. In the emission spectra an intermediate to broad emission band is generally noticed due to the loss of vibrational energy in the relaxation process in the excited state. There is an increase of the configurational coordinate from R_0 to R due to the occupation of non-bonding or anti-bonding orbitals in the electronic excited state.

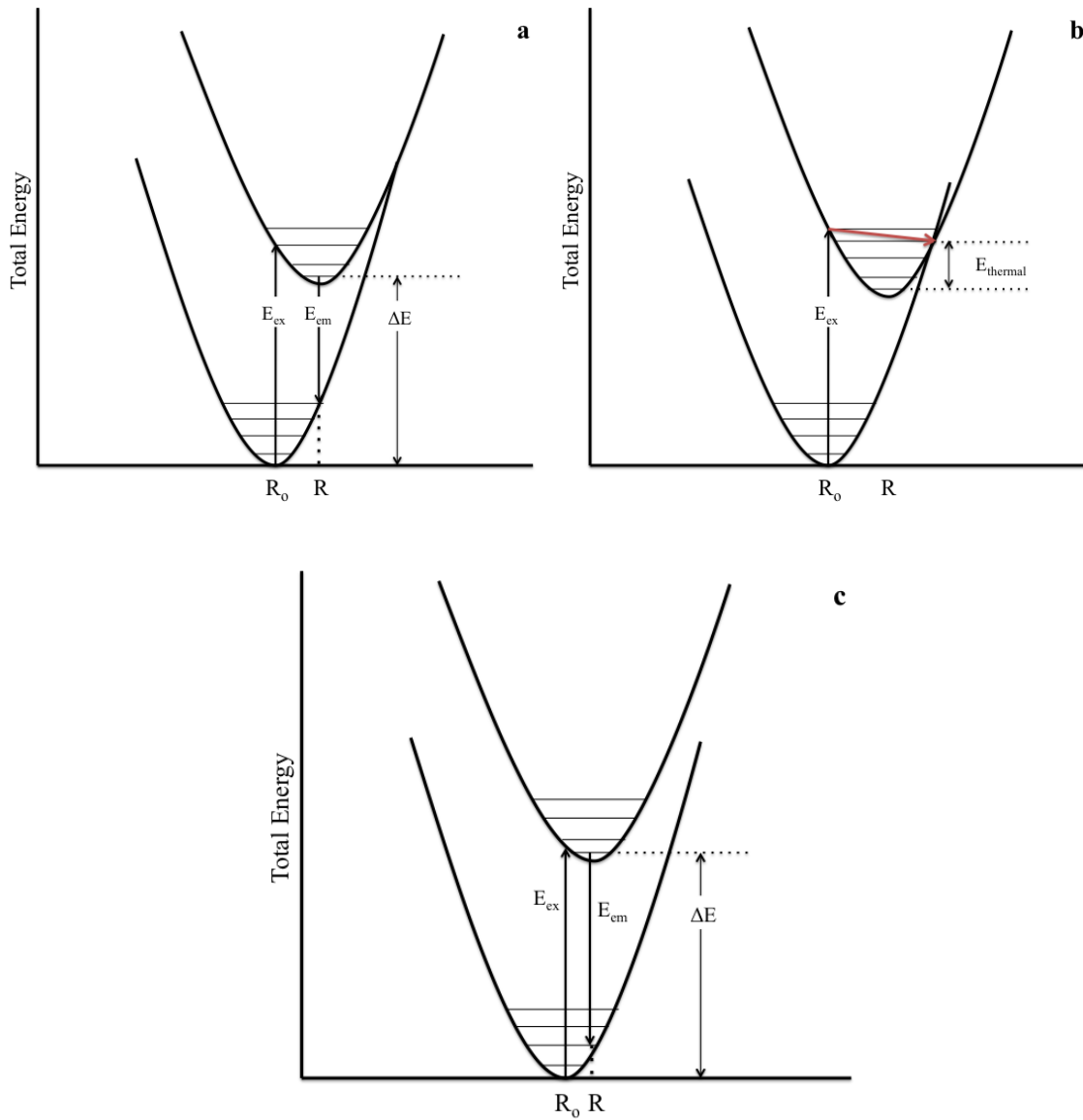


Figure 1.2: The configurational coordinate diagram for luminescence of phosphor materials

A major concern for phosphor based LEDs is the availability of phosphors that are chemically stable and have low thermal quenching properties. The largest decrease in the photoluminescence emission intensity occurs between 150°C-200°C. Thermal quenching is a phenomenon where luminescence is decreased at higher temperatures. The temperature dependence of luminescence depends on the energy difference between the

excited state and its intersection with the ground state, through which a radiationless transition to the ground state can be made as depicted in the configurational coordinate model. The addition of thermal energy (E_{thermal} in Figure 1.2b) may be sufficient to raise the vibrational energy of the system to the point where an electron in the excited state can return to the ground state without emitting photons. This occurs when there is an increased coupling between the luminescent center and its host.

When two parabolas lie above one another in the configurational coordinate diagram seen in Figure 1.2c, a narrow line represents the bandwidth of the optical transition. This is called a weak-coupling scheme, where $\Delta R \approx 0$. This case is normally seen when trivalent rare-earth ions are substituted into a host.

Concentration Quenching

In addition to thermal quenching reducing the PL intensity of phosphor materials at high temperature, the concentration of RE ions or other luminescent centers doped within a structure also impacts the photoluminescence yield. As the concentration of luminescent centers/ RE ions increases, the PL intensity will increase until a critical concentration is reached. The critical concentration is the level of substitution where the highest PL emission intensity occurs. Substitution above the critical concentration results in a decrease of the photoluminescence intensity. This effect is called concentration quenching. The quenching effect can be attributed to the reduced distance between luminescent centers, which allow for the excitation energy to be transferred several times before emission occurs. The critical distance (R_c) can be defined as the distance between RE ions and is calculated using Blasse's equation¹²

$$R_c \approx 2 \left(\frac{3V}{4\pi\chi_c N} \right)^{1/3} \quad (1.1)$$

, where V is the volume of the unit cell, N is the number of the available cation sites in the unit cell, and χ_c denotes the critical concentration of RE ions. It is to be expected that the luminescent centers aggregate/cluster, which will affect luminescence and reduce the yield compared to ideally separated centers¹⁰. The luminescence caused by the substitution of rare-earth ions/activators needs to also take into account the selection rules for allowed electronic transitions.

Selection Rules for Photoluminescence

The luminescence caused by the substitution of rare-earth ions/activators needs to also take into account the selection rules, which dictate whether optical transitions are allowed or not. The selection rules are expressed in Russell-Saunders terminology, where L is the sum of the angular momentum (Σl) of the electron, S is the sum of the spin quantum number (Σs), and J represents the total angular momentum ($L \pm S$)⁷. The combination of the terms L and S allows is known as Russell-Saunders coupling or L-S coupling. The spectroscopic terms given in Russell-Saunders are written as $^{2S+1}L_J$. The L values (0, 1, 2, and 3) correspond with the terms S, P, D, and F, respectively. These terms were originated by Balmer in 1890 for the characterization of the spectra for the hydrogen atom⁷.

These rules, which apply to dipole transitions, are defined by the following conditions:

$$\Delta L = \pm 1 \quad \Delta S = 0 \quad \Delta J = \pm 1, 0. \quad (1.2)$$

However an electronic transition between two spectroscopic terms, where $J = 0$ is not allowed⁷.

Although selection rules may characterize an electronic transition to be “forbidden”, photoluminescence will still be observed due to crystal field splitting caused by structural distortions (i.e. Jahn-Teller effect) but with lower intensities.

The trivalent lanthanide ions (RE^{3+}) have an outer electron configuration $5s, 5p, 4f^n$, where n varies from 1 (Ce^{3+}) to 13 (Yb^{3+}), which corresponds to the number of electrons occupying the unfilled $4f$ shell. These valence $4f^n$ electrons are responsible for the observed optical transitions in PL and are shielded by the outer electrons of the $5s$ and $5p$ electrons of the $5s^2 5p^6$ less electron configurations¹⁰. Due to shielding by the $5s$ and $5p$ electrons, the valence electrons of the RE^{3+} ions are weakly affected by the ligand ions in crystals, which correspond to a weak crystal field. Consequently, the spin-orbit interaction term of the free ion Hamiltonian is dominant over the crystalline field Hamiltonian term, causing the $^{2S+1}L_J$ states of the $(RE)^{3+}$ ions to be slightly perturbed when these ions are incorporated into the crystals⁷. The crystal field effect produces a slight shift in the energy of these states and cause additional level splitting. The extent to which this shift occurs as well as the splitting energy is much smaller than the spin-orbit splitting. This results in optical spectra that resemble those of free ions. Additionally, the main features of the absorption and luminescence of the trivalent lanthanide ions varies little from one structure to the next. This observation made by Dieke and collaborators produced what is now known as Dieke diagrams in 1968^{5,7,10}.

The spectroscopic terms for the ground state Ce^{3+} ion according to Russell-Saunders can be determined by its ground state electron configuration ($4f^1$). Since there is only one valence electron in the outer 4f shell, the $+1/2$ spin state (S) yields $2S+1 = 2$. The L term has a value of 3, thus the ^{2S+1}L designation is 2F . As previously stated, the J term is defined as $L \pm S$, which yields values of $7/2$ and $5/2$, respectively. When the excited electron returns to the ground state, it may go to either the $^2F_{7/2}$ or $^2F_{5/2}$ level. This splitting gives the Ce^{3+} ion a characteristic double band shape.

In order to increase the efficiency of the photoluminescence emission in phosphors, sensitizers are often used. Sensitizers are used to transfer energy to the activator ions. An example of a phosphor that employs sensitizers is the aforementioned $Ca_5(PO_4)_3(Cl,F): Sb^{3+}, Mn^{2+}$, where Sb^{2+} serves a dual role as sensitizer *and* activator. The Mn^{2+} also serves as an activator ion. The sensitization process is detected by photoluminescence excitation spectra, where these two ions have similar energy bands. As the concentration of Mn^{2+} increases, the energy band for Sb^{2+} decreases due to the energy transfer process. This process is also seen when Ce^{3+} and Tb^{3+} are co-doped in Sr_3AlO_4F , where Ce^{3+} acts as a sensitizer and activator^{4,13}.

Host structures are also capable of sensitizing luminescent centers. This process, called host sensitization, occurs by energy transferring from recombined electron-hole pairs or thermalized electron-hole pairs to luminescent centers. Rare-earth ions as well as transition metal ions absorb this energy by acting as electronic traps⁴.

Photoluminescence Measurements

Photoluminescence data was collected using a Perkin Elmer LS 55 fluorescence spectrometer with a fiber optic attachment. This instrument is equipped with a xenon flash tube that travels along the path outlined in Figure 1.3. The spectral range of the excitation monochromator is 200-800nm, while the emission of the monochromator ranges from 200-900nm. The slit widths can also be varied from 2.5 to 15 nm for the excitation monochromator and between 2.5 and 20 nm for the emission monochromator. Results from the emission spectrum can be used in the Color Calculator program by Osram Sylvania to provide the CIE chromaticity coordinates within this dissertation¹⁴.

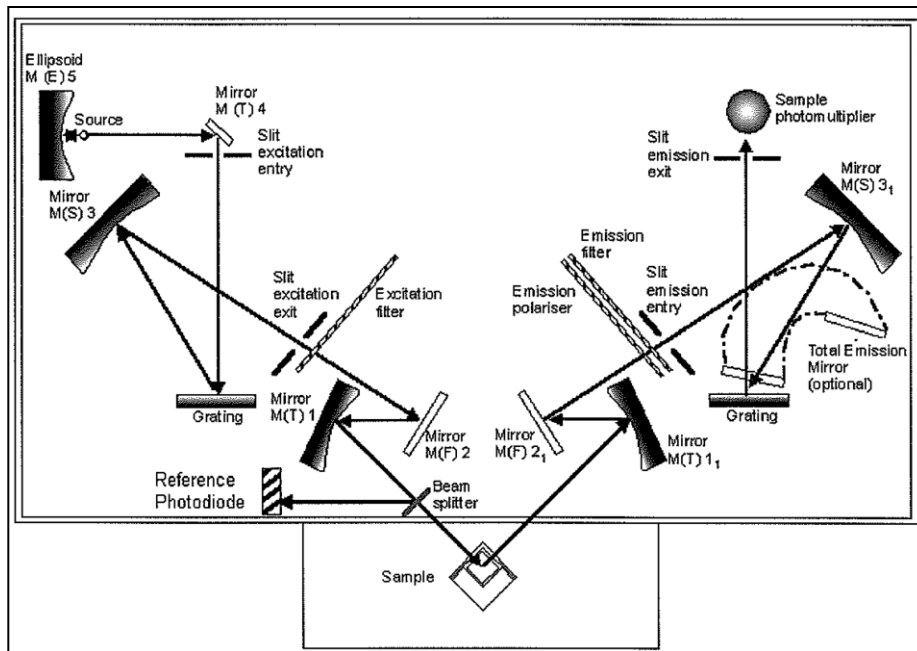


Figure 1.3: Diagram of the Perkin Elmer LS55 spectrofluorometer¹⁵

The generation of chromaticity coordinates is a wonderful tool that allows for researchers to effectively communicate the color that the phosphor materials produce when excited. These values, denoted by x and y , are normalized and can be used to

compare colors with different intensity values. The equation $x + y + z = 1$ is derived from equation relating to color specification $x = X/X+Y+Z$, $y = Y/X+Y+Z$ and $z = Z/X+Y+Z$, where X , Y , and Z represent the tristimulus values for the colors red, green and blue, respectively¹⁶. The CIE chromaticity diagram used throughout this dissertation is shown in Figure 1.4.

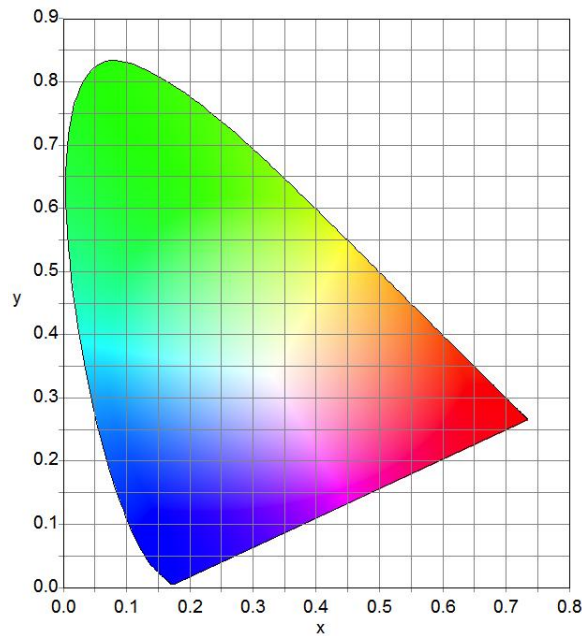


Figure 1.4: CIE chromaticity diagram¹⁴

Diffraction and Crystallographic Techniques

X-rays are generated when electrons collide with a metal target within an evacuated x-ray tube. The irradiation of the metal target by electrons produces a significant amount of heat and cooling is a must. Approximately 30 to 50 kilovolts are needed for diffraction work to take place¹⁷. Copper targets have K lines near 1.5418 \AA . Ordinarily only the K lines are useful in x-ray diffraction, since the longer-wavelength x-rays are too easily absorbed by materials. There are several lines in the K set, but only

the three strongest are observed in normal diffraction work. These are the $K\alpha_1$, $K\alpha_2$, and $K\beta_1$. The α_1 and α_2 components have wavelengths so close together that they are not clearly resolved as separate lines; if they are resolved, it is called the $K\alpha$ doublet, but if they are not it is referred to as the $k\alpha$ line. Similarly $K\beta$ is referred to as the $K\beta$ line¹⁷⁻¹⁸.

In order for samples to be analyzed by the diffractometer the incident radiation generated by the source must be diffracted by the atoms in the planes of the crystal structure. The condition, which must be met for diffraction to occur is Bragg's law:

$$n\lambda = 2d\sin \theta. \quad (1.3)$$

The variable n is known as the order of diffraction and is equal to the number of wavelengths in the path difference between x-rays scattered by adjacent planes.

Therefore for fixed values of λ and d , the angles of incidence (θ) may have many values at which diffraction can occur¹⁸⁻²⁰. In a first order case, where $n = 1$ reflection, the scattered x-rays in Figure 1.5 would differ in path length by one wavelength. The rays scattered by the atoms in each plane are considered to be in phase and forms a diffracted beam.

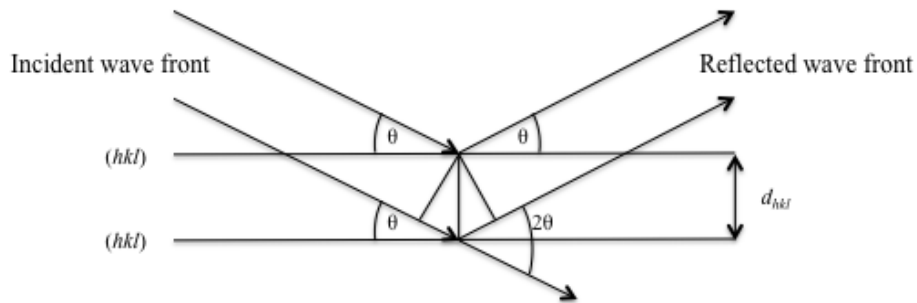


Figure 1.5: Diffraction of x-rays in accordance with Bragg's law

Bragg's law can be applied experimentally by using x-ray, neutron, or electron beams of a known wavelength and measuring θ . This will allow for the determination of the d spacing, which is the basis for structural analysis.

After synthesis of solid samples, a Rigaku Miniflex was used in the analysis of these solid samples via powder x-ray diffraction. The Rigaku Miniflex uses a Cu target that produces Cu- α x-rays needed for analysis. A Ni filter is used to suppress the $k\beta$ radiation for a monochromatic beam with a wavelength of 1.5406\AA . The diffractometer is equipped with a vertical goniometer with a radius of 150 mm. The scanning range is between -3° to $150^\circ 2\theta$, while the measurement range is between $+2^\circ$ to $150^\circ 2\theta$. The detector in the Rigaku Miniflex has a 24mm diameter and a 45 mm length. The scintillator material in the x-ray detector is made of NaI, while the window material is composed of Beryllium²¹.

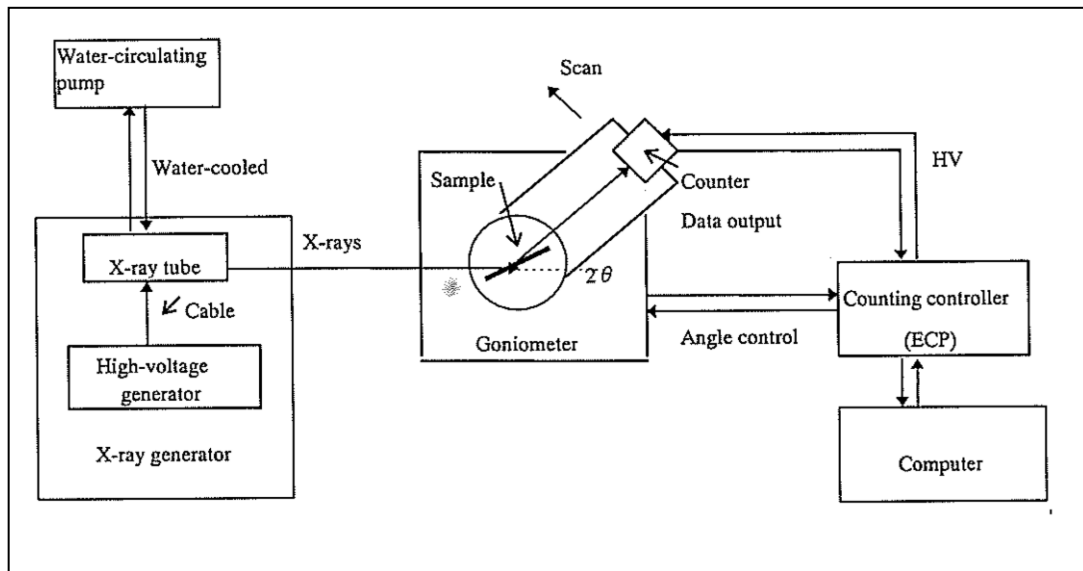


Figure 1.6: Diagram of the Rigaku Miniflex X-ray diffractometer²¹

Neutron beams

Neutron beams are often produced in a nuclear reactor and have a nearly continuous spectrum which can be used in a variety of ways^{17,20}. X-rays differ from neutrons in terms of their scattering by the atomic nuclei. Since nuclei are much smaller than the electron clouds used to scatter x-rays, nuclear neutron scattering is called point scattering. The scattering factors are therefore constant over the entire range of Bragg angles. The greatest advantage of neutron diffraction is that the scattering functions are not proportional to the atomic number and they also are different for isotopes of the same element.

These advantages for neutron diffraction allows for the neighboring elements on the periodic table to be distinguished from one another. The neutron scattering lengths for Sr, Al, O, and F are 7.02(2) fm, 3.449(5) fm, 5.805(4) fm, and 5.654(12) fm, respectively. These scattering lengths are consistent for the entire range of data collection while the x-ray scattering factor decreases over the range of $\sin \theta/\lambda = 0$ ²².

The neutron data used in this dissertation were collected at the Australian Nuclear Science and Technology Organization's (ANSTO) research reactor at Lucas Heights, Australia by Dr. Maxim Avdeev. The $\text{Sr}_3\text{AlO}_4\text{F}$ samples analyzed *via* neutron diffraction were sealed in a vanadium container using an indium wire. The data was collected using a neutron beam with a $\lambda = 1.300\text{\AA}$ generated by a Ge 355 monochromator²³.

Rietveld Refinement

After samples are measured by x-ray diffraction or neutron diffraction, Rietveld refinement is used to determine various structural properties of the samples such as lattice parameters, number of phases, and pertinent structural parameters. Rietveld refinement is a powerful tool that is often used to refine the structural properties of materials as well as determine the components of unknown materials based on their diffraction pattern.

The x-ray diffraction patterns are refined using the GSAS suite of programs²⁴, where the observed diffraction pattern is used to refine a calculated diffraction pattern based on a model. A “goodness of fit” determines the quality of the structural model²⁴. In this method, the powder data is digitized in order to be used by computers. These values are represented as a numerical intensity (y_i) at each of several thousand steps (i) in the diffraction pattern²². These increments or steps may be in terms of scattering angle, 2θ , or some energy parameter such as velocity (time of flight neutron data) or wavelength (for X-ray data collected with energy dispersive detector and an incident beam of white X-radiation)²³. For data collected by a diffractometer at a constant wavelength, the steps are usually in terms of scattering angle and the intensity y_i at each step i , in the pattern²².

The main goal for employing the Rietveld method is to have an optimal least squares fit to all of the y_i values simultaneously. The quantity minimized in the least-squares refinement is the residual S_y :

$$S_y = \sum_i w_i (y_i - y_{ci})^2 \quad (1.4)$$

where, $w_i = 1/y_i$, y_i = observed intensity at the i th step, y_{ci} = calculated intensity at the i th step, and the sum is overall data points.

A powder diffraction pattern is a series of individual profiles, each possessing a peak height, a peak position, a breadth, tails which decay gradually with a distance from peak position, and an integrated area which is proportional to the Bragg intensity, I_K , where K represents the Miller indices, h , k , and l . The value I_K is proportional to the square of the absolute value of the structure factor $|F_K|^2$.

Typically, many Bragg reflections contribute to the intensity, y_i , observed at any arbitrary chosen point i in the pattern. The calculated intensities (y_{ci}) are determined from the $|F_K|^2$ values calculated from the structural model from summing of the calculated contributions from neighboring Bragg reflections in addition to the background expressed by:

$$y_{ci} = s \sum_K L_K |F_K|^2 \phi \sin^2 2\theta_K - 2\theta_K P_K A + y_{bi} \quad (1.5)$$

In this equation s is the scale factor, K represents the Miller indices h , k , and l for a Bragg reflection, L_K contains the Lorentz polarization, and multiplicity factors, ϕ is the reflection profile function, P_K is the preferred orientation function, A is an absorption factor, F_K is the structure factor for the K th Bragg reflection and y_{bi} is the background intensity at the i th step.

When analyzing samples via x-ray diffraction, parameters are likely to change from one sample to the next. One of these parameters is preferred orientation. Preferred orientation of analyzed samples occurs when there is a tendency for the crystallites to be

oriented in a random fashion. This may produce systematic distortions in the reflection intensities. This can be a result of how the sample is packed.

The background intensity may be obtained from a table of background intensities, a linear interpolation between user-selected points in the pattern, or a specified background function. Background functions in the GSAS program include as many as 36 parameters, however it is common to use 1-12 parameters.

The reflection profile function (ϕ) predicts/models the effects of both instrumental features and specimen features, which may include aberrations due to absorption, specimen displacement, and specimen-caused broadening of the reflection profiles. In refinement programs, some of the most widely used programs include two different pseudo-Voigt functions, the Pearson VII function, and Gaussian, Lorentzian and modified Lorentzian functions.

The structure factor (F_K) is given by

$$F_K = \sum_j N_j f_j B_j \exp \left[2\pi i (hx_j + ky_j + lz_j) \right] \quad (1.6)$$

, where h , k , and l are the Miller indices, x_j , y_j , and z_j are the position parameters of the j th atom in the unit cell and f_j is the x-ray atomic scattering factor and N_j = site occupancy multiplier for the j th atom site. The term B_j refers to the temperature factor, which describes the thermal motion of the j th atom.

The Rietveld method can be applied to both x-ray and neutron diffraction, however, the expression f_j is replaced by b_j (neutron scattering length) when refining

neutron data. This is due to the x-rays being scattered solely by electrons, whereas the scattering factors for neutrons¹ are constants and do not vary with increasing Z ^{17,22}.

The Rietveld method allows for the aforementioned variables/ parameters to be changed until a global minimum is reached. R-values are used to compare the observed and calculated diffraction patterns, where R_{wp} is considered to be the most useful due to the numerator of the residual being minimized and subsequently reflects the progress of the refinement. R_{wp} is defined by the formula:

$$R_{wp} = \left\{ \frac{\sum w_i (y_i(obs) - y_i(calc))^2}{\sum w_i (y_i(obs))^2} \right\}^{1/2} \quad (1.7)$$

Calculating the Bond Valence sums of Sr_3MO_4F

According to a formalism developed by I.D. Brown²⁵ the individual bond valence of an atom can be calculated using the equation:

$$S_{ij} = \exp((r_0 - r_{ij}) / B) \quad (1.8)$$

where S_{ij} is the individual bond valence between atoms i and j in the material, r_{ij} is the actual bond length between atoms i and j , r_0 is the ideal bond length tabulated by Brown and Wu²⁶ and B is an empirical constant with a value of 0.37 \AA^{26} . After refining the Sr_3MO_4F structure, we obtain bond lengths that are sufficient to calculate the bond valence sum (BVS) values. The 10-coordinated Sr occupy the A(1) site, where 8 bonds are formed with O and the other 2 with F. The 8-coordinated Sr located at the A(2) site has 2 different types of bonds between Sr and O (4x, 2x) and 2 bonds with F. A diagram

¹ Neutrons can scatter electrons via spin interactions

of the Sr(1) and Sr(2) coordination environments can be found in Prodjosantoso *et al*²⁸. The *M* ions are coordinated to 4 O atoms forming a tetrahedra. The F ions are 6-coordinated as a FSr_6 octahedra, where F-Sr(2) bonds are the equatorial bonds and the F-Sr(1) bonds are the axial bonds. The BVS values for O can be calculated by simply adding the individual bond valences of the nearest neighbors. These nearest neighbors are show in Figure 1.7. The bonds with the nearest neighbors consist of 2 Sr(1)-O, 2 Sr(2)-O short bonds, 1 Sr(2)-O long bond, and 1 *M*-O bond.

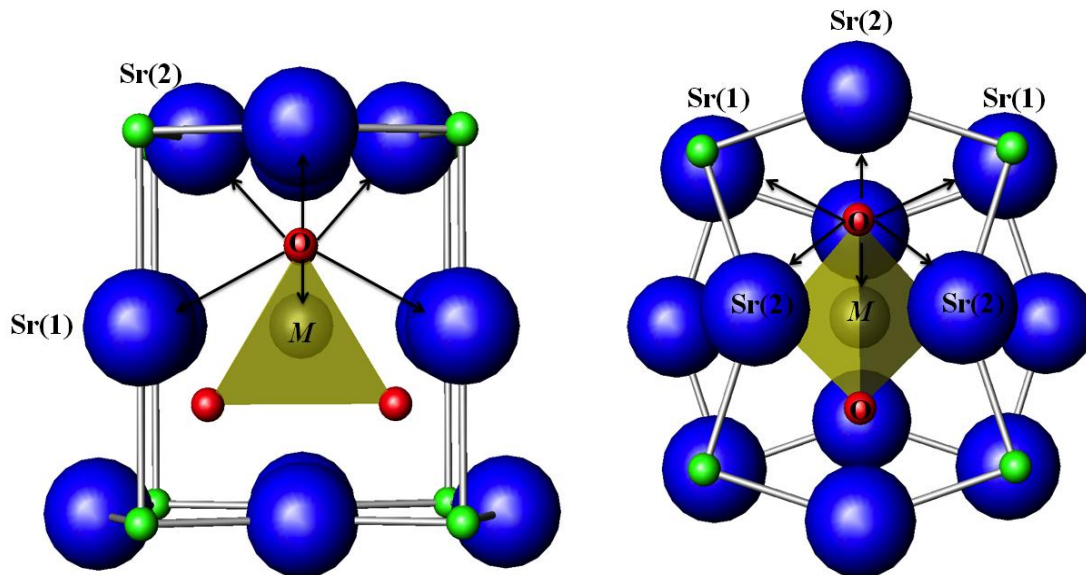


Figure 1.7: Oxygen nearest neighbors in $\text{Sr}_3\text{AlO}_4\text{F}$

Applying the bond-valence method, developed by I.D. Brown²⁹ to $\text{Sr}_3\text{MO}_4\text{F}$ reveals that the Sr^{2+} in the A(1) site is “under bonded” as shown by its valence sum of only 1.30. Prodjosantoso *et al.* experimentally confirmed by structural refinements of x-ray data that therefore the smaller Ca^{2+} ions preferentially occupy the A(2) sites, while the larger Ba^{2+} ions have a tendency to occupy the A(1) sites within the $\text{Sr}_3\text{MO}_4\text{F}$ host lattice²⁸. The bond lengths for Ba^{2+} in a A(1) site are closer to its ideal bond lengths (R_0)

and yields a bond valence sum near 2, while the coordination in a A(2) site will result in the bond-valence sum rising significantly above 2. In the solid solution $\text{Sr}_{3-x}\text{Ca}_x\text{AlO}_4\text{F}$ ($0 \leq x \leq 1$) only the A(2) sites contain Ca^{2+} . Likewise in the solid solution $\text{Sr}_{3-x}\text{Ba}_x\text{AlO}_4\text{F}$, only when $x \geq 0.8$ will Ba^{2+} occupy the A(2) sites²⁸.

$A_3\text{MO}_4\text{F}$ Synthesis and Structure

This dissertation focuses on the exploration of oxyfluorides in the $A_3\text{MO}_4\text{F}$ family as potential phosphors for CFL and LED phosphors. Oxyfluoride host structures can combine the positive physical attributes of oxide and fluoride structures. Oxides exhibit chemical stability to withstand UV photons; however their high phonon frequency usually results in significant thermal quenching. Fluoride materials experience reduced phonon modes due to the increased bond strength.

Solid-state synthesis of $A_3\text{MO}_4\text{F}$ Materials

The synthesis of $A_3\text{MO}_4\text{F}$ materials involves the intimate mixing of solid starting materials in a mortar and pestle followed by heating in 24h cycles at 700°C, 800°C, 900°C and annealed between 1050°C to 1100°C. Information regarding the specific formulations of $A_3\text{MO}_4\text{F}$ materials is given in the respective chapters. The process for synthesizing this class of materials is known as the solid-state or ceramic method. Traditionally, this synthetic method requires more time for the reactants to diffuse through the solid interfaces. To increase the reaction rate in the ceramic method, the solid reactants are pressed into pellets before heating³⁰⁻³¹. As products form, the reaction rate steadily decreases as the diffusion path length increases. To further improve the reaction and allow the reaction to proceed towards completion, the solid sample is

crushed and re-ground to allow for new interactions to occur between unreacted solid materials³¹.

The photoluminescent properties of these materials are induced by a post-synthesis reduction step using a 5% H₂/95% Ar gas mixture. Each sample is placed into an alumina boat and heated in a Lindberg/Blue Mini-Mite™ tube furnace, where the tube is made of alumina. The ends of the tube are fitted with hollow aluminum fittings that allow the reducing gas to freely flow through and control the atmosphere surrounding the sample. Figure 1.8 shows the setup of the tube furnace. Each sample, regardless of reducing temperature, was heated at the reducing temperature for three hours.



Figure 1.8: Tube furnace setup for reduction of materials

Structure of A₃MO₄F materials

The A₃MO₄F-type materials Sr₃AlO₄F and Sr₃GaO₄F (shown in Figure 1.9) were first structurally characterized by Vogt *et al.* and belong to the tetragonal *I4/mcm* space group. The lattice parameters for the Sr₃AlO₄F structure is $a = 6.7819(1) \text{ \AA}$ and

$c = 11.1437(2) \text{ \AA}$, while the lattice parameters for the $\text{Sr}_3\text{GaO}_4\text{F}$ structure is $a = 6.7819(1) \text{ \AA}$ and $c = 11.3662(3) \text{ \AA}$ ³².

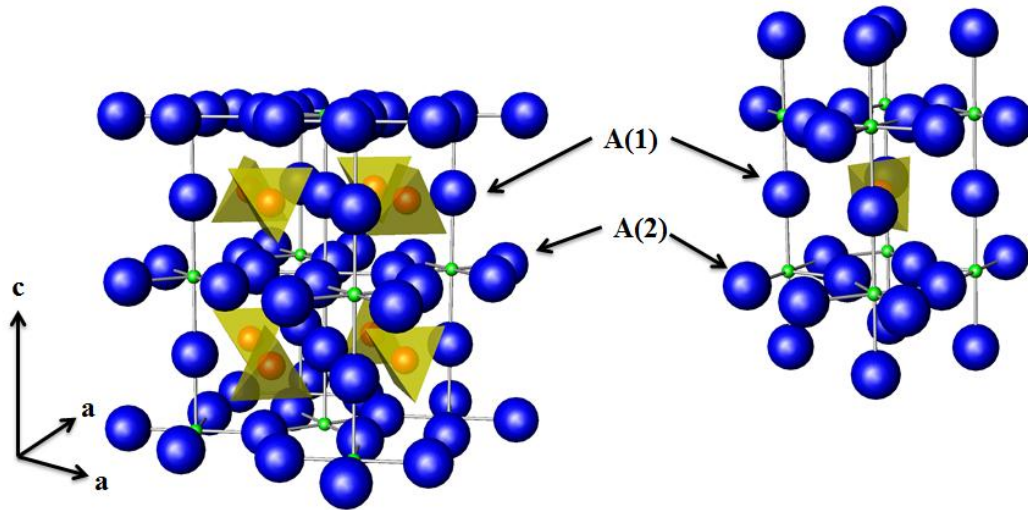


Figure 1.9: Structure of A_3MO_4F

One way of describing the structure of $\text{Sr}_3\text{MO}_4\text{F}$ lattice is as a distorted anti-perovskite structure. The traditional perovskite structure has the formula ABX_3 shown in Figure 10a and refers to the highly symmetric cubic structure ($Pm-3m$), where A and B are cations and X are anions. The overall structure is an arrangement of corner-sharing octahedra, with the B cation occupying the center position of the octahedra.

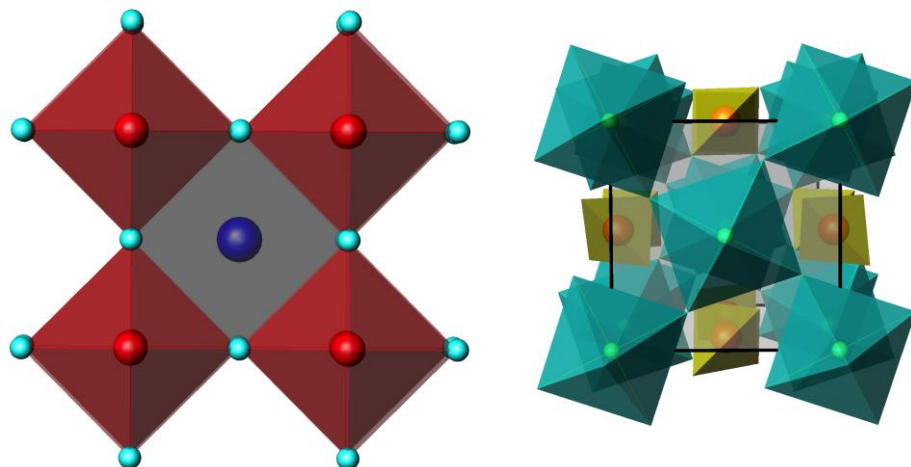


Figure 1.10: Comparison of Perovskite structure of (a) SrTiO_3 and distorted anti-Perovskite (b) $\text{Sr}_3\text{MO}_4\text{F}$ in the 001 direction.

In the anti-perovskite structure, F^- occupies the octahedral B site while the 6 Sr^{2+} ions occupy the corner-sharing octahedral X sites (anion sites in an oxide or halide perovskite), and the AlO_4^{5-} ions occupy the A-site. Compared to cubic perovskite structures, the symmetry is lowered by an axial elongation of the FSr_6 octahedra in $\text{Sr}_3\text{AlO}_4\text{F}$. The axial $\text{F}-\text{Sr}(1)$ distance is $2.7869(1)\text{\AA}$, while the equatorial $\text{F}-\text{Sr}(2)$ distance is $2.5188(8)\text{\AA}$ in $\text{Sr}_3\text{AlO}_4\text{F}$ ³². This distortion of the octahedra gives rise to two distinct A sites shown in Figure 1.6. The A(1) site is in the axial positions of the corner sharing octahedra, and the A(2) site occupies the equatorial positions. A(1) sites are 10-coordinated and A(2) sites are 8-coordinated. In $\text{Sr}_3\text{MO}_4\text{F}$, the octahedra are rotated by approximately 18° about the c-axis. The direction of the rotation alternates from one layer to the next and is represented by the Glazer notation $a^0a^0c^-$ ³³⁻³⁴.

References

- (1) Srivastava, A. M.; Sommerer, T. J. *Interface-Electrochemical Society* **1998**, *7*, 28-33.
- (2) Howe, B.; Diaz, A. L. *Journal of Luminescence* **2004**, *109*, 51-59.
- (3) Stevels, A. L. N. *Journal of Luminescence* **1976**, *12*, 97-107.
- (4) Shionoya, S.; Yen, W. M.; Yamamoto, H. *Phosphor Handbook*; CRC Press: 2006; pp. 1080.
- (5) Blasse, G.; Grabmaier, B. C. *Luminescent Materials*; Springer-Verlag Berlin: 1994; pp. 10-106.
- (6) Ronda, C. R. *Luminescence: From Theory to Applications*; Wiley: 2007; pp. 3-34.
- (7) Ropp, R. C. *Luminescence and the Solid State, Second Edition (Studies in Inorganic Chemistry)*; Elsevier Science: 2004; pp. 730.
- (8) Philips Lighting Company. *Phosphor: A Critical Component in Fluorescent Lamps* **2011**. <http://www.usa.lighting.philips.com/pwc_li/us_en/lightcommunity/trends/phosphor/assets/philips_reo_brochure_p-6281.pdf>
- (9) Basic Research Needs for Solid-State Lighting, Report for the Basic Energy Sciences Workshop on Solid-State Lighting, May 22-24, 2006, US Department of Energy, <<http://science.energy.gov/~media/bes/pdf/reports/files/sslrpt.pdf>>.
- (10) Solé, J.; Bausa, L.; Jaque, D. *An Introduction to the Optical Spectroscopy of Inorganic Solids*; John Wiley & Sons: 2005; pp. 173-206.
- (11) Chen, L.; Lin, C.C.; Yeh, C.W.; Liu, R.S. *Materials* **2010**, *3*, 2172-2195.
- (12) Blasse, G. *Physics Letters A* **1968**, *28*, 444-445.
- (13) Shang, M.; Li, G.; Kang, X.; Yang, D.; Geng, D.; Lin, J. *ACS Applied Materials & Interfaces* **2011**, *3*, 2738-2746.
- (14) OSRAM Sylvania LED Color Calculator. <https://www.sylvania.com/en-us/tools-and-resources/Pages/led-color-calculator.aspx>. (Accessed July 6, 2013)

- (15) Perkin Elmer, Inc. *LS 55 User Guide*; United Kingdom, 2000.
- (16) Hoffmann, G. *J online* <http://www.fho-emden.de/hoffmann/-ciexyz29082000.pdf> **2000**
- (17) Cullity, B. D.; Stock, S. R. *Elements of X-ray Diffraction*; Prentice Hall Upper Saddle River, NJ: 2001; pp. 89-122.
- (18) Azaroff, L. V.; Buerger, M. J. *The Powder Method in X-ray Crystallography*; New York. McGraw-Hill Book Co.: 1953; pp. 4-11.
- (19) Rosenberg, H. M. *The Solid State*; Oxford University Press Oxford: 1988; pp. 18-28.
- (20) Pecharsky, V. K.; Zavalij, P. Y. *Fundamentals of Powder Diffraction and Structural Characterization of Materials*; Springer: 2004;
- (21) Rigaku Corporation. *Rigaku Miniflex Instruction Manual*, 4th ed.; Tokyo, 2006.
- (22) Young, R. A. *The Rietveld Method*; Wiley-VCH: 1995; pp. 2-38.
- (23) ANSTO: Specifications, <http://www.ansto.gov.au/research/bragg_institute/facilities/instruments/echidna/specifications>.
- (24) Larson, A. C.; Von Dreele, R. B. *General Structure Analysis System. LANSCE, MS-H805, Los Alamos, New Mexico 1994*,
- (25) Altermatt, D.; Brown, I. D. *Acta Crystallographica Section B: Structural Science* **1985**, *41*, 240-244.
- (26) Brown, I. D.; Wu, K. K. *Acta Crystallographica* **1976**, *32*, 1957-1959.
- (27) Brown, I. D.; Altermatt, D. *Acta Crystallographica Section B: Structural Science* **1985**, *41*, 244-247.
- (28) Prodjosantoso, A. K.; Kennedy, B. J.; Vogt, T.; Woodward, P. M. *Journal of Solid State Chemistry* **2003**, *172*, 89-94.
- (29) Brown, I. D. *The Chemical Bond in Inorganic Chemistry: The Bond Valence Model, International Union of Crystallography Monographs on Crystallography No. 12*; Oxford University Press, New York: 2002.
- (30) West, A. R. *Basic Solid State Chemistry*; Wiley New York: 1988; pp. 407-429.

- (31) Rao, C. N. R. *New Directions in Solid State Chemistry. Edition en anglais*; Cambridge University Press: 1997.; pp.112-118.
- (32) Vogt, T.; Woodward, P. M.; Hunter, B. A.; Prodjosantoso, A. K.; Kennedy, B. J. *Journal of Solid State Chemistry* **1999**, *144*, 228-231.
- (33) Woodward, P. M. *Acta Crystallographica Section B* **1997**, *53*, 32-43.
- (34) Mitchell, R. H. *Perovskites: Modern and Ancient*; Almaz Press Thunder Bay: 2002; pp. 14-24.

CHAPTER 2

PHOTOLUMINESCENCE AND STRUCTURAL STUDY OF AIR-ANNEALED AND REDUCED $\text{Sr}_3\text{AlO}_4\text{F}$ USING HIGH RESOLUTION NEUTRON POWDER DIFFRACTION

Introduction

In 1999, the $\text{Sr}_3\text{AlO}_4\text{F}$ and $\text{Sr}_3\text{GaO}_4\text{F}$ analogues of the $A_3\text{MO}_4\text{F}$ host lattice were structurally characterized by Vogt *et al*¹. Over the years, these structures have been used as host lattices for solid-state lighting materials by Chen *et al*², Bin Im *et al*³, Setlur *et al*⁴, Shang *et al*⁵, and Park⁶. Prodjosantoso *et al*⁷ studied the structural properties of the Ba^{2+} and Ca^{2+} substituted $\text{Sr}_3\text{AlO}_4\text{F}$ host lattice. Green and Vogt⁸ studied the structural properties of Ba^{2+} and Ca^{2+} substituted $\text{Sr}_3\text{GaO}_4\text{F}$ in addition to the characterization of the self-activating photoluminescent (PL) properties, which will be presented in Chapter 3. In Vogt *et al*, the initial refinement of $\text{Sr}_3\text{GaO}_4\text{F}$ was compared to $\text{Sr}_2\text{GdGaO}_5$ since it is isostructural^{1,9} ($I4/mcm$ space group). The $\text{Sr}_2\text{GdGaO}_5$ structure consists of two O sites, where one oxygen site coordinates in the Wyckoff position $4c$ similar to F in $\text{Sr}_3\text{GaO}_4\text{F}$. The other O site coordinates in Wyckoff position $16l$. The Gd^{3+} ions can occupy either the $4a$ or $8h$ sites in the $I4/mcm$ structure.

The $\text{Sr}_3\text{MO}_4\text{F}$ structure can also be described as alternating Sr_2F^{3+} and SrMO_4^{3-} layers, where the Sr located in each of the layers differ in coordination environments. These alternating layers consist of ionic and covalent interactions for the Sr_2F^{3+} and SrMO_4^{3-} layers, respectively. The Sr atoms located in the SrMO_4 layer will be designated as the Sr(1) atom. These Sr atoms are 10-coordinated by two fluorine atoms located 180° from each other and eight oxygen atoms from nearby MO_4 tetrahedra. The Sr in the Sr_2F layer (also known as the A(2) layer) is often referred to as Sr(2) and will be referred to as such throughout this work. Sr(2) is in an 8-coordinated environment, where each Sr(2) atom is bonded to two F atoms as well as three oxygen atoms above and below the plane.

The lattice parameters of $\text{Sr}_3\text{MO}_4\text{F}$ were measured by both x-ray and neutron diffraction of these materials, and determined to be $a = 6.78221(9) \text{ \AA}$ and $c = 11.1437(2) \text{ \AA}$ for $\text{Sr}_3\text{AlO}_4\text{F}$, and $a = 6.78147(5) \text{ \AA}$ and $c = 11.3692(1) \text{ \AA}$ for $\text{Sr}_3\text{GaO}_4\text{F}$ using synchrotron radiation¹. Additional neutron diffraction data determined for $\text{Sr}_3\text{GaO}_4\text{F}$ confirmed that the lattice parameters were accurate with $a = 6.7819(1) \text{ \AA}$ and $c = 11.3662(3) \text{ \AA}$ ¹. The structural analyses of $\text{Sr}_3\text{AlO}_4\text{F}$ structures used the bond valence method described in the introduction as a means of comparing the sum of all of the individual bond valences to the formal charges of the atoms/ions in the structure. Vogt *et al* determined from the refinement of these structures that the Sr(1) is “underbonded”, which means that the bonds to this site are elongated. This suggested that this structure is able to accommodate larger ions such as Ba^{2+} , while maintaining its structural integrity.

Park and Vogt initially showed that these oxyfluoride structures exhibit self-activating photoluminescence properties when $\lambda_{\text{ex}} = 254\text{nm}$ after exposure to a reducing (5% $\text{H}_2/95\% \text{ Ar}$) atmosphere¹⁰. In addition to heating these materials in a reducing

atmosphere, the color emitted in the photoluminescence can be tailored by substitutions made at the A(1), A(2) and *M* sites in the host structure as well as by varying the gas flow rate and temperature of the reducing atmosphere¹⁰. While many of the aforementioned researchers focused on the changes in PL caused by iso- and aliovalent substitutions in the Sr_3MO_4F host structure, the fact that the reducing atmosphere changes the PL has not been studied in detail. The purpose of this chapter is to study the PL and structural changes in Sr_3AlO_4F caused by tempering in a reducing atmosphere. These will be done using high-resolution neutron diffraction data as well as photoluminescence measurements. High resolution neutron powder diffraction can also detect minor impurities such as SrF_2 which was seen by Setlur *et al* in $(Sr_{0.5925}Ca_{0.4}Ce_{0.0075})_3Al_{0.6}Si_{0.4}O_{4.4225}F_{0.5775}$ ³ and Im *et al* in $Sr_{2.975}Ba_xCe_{0.025}AlO_4F$ ⁴ materials within powder samples made *via* solid-state synthesis/ceramic method. SrF_2 is a common impurity in most samples

Experimental

The Sr_3AlO_4F samples were synthesized using the solid-state synthesis method, where the solid starting materials $SrCO_3$ (Sigma-Aldrich, 99.995%), Al_2O_3 (Sigma-Aldrich, 99.95%), and SrF_2 (Sigma-Aldrich, 99.995%) were mixed thoroughly in an agate mortar and pestle followed by heating in 24 hour cycles at 700°C, 800°C and 900°C. These samples were annealed in air for 48 hours at 1050°C as suggested in the experimental section in Vogt *et al*. Initial structural information was determined by data collected by a Rigaku Miniflex diffractometer with Cu- α radiation ($\lambda = 1.5406\text{\AA}$) over a range of $3^\circ - 149^\circ 2\theta$. Once the diffraction pattern does not exhibit any discernable impurities, it is heated for 3 hours at 900°C in a 5% H_2 /95% Ar atmosphere to induce

photoluminescence emission. Photoluminescence emission and excitation data are collected using a Perkin-Elmer LS 55 fluorescence spectrometer. The $\text{Sr}_3\text{AlO}_4\text{F}$ samples were sealed in a vanadium container using an indium wire to ensure no oxidation during the collection of neutron powder diffraction data. The data was collected by Dr. Maxim Avdeev using a neutron beam with a $\lambda = 1.300\text{\AA}$ generated by a Ge 355 monochromator at the Australian Nuclear Science and Technology Organization's (ANSTO) research reactor at Lucas Heights, Australia. This instrument also provides data in a d-spacing range of 0.8-18.6 \AA and a Q-range of 0.3-7.7 \AA^{-1} .¹¹

The GSAS suite of programs were used to refine the neutron diffraction data presented in this chapter, where the lattice parameters, atomic coordinates, isotropic thermal parameters, histogram scale factor, pseudo-Voigt peak profiles and linear interpolation function background parameters are refined¹².

Results and Discussion

Photoluminescence of $\text{Sr}_3\text{AlO}_4\text{F}$

It is common that materials such as $\text{Sr}_4\text{Al}_{14}\text{O}_{25}$ and $\text{Mg}_x\text{Sr}_{1-x}\text{Al}_2\text{O}_4$ phosphors, as well as calcium aluminate glass¹³ materials, are heated in reducing atmospheres to enhance their photoluminescent properties when doped with rare-earth ions. The photoluminescent properties of $\text{Sr}_3\text{AlO}_4\text{F}$ materials are produced by tempering in a 5% H_2 /95% Ar atmosphere. Park and Vogt have determined that the self-activated photoluminescence in $\text{Sr}_3\text{AlO}_4\text{F}$ can be tailored by varying the temperature and gas flow rate in the reducing step¹⁰. In this study, the samples were tempered for three hours in a 5% H_2 /95% Ar atmosphere in a tube furnace at 900°C, which resulted in a fine powder

material that exhibits a bright white color when excited by 254 nm light as shown in Figure 2.1. Similarly, exposing various strontium aluminate phosphors to reducing atmosphere greatly impacts the photoluminescence of both rare-earth substituted (i.e. reducing Eu^{3+} to Eu^{2+}) and unsubstituted materials¹⁴. Air-annealed $\text{Sr}_3\text{AlO}_4\text{F}$ materials ($\text{Sr}_3\text{AlO}_4\text{F}_{(\text{air})}$) do not show photoluminescence without this reduction step.

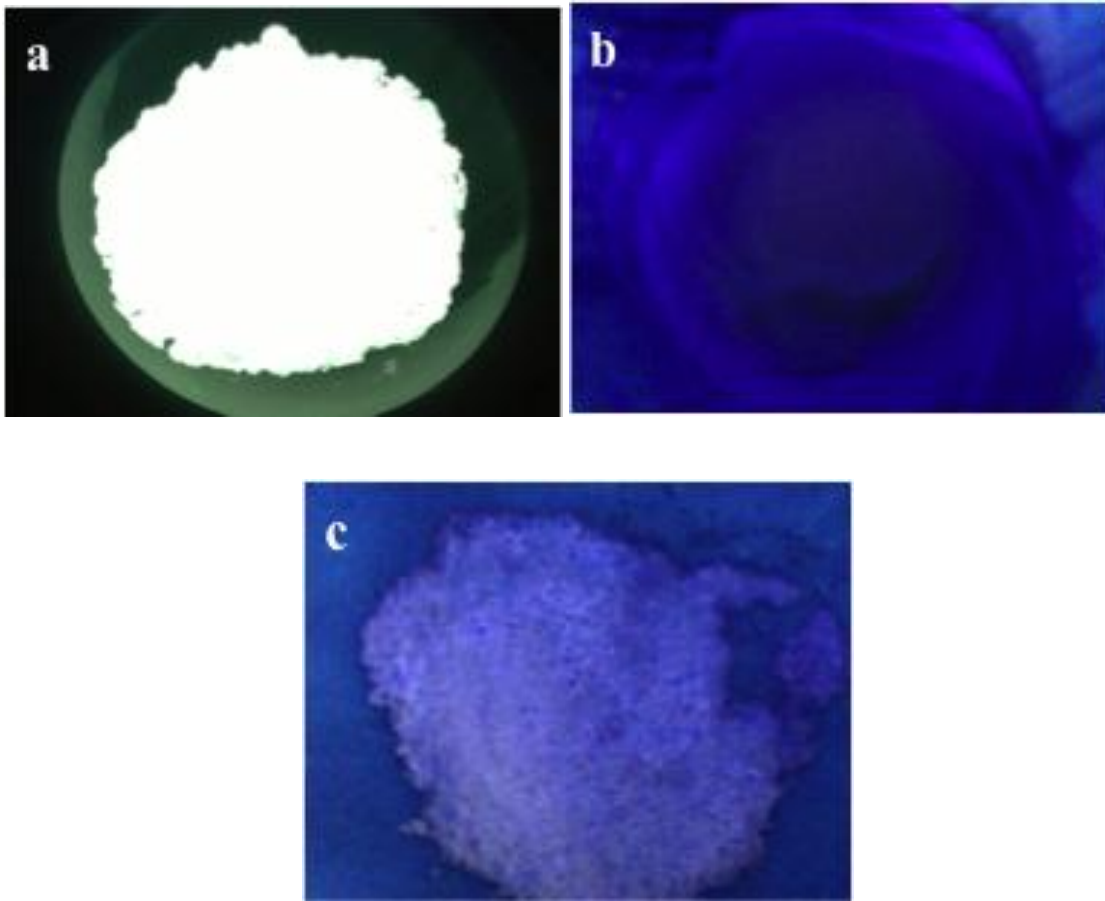


Figure 2.1: Images of (a) $\text{Sr}_3\text{AlO}_4\text{F}_{(\text{r})}$, (b) $\text{Sr}_3\text{AlO}_4\text{F}_{(\text{air})}$, and (c) SrF_2 . ($\lambda_{\text{ex}} = 254\text{nm}$)

Figure 2.2 shows the broad-band emission of the reduced $\text{Sr}_3\text{AlO}_4\text{F}$ material ($\text{Sr}_3\text{AlO}_4\text{F}_{(\text{r})}$), where the emission ranges from 430-650nm. The excitation spectra shows a maximum intensity near 250 nm and a lower intensity peak /shoulder near 230nm. The

excitation spectrum also shows a sharp decline in intensity from 250-300nm. The maximum emission intensity is near 495nm, which corresponds to a 250nm excitation. However, the PL spectra in Figure 2.2 also shows that $\text{Sr}_3\text{AlO}_4\text{F}_{(\text{air})}$ exhibits a very low emission intensity. When compared to the PL spectra of SrF_2 in Figure 2.3, the emission spectra both have peaks appearing near 488 in the emission spectrum, which confirms the presence of SrF_2 as an impurity. $\text{Sr}_3\text{AlO}_4\text{F}_{(\text{r})}$ also had traces of this impurity, however, the high intensity of the $\text{Sr}_3\text{AlO}_4\text{F}$ sample allow for the PL of SrF_2 to be masked. Data from the emission spectrum, with $\lambda_{\text{ex}} = 254\text{nm}$ can be converted to CIE chromaticity coordinates (given as x, y coordinates) to characterize the color of the samples. These coordinates, plotted in Figure 2.4, are $x = 0.2160$ and $y = 0.3764$ for $\text{Sr}_3\text{AlO}_4\text{F}_{(\text{r})}$, where the values correspond to a blue-green color and are very similar to the ones given by Park and Vogt ($x = 0.2429$, $y = 0.3387$)¹⁰. This blue-green color does not account for the brightness or intensity of the material, but simply the hue; however, the intensity is significant compared to a $\text{Sr}_3\text{AlO}_4\text{F}$ sample synthesized completely in a 5% $\text{H}_2/95\%$ Ar atmosphere¹⁰.

Due to the ideal λ_{ex} being near 254nm, the $\text{Sr}_3\text{AlO}_4\text{F}_{(\text{r})}$ host may have a potential use as a phosphor for compact fluorescent lamps (CFLs), where the mercury vapor contained within the bulb emits UV light near 254nm.

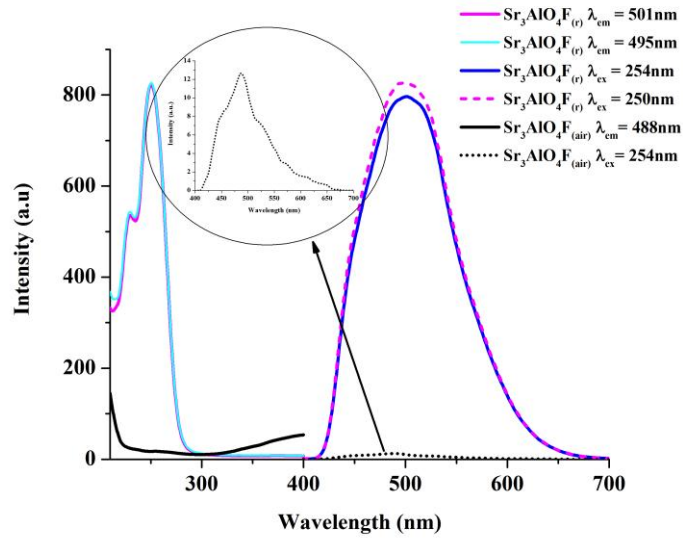


Figure 2.2: Emission and excitation spectra of $\text{Sr}_3\text{AlO}_4\text{F}_{(\text{air})}$ and $\text{Sr}_3\text{AlO}_4\text{F}_{(\text{tr})}$ samples.

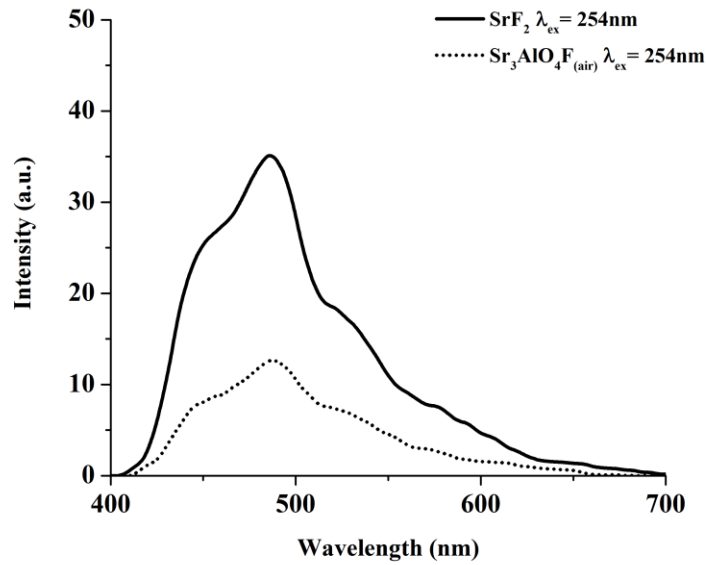


Figure 2.3: Photoluminescence of $\text{Sr}_3\text{AlO}_4\text{F}_{(\text{air})}$ and SrF_2 , where $\lambda_{\text{ex}} = 254\text{nm}$.

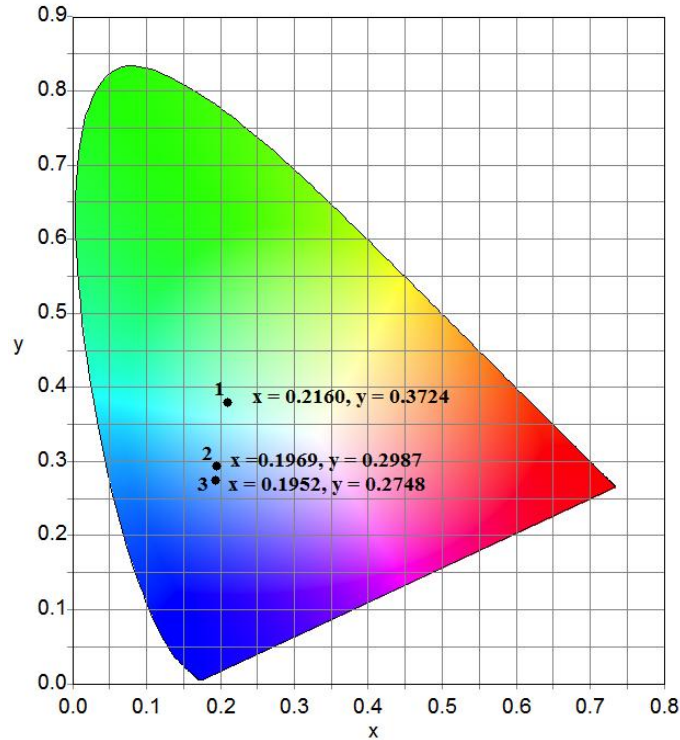


Figure 2.4: Plot of CIE chromaticity coordinates, (1) denotes $\text{Sr}_3\text{AlO}_4\text{F}_{(r)}$, (2) denotes $\text{Sr}_3\text{AlO}_4\text{F}_{(\text{air})}$ and (3) is SrF_2 ($\lambda_{\text{ex}} = 254\text{nm}$)

Structural Analysis

To fully characterize the air annealed and reduced structural parameters of $\text{Sr}_3\text{AlO}_4\text{F}$, high-resolution neutron powder diffraction (NPD) was used. In order to minimize the systemic errors and allow for comparison, both samples were measured with the same instrument configuration one after the other. The Rietveld refinement of the neutron diffraction data show a slight change in the refined lattice parameters as well as the site coordinates in the unit cell between $\text{Sr}_3\text{AlO}_4\text{F}_{(\text{air})}$ and $\text{Sr}_3\text{AlO}_4\text{F}_{(r)}$. Using the GSAS suite of programs, the same 42 variables were used to refine the neutron diffraction data for the $\text{Sr}_3\text{AlO}_4\text{F}_{(\text{air})}$ and $\text{Sr}_3\text{AlO}_4\text{F}_{(r)}$ samples. Plots of the Rietveld

refinement data are shown in Figures 2.5 and 2.6 for $\text{Sr}_3\text{AlO}_4\text{F}_{(\text{air})}$ and $\text{Sr}_3\text{AlO}_4\text{F}_{(\text{r})}$, respectively. These plots show that a 2-phase refinement was performed for both the air-annealed and reduced samples, where SrF_2 is the second phase. The presence of SrF_2 , as stated in the previous section, causes a low intensity emission and is approximately 0.3% of $\text{Sr}_3\text{AlO}_4\text{F}_{(\text{air})}$ and 0.14% in $\text{Sr}_3\text{AlO}_4\text{F}_{(\text{r})}$.

The neutron diffraction data of $\text{Sr}_3\text{AlO}_4\text{F}_{(\text{r})}$ compared to $\text{Sr}_3\text{AlO}_4\text{F}_{(\text{air})}$ shows a slight contraction in the a -parameter by 0.11%, while the c -parameter expands by 0.016%. The unit cell volume decreases by $\approx 0.2\%$ from 513.84\AA^3 in $\text{Sr}_3\text{AlO}_4\text{F}_{(\text{air})}$ to 512.76\AA^3 in $\text{Sr}_3\text{AlO}_4\text{F}_{(\text{r})}$. The site coordinates and refined thermal parameters of $\text{Sr}_3\text{AlO}_4\text{F}_{(\text{air})}$ and $\text{Sr}_3\text{AlO}_4\text{F}_{(\text{r})}$ are given in Table 2.1 and 2.2, respectively. In addition to these tables, selected distances and angles are given for both sets of data in Table 2.3, where the metric Δ_{esd} is used to determine the significance of the changes in distances and bond angles. This value is calculated by the equation:

$$\Delta_{\text{esd}} = (d_{(\text{air})} - d_{(\text{r})}) / \sigma \quad (2.1)$$

, where $d_{(\text{air})}$ represents a refined value for $\text{Sr}_3\text{AlO}_4\text{F}_{(\text{air})}$, $d_{(\text{r})}$ is a refined value for $\text{Sr}_3\text{AlO}_4\text{F}_{(\text{r})}$, and σ represents the associated standard deviation given from the refinement output file for a structural parameter. A Δ_{esd} value greater than $\pm 5\sigma$ is considered to be significant change between $\text{Sr}_3\text{AlO}_4\text{F}_{(\text{air})}$ and $\text{Sr}_3\text{AlO}_4\text{F}_{(\text{r})}$, where (+) values indicates a decrease and (-) values indicate an increase. This metric determines the changing lattice parameters to be significant, where there is a $\Delta_{\text{esd}} = 76\sigma$ for the a -parameter and -7.5σ for the c -parameter. These changes indicate a slight elongation of the c -parameter and a large decrease in the a -parameter after $\text{Sr}_3\text{AlO}_4\text{F}_{(\text{air})}$ is exposed to a reducing atmosphere.

The associated bond distances and angles of $\text{Sr}_3\text{AlO}_4\text{F}_{(\text{air})}$ and $\text{Sr}_3\text{AlO}_4\text{F}_{(\text{r})}$ listed in Table 2.3 show that there is a nominal elongation of the Sr(1)-F bonds, while the Sr(2)-F bonds are nominally shortened when these materials are tempered in a reducing atmosphere. This in turn causes a minute distortion of the F-Sr₆ octahedra within the $\text{Sr}_3\text{AlO}_4\text{F}$ structure. In addition to the distortion of the F-Sr₆ octahedra, there is also a significant decrease in the Sr(1)-O distance. The greatest change in bond distances is between Sr(1) and Al, where the $\Delta_{\text{esd}} = 63\sigma$. This effect, accompanied with the increase of the tilt angle from 17.86° to 17.97° has a $\Delta_{\text{esd}} = 3.7\sigma$ ($\approx 0.6\%$), which suggests that the AlO_4 tetrahedra are packed more efficiently within the host structure after being exposed to the 5% H_2 /95% Ar atmosphere. The representative changes in the structure between $\text{Sr}_3\text{AlO}_4\text{F}_{(\text{air})}$ and $\text{Sr}_3\text{AlO}_4\text{F}_{(\text{r})}$ are illustrated in Figure 2.7.

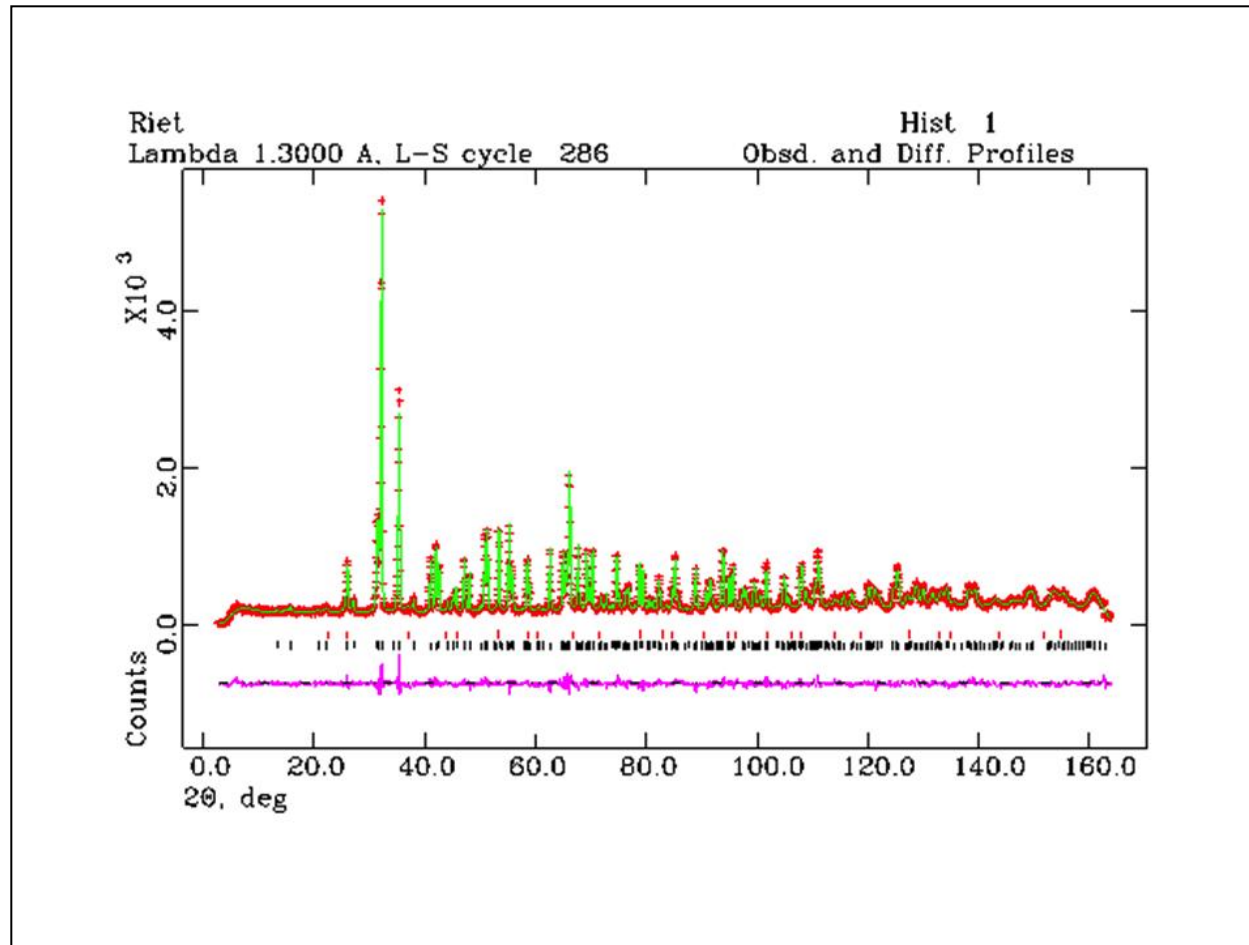


Figure 2.5: Rietveld refinement plot of neutron diffraction data of $\text{Sr}_3\text{AlO}_4\text{F}_{(\text{air})}$. The red green and pink profiles represent the observed, calculated and difference plots, respectively. The black vertical lines represent the peaks in the $\text{Sr}_3\text{AlO}_4\text{F}$ phase, while the red vertical lines represent the peaks in the SrF_2 phase.

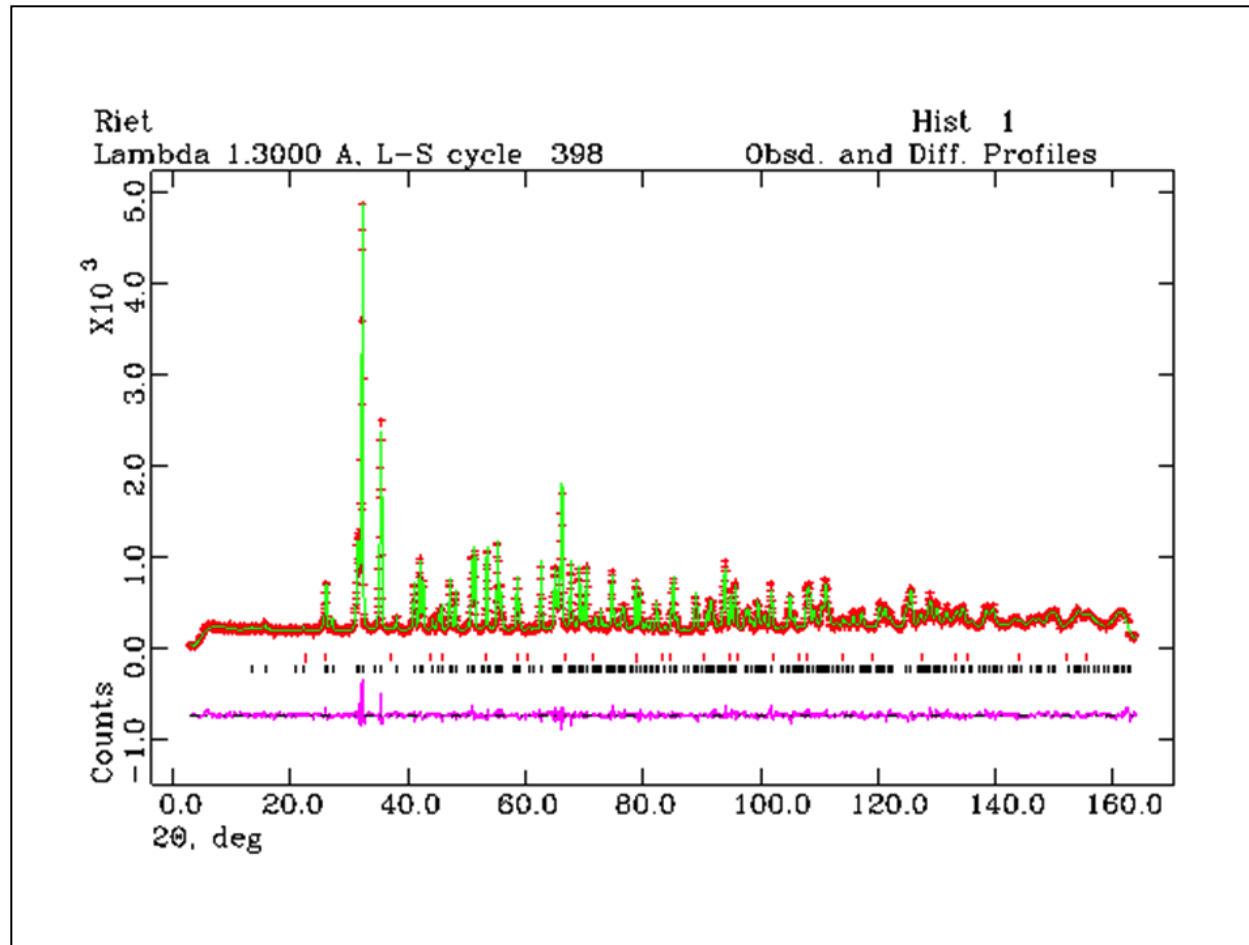


Figure 2.6: Rietveld refinement plot of neutron diffraction data of $\text{Sr}_3\text{AlO}_4\text{F}_{(r)}$. The red green and pink profiles represent the observed, calculated and difference plots, respectively. The black vertical lines represent the peaks in the $\text{Sr}_3\text{AlO}_4\text{F}$ phase, while the red vertical lines represent the peaks in the SrF_2 phase

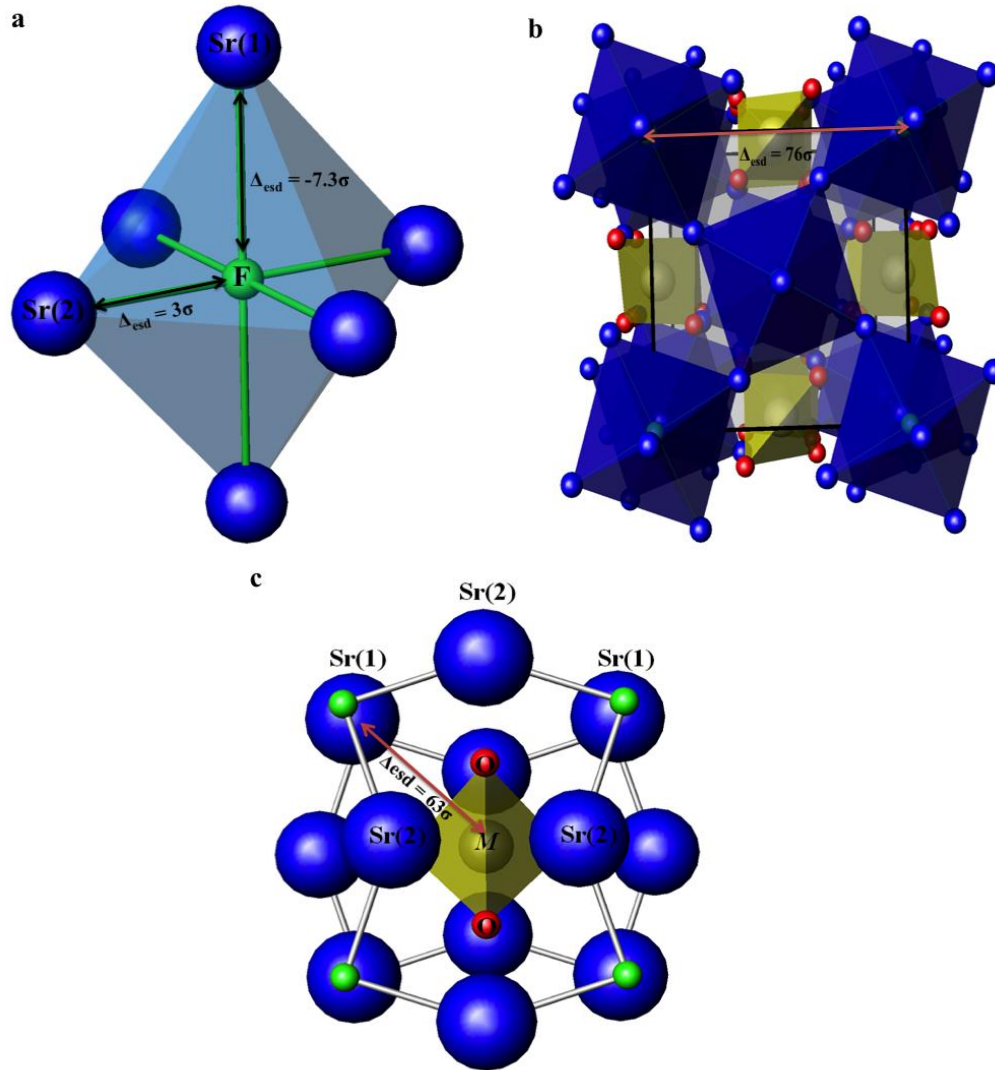


Figure 2.7: Plot of Δ_{esd} values for (a) F in Sr₆ octahedra, (b) *a*-parameter, and (c) Al-Sr(1) distance.

Table 2.1: Refined lattice parameters and atomic positions for Sr₃AlO₄F_(air)

Atom	Wyckoff position	x	y	z	Occupancy	U _{iso}
Sr(1)	4a	0	0	0.25	1	1.49(5)
Sr(2)	8h	0.1695(2)	0.6695(2)	0	1	0.56(3)
Al	4b	0	0.5	0.25	1	0.61(7)
F	4c	0	0	0	1	1.13(5)
O	16l	0.1418(1)	0.6418(1)	0.6483(1)	1	1.08(2)

Crystallographic data: Space group = *I4/mcm*, $a = 6.7873(1)\text{\AA}$, $c = 11.1542(2)\text{\AA}$,
Vol. = $513.84(2)\text{\AA}^3$. $\chi^2 = 1.730$, $R_{wp} = 7.18\%$, $R_p = 5.52\%$.

Table 2.2: Refined lattice parameters and atomic positions for Sr₃AlO₄F_(r)

Atom	Wyckoff position	x	y	z	Occupancy	U _{iso}
Sr(1)	4a	0	0	0.25	1	1.33(5)
Sr(2)	8h	0.1689(1)	0.6689(1)	0	1	0.54(3)
Al	4b	0	0.5	0.25	1	0.38(7)
F	4c	0	0	0	1	1.10(5)
O	16l	0.1416(1)	0.6416(1)	0.6484(1)	1	0.97(2)

Crystallographic data: Space group = *I4/mcm*, $a = 6.7797(1)\text{\AA}$, $c = 11.1557(2)\text{\AA}$,
Vol. = $512.76(2)\text{\AA}^3$. $\chi^2 = 1.550$, $R_{wp} = 6.90\%$, $R_p = 5.33$

Table 2.3: Changes in distances and angles between Sr₃AlO₄F_(air) and Sr₃AlO₄F_(r)

Sr ₃ AlO ₄ F	Sr ₃ AlO ₄ F _(air) (Å) NPD	Sr ₃ AlO ₄ F _(r) (Å) NPD	Δ_{esd} (N σ)
<i>a</i> -parameter (Å)	6.7873(1)	6.7797(1)	76 σ
<i>c</i> -parameter (Å)	11.1542(2)	11.1557(2)	-7.5 σ
Volume (Å ³)	513.84(2)	512.76(2)	56 σ
Sr(1)-O (x8) (Å)	2.8503(7)	2.8478(7)	3.6 σ
Sr(1)-F (x2) (Å)	2.78854(6)	2.78898(6)	-7.3 σ
Sr(2)-O (x2) (Å)	2.453(2)	2.458(2)	-2.5 σ
Sr(2)-O (x4) (Å)	2.690(1)	2.685(1)	5 σ
Sr(2)-F (x2) (Å)	2.5211(4)	2.5199(4)	3 σ
Sr(1)-Al (Å)	3.39365(6)	3.38986(6)	63 σ
Al-O (x4) (Å)	1.771(1)	1.768(1)	3 σ
O-Al-O	114.20(4)°	114.25(4)°	-1.25 σ
O-Al-O	100.37(8)°	100.29(8)°	σ
F-Sr(2)-F	144.28(6)°	144.06(6)°	3.7 σ
Sr(2)-Sr(1)-Sr(2)	100.667(8) °	100.757(8) °	-11.38 σ

The BVS values for ions shown in Table 2.4 between Sr₃AlO₄F_(air) and Sr₃AlO₄F_(r) are essentially the same. The most significant change in the BVS values between Sr₃AlO₄F_(air) and Sr₃AlO₄F_(r) involves the Al³⁺ ion. Overall, the BVS values are in good agreement with the values published by Vogt *et al.*¹ When studying the BVS values generated from the neutron data closely, we notice a minute increase. This could be attributed to the average bond distance surrounding each ion decreasing. For instance, Sr(1) is in a 10-coordinated environment, where 8 out of 10 bonds are with O, while the other two are with F. The refined neutron data show a decrease in the Sr(1)-O bond length of 0.0025(7)Å. This difference suggests a contraction in the overall environment

resulting in an increased BVS value. The calculation of the discrepancy factors and global instability indices (G) in Table 2.5 show that the overall changes of the bond lengths causes very subtle changes to the structure overall. These metrics describe the entire structure and provides evidence of subtle distortions caused by exposing $\text{Sr}_3\text{AlO}_4\text{F}$ to a 5% H_2 /95% Ar atmosphere.

Table 2.4: Bond valence sums (BVS) of ions in $\text{Sr}_3\text{AlO}_4\text{F}_{(\text{air})}$ and $\text{Sr}_3\text{AlO}_4\text{F}_{(\text{r})}$

Ion	$\text{Sr}_3\text{AlO}_4\text{F}_{(\text{air})}$ NPD	$\text{Sr}_3\text{AlO}_4\text{F}_{(\text{r})}$ NPD
Sr(1)	1.33	1.34
Sr(2)	2.13	2.14
Al	3.28	3.31
F	1.20	1.21
O	1.92	1.93

Table 2.5: Discrepancy factors (d_i) of ions and global instability indices (G) of $\text{Sr}_3\text{AlO}_4\text{F}_{(\text{air})}$ and $\text{Sr}_3\text{AlO}_4\text{F}_{(\text{r})}$

Ion	$\text{Sr}_3\text{AlO}_4\text{F}_{(\text{air})}$ NPD	$\text{Sr}_3\text{AlO}_4\text{F}_{(\text{r})}$ NPD
Sr(1)	-0.67	-0.66
Sr(2)	0.13	0.14
Al	0.28	0.31
F	0.20	0.21
O	-0.08	-0.07
Global Instability Index (G)	0.2562	0.2583

Conclusions

This study was done to gain insight about the effect that reducing conditions have on the structure of $\text{Sr}_3\text{AlO}_4\text{F}$ materials. It is apparent that the reducing atmosphere has a significant impact on the photoluminescence in $\text{Sr}_3\text{AlO}_4\text{F}$. This material exhibits a bright white color when excited by 254 nm light. There is evidence of a significant contraction of the a -parameter along with a minute elongation of the c -parameter. The FSr_6 octahedra reveal small distortions including small contraction of the equatorial F-Sr(2) bonds. Although the FSr_6 octahedra do not change significantly, a significant decrease in the Al-Sr(1) distance accounts for the decrease in the a -parameter.

To gain further insight in this phenomenon, a similar study must be conducted with a series of air-annealed and reduced materials to substantiate our claims.

References

- (1) Vogt, T.; Woodward, P. M.; Hunter, B. A.; Prodjosantoso, A. K.; Kennedy, B. J. *Journal of Solid State Chemistry* **1999**, *144*, 228-231.
- (2) Chen, W.; Liang, H.; Han, B.; Zhong, J. and Su, Q. *J. Phys Chem C* **113**, 17194-17199.
- (3) Im, W. B.; Brinkley, S.; Hu, J.; Mikhailovsky, A.; DenBaars, S. P.; Seshadri, R. *Chemistry of Materials* **2010**, *22*, 2842-2849.
- (4) Setlur, A. A.; Radkov, E. V.; Henderson, C. S.; Her, J.-H.; Srivastava, A. M.; Karkada, N.; Kishore, M. S.; Kumar, N. P.; Aesram, D.; Deshpande, A. *Chemistry of Materials* **2010**, *22*, 4076-4082.
- (5) Shang, M.; Li, G.; Kang, X.; Yang, D.; Geng, D.; Lin, J. *ACS Applied Materials & Interfaces* **2011**, *3*, 2738-2746.
- (6) Park, S. *Optical Materials* **2013**, *35*, 516-519.
- (7) Prodjosantoso, A. K.; Kennedy, B. J.; Vogt, T.; Woodward, P. M. *Journal of Solid State Chemistry* **2003**, *172*, 89-94.
- (8) Green, R. and Vogt, T. *Journal of Solid State Chemistry* **2012**, *194*, 375-384.
- (9) Nguyen- trut- Dinh, M.; Fava, J.; Flem, G. L. *Zeitschrift für Anorganische und Allgemeine Chemie* **1977**, *433*, 275-283.
- (10) Park, S. and Vogt, T. *Journal of Physical Chemistry C* **2010**, *114*, 11576-11583.
- (11) ANSTO: Specifications, <http://www.ansto.gov.au/research/bragg_institute/facilities/instruments/echidna/specifications>
- (12) Larson, A. C.; Von Dreele, R. B. *General Structure Analysis System*. Los Alamos National Laboratory Report LAUR 860-748 (2000)
- (13) Hosono, H.; Kinoshita, T.; Kawazoe, H.; Yamazaki, M.; Yamamoto, Y.; Sawanobori, N. *Journal of Physics: Condensed Matter* **1998**, *10*, 9541-9547.

- (14) Haranath, D.; Shanker, V.; Chander, H.; Sharma, P. *Journal of Physics D: Applied Physics* **1998**, *10*, 2244-2248.

CHAPTER 3

STRUCTURES AND SELF-ACTIVATING PHOTOLUMINESCENT PROPERTIES OF



² Green, Robert and Vogt, Thomas. 2012. *Journal of Solid State Chemistry*. 194, 375-384. Reprinted here with permission of publisher

Introduction

More than a decade ago, a new family of ordered oxyfluorides with the chemical composition $\text{Sr}_3\text{MO}_4\text{F}$ ($M = \text{Al}, \text{Ga}$) was discovered ¹. This family of materials has been investigated as potential host lattices for luminescent phosphors since isovalent and aliovalent substitutions on the cation sites are facile ²⁻⁶ and a post-synthesis reduction step allows a flexible tuning of the photoluminescent properties ⁷⁻⁸. In order to make photoluminescent materials, substitutions are commonly made using trivalent rare earth (RE) ions, which act as activators when excited with light of an appropriate wavelength. Given the proper chemical reaction conditions, these materials can also become self-activated phosphors, exhibiting photoluminescence without the presence of activator ions. Park and Vogt ⁷⁻⁸ show the significance of a reducing atmosphere by comparing the photoluminescent behavior of $\text{Sr}_3\text{AlO}_4\text{F}$ when synthesized in a reducing atmosphere, air, and post-synthesis reduction. This study showed that the reduced $\text{Sr}_3\text{AlO}_4\text{F}$ materials exhibited photoluminescence, whilst the material synthesized without a reduction step did not ⁷.

The $\text{Sr}_3\text{MO}_4\text{F}$ structure, as shown in Figure 3.1, can be described as an anti-perovskite structure. The perovskite structure has the formula ABX_3 , where A and B are cations and X are anions. The structure is built up of corner-sharing $\text{BX}_{6/2}$ octahedra, (ReO_3 -type lattice) and the A cations occupy large voids within a ReO_3 -type lattice. In an anti-perovskite structure the cation and anion positions are interchanged.

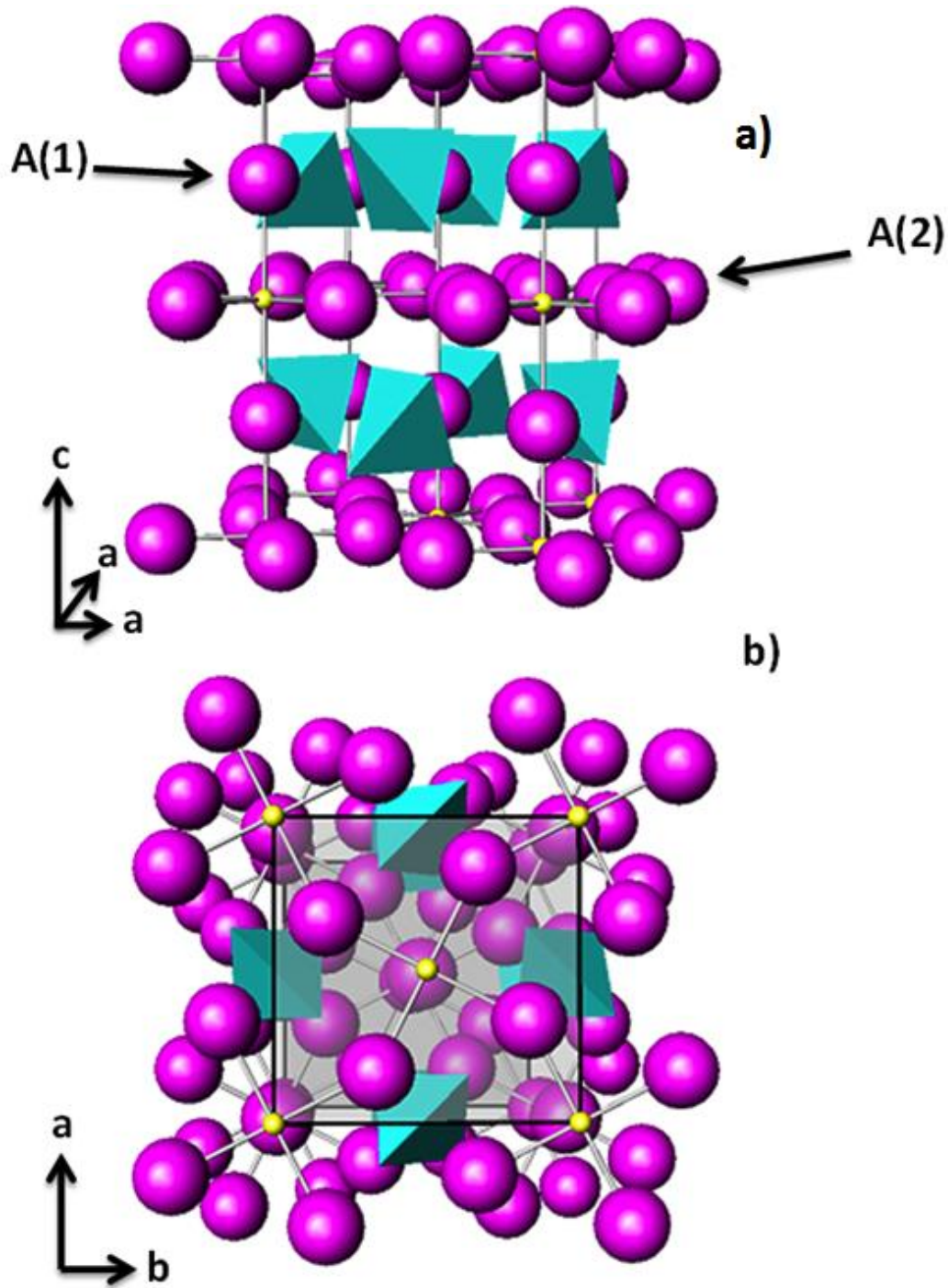


Figure 3.1: Structure of Sr_3MO_4F where the yellow atoms are F, the purple atoms are Sr, and the blue tetrahedrons represent the MO_4 : a) Unit cell viewed along the 101 plane, while b) $Sr_{3-x}MO_4F$ viewed down the 001 direction.

This structure type is often observed in metal-rich carbides and nitrides such as Ni_3CMg and Mg_3NSb ⁹. In the anti-perovskite structure of the oxyfluoride $\text{Sr}_3\text{MO}_4\text{F}$, the F anions occupy the octahedral B site while the 6 Sr^{2+} cations occupy the corner-sharing X sites, and the MO_4^{5-} ions occupy the larger A-site. $\text{Sr}_3\text{MO}_4\text{F}$ materials with $M = \text{Al}$ and Ga crystallize with tetragonal symmetry ($I4/mcm$ space group) and the lattice parameters $a = 6.78221(9) \text{ \AA}$ and $c = 11.1437(2) \text{ \AA}$ for $\text{Sr}_3\text{AlO}_4\text{F}$; and $a = 6.78147(5) \text{ \AA}$ and $c = 11.3692(1) \text{ \AA}$ for $\text{Sr}_3\text{GaO}_4\text{F}$, respectively ¹.

In the $\text{A}_3\text{MO}_4\text{F}$ ($A = \text{Ca}^{2+}, \text{Sr}^{2+}, \text{Ba}^{2+}$) anti-perovskite structure ², the A^{2+} cations occupy two different sites denoted A(1) and A(2). The A(1) cation, located in the Wyckoff site 4a, has a bicapped square antiprismatic tenfold coordination, with eight oxygen atoms forming a square antiprism. In $\text{Sr}_3\text{GaO}_4\text{F}$ the A(1)–O distance is $2.8380(1) \text{ \AA}$ and the two distances to the F ions providing the capping A(1)–F distances are $2.8422(1) \text{ \AA}$. The 8-coordinated A(2) cation, which sits in the Wyckoff site 8h, is more distorted. The A(2) ions are connected to 2 F and 6 O atoms with two different types of bonds to the oxygen. In $\text{Sr}_3\text{GaO}_4\text{F}$ the A(2)–F distance is reported as $2.523(3) \text{ \AA}$, while the six A(2)–O distances are $2 \times 2.423(2) \text{ \AA}$ and $4 \times 2.699(2) \text{ \AA}$ ². The octahedra within the $\text{Sr}_{3-x}\text{A}_x\text{GaO}_4\text{F}$ structure rotate approximately 18° in both a clockwise and counterclockwise direction about the c -axis in alternate layers in a pattern classified as an $a^0a^0c^-$ tilt system using the Glazer nomenclature ^{2,10-11}.

Prodjosantoso *et al.* ² studied the isovalent substitution of Sr^{2+} by Ba^{2+} and Ca^{2+} in $\text{Sr}_{3-x}\text{A}_x\text{AlO}_4\text{F}$ and reported that with increased substitution of Ba^{2+} there is a systematic increase in the lattice parameters, whilst increased substitution of Ca^{2+} causes a decrease in the lattice parameters. The Ba^{2+} ions preferentially occupy the A(1) sites, which are

located at the axial positions of the corner sharing octahedral. The Ca^{2+} ions prefer to occupy the A(2) sites, which are located at the equatorial positions of the corner sharing octahedra along c as shown in Figure 3.1a¹. The bond valence sum (BVS)¹²⁻¹³, which can be used to provide a measure of the stability of atoms/ions in their local environment, was determined for each atom in the unsubstituted $\text{Sr}_3\text{AlO}_4\text{F}$ material as well as the Ba^{2+} - and Ca^{2+} -substituted material. In $\text{Sr}_3\text{AlO}_4\text{F}$ the Sr^{2+} ions occupying the A(1) sites are underbonded with a value of 1.30, whereas the Sr^{2+} ions in the A(2) site have a BVS of 2.20. The underbonded Sr^{2+} ion ($r = 1.36 \text{ \AA}$) occupying the A(1) site allows the substitution by a larger isovalent ion such as Ba^{2+} ($r = 1.52 \text{ \AA}$)¹⁴.

A considerable amount of research has been conducted since the discovery of the $\text{Sr}_3\text{MO}_4\text{F}$ materials focused primarily on rare-earth substituted phosphors. Chen *et al.* explored $\text{Sr}_{3-2x}\text{Ce}_x\text{Na}_x\text{GaO}_4\text{F}$ and were able to shift the emission of the material to longer wavelengths by increasing the Ce^{3+} concentration. Spectroscopic evidence that the Ce^{3+} ions occupy both the A(1) and A(2) sites was also presented¹⁵. Im *et al.* synthesized $\text{Sr}_{2.975}\text{BaCe}_{0.025}\text{AlO}_4\text{F}$ and found that its photoluminescence properties rival those of the Ce^{3+} -doped $\text{Y}_3\text{Al}_5\text{O}_{12}$ (YAG) phosphor, which is a widely used in industry as a phosphor for cold-light light emitting diodes (LEDs). The quantum efficiency of $\text{Sr}_{2.975}\text{BaCe}_{0.025}\text{AlO}_4\text{F}$ at room temperature excited by 400 nm light was close to 95%. Furthermore, the material exhibited less thermal quenching than Ce^{3+} -doped $\text{Y}_3\text{Al}_5\text{O}_{12}$ ⁴. Setlur *et al.* synthesized $(\text{Sr}_{1-x-y}\text{Ca}_x\text{Ce}_y)_3\text{Al}_{1-z}\text{Si}_z\text{O}_{4+3y+z}\text{F}_{1-3y-z}$ materials, in which the photoluminescent properties of these materials are varied by the substitution of Ca^{2+} and Ce^{3+} ⁵. Most recently, Park showed that doping Sm^{3+} into $\text{Sr}_{2.5}\text{Ba}_{0.5}\text{AlO}_4\text{F}$ produces an orange-emitting phosphor when excited with 254 nm light⁶.

The goal of this research is to structurally characterize $\text{Sr}_{3-x}\text{Ba}_x\text{GaO}_4\text{F}$ and $\text{Sr}_{3-x}\text{Ca}_x\text{GaO}_4\text{F}$ materials, investigate their self-activating photoluminescent properties and compare these results to the $\text{Sr}_{3-x}\text{Ba}_x\text{AlO}_4\text{F}$ and $\text{Sr}_{3-x}\text{Ca}_x\text{AlO}_4\text{F}$ materials as previously reported by Prodjosantoso *et al.*

Experimental

The samples of $\text{Sr}_{3-x}\text{A}_x\text{GaO}_4\text{F}$ ($A = \text{Ca}, \text{Ba}; x \leq 1$) and $\text{Sr}_{3-x}\text{A}_x\text{AlO}_4\text{F}$ ($A = \text{Ca}, \text{Ba}; x \leq 1$) were prepared by heating the appropriate stoichiometric amounts of CaCO_3 (Alfa-Aesar, 99%), BaCO_3 (Alfa-Aesar, 99.8%), SrCO_3 (Sigma-Aldrich, 99.995%), SrF_2 (Alfa-Aesar, 99%), Ga_2O_3 (Sigma-Aldrich, 99.99%) and Al_2O_3 (Sigma-Aldrich, 99.95%) in air. The oxyfluoride materials formed after heating cycles at 700°C, 800°C, and 900°C for 24 h with repeated grinding between heating cycles. The materials were annealed for 72 h at 1050°C and 1100°C for $\text{Sr}_{3-x}\text{Ca}_x\text{GaO}_4\text{F}$ and $\text{Sr}_{3-x}\text{Ba}_x\text{GaO}_4\text{F}$, respectively. Materials were reduced by heating to 1050°C in a 5% H_2 /95% Ar atmosphere for 3 hours. For reproducibility, the gas flow rate was controlled by allowing the gas to be collected in an empty 500 ml flask attached to a bubbler filled with ethylene glycol. The flow rate was determined by counting the number of bubbles, which was set at 1 bubble every 4 seconds (1b/4s)⁷. Rietveld refinements were based upon powder X-ray diffraction data obtained from a Rigaku MiniFlexTM diffractometer (Cu $K\alpha$ radiation $\lambda = 1.54059 \text{ \AA}$). The range for data collection was from $2\theta = 3^\circ$ -149°, with a step size of $2\theta = 0.02^\circ$ and a scan speed of 0.25 deg/min. The unit cell parameters were refined by both the LeBail and Rietveld methods using the least squares refinement program GSAS¹⁶.

Atomic coordinates and lattice parameters for $\text{Sr}_3\text{GaO}_4\text{F}$ in the tetragonal $I4/mcm$ space group were used as a starting model in the Rietveld analysis of $\text{Sr}_{3-x}\text{A}_x\text{GaO}_4\text{F}$ ².

Initially, it was assumed that the Sr^{2+} , Ba^{2+} and Ca^{2+} cations were fully disordered, and statistically occupying the A(1) and A(2) sites as reported in previous work ². During the Rietveld analysis, the atomic coordinates and displacement parameters of cations occupying the same site were constrained to equal values. Site occupancies were allowed to vary equally once the refinements had converged ². Our lower resolution laboratory X-ray diffractometer provides data that allow us to refine the crystal structures in agreement to those based on more accurate synchrotron diffraction data published in earlier works ².

Results and Discussion

In order to assess our findings as accurately as possible for the $\text{Sr}_{3-x}\text{A}_x\text{GaO}_4\text{F}$ materials and compare them to the $\text{Sr}_{3-x}\text{A}_x\text{AlO}_4\text{F}$ analogues; $\text{Sr}_{2.8}\text{Ba}_{0.2}\text{AlO}_4\text{F}$ and $\text{Sr}_{2.8}\text{Ca}_{0.2}\text{AlO}_4\text{F}$ were synthesized, refined and compared to data published by Prodjosantoso *et al.* ². The refined lattice parameters for $\text{Sr}_{2.8}\text{Ba}_{0.2}\text{AlO}_4\text{F}$ and $\text{Sr}_{2.8}\text{Ca}_{0.2}\text{AlO}_4\text{F}$ were $a = 6.8212(1) \text{ \AA}$, $c = 11.1558(5) \text{ \AA}$ and $a = 6.7597(3) \text{ \AA}$, $c = 11.1247(8) \text{ \AA}$, respectively; which are comparable to the published values $a = 6.8183(1) \text{ \AA}$, $c = 11.1499(2) \text{ \AA}$ and $a = 6.7551(2) \text{ \AA}$, $c = 11.1170(4) \text{ \AA}$ ². Similar stoichiometric concentrations of Ba^{2+} and Ca^{2+} as detailed in the paper by Prodjosantoso *et al.*, were substituted in $\text{Sr}_{3-x}\text{A}_x\text{GaO}_4\text{F}$ ($0 \leq x \leq 1$). Powder X-ray diffraction data showed a single phase present for all $\text{Sr}_{3-x}\text{Ba}_x\text{GaO}_4\text{F}$ materials up to $x \leq 1.2$ (Figure 3.2). An expansion of the lattice parameters with increased substitution of the Ba^{2+} ion is noted and will be discussed shortly.

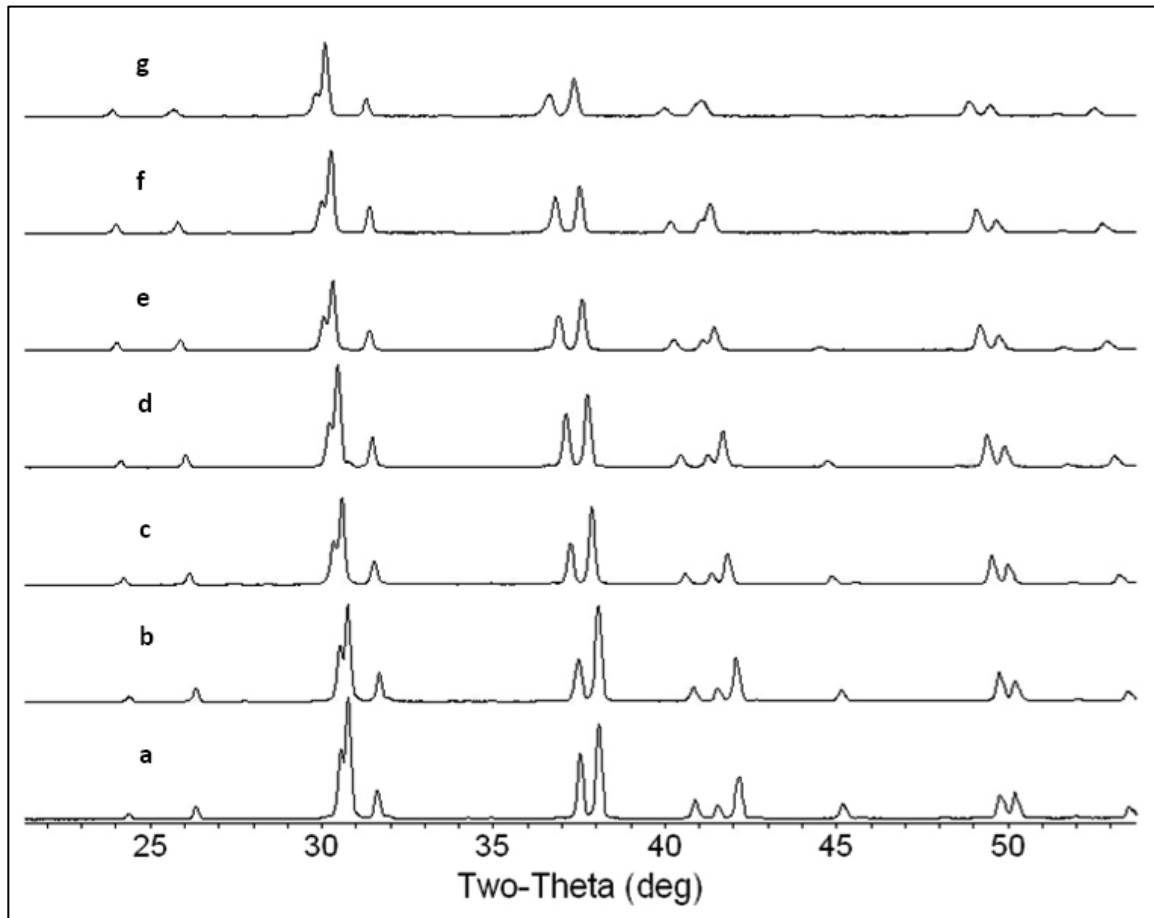


Figure 3.2 $\text{Sr}_{3-x}\text{Ba}_x\text{GaO}_4\text{F}$ powder diffraction pattern, where (a) $x = 0.1$, (b) $x = 0.2$, (c) $x = 0.4$, (d) $x = 0.5$, (e) $x = 0.8$, (f) $x = 1.0$, and (g) $x = 1.2$

In the $\text{Sr}_{3-x}\text{Ca}_x\text{GaO}_4\text{F}$ series, the diffraction pattern revealed CaO impurity peaks when $x \geq 0.4$ (Figure 3.3). According to the published data for $\text{Sr}_{3-x}\text{Ca}_x\text{AlO}_4\text{F}$, a second phase was not present until $x \geq 1^1$. In addition to the CaO impurity, there is a peak located near $2\theta = 43^\circ$ that belongs to a phase similar to $\text{Sr}_3\text{Ga}_2\text{O}_6$. Due to the presence of the aforementioned impurities, structural comparisons will only be made for

$\text{Sr}_{3-x}\text{Ca}_x\text{GaO}_4\text{F}$ where $x \leq 0.3$ which is below the solubility limit. A selection of Rietveld refinements of $\text{Sr}_{3-x}\text{A}_x\text{GaO}_4\text{F}$ ($A = \text{Ba}, \text{Ca}$) based upon XRD data are shown in Figure 3.4.

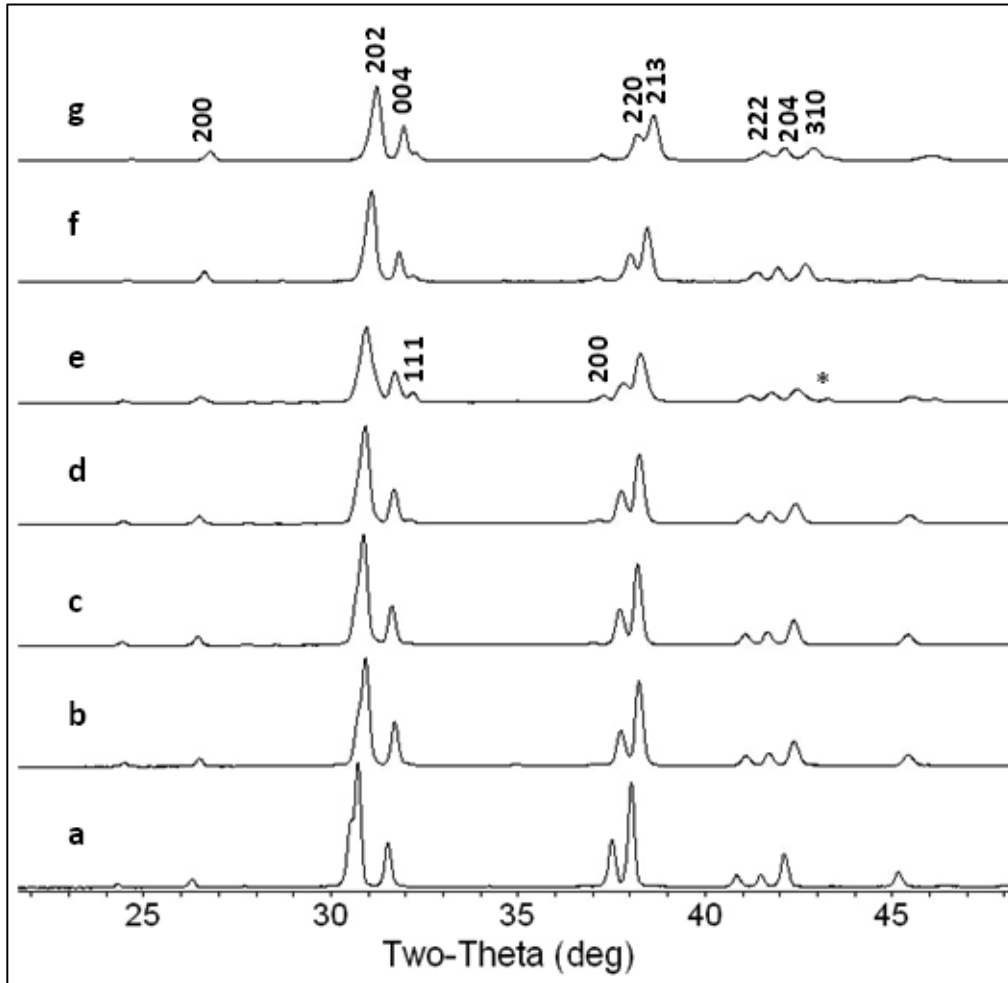


Figure 3.3 Diffraction patterns of $\text{Sr}_{3-x}\text{Ca}_x\text{GaO}_4\text{F}$: where (a) $x = 0.0$, (b) $x = 0.2$, (c) $x = 0.3$, (d) $x = 0.4$, (e) $x = 0.6$, (f) $x = 0.8$, and (g) $x = 1.0$. The hkl values along pattern (g) indicate $\text{Sr}_3\text{GaO}_4\text{F}$ phase, while the hkl values along pattern (e) indicate the CaO phase. The star along diffraction pattern (e) represents an impurity peak appearing at approximately $2\theta = 43^\circ$.

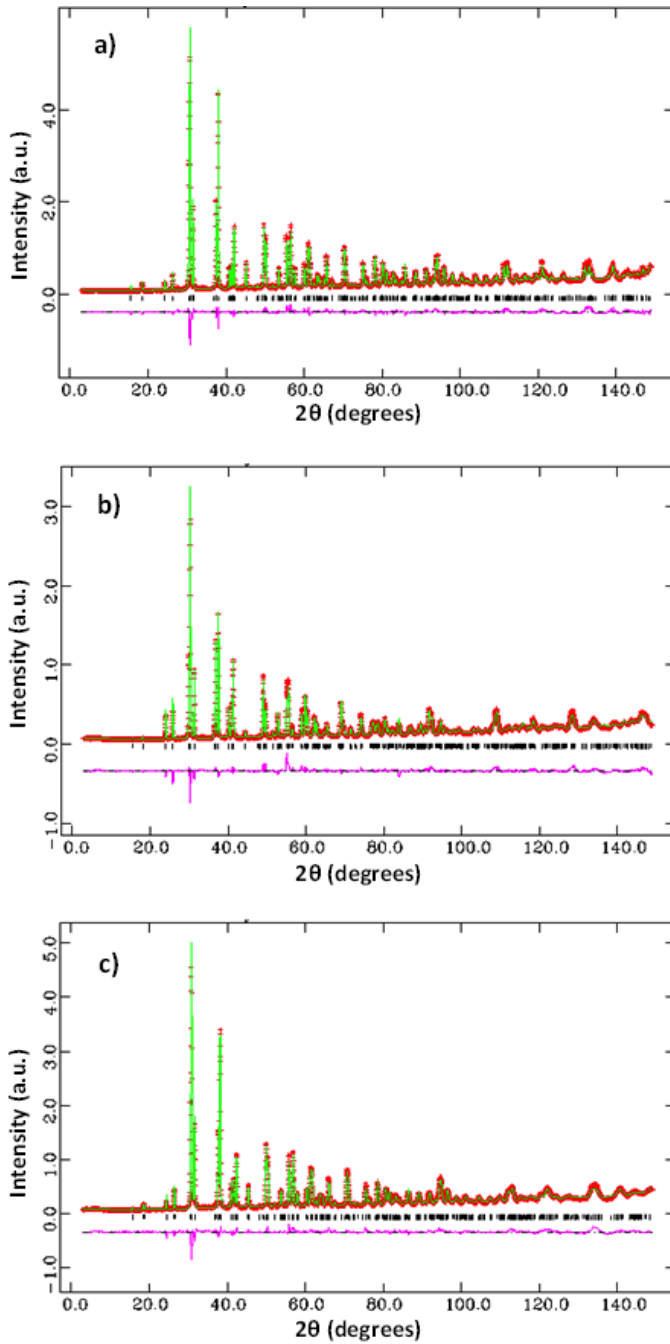


Figure 3.4 Rietveld refinement plots of selected powder diffraction patterns using the space group $I4/mcm$ a) Sr_3GaO_4F b) Sr_2BaGaO_4F and c) $Sr_{2.8}Ca_{0.2}GaO_4F$. The red plot denotes observed data, green pattern indicates calculated pattern, and purple line indicates the difference between observed and calculated patterns.

The refined lattice parameters based upon powder X-ray diffraction data for $Sr_{3-x}A_xGaO_4F$ ($A = Ba^{2+}, Ca^{2+}$) are shown in Table 3.1. When Ba^{2+} is substituted into the

material, both the a and c parameters increase, as would be expected due to its larger cationic radius, while the substitution of Ca^{2+} results in a decrease of the lattice parameters. These trends are illustrated graphically in Figure 3.5.

Table 3.1 Structural Parameters of $\text{Sr}_{3-x}\text{A}_x\text{GaO}_4\text{F}$ obtained by Rietveld analysis of X-ray diffraction patterns

	a (Å)	c (Å)	R_p	R_{wp}	A(2) x	O x	O z
$\text{Sr}_3\text{GaO}_4\text{F}$	6.7915(2)	11.3689(5)	5.92	7.67	0.1674(1)	0.1532(1)	0.6450(1)
A = Ba							
0.1	6.8084(2)	11.3745(3)	5.69	7.56	0.1678(1)	0.1531(5)	0.6426(4)
0.2	6.8258(1)	11.3794(2)	5.27	6.72	0.1681(1)	0.1493(4)	0.6439(4)
0.4	6.8487(1)	11.3916(2)	5.92	7.66	0.1677(1)	0.1545(5)	0.6448(4)
0.5	6.8665(1)	11.3994(3)	6.32	8.30	0.1691(1)	0.1533(6)	0.6450(5)
0.8	6.8996(1)	11.4151(3)	6.60	8.86	0.1681(2)	0.1558(7)	0.6470(6)
1.0	6.9240(1)	11.4285(3)	5.68	7.60	0.1687(1)	0.1528(5)	0.6460(5)
1.2	6.9598(2)	11.4592(4)	6.53	9.08	0.1699(2)	0.1435(8)	0.6449(7)
A = Ca							
0.1	6.7773(2)	11.3579(4)	5.66	7.54	0.1674(1)	0.1538(4)	0.6412(3)
0.2	6.7712(1)	11.3440(3)	5.04	6.65	0.1678(1)	0.1537(4)	0.6405(3)
0.3	6.7594(1)	11.3369(3)	5.33	7.00	0.1678(1)	0.1551(4)	0.6397(3)

The structures were refined in the $I4/mcm$ space group. The atomic positions for this space group are: A(1): 0, 0, $\frac{1}{4}$; A(2): x , $x+\frac{1}{2}$, 0; Ga: 0, $\frac{1}{2}$, $\frac{1}{4}$; F: 0, 0, 0; O: x , $x+\frac{1}{2}$, z . Due to high absorption, U_{iso} values were fixed at zero.

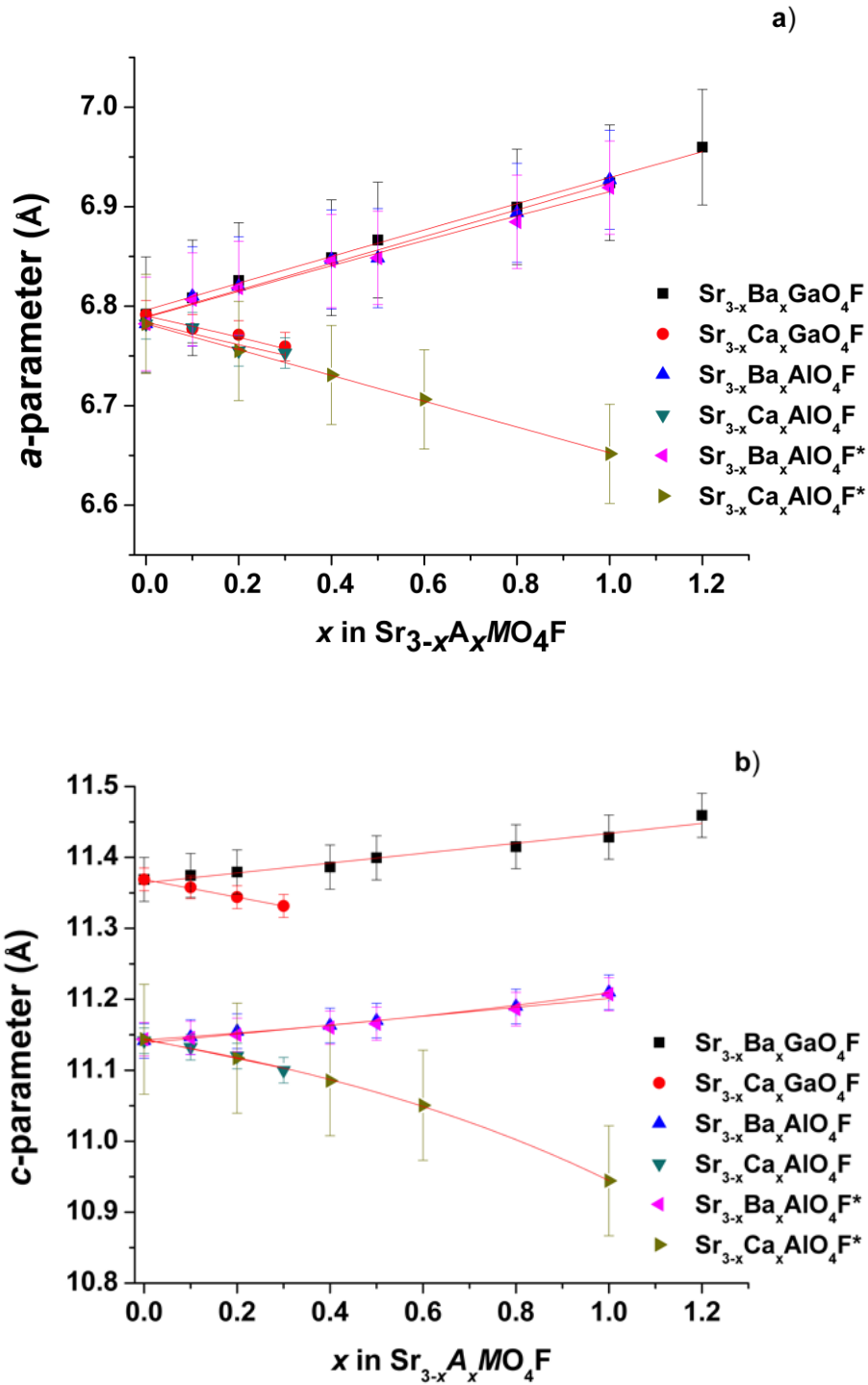


Figure 3.5 Composition dependence of the tetragonal lattice parameters in $\text{Sr}_{3-x}\text{A}_x\text{AlO}_4\text{F}$ and $\text{Sr}_{3-x}\text{A}_x\text{GaO}_4\text{F}$, where a) plots the a -parameter as x increases and b) plots the c -parameter. (* indicates data plotted from Prodjosantoso *et al.* ²)

In the $\text{Sr}_{3-x}\text{Ba}_x\text{GaO}_4\text{F}$ materials, the A(1)-O, A(1)-F, and the A(2)-F bond lengths elongate with increasing Ba^{2+} concentration (Table 3.2). The O-Ga-O bond angles remain relatively constant with further substitution for Ba^{2+} . Conversely, for $\text{Sr}_{3-x}\text{Ca}_x\text{GaO}_4\text{F}$, there is a noticeable decrease of the A(2)-O and A(2)-F bond distances with increasing Ca^{2+} content. This can be attributed to the smaller size of the Ca^{2+} ion compared to Sr^{2+} . As the Ca^{2+} content increases, the O-Ga-O bond angles for the GaO_4 tetrahedra remains effectively constant at approximately 107° .

Table 3.2 Selected Atomic Distances (Å) and Angles (deg) of $\text{Sr}_{3-x}\text{A}_x\text{GaO}_4\text{F}$

Ba	$x = 0.1$	$x = 0.2$	$x = 0.4$	$x = 0.5$
A(1)-O (x8)	2.856(2)	2.868(2)	2.856(3)	2.865(3)
A(1)-F (x2)	2.8436 (1)	2.8448 (1)	2.8479(1)	2.8498(1)
A(2)-O (x2)	2.366 (5)	2.405(4)	2.385(5)	2.389(6)
A(2)-O (x4)	2.723 (3)	2.719(3)	2.757 (4)	2.765(4)
Mean A(2)-O	2.604(4)	2.614(4)	2.633(5)	2.640(5)
A(2)-F (x2)	2.5336 (4)	2.5395(3)	2.5491(4)	2.5516(4)
Ga-O (x4)	1.915(4)	1.881(4)	1.917 (5)	1.909(5)
O-Ga-O	114.0 (1)	114.4(1)	113.0(2)	113.1(2)
O-Ga-O	100.7(3)	100.1(2)	102.6 (3)	102.4 (3)
Mean O-Ga-O	107.4(2)	107.2(2)	107.8(3)	107.8(3)

Table 3.2 (continued) Selected Atomic Distances (Å) and Angles (deg) of Sr_{3-x}A_xGaO₄F

Ba	<i>x</i> = 0.8	<i>x</i> = 1.0	<i>x</i> = 1.2
A(1)-O (x8)	2.860(3)	2.883 (3)	2.933(4)
A(1)-F (x2)	2.8537(1)	2.8571(1)	2.8648(1)
A(2)-O (x2)	2.402(7)	2.416(5)	2.475(7)
A(2)-O (x4)	2.796(5)	2.784(4)	2.747(6)
Mean A(2)-O	2.665(6)	2.661(5)	2.656(7)
A(2)-F (x2)	2.5669(5)	2.5740(4)	2.5838(5)
Ga-O (x4)	1.922(7)	1.911(5)	1.857(7)
O-Ga-O	112.0(2)	112.8(2)	114.9 (3)
O-Ga-O	104.6(4)	103.05(3)	99.1(5)
Mean O-Ga-O	108.3(3)	107.9(3)	107.0(4)

Ca	<i>x</i> = 0.0	<i>x</i> = 0.1	<i>x</i> = 0.2	<i>x</i> = 0.3
A(1)-O (x8)	2.837(2)	2.849(2)	2.850(2)	2.846(2)
A(1)-F (x2)	2.8422(1)	2.8395(1)	2.8360(1)	2.8342(1)
A(2)-O (x2)	2.381(4)	2.347(4)	2.336(4)	2.318(4)
A(2)-O (x4)	2.735(3)	2.706(3)	2.700(3)	2.698(3)
Mean A(2)-O	2.617(4)	2.586(4)	2.579(4)	2.571(4)
A(2)-F (x2)	2.5287(3)	2.5234(3)	2.5199(3)	2.5156(3)
Ga-O (x4)	1.898(4)	1.923(4)	1.926(4)	1.940(4)
O-Ga-O	113.3 (1)	114.4(1)	114.6(1)	114.6(1)
O-Ga-O	102.0 (2)	100.1 (2)	99.7(2)	99.7 (2)
Mean O-Ga-O	107.7(2)	107.2(2)	107.1(2)	107.1(2)

A_3MO_4F -type materials adopt the $a^0a^0c^-$ tilt system consistent with the $I4/mcm$ space group in which there is a rotation of the $FA_{6/2}$ octahedra about the c -axis in which they alternately rotate in clockwise and counterclockwise directions in adjacent layers ¹¹. The data obtained from the Rietveld analyses detailed in Table 3.2 for the Sr_{3-x}A_xGaO₄F and Sr_{3-x}A_xAlO₄F materials show that the MO_4 tetrahedra are distorted. According to

Prodjosantoso *et al.*, the tilt angles in the $\text{Sr}_{3-x}\text{A}_x\text{AlO}_4\text{F}$ materials are approximately 18° .² Table 3.3 shows that the tilt angles for both the $\text{Sr}_{3-x}\text{A}_x\text{GaO}_4\text{F}$ and $\text{Sr}_{3-x}\text{A}_x\text{AlO}_4\text{F}$ materials determined from this experiment are in agreement with the findings by Prodjosantoso *et al.*; furthermore, the tilt angles for the $\text{Sr}_{3-x}\text{Ba}_x\text{GaO}_4\text{F}$ materials are marginally larger than those reported by Prodjosantoso *et al.* for $\text{Sr}_{3-x}\text{Ba}_x\text{AlO}_4\text{F}$, which is supported by our X-ray diffraction data. Likewise, X-ray diffraction data collected under similar conditions shows that the tilt angles for $\text{Sr}_{3-x}\text{Ca}_x\text{GaO}_4\text{F}$ are also marginally larger than the Al-analogue, $\text{Sr}_{3-x}\text{Ca}_x\text{AlO}_4\text{F}$. This increase in the tilt angles scales with the larger GaO_4 tetrahedra compared to the AlO_4 tetrahedra and can be attributed to the difference in the ionic radii between Ga^{3+} (0.47 Å) and Al^{3+} (0.39 Å) for coordination number (CN) of 4.¹⁴

Table 3.3 Tilt angles of $\text{Sr}_{3-x}\text{A}_x\text{GaO}_4\text{F}$ and $\text{Sr}_{3-x}\text{A}_x\text{AlO}_4\text{F}$ materials from the $a^0a^0c^-$ tilt system of $I4/mcm$. Data in set 1 and set 2 were produced by the authors and data from set 3 from Prodjosantoso *et al.*²

(1) Composition	Tilt Angle (deg)	(2) Composition	Tilt Angle (deg)	(3) Composition	Tilt Angle (deg)
$\text{Sr}_3\text{GaO}_4\text{F}$	18.27 (4)	$\text{Sr}_3\text{AlO}_4\text{F}$	17.82 (5)	$\text{Sr}_3\text{AlO}_4\text{F}$	17.82
A = Ba		A = Ba		A = Ba	
0.1	18.18 (5)	0.1	17.90 (5)	0.1	17.85
0.2	18.14 (4)	0.2	17.58 (6)	0.2	17.91
0.4	18.21 (5)	0.4	17.67 (6)	0.4	17.86
0.5	17.93 (5)	0.5	17.90 (7)	0.5	17.91
0.8	18.14 (6)	0.8	17.69 (8)	0.8	17.90
1	18.00 (6)	1	17.23 (8)	1	17.67
1.2	17.76 (7)				
A = Ca		A = Ca		A = Ca	
0.1	18.28 (4)	0.1	17.69 (5)	0.2	17.84
0.2	18.19 (5)	0.2	17.53 (8)	0.4	18.22
0.3	18.20 (5)	0.3	17.85 (7)	0.6	18.12
		0.4	17.70 (6)	1.0	18.14

Bond valence sums (BVS) were calculated to assess the valence of individual atoms within their local environment. In the unsubstituted Sr₃GaO₄F host, the Sr²⁺ ion at the A(1) site has a BVS value of 1.30, which is considered to be significantly underbonded. The underbonding of Sr²⁺ in the A(1) site points towards the possibility of substitution of an isovalent ion with a larger ionic radius. The Ba²⁺ ion with a coordination number (CN) = 10 has an ionic radius of 1.52 Å compared to 1.36 Å for the Sr²⁺ ion¹⁴. The BVS values were calculated by using the following equation:

$$S_{ij} = \exp((r_0 - r_{ij}) / B) \quad (3.1)$$

^{13, 17} where S_{ij} is the individual bond valence between atoms i and j in the material, r_{ij} is the actual bond length between atoms i and j , r_0 is the ideal bond length and B is an empirical constant with a value of 0.37 Å.

The final BVS value is given by $\sum S_{ij}$, which is dependent upon the coordination of the individual atoms. The r_0 values for the Ba-O, Ba-F, Ca-O, and Ca-F bonds are 2.285 Å, 2.188 Å, 1.967 Å, and 1.842 Å, respectively¹⁸. This allows for the calculation of the BVS value to include a weighted r_0 to account for the substituted ions based on their occupancy within Sr_{3-x}A_xMO₄F. The equation for the weighted r_0 is:

$$r_{0(\text{weighted})} = [(r_{0(\text{ion } a)}) \times (\text{occupancy}_{(\text{ion } a)})] + [(r_{0(\text{ion } b)}) \times (\text{occupancy}_{(\text{ion } b)})] \quad (3.2)$$

The BVS values listed in Table 3.4 indicate that the Ba²⁺ substitution in the A(1) site is favorable due to the values approaching the formal oxidation number, however the substitution of the Ba²⁺ ion at the A(2) site would increase the overbonding of this site. When substituted into Sr_{3-x}A_xGaO₄F, Ca²⁺ preferentially occupies the A(2) site due to Ca²⁺ having a smaller ionic radius (1.12 Å)¹⁴ than Sr²⁺. This difference in size causes the BVS values of Ca²⁺ to be consistently lower than those obtained for Sr²⁺ at the A(2) site.

The BVS values for Ga³⁺ from our data are lower than the formal oxidation number 3, however the values are consistent with each other. The BVS values for F and O listed in Table 3.4 are similar to the values given in the paper by Vogt *et al.*, which are 1.23 and 1.86 for Sr₃GaO₄F¹. The BVS values for both the Sr_{3-x}A_xGaO₄F and Sr_{3-x}A_xAlO₄F materials are consistent with the values reported by Prodjosantoso *et al.* where the Sr²⁺ at the A(1) site (denoted Sr1) is significantly lower than the formal oxidation number of 2, while the Sr²⁺ ions located at the A(2) site (denoted Sr2) have BVS values slightly above but closer to their formal oxidation number.

Table 3.4: Bond Valence Sums of Ba and Ca substituted Sr_{3-x}A_xGaO₄F and Sr_{3-x}A_xAlO₄F. Data in Set 1 and set 2 were produced by the author and data from set 3 from Prodjosantoso *et al.*²

(1) Sr _{3-x} Ba _x GaO ₄ F	x = 0.1	x = 0.2	x = 0.4	x = 0.5	x = 0.8	x = 1.0	x = 1.2
Ba1	2.20	2.14	2.20	2.15	2.17	2.06	1.83
Sr1	1.29	1.25	1.28	1.26	1.27	1.20	1.07
Sr2	2.26	2.16	2.12	2.09	1.99	1.97	1.89
Ga	2.58	2.51	2.57	2.51	2.64	2.55	2.57
F	1.14	1.12	1.10	1.09	1.05	1.03	1.01
O	1.66	1.68	1.63	1.63	1.60	1.62	1.66
Sr _{3-x} Ca _x GaO ₄ F	x = 0.0	x = 0.1	x = 0.2	x = 0.3			
Sr1	1.34	1.31	1.31	1.32			
Sr2	2.20	2.36	2.41	2.48			
Ca		1.64	1.67	1.71			
Ga	2.62	2.44	2.45	2.35			
F	1.15	1.14	1.12	1.10			
O	1.66	1.66	1.65	1.63			

Table 3.4 (continued): Bond Valence Sums of Ba and Ca substituted $\text{Sr}_{3-x}\text{A}_x\text{GaO}_4\text{F}$ and $\text{Sr}_{3-x}\text{A}_x\text{AlO}_4\text{F}$. Data in Set 1 and set 2 were produced by the author and data from set 3 from Prodjosantoso *et al.* ²

(2) $\text{Sr}_{3-x}\text{Ba}_x\text{AlO}_4\text{F}$	$x = 0.1$	$x = 0.2$	$x = 0.4$	$x = 0.5$	$x = 0.8$	$x = 1.0$
Ba1	2.34	2.31	2.30	2.28	2.17	1.86
Sr1	1.37	1.35	1.34	1.33	1.27	1.09
Sr2	2.02	2.10	2.00	2.07	2.08	2.14
Al	2.66	2.67	2.61	2.57	2.58	2.56
F	1.21	1.22	1.21	1.21	1.23	1.24
O	1.75	1.80	1.76	1.79	1.83	1.87
$\text{Sr}_{3-x}\text{Ca}_x\text{AlO}_4\text{F}$	$x = 0.0$	$x = 0.1$	$x = 0.2$	$x = 0.3$		
Sr1	1.48	1.46	1.56	1.40		
Sr2	1.99	2.01	2.46	2.17		
Ca		1.39	1.71	1.87		
Al	2.66	2.74	2.68	2.78		
F	1.21	1.19	1.17	1.15		
O	1.69	1.70	1.74	1.72		

(3) $\text{Sr}_{3-x}\text{Ba}_x\text{AlO}_4\text{F}$	$x = 0.1$	$x = 0.2$	$x = 0.4$	$x = 0.5$	$x = 0.8$	$x = 1.0$
Ba1	2.07	2.05	1.97	1.95	1.87	1.81
Sr1	1.30	1.29	1.24	1.23	1.18	1.14
Sr2	2.14	2.12	2.08	2.09	2.04	1.99
Al	2.65	2.63	2.68	2.66	2.64	2.62
F	1.20	1.20	1.21	1.22	1.23	1.24
O	1.80	1.80	1.78	1.78	1.78	1.77
$\text{Sr}_{3-x}\text{Ca}_x\text{AlO}_4\text{F}$	$x = 0.0$	$x = 0.2$	$x = 0.4$	$x = 0.6$	$x = 1.0$	
Sr1	1.37	1.46	1.40	1.37	1.51	
Sr2	1.92	2.20	2.33	2.42	2.69	
Ca		1.45	1.54	1.61	1.78	
Al	2.73	2.51	2.62	2.77	2.74	
F	1.21	1.18	1.14	1.11	1.16	
O	1.66	1.68	1.74	1.78	1.86	

Another approach to rationalize the structure of $\text{Sr}_3\text{MO}_4\text{F}$ is by evaluating the BVS values of ions in different layers along the c -axis. A discrepancy factor, d_i , is calculated using the equation:

$$d_i = \Sigma S_{ij} - v_i \quad (3.3)$$

¹²⁻¹³ where v_i represents the formal oxidation state and ΣS_{ij} represents the BVS value determined from the bond distances. Positive values for d_i indicate that the respective ions are engaged in elongated bonds, while negative values indicate a compression of the bond length when compared to the standard r_0 value ^{13,17}.

Upon calculation of d_i , one observes several trends. As shown in Table 3.5, positive d_i values are associated with cations that appear in the A(1) layer, while negative d_i values are observed for cations appearing in the A(2) layer. Figure 3.6 illustrates the $\text{Sr}_{3-x}\text{A}_x\text{MO}_4\text{F}$ structure viewed as alternating layers of compressed and elongated bonds. The substitution of Ba^{2+} for Sr^{2+} at the A(1) site causes the BVS values for Ba^{2+} to rise above 2.00, which is considerably higher compared to the BVS value of 1.30 for the Sr^{2+} ion in $\text{Sr}_3\text{MO}_4\text{F}$ with $M = \text{Al}, \text{Ga}$. This substitution subsequently produces negative d_i values, indicating a compression of bonds in the A(1) layer. However when the weighted sum of the d_i values are taken into account, which are based on the site occupancies of Ba^{2+} and Sr^{2+} , an overall elongation results. The weighted sum is calculated by using the equation:

$$d_i \text{ (weighted)} = [(d_i \text{ (ion a)}) \times (\text{occupancy}_{\text{(ion a)}})] + [(d_i \text{ (ion b)}) \times (\text{occupancy}_{\text{(ion b)}})]. \quad (3.4)$$

A similar relationship is apparent for the substitution of Ca^{2+} for Sr^{2+} . The larger Sr^{2+} ions produce negative d_i values, while the smaller Ca^{2+} ions produce positive d_i values.

The weighted sum of the d_i values at the A(2) position produces an overall negative value, indicating the compression of bond lengths within the A(2) layer. For all of the $\text{Sr}_{3-x}\text{A}_x\text{MO}_4\text{F}$ materials presented here, the d_i values for F^- indicate an overall compression, while the O^{2-} d_i values indicate an overall elongation (Figure 3.6).

Table 3.5: d_i values for cations in $\text{Sr}_{3-x}\text{A}_x\text{MO}_4\text{F}$ materials, where data in set 1 and set 2 were produced by the author and data from set 3 were calculated from data published by Prodjosantoso *et al.*²

(1) $\text{Sr}_{3-x}\text{Ba}_x\text{GaO}_4\text{F}$	$x = 0.1$	$x = 0.2$	$x = 0.4$	$x = 0.5$	$x = 0.8$	$x = 1.0$	$x = 1.2$
Ba1	-0.20	-0.14	-0.20	-0.15	-0.17	-0.06	0.17
Sr1	0.71	0.75	0.72	0.74	0.73	0.80	0.93
A1_(weighted)	0.62	0.57	0.35	0.30	0.01	-0.02	0.21
Sr2	-0.26	-0.16	-0.12	-0.09	0.01	0.03	0.11
Ga	0.42	0.49	0.43	0.49	0.36	0.45	0.43
F	-0.14	-0.12	-0.10	-0.09	-0.05	-0.03	-0.01
O	0.34	0.32	0.37	0.37	0.40	0.38	0.34
$\text{Sr}_{3-x}\text{Ca}_x\text{GaO}_4\text{F}$	$x = 0.0$	$x = 0.1$	$x = 0.2$	$x = 0.3$			
Sr1	0.66	0.69	0.69	0.68			
Sr2	-0.20	-0.36	-0.41	-0.48			
Ca		0.36	0.33	0.29			
A2_(weighted)		-0.29	-0.26	-0.25			
Ga	0.38	0.56	0.55	0.65			
F	-0.15	-0.14	-0.12	-0.10			
O	0.34	0.34	0.35	0.37			

Table 3.5 (continued): d_i values for cations in $\text{Sr}_{3-x}\text{A}_x\text{MO}_4\text{F}$ materials, where data in set 1 and set 2 were produced by the author and data from set 3 were calculated from data published by Prodjosantoso *et al.* ²

(2) $\text{Sr}_{3-x}\text{Ba}_x\text{AlO}_4\text{F}$	$x = 0.1$	$x = 0.2$	$x = 0.4$	$x = 0.5$	$x = 0.8$	$x = 1.0$
Ba1	-0.34	-0.31	-0.30	-0.28	-0.17	0.14
Sr1	0.63	0.65	0.66	0.67	0.73	0.91
A1_(weighted)	0.53	0.46	0.28	0.20	0.01	0.18
Sr2	-0.02	-0.10	0.00	-0.07	-0.08	-0.14
Al	0.34	0.33	0.39	0.43	0.42	0.44
F	-0.21	-0.22	-0.21	-0.21	-0.23	-0.24
O	0.25	0.20	0.24	0.21	0.17	0.13
$\text{Sr}_{3-x}\text{Ca}_x\text{AlO}_4\text{F}$	$x = 0.0$	$x = 0.1$	$x = 0.2$	$x = 0.3$		
Sr1	0.52	0.54	0.44	0.6		
Sr2	0.01	-0.01	-0.46	-0.17		
Ca		0.61	0.29	0.13		
A2_(weighted)		0.052	-0.31	-0.08		
Al	0.34	0.26	0.32	0.22		
F	-0.21	-0.19	-0.17	-0.15		
O	0.31	0.30	0.26	0.28		

(3) $\text{Sr}_{3-x}\text{Ba}_x\text{AlO}_4\text{F}$	$x = 0.1$	$x = 0.2$	$x = 0.4$	$x = 0.5$	$x = 0.8$	$x = 1.0$
Ba1	-0.07	-0.05	0.03	0.05	0.13	0.19
Sr1	0.70	0.71	0.76	0.77	0.82	0.86
A1_(weighted)	0.62	0.56	0.47	0.41	0.27	0.22
Sr2	-0.14	-0.12	-0.08	-0.09	-0.04	0.01
Al	0.35	0.37	0.32	0.34	0.36	0.38
F	-0.20	-0.20	-0.21	-0.22	-0.23	-0.24
O	0.20	0.20	0.22	0.22	0.22	0.23
$\text{Sr}_{3-x}\text{Ca}_x\text{AlO}_4\text{F}$	$x = 0.0$	$x = 0.2$	$x = 0.4$	$x = 0.6$	$x = 1.0$	
Sr1	0.63	0.54	0.60	0.63	0.49	
Sr2	0.08	-0.20	-0.33	-0.42	-0.69	
Ca		0.55	0.46	0.39	0.22	
A2_(weighted)		-0.05	-0.01	0.07	0.22	
Al	0.27	0.49	0.38	0.23	0.26	
F	-0.21	-0.18	-0.14	-0.11	-0.16	
O	0.34	0.32	0.26	0.22	0.14	

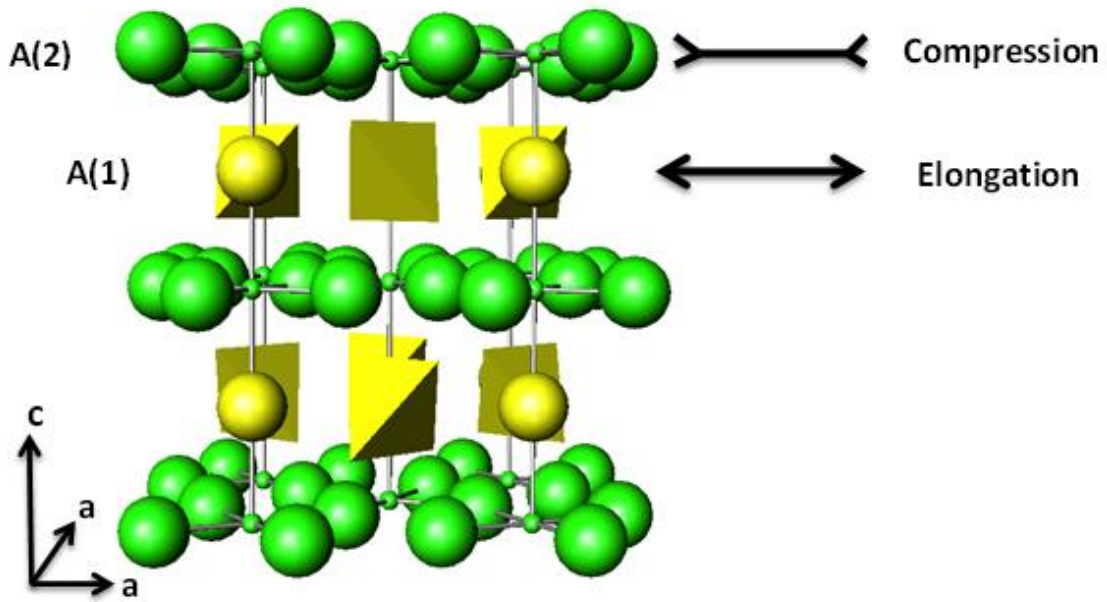


Figure 3.6: The structure of $\text{Sr}_3\text{MO}_4\text{F}$, where all the atoms in the A(1) layer are shown in yellow and the atoms in the A(2) layer are shown in green. Elongation is evidenced by positive d_i values, while compression is determined by negative d_i values for the A(1) and A(2) layers, respectively.

The global instability index (G)¹²⁻¹³ is a measure of the overall structure stability by comparing the calculated BVS values to the formal valence of the atoms/ions represented by the formula:

$$G = (\sum_i \{d_i^2\} / N)^{1/2}. \quad (3.5)$$

In this equation, N represents the total number of atoms in the formula unit¹²⁻¹³. Typical values for G are less than 0.1 valence units (v.u.) when the structure is considered to be unstrained, while structures that have significant lattice strains can have values near 0.2 v.u. Structures with G values significantly larger than 0.2 v.u., are considered unstable¹²⁻¹³. The $\text{Sr}_{3-x}\text{A}_x\text{MO}_4\text{F}$ structure in general has G values slightly above 0.2 v.u.. When Ba^{2+} is substituted into the host, G decreases to a value near or lower than 0.2 v.u., as shown in Table 6. The substitution of Ba^{2+} into $\text{Sr}_{3-x}\text{A}_x\text{GaO}_4\text{F}$ decreases G , although

the G value increases when Ca^{2+} is substituted. This increased G value of the Ca^{2+} substituted $\text{Sr}_{3-x}\text{A}_x\text{GaO}_4\text{F}$ can be attributed to the larger size of the GaO_4 tetrahedra contained in a smaller ReO_3 -type lattice, which causes greater lattice strain in the overall structure. The substitution of Ba^{2+} into $\text{Sr}_{3-x}\text{A}_x\text{GaO}_4\text{F}$ causes G to decrease below 0.2 v.u. when $x = 0.8$, indicating greater stability of the overall structure. The larger Ba^{2+} ion occupying the A(1) site relieves the underbonding of atoms at this site and increases the size of the cavity in which the GaO_4 tetrahedra occupies, subsequently relieving lattice strain. The substitution of Ba^{2+} and Ca^{2+} lead to a decrease in the G values in $\text{Sr}_{3-x}\text{A}_x\text{AlO}_4\text{F}$ indicating that the substitution of both ions are favorable. When the G values are calculated by layer, the A(2) layer is well within the acceptable range of stability (< 0.1 v.u.), while the A(1) layer values indicate the presence of strain (> 0.2 v.u.). One interesting observation is that G increases significantly for the A(1) layer upon the substitution of Ca^{2+} into $\text{Sr}_{3-x}\text{A}_x\text{GaO}_4\text{F}$, which subsequently increases the total G value. This increase can be attributed to the larger size of the GaO_4 tetrahedra combined with the decrease in the lattice parameters corresponding to the decrease in size of the ions occupying the A(2) site, thus causing an increase in lattice strain. The trends for G are illustrated in Figure 3.7.

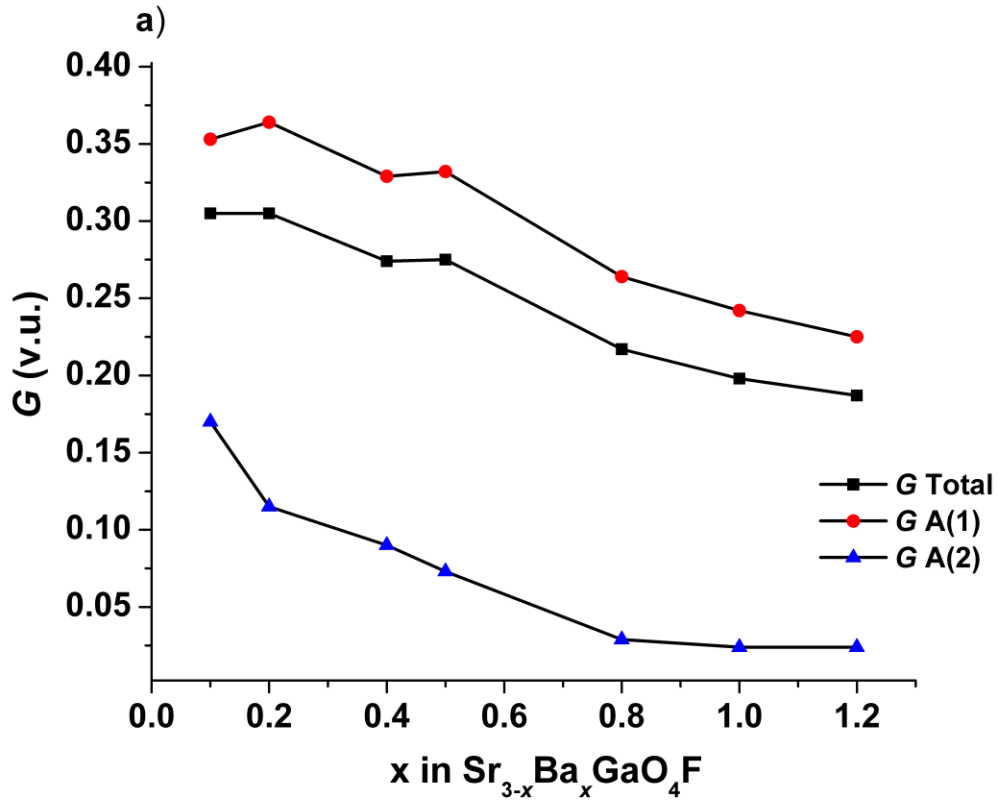


Figure 3.7: Global instability index plots of $\text{Sr}_{3-x}\text{A}_x\text{MO}_4\text{F}$, where a) $\text{Sr}_{3-x}\text{Ba}_x\text{GaO}_4\text{F}$ b) $\text{Sr}_{3-x}\text{Ca}_x\text{GaO}_4\text{F}$ c) $\text{Sr}_{3-x}\text{Ba}_x\text{AlO}_4\text{F}$ d) $\text{Sr}_{3-x}\text{Ca}_x\text{AlO}_4\text{F}$ e) $\text{Sr}_{3-x}\text{Ba}_x\text{AlO}_4\text{F}^*$ and f) $\text{Sr}_{3-x}\text{Ca}_x\text{AlO}_4\text{F}^*$. (*indicates data calculated from Prodjosantoso *et al.* ²)

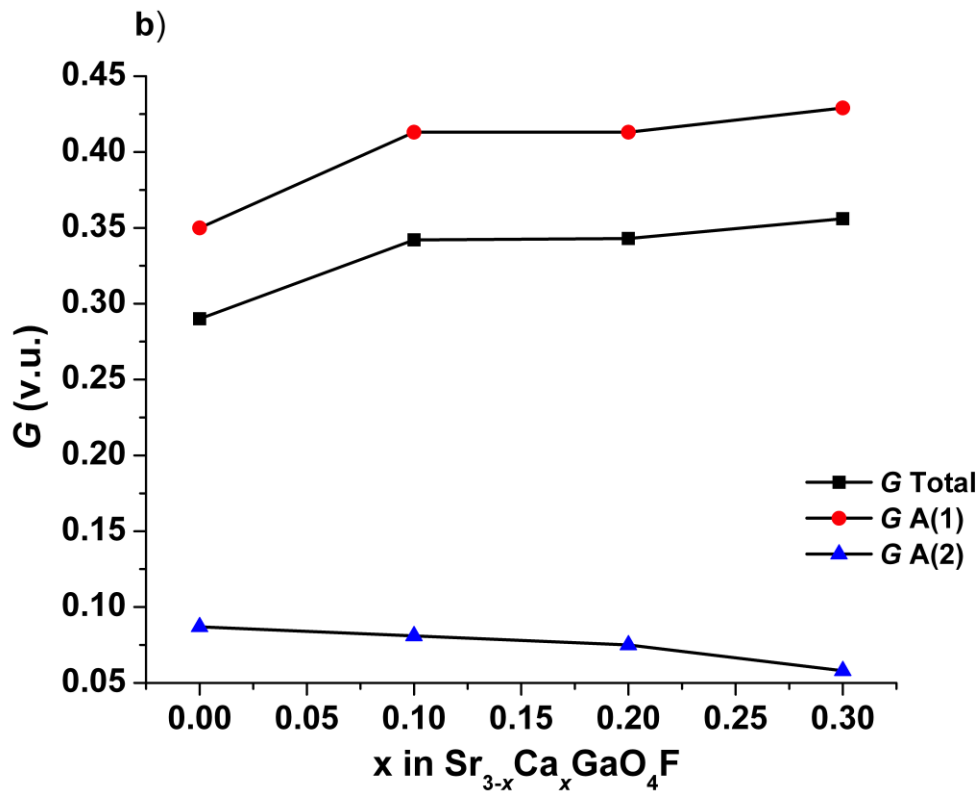


Figure 3.7 (cont'd): Global instability index plots of $\text{Sr}_{3-x}\text{A}_x\text{MO}_4\text{F}$, where a) $\text{Sr}_{3-x}\text{Ba}_x\text{GaO}_4\text{F}$ b) $\text{Sr}_{3-x}\text{Ca}_x\text{GaO}_4\text{F}$ c) $\text{Sr}_{3-x}\text{Ba}_x\text{AlO}_4\text{F}$ d) $\text{Sr}_{3-x}\text{Ca}_x\text{AlO}_4\text{F}$ e) $\text{Sr}_{3-x}\text{Ba}_x\text{AlO}_4\text{F}^*$ and f) $\text{Sr}_{3-x}\text{Ca}_x\text{AlO}_4\text{F}^*$. (*indicates data calculated from Prodjosantoso *et al.* ²)

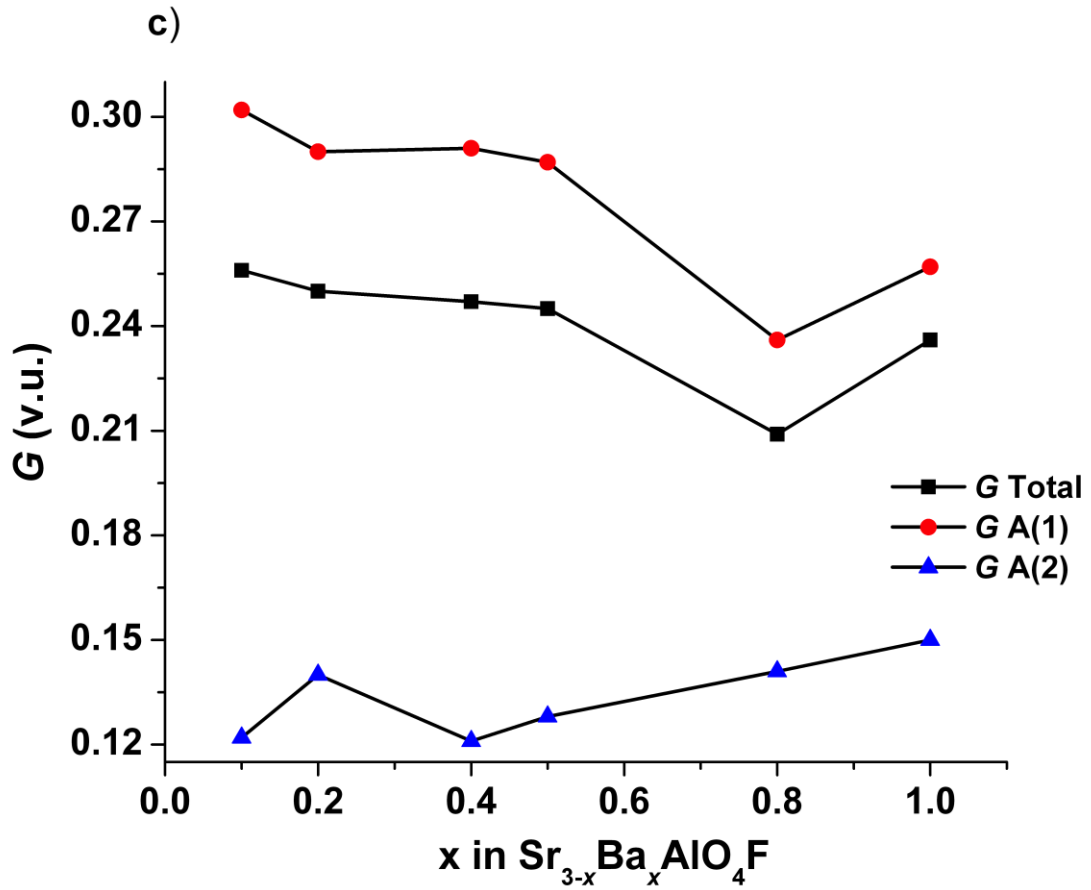


Figure 3.7 (cont'd): Global instability index plots of $\text{Sr}_{3-x}\text{A}_x\text{MO}_4\text{F}$, where a) $\text{Sr}_{3-x}\text{Ba}_x\text{GaO}_4\text{F}$ b) $\text{Sr}_{3-x}\text{Ca}_x\text{GaO}_4\text{F}$ c) $\text{Sr}_{3-x}\text{Ba}_x\text{AlO}_4\text{F}$ d) $\text{Sr}_{3-x}\text{Ca}_x\text{AlO}_4\text{F}$ e) $\text{Sr}_{3-x}\text{Ba}_x\text{AlO}_4\text{F}^*$ and f) $\text{Sr}_{3-x}\text{Ca}_x\text{AlO}_4\text{F}^*$. (*indicates data calculated from Prodjosantoso *et al.* ²)

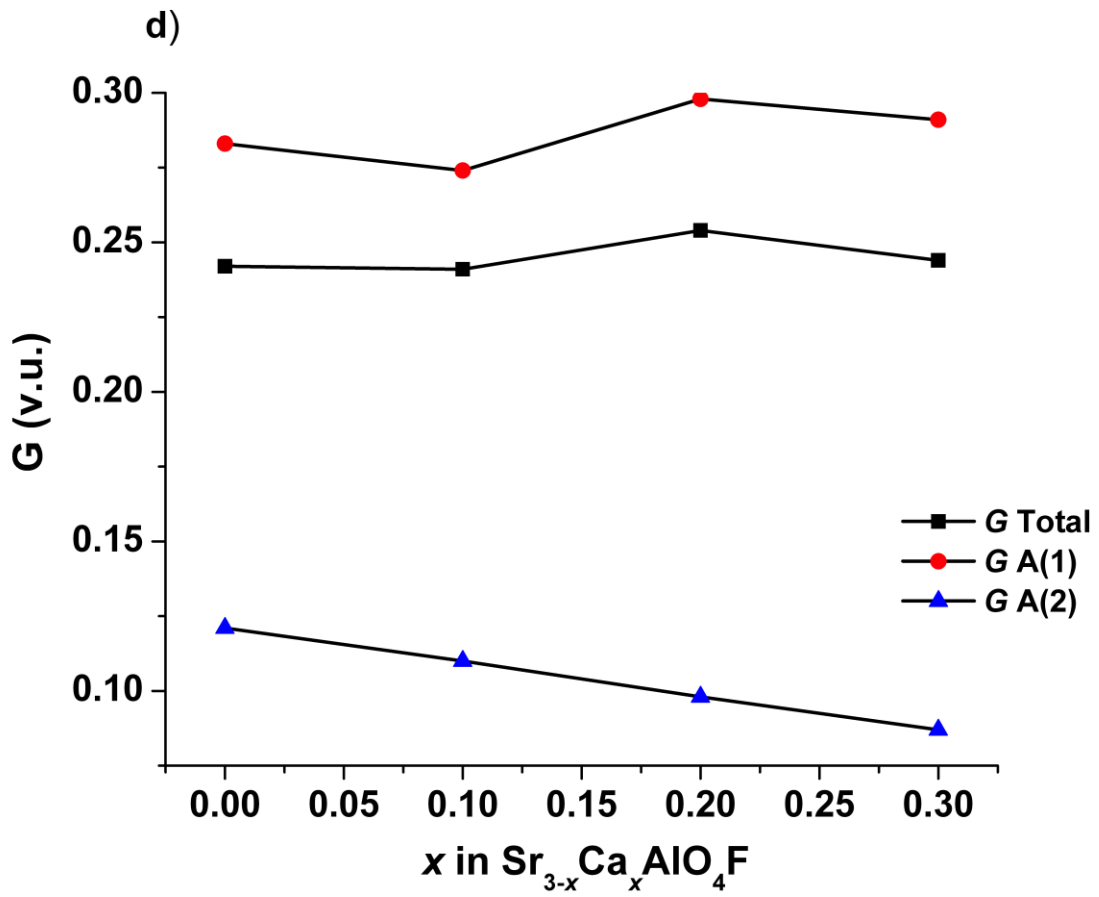


Figure 3.7 (cont'd): Global instability index plots of $Sr_{3-x}A_xMO_4F$, where a) $Sr_{3-x}Ba_xGaO_4F$ b) $Sr_{3-x}Ca_xGaO_4F$ c) $Sr_{3-x}Ba_xAlO_4F$ d) $Sr_{3-x}Ca_xAlO_4F$ e) $Sr_{3-x}Ba_xAlO_4F^*$ and f) $Sr_{3-x}Ca_xAlO_4F^*$. (*indicates data calculated from Prodjosantoso *et al.* ²)

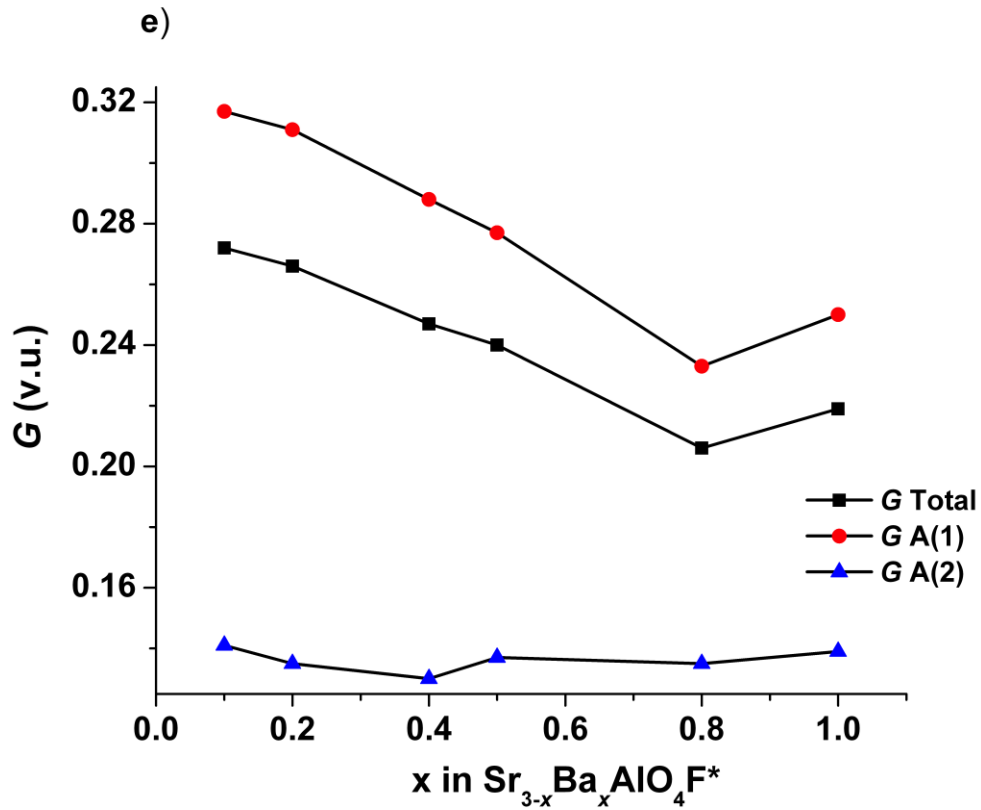


Figure 3.7 (cont'd): Global instability index plots of $Sr_{3-x}A_xMO_4F$, where a) $Sr_{3-x}Ba_xGaO_4F$ b) $Sr_{3-x}Ca_xGaO_4F$ c) $Sr_{3-x}Ba_xAlO_4F$ d) $Sr_{3-x}Ca_xAlO_4F$ e) $Sr_{3-x}Ba_xAlO_4F^*$ and f) $Sr_{3-x}Ca_xAlO_4F^*$. (*indicates data calculated from Prodjosantoso *et al.* ²)

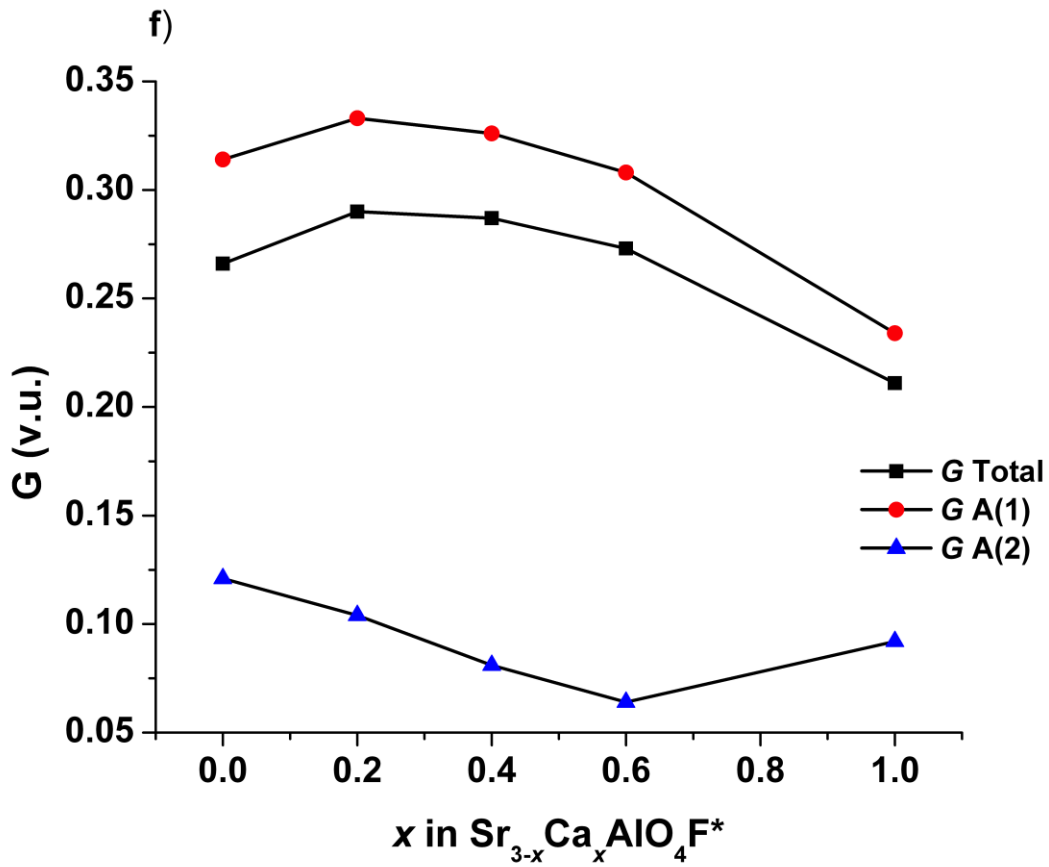


Figure 3.7 (cont'd): Global instability index plots of $Sr_{3-x}A_xMO_4F$, where a) $Sr_{3-x}Ba_xGaO_4F$ b) $Sr_{3-x}Ca_xGaO_4F$ c) $Sr_{3-x}Ba_xAlO_4F$ d) $Sr_{3-x}Ca_xAlO_4F$ e) $Sr_{3-x}Ba_xAlO_4F^*$ and f) $Sr_{3-x}Ca_xAlO_4F^*$. (*indicates data calculated from Prodjosantoso *et al.* ²)

Photoluminescence of $Sr_{3-x}A_xMO_4F$ Materials

When heating Sr_3MO_4F -type materials to elevated temperatures near $1000^\circ C$ in a 5% $H_2/95\%$ Ar atmosphere, self-activating phosphors are formed *via* the creation of defects. Their luminescent properties can be controlled significantly by varying the gas flow rate, temperature, and reaction time. It is known that these materials exhibit broad band photoluminescence emissions ⁷. In $Sr_{3-x}Ba_xAlO_4F$ and $Sr_{3-x}Ba_xGaO_4F$, two types of blue-white and yellow-white light emission are produced when the materials are heated at $1050^\circ C$ for 3 hours in a 5% $H_2/95\%$ Ar reducing atmosphere as shown in Figure 3.8. The chromaticity coordinates corresponding to the emission of these materials were calculated (see Table 3.6) and plotted in an International Commission on Illumination (CIE) diagram. (see Figures 3.10 and 3.12)

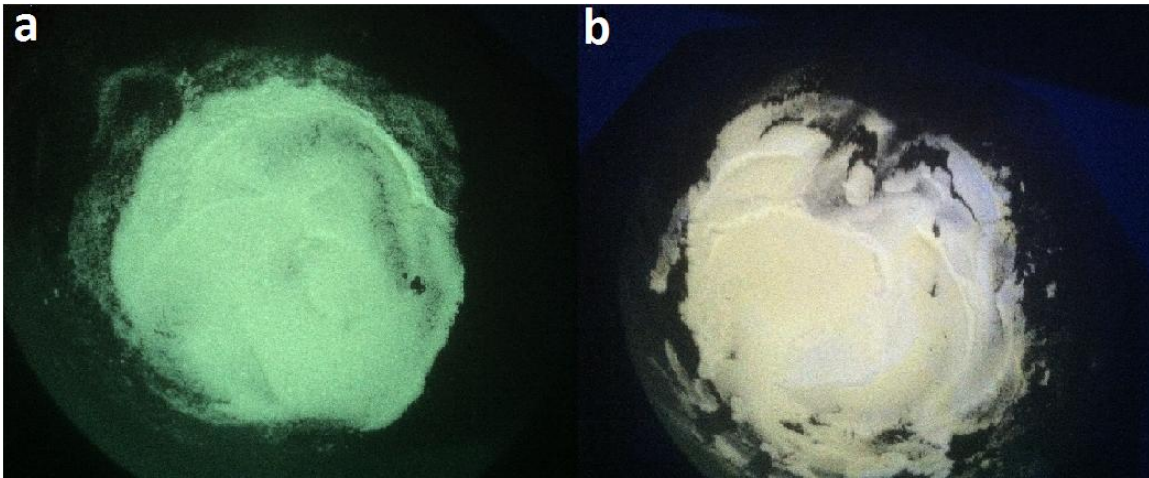


Figure 3.8: Images of Ba substituted $Sr_{3-x}A_xAlO_4F$ and $Sr_{3-x}A_xGaO_4F$ host structures reduced in 5% $H_2/95\%$ Ar excited under 254 nm lamp a) $Sr_{2.6}Ba_{0.4}AlO_4F$ b) $Sr_{2.5}Ba_{0.5}GaO_4F$

Table 3.6 Chromaticity coordinates of Selected $\text{Sr}_{3-x}\text{A}_x\text{MO}_4\text{F}$ phosphors

	Sample	x	y
	$\text{Sr}_3\text{GaO}_4\text{F}$	0.2704	0.4336
	$\text{Sr}_{3-x}\text{Ba}_x\text{GaO}_4\text{F}$		
$x =$	0.1	0.2807	0.4592
	0.2	0.2786	0.4562
	0.4	0.2518	0.4166
	0.5	0.2644	0.4310
	0.8	0.2277	0.3637
	$\text{Sr}_{3-x}\text{Ca}_x\text{GaO}_4\text{F}$		
$x =$	0.2	0.2482	0.4014
	0.3	0.2256	0.3683
	$\text{Sr}_3\text{AlO}_4\text{F}$	0.2105	0.3827
	$\text{Sr}_{3-x}\text{Ba}_x\text{AlO}_4\text{F}$		
$x =$	0.1	0.2120	0.3769
	0.2	0.2077	0.3602
	0.4	0.2091	0.3653
	0.5	0.2081	0.3649
	0.8	0.1912	0.3081
	$\text{Sr}_{3-x}\text{Ca}_x\text{AlO}_4\text{F}$		
$x =$	0.2	0.2044	0.3566

Figure 3.9 shows the emission and excitation spectra for the $\text{Sr}_{3-x}\text{Ba}_x\text{GaO}_4\text{F}$ series where $x = 0.1, 0.2, 0.4, 0.5,$ and $0.8,$ respectively. Each of these materials produced a broad band emission ranging in color from yellow to yellow-white when excited by 254 nm light; however for similar concentrations of Ba^{2+} in $\text{Sr}_{3-x}\text{Ba}_x\text{AlO}_4\text{F}$, a bluish-white emission is produced. There is a progressive shift in the color of these materials from a yellow-white to a bluish-white color with increasing Ca^{2+} content in $\text{Sr}_{3-x}\text{Ca}_x\text{GaO}_4\text{F}$ (Figure 3.10). The excitation spectra of each of the $\text{Sr}_{3-x}\text{Ba}_x\text{GaO}_4\text{F}$ materials were measured at $\lambda_{\text{em}} = 520\text{nm}$. The emission maximum, λ_{max} , for the emission spectra shifts to a longer wavelength as the Ba^{2+} concentration increases. The excitation wavelength, λ_{ex} , at which the λ_{max} is reached for $x = 0.1, 0.2, 0.4, 0.5, 0.8,$ and 1.2 are 248 nm, 254 nm, 256 nm, 257 nm, 260 nm, and 285 nm, respectively.

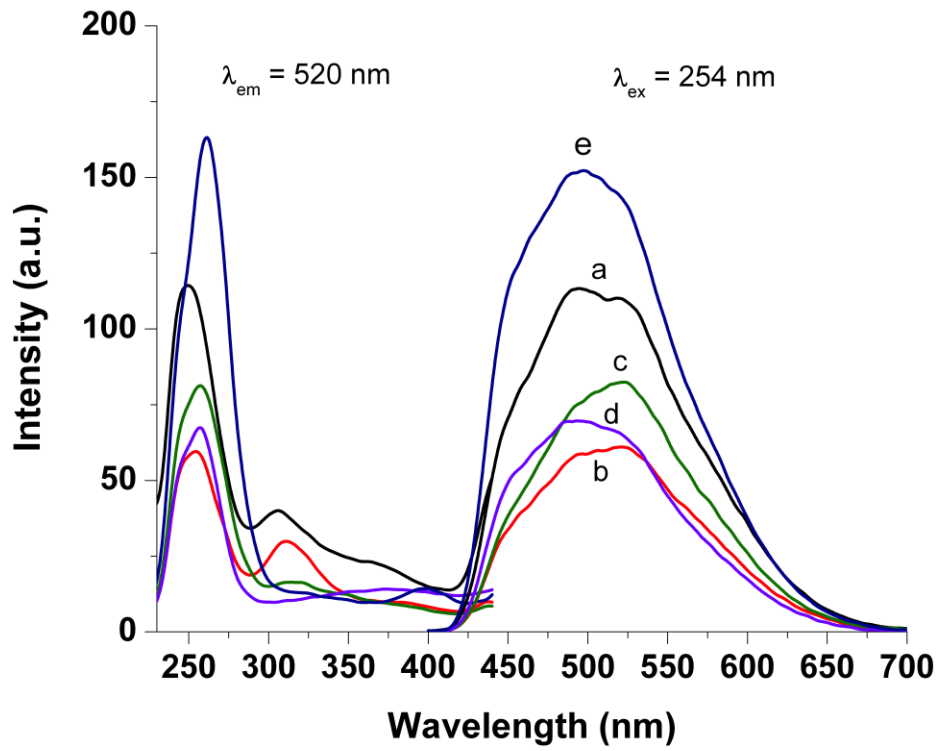


Figure 3.9 Emission and Excitation spectra of $\text{Sr}_{3-x}\text{Ba}_x\text{GaO}_4\text{F}$ where a) $x = 0.1$ b) $x = 0.2$ c) $x = 0.4$ d) $x = 0.5$ and e) $x = 0.8$.

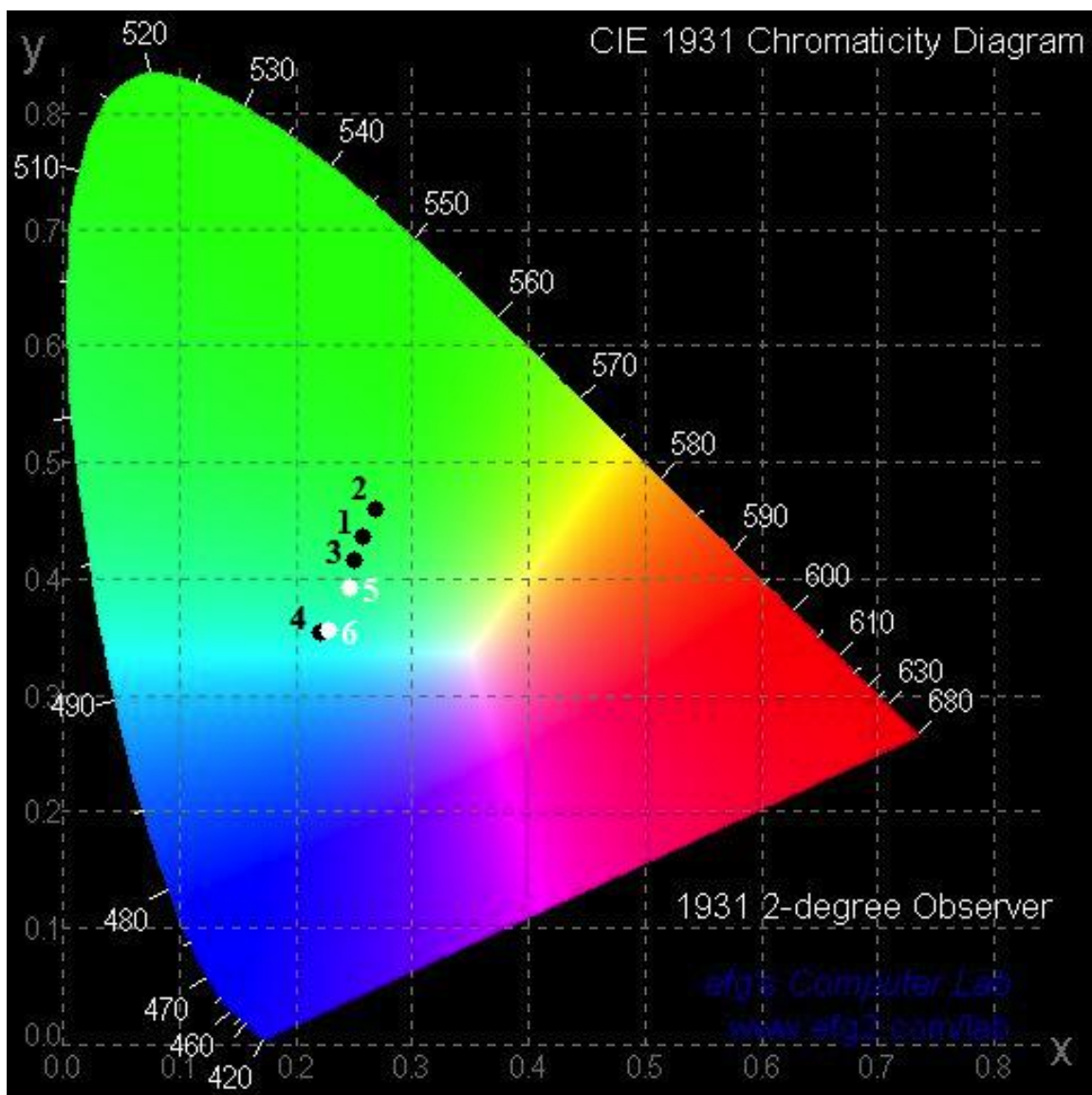


Figure 3.10: CIE chromaticity diagram of $\text{Sr}_{3-x}\text{A}_x\text{GaO}_4\text{F}$ materials with $\lambda_{\text{ex}} = 254 \text{ nm}$ where (1) $\text{Sr}_3\text{GaO}_4\text{F}$ (2) $\text{Sr}_{2.9}\text{Ba}_{0.1}\text{GaO}_4\text{F}$ (3) $\text{Sr}_{2.6}\text{Ba}_{0.4}\text{GaO}_4\text{F}$ (4) $\text{Sr}_{2.2}\text{Ba}_{0.8}\text{GaO}_4\text{F}$ (5) $\text{Sr}_{2.8}\text{Ca}_{0.2}\text{GaO}_4\text{F}$ and (6) $\text{Sr}_{2.6}\text{Ca}_{0.3}\text{GaO}_4\text{F}$. Black dots indicate Ba^{2+} substitutions and white dots indicate Ca^{2+} substitutions

The luminescence of $\text{Sr}_{3-x}\text{Ca}_x\text{AlO}_4\text{F}$ and $\text{Sr}_{3-x}\text{Ba}_x\text{AlO}_4\text{F}$, for $x = 0.2$ and 0.4 , were compared to gauge the effect of Ca^{2+} and Ba^{2+} on the self-activating photoluminescent emission. In both materials, the emission and excitation spectra were similar, as shown in Figure 3.11. For this comparison, the emission spectra show a slight blue-shift as the

concentration of Ca^{2+} increases. Conversely, a slight red-shift occurs in the emission as the concentration of Ba^{2+} is increased. The CIE diagram (Figure 3.12) shows this relationship in both the Ca^{2+} and Ba^{2+} substituted $\text{Sr}_{3-x}\text{A}_x\text{GaO}_4\text{F}$ materials.

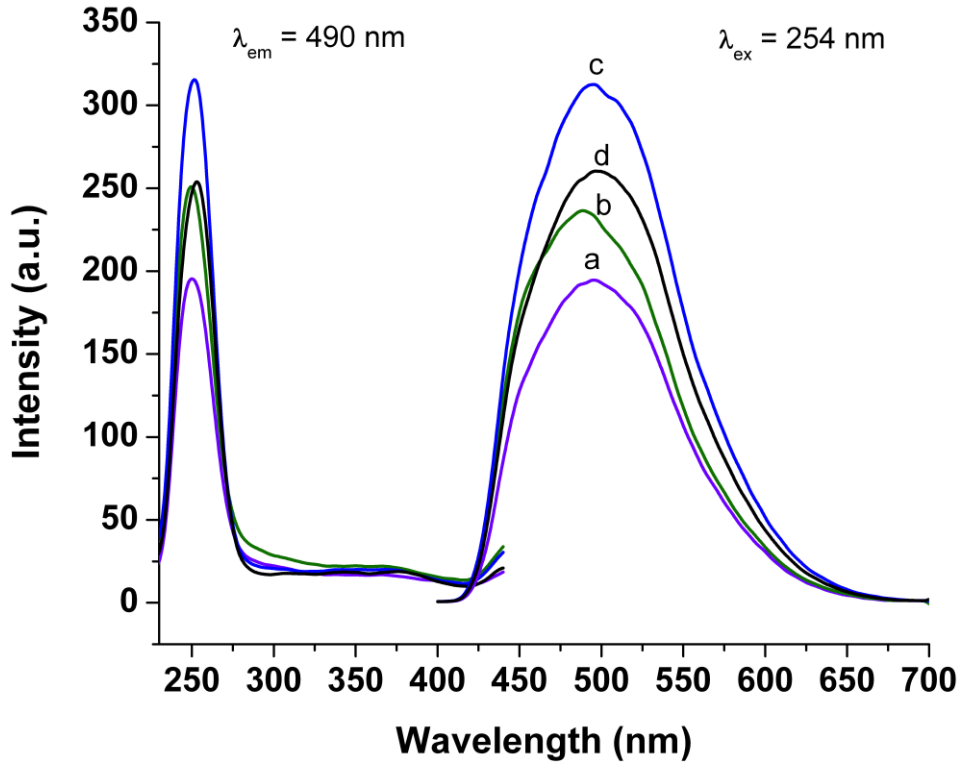


Figure 3.11 Emission and excitation spectra of $\text{Sr}_{3-x}\text{A}_x\text{AlO}_4\text{F}$, where a) $\text{Sr}_{2.8}\text{Ca}_{0.2}\text{AlO}_4\text{F}$ b) $\text{Sr}_{2.6}\text{Ca}_{0.4}\text{AlO}_4\text{F}$ c) $\text{Sr}_{2.8}\text{Ba}_{0.2}\text{AlO}_4\text{F}$ and d) $\text{Sr}_{2.6}\text{Ba}_{0.4}\text{AlO}_4\text{F}$.

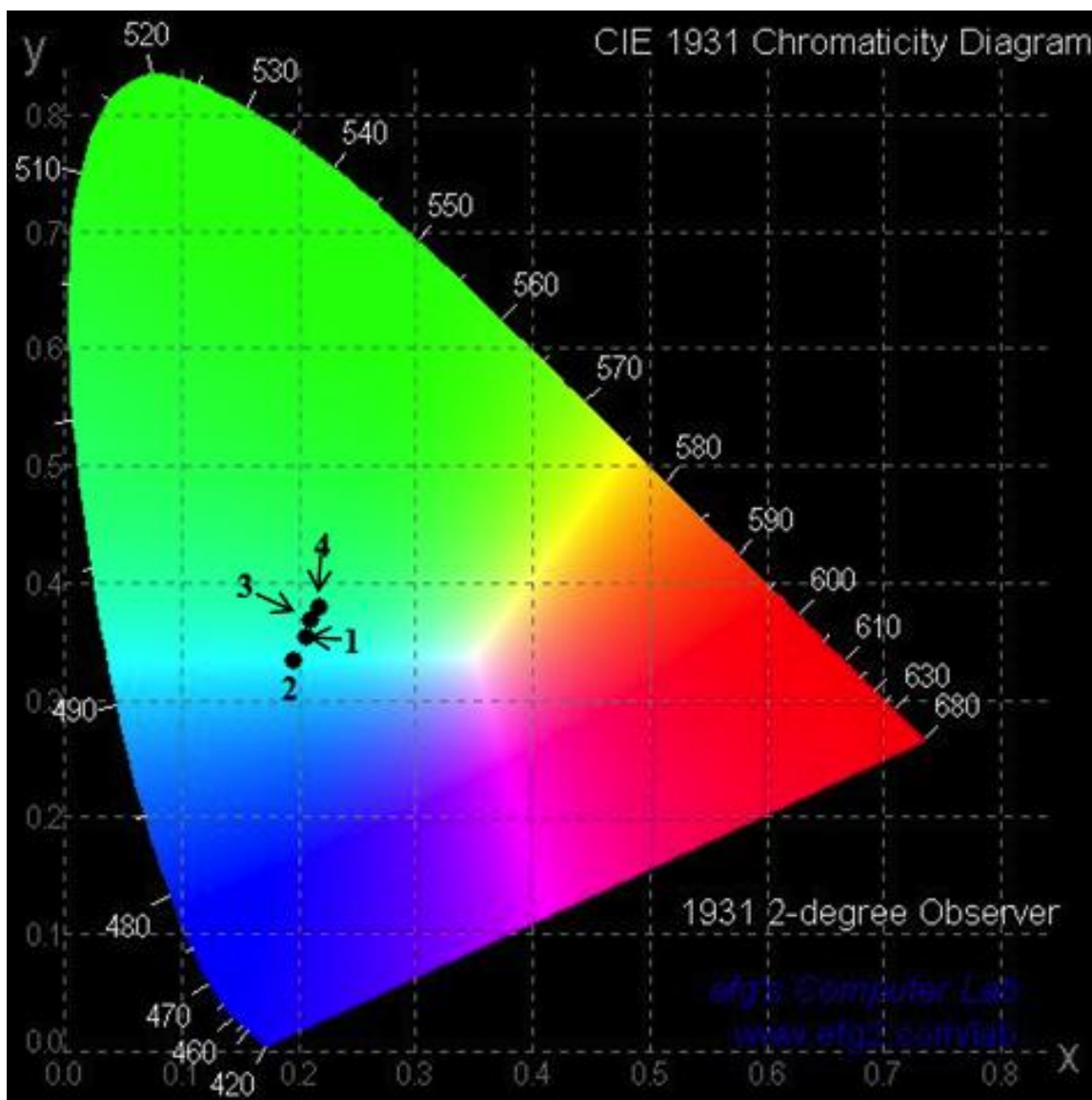


Figure 3.12: CIE chromaticity diagram of $\text{Sr}_{3-x}\text{A}_x\text{AlO}_4\text{F}$ excited by 254 nm light, where 1) $\text{Sr}_{2.8}\text{Ca}_{0.2}\text{AlO}_4\text{F}$ 2) $\text{Sr}_{2.6}\text{Ca}_{0.4}\text{AlO}_4\text{F}$ 3) $\text{Sr}_{2.8}\text{Ba}_{0.2}\text{AlO}_4\text{F}$ and 4) $\text{Sr}_{2.6}\text{Ba}_{0.4}\text{AlO}_4\text{F}$.

The changes in the photoluminescence emission of these self-activating phosphors are correlated with the changes in the local environment, caused by the substitution of Ba^{2+} and Ca^{2+} ions at the A(1) and A(2) sites. The overall trend of the shift of the photoluminescence emission when substituting both $\text{Sr}_{3-x}\text{Ba}_x\text{GaO}_4\text{F}$ and $\text{Sr}_{3-x}\text{Ba}_x\text{AlO}_4\text{F}$, as well as $\text{Sr}_{3-x}\text{Ca}_x\text{GaO}_4\text{F}$ and $\text{Sr}_{3-x}\text{Ca}_x\text{AlO}_4\text{F}$ materials, is a blue-shift

when excited by 254 nm light. As shown by the excitation spectra in Figure 3.9, the λ_{\max} of the emission shifts to a longer wavelength with increased substitution of Ba^{2+} . The increased substitution of Ca^{2+} causes a blue-shift in the emission, however, the range of colors that the substitution produces are limited to just the blue region. The color range of the Ba^{2+} substitution ranges from blue-white, yellow to yellow-white.

This difference in the range of the photoluminescent emission can be correlated to the fact that the substituted Ba^{2+} exhibits a preference for the 10-coordinated A(1) layer in these ordered oxyfluorides, while the Ca^{2+} substitution occurs in the 8-coordinated A(2) layer. Due to the larger size of the Ba^{2+} ions, the substitution in the A(1) layer will cause greater distortions in the local environment, while ions in the A(2) layer will have less of an impact due to the larger distance between the A(2) ion and the MO_4 tetrahedra.

Conclusions

When substituted into $\text{Sr}_{3-x}\text{Ba}_x\text{GaO}_4\text{F}$, Ba^{2+} cations preferentially occupy the A(1) sites, while the Ca^{2+} cations exhibit preference for the A(2) sites. While this trend is the same as the one observed by Prodjosantoso *et al.* for the $\text{Sr}_{3-x}\text{Ba}_x\text{AlO}_4\text{F}$ and $\text{Sr}_{3-x}\text{Ca}_x\text{AlO}_4\text{F}$ materials, the solubility of Ba^{2+} and Ca^{2+} for $M = \text{Ga}$ are different and reveal a dependence on the size difference between the GaO_4 and AlO_4 tetrahedra. In previous studies on $\text{Sr}_{3-x}\text{Ba}_x\text{AlO}_4\text{F}$ materials, the maximum solubility limit is at $x = 1.0$ ². The larger size of the GaO_4 tetrahedra allows more Ba^{2+} ions to be substituted in $\text{Sr}_{3-x}\text{Ba}_x\text{AlO}_4\text{F}$ up to $x = 1.2$. Rietveld analysis shows that this increase in size also allows Ba^{2+} to fully occupy the A(1) site.

For the $\text{Sr}_{3-x}\text{Ca}_x\text{AlO}_4\text{F}$ materials, it has been previously reported that the maximum amount of Ca^{2+} that can be substituted for Sr^{2+} is $x = 1.0$. At $x = 0.4$ in $\text{Sr}_{3-x}\text{Ca}_x\text{GaO}_4\text{F}$, CaO begins to appear as a second phase in the powder diffraction pattern, accompanied by an impurity peak similar to $\text{Sr}_3\text{Ga}_2\text{O}_6$. Rietveld analysis of the $\text{Sr}_{3-x}\text{Ca}_x\text{GaO}_4\text{F}$ materials shows that the lattice parameters gradually decrease with increasing Ca^{2+} content. The reduced $\text{Sr}_{3-x}\text{A}_x\text{AlO}_4\text{F}$ materials consistently produce blue to blue-white photoluminescence emission, while the $\text{Sr}_{3-x}\text{A}_x\text{GaO}_4\text{F}$ materials produce yellow-green to yellow-white emission when excited by 254 nm light. Increasing the Ba^{2+} content for the $\text{Sr}_{3-x}\text{Ba}_x\text{GaO}_4\text{F}$ materials shifts the color of the materials from yellow to yellow-white. While limited, the substitution of Ca^{2+} produces a deep yellow-green emission that is almost completely quenched when $x = 0.3$. This correlates with the increase in global stability index as Ca^{2+} is substituted into $\text{Sr}_{3-x}\text{A}_x\text{GaO}_4\text{F}$

References

- (1) Vogt, T.; Woodward, P. M.; Hunter, B. A.; Prodjosantoso, A. K.; Kennedy, B. J. *Journal of Solid State Chemistry* **1999**, *144*, 228-231.
- (2) Prodjosantoso, A. K.; Kennedy, B. J.; Vogt, T.; Woodward, P. M. *Journal of Solid State Chemistry* **2003**, *172*, 89-94.
- (3) Park, S.; Vogt, T. *Journal of Luminescence* **2009**, *129*, 952-957.
- (4) Im, W. B.; Brinkley, S.; Hu, J.; Mikhailovsky, A.; DenBaars, S. P.; Seshadri, R. *Chemistry of Materials* **2010**, *22*, 2842-2849.
- (5) Setlur, A. A.; Radkov, E. V.; Henderson, C. S.; Her, J.H.; Srivastava, A. M.; Karkada, N.; Kishore, M. S.; Kumar, N. P.; Aesram, D.; Deshpande, A. *Chemistry of Materials* **2010**, *22*, 4076-4082.
- (6) Park, S. *Journal of Solid State Chemistry* **2012**, 875-878.
- (7) Park, S.; Vogt, T. *Journal of Physical Chemistry C* **2010**, *114*, 11576-11583.
- (8) Park, S.; Vogt, T. *Journal of the American Chemical Society* **2010**, *132*, 4516-4517.
- (9) Krivovichev, S. V. *Zeitschrift für Kristallographie* **2008**, *223*, 109-113.
- (10) Woodward, P. M. *Acta Crystallographica Section B*. **1997**, *53*, 32-43.
- (11) Woodward, P. M. *Acta Crystallographica Section B*. **1997**, *53*, 44-66.
- (12) Lufaso, M. W.; Woodward, P. M. *Acta Crystallographica Section B: Structural Science* **2001**, *57*, 725-738.
- (13) Brown, I. D. *Chem. Rev.* **2009**, *109*, 6858-6919.
- (14) Shannon, R. D. *Acta Crystallographica Section A: Crystal Physics, Diffraction, Theoretical and General Crystallography* **1976**, *32*, 751-767.
- (15) Chen, W.; Liang, H.; Han, B.; Zhong, J.; Su, Q. *The Journal of Physical Chemistry C* **2009**, *113*, 17194-17199.

- (16) Larson, A. C.; Von Dreele, R. B. *General Structure Analysis System*. Los Alamos National Laboratory Report *LAUR 860-748* (2000)
- (17) Brown, I. D.; Altermatt, D. *Acta Crystallographica Section B: Structural Science* **1985**, *41*, 244-247.
- (18) Brese, N. E.; O'keeffe, M. *Acta Crystallographica Section B: Structural Science* **1991**, *47*, 192-197.

CHAPTER 4

STRUCTURES AND SELF-ACTIVATING PHOTOLUMINESCENT PROPERTIES OF



Introduction

Due to the versatility of iso- and aliovalent substitutions on the Sr^{2+} and M cation sites, the $\text{Sr}_3\text{MO}_4\text{F}$ ($M = \text{Al, Ga}$) family of ordered oxyfluorides has been investigated as potential host lattices for luminescent phosphors containing rare earths¹⁻⁶. Park and Vogt demonstrated that $\text{Sr}_3\text{MO}_4\text{F}$ type materials can also be turned into self-activating phosphors by tempering the materials in a reducing atmosphere as well as varying the gas flow rate and temperature⁷, which might allow this family of phosphor materials to be used in CFLs and LED lights. Recently, Green and Vogt studied the structural and photoluminescent properties of $\text{Sr}_{3-x}\text{A}_x\text{GaO}_4\text{F}$ materials and compared them to $\text{Sr}_{3-x}\text{A}_x\text{AlO}_4\text{F}$ ⁸⁻⁹. Both $\text{Sr}_{3-x}\text{A}_x\text{GaO}_4\text{F}$ and $\text{Sr}_{3-x}\text{A}_x\text{AlO}_4\text{F}$ materials exhibit photoluminescence when tempered in a reducing atmosphere with emitted colors of $\text{Sr}_{3-x}\text{A}_x\text{GaO}_4\text{F}$ materials ranging from yellow to yellow-white, while the $\text{Sr}_{3-x}\text{A}_x\text{AlO}_4\text{F}$ materials showed blue-white emissions when excited by 254 nm light.

The $A_3\text{MO}_4\text{F}$ ($A = \text{Ca}^{2+}, \text{Sr}^{2+}, \text{Ba}^{2+}$) structure, as shown in Figure 4.1, is a distorted anti-Perovskite formed by corner-sharing FA_6 octahedra, where the A^{2+} cations occupy two different sites denoted A(1) and A(2). The MO_4 tetrahedra occupy the center of the

unit cell. Substitutions made at the 10-coordinated A(1) and 8-coordinated A(2) site cause structural changes due to cation size and charge differences, which subsequently alter the optical properties. For isovalent substitutions of Ba^{2+} and Ca^{2+} in $Sr_{3-x}A_xMO_4F$, the larger Ba^{2+} ions preferentially occupy the A(1) sites, which are located at the axial positions of the corner sharing $FA(1)_2A(2)_4$ octahedra, while smaller Ca^{2+} ions prefer to occupy the equatorial A(2) sites (Prodjosantoso, et al. 2003). Aliovalent substitutions made within the A_3MO_4F structure result in $A_{3-(3a/2)}RE_aMO_4F$ and $A_{3-2a}RE_aNa_aMO_4F$ type materials, where no charge compensation is present and therefore defects must be created^{1, 10-11}.

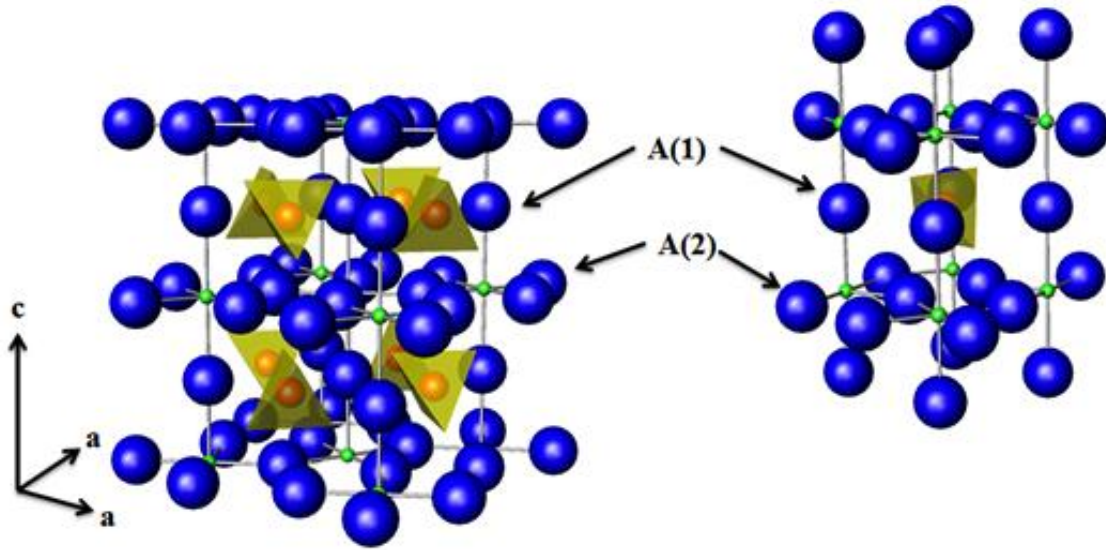


Figure 4.1: Structure of Sr_3MO_4F , where F is represented by green spheres, Sr is represented by blue spheres and MO_4 is represented by yellow tetrahedra with a centered red sphere.

The substitution of In^{3+} into the Sr_3MO_4F type host lattice shifts the excitation wavelengths of these phosphors towards 370nm, which is at the lower end of the

emission wavelength of $\text{In}_x\text{Ga}_{1-x}\text{N}$ based LEDs ⁷. Known materials in the $\text{Sr}_3\text{MO}_4\text{F}$ family with two ions occupying the M -site include the self-activating $\text{Sr}_{3-x}\text{Ba}_x\text{Al}_{1-c}\text{In}_c\text{O}_{4-a}\text{F}_{1-\delta}$ ⁷ as well as rare-earth containing $\text{Sr}_{2.25}\text{Ba}_{0.6}\text{Eu}_{0.1}\text{Ga}_{0.95}\text{In}_{0.05}\text{O}_{4-a}\text{F}_{1-\delta}$ ¹⁰⁻¹¹, $\text{Sr}_{2.5-3x/2}\text{Ba}_{0.5}\text{Sm}_x\text{Al}_{1-y}\text{In}_y\text{O}_4\text{F}$ ¹² and $\text{Sr}_{2.5-3x/2}\text{Ca}_{0.5}\text{Pr}_x\text{Al}_{1-y}\text{In}_y\text{O}_4\text{F}$ ¹³ materials.

This work describes the synthesis, structural and optical characterization of two new families of $\text{Sr}_3\text{MO}_4\text{F}$ -type materials; $\text{Sr}_{3-x}\text{Ba}_x\text{Al}_y\text{Ga}_{1-y}\text{O}_4\text{F}$ and $\text{Sr}_{3-x}\text{Ba}_x\text{Al}_y\text{Ga}_{1-y-z}\text{In}_z\text{O}_4\text{F}$ materials, where substitutions are made at the A(1) sites and up to 3 cations are located on the M sites in order to tune the self-activating PL properties at room temperature. We focus on varying the temperature during annealing in a reducing atmosphere of 5% H_2 /95% Ar for $\text{Sr}_{2.4}\text{Ba}_{0.6}\text{Al}_y\text{Ga}_{1-y-z}\text{In}_z\text{O}_4\text{F}$ materials, where Al^{3+} , Ga^{3+} , and In^{3+} ions simultaneously occupy the M -site. Substitutions in these host structures, as well as the reducing/ annealing conditions, may provide a way to reduce the need of rare-earth oxide materials for certain lighting applications.

Experimental

Samples of $\text{Sr}_{3-x}\text{Ba}_x\text{Al}_y\text{Ga}_{1-y}\text{O}_4\text{F}$ and $\text{Sr}_{3-x}\text{Ba}_x\text{Al}_y\text{Ga}_{1-y}\text{In}_z\text{O}_4\text{F}$ were prepared by intimately mixing and heating the appropriate stoichiometric amounts of BaCO_3 (Alfa-Aesar 99%), SrCO_3 (Sigma-Aldrich 99.995%), SrF_2 (Alfa-Aesar 99%), Ga_2O_3 (Sigma-Aldrich 99%), Al_2O_3 (Sigma-Aldrich 99%) and In_2O_3 (Alfa-Aesar 99%) in air. The oxyfluoride materials formed after 24h heating cycles at 700°C, 800°C, and 900°C accompanied with grinding of these materials between successive heating cycles. Both $\text{Sr}_{3-x}\text{Ba}_x\text{Al}_y\text{Ga}_{1-y}\text{O}_4\text{F}$ and $\text{Sr}_{3-x}\text{Ba}_x\text{Al}_y\text{Ga}_{1-y}\text{In}_z\text{O}_4\text{F}$ materials were annealed in air for 72 h at

1100°C. Self-activating photoluminescence in $\text{Sr}_{3-x}\text{Ba}_x\text{Al}_y\text{Ga}_{1-y}\text{O}_4\text{F}$ samples was observed after heating at 1050°C in a 5% $\text{H}_2(\text{g})/95\% \text{Ar}(\text{g})$ atmosphere for 3 hours. In order to study the effect of reducing conditions on the photoluminescence of $\text{Sr}_{2.4}\text{Ba}_{0.6}\text{Al}_y\text{Ga}_{1-y}\text{In}_z\text{O}_4\text{F}$ materials, each sample type was heated at 800°C, 900°C, and 1050°C in a 5% $\text{H}_2(\text{g})/95\% \text{Ar}(\text{g})$ atmosphere for 3 hours. The GSAS suite of programs was used to perform Rietveld refinement based upon powder diffraction data obtained from a Rigaku MiniFlexTM diffractometer (Cu $K\alpha$ radiation $\lambda = 1.54059 \text{ \AA}$)¹⁴. Data was collected in the range $2\theta = 3^\circ\text{-}149^\circ$, at 0.02° intervals and a scan speed of 0.25 deg/min. Emission and excitation data was collected using a Perkin Elmer LS55 spectrofluorometer equipped with a fiber-optic attachment for solid samples.

Results and Discussion

Structural Properties of $\text{Sr}_{3-x}\text{Ba}_x\text{Al}_y\text{Ga}_{1-y}\text{O}_4\text{F}$ materials

$\text{Sr}_{3-x}\text{Ba}_x\text{Al}_y\text{Ga}_{1-y}\text{O}_4\text{F}$ materials have the $\text{Sr}_3\text{MO}_4\text{F}$ structure, where Ba^{2+} substitutes Sr^{2+} at the A(1) position, while Al^{3+} and Ga^{3+} simultaneously occupy the *M* site. The occupation of Al^{3+} and Ga^{3+} at the *M* site results in disordered AlO_4 and GaO_4 tetrahedra located within this anti-Perovskite structure. In order to gauge the effect of substitution in the MO_4 tetrahedra, the Al^{3+} content was varied while holding the Ba^{2+} concentration constant. The substitution of Ba^{2+} in these materials was varied by $x = 0.2, 0.4, 0.6, \text{ and } 0.8$. At each x value, materials with three different levels of Al^{3+} contents were synthesized: $y = 0.25, 0.5, \text{ and } 0.75$. Powder X-ray diffraction data of $\text{Sr}_{3-x}\text{Ba}_x\text{Al}_y\text{Ga}_{1-y}\text{O}_4\text{F}$ materials confirm that all materials synthesized were single-phase (Figure 4.2) and do not indicate the presence of a superstructure arising from an ordering

of the AlO_4 and GaO_4 tetrahedra. Refined lattice parameters of the $\text{Sr}_{3-x}\text{Ba}_x\text{Al}_y\text{Ga}_{1-y}\text{O}_4\text{F}$ materials are shown in Table 4.1. At constant Ba^{2+} concentration the c -parameters of $\text{Sr}_{3-x}\text{Ba}_x\text{Al}_y\text{Ga}_{1-y}\text{O}_4\text{F}$ materials decrease by approximately 1.1%, while the a -parameters remain constant within error, as the Al^{3+} content increases from 0.25 to 0.75. According to data provided by Vogt *et al*, when comparing the lattice parameters of $\text{Sr}_3\text{GaO}_4\text{F}$ to $\text{Sr}_3\text{AlO}_4\text{F}$, the a -parameter shows little change, while the c -parameter decreases by 1.9%¹⁵.

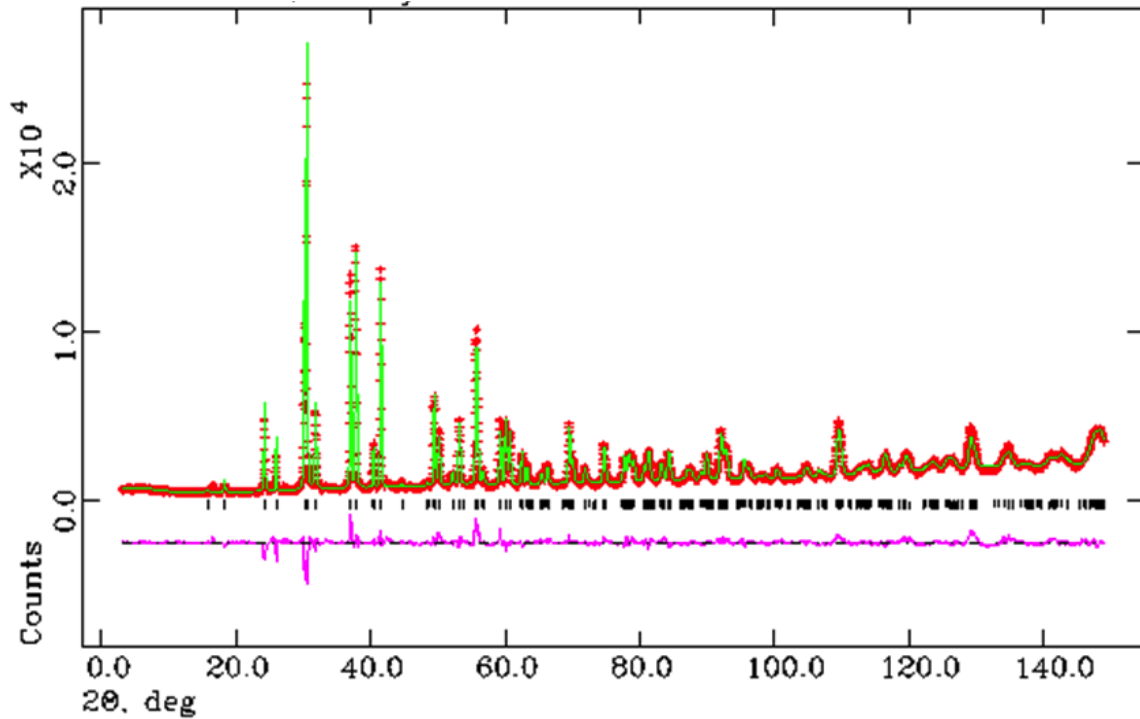


Figure 4.2: Rietveld refinement plots of $\text{Sr}_{2.2}\text{Ba}_{0.8}\text{Al}_{0.25}\text{Ga}_{0.75}\text{O}_4\text{F}$ using the space group $I4/mcm$. The red diffraction pattern denotes observed data, the green line pattern indicates the calculated pattern, and the difference between observed and calculated patterns is shown below.

Table 4.1: Structural Parameters and tilt angles obtained by Rietveld analysis of X-ray diffraction patterns for $\text{Sr}_{3-x}\text{Ba}_x\text{Al}_y\text{Ga}_{1-y}\text{O}_4\text{F}$.

	a (Å)	c (Å)	R_p	R_{wp}
$\text{Sr}_{2.2}\text{Ba}_{0.8}\text{Al}_{0.25}\text{Ga}_{0.75}\text{O}_4\text{F}$	6.9036(2)	11.3731(5)	6.73	9.04
$\text{Sr}_{2.2}\text{Ba}_{0.8}\text{Al}_{0.5}\text{Ga}_{0.5}\text{O}_4\text{F}$	6.9021(1)	11.3044(4)	6.06	8.16
$\text{Sr}_{2.2}\text{Ba}_{0.8}\text{Al}_{0.75}\text{Ga}_{0.25}\text{O}_4\text{F}$	6.9040(1)	11.2476(4)	6.29	8.52
$\text{Sr}_{2.4}\text{Ba}_{0.6}\text{Al}_{0.25}\text{Ga}_{0.75}\text{O}_4\text{F}$	6.8761(1)	11.3555(3)	7.12	9.70
$\text{Sr}_{2.4}\text{Ba}_{0.6}\text{Al}_{0.5}\text{Ga}_{0.5}\text{O}_4\text{F}$	6.8727(1)	11.2893(3)	6.12	8.11
$\text{Sr}_{2.4}\text{Ba}_{0.6}\text{Al}_{0.75}\text{Ga}_{0.25}\text{O}_4\text{F}$	6.8755(1)	11.2341(4)	7.75	10.69
$\text{Sr}_{2.6}\text{Ba}_{0.4}\text{Al}_{0.25}\text{Ga}_{0.75}\text{O}_4\text{F}$	6.8537(2)	11.3553(4)	7.18	9.70
$\text{Sr}_{2.6}\text{Ba}_{0.4}\text{Al}_{0.5}\text{Ga}_{0.5}\text{O}_4\text{F}$	6.8484(1)	11.2802(4)	6.38	8.68
$\text{Sr}_{2.6}\text{Ba}_{0.4}\text{Al}_{0.75}\text{Ga}_{0.25}\text{O}_4\text{F}$	6.8482(2)	11.2227(5)	6.92	9.32
$\text{Sr}_{2.8}\text{Ba}_{0.2}\text{Al}_{0.25}\text{Ga}_{0.75}\text{O}_4\text{F}$	6.8362(1)	11.3330(3)	7.08	9.25
$\text{Sr}_{2.8}\text{Ba}_{0.2}\text{Al}_{0.5}\text{Ga}_{0.5}\text{O}_4\text{F}$	6.8298(1)	11.2694(5)	8.19	10.99
$\text{Sr}_{2.8}\text{Ba}_{0.2}\text{Al}_{0.75}\text{Ga}_{0.25}\text{O}_4\text{F}$	6.8163(2)	11.2101(7)	8.66	11.98

	A(2)x	O x	O z	Tilt angle
$\text{Sr}_{2.2}\text{Ba}_{0.8}\text{Al}_{0.25}\text{Ga}_{0.75}\text{O}_4\text{F}$	0.1691(2)	0.1522(6)	0.6510(6)	17.93(6)
$\text{Sr}_{2.2}\text{Ba}_{0.8}\text{Al}_{0.5}\text{Ga}_{0.5}\text{O}_4\text{F}$	0.1700(1)	0.1459(6)	0.6473(5)	17.75(6)
$\text{Sr}_{2.2}\text{Ba}_{0.8}\text{Al}_{0.75}\text{Ga}_{0.25}\text{O}_4\text{F}$	0.1706(1)	0.1482(5)	0.6473(5)	17.63(5)
$\text{Sr}_{2.4}\text{Ba}_{0.6}\text{Al}_{0.25}\text{Ga}_{0.75}\text{O}_4\text{F}$	0.1688(1)	0.1512(6)	0.6480(6)	18.01(6)
$\text{Sr}_{2.4}\text{Ba}_{0.6}\text{Al}_{0.5}\text{Ga}_{0.5}\text{O}_4\text{F}$	0.1690(1)	0.1501(5)	0.6503(5)	17.96(5)
$\text{Sr}_{2.4}\text{Ba}_{0.6}\text{Al}_{0.75}\text{Ga}_{0.25}\text{O}_4\text{F}$	0.1695(2)	0.1467(6)	0.6543(7)	17.86(6)
$\text{Sr}_{2.6}\text{Ba}_{0.4}\text{Al}_{0.25}\text{Ga}_{0.75}\text{O}_4\text{F}$	0.1699(2)	0.1525(7)	0.6430(6)	17.78(7)
$\text{Sr}_{2.6}\text{Ba}_{0.4}\text{Al}_{0.5}\text{Ga}_{0.5}\text{O}_4\text{F}$	0.1686(1)	0.1532(6)	0.6463(7)	18.03(6)
$\text{Sr}_{2.6}\text{Ba}_{0.4}\text{Al}_{0.75}\text{Ga}_{0.25}\text{O}_4\text{F}$	0.1710(2)	0.1474(6)	0.6452(7)	17.53(6)
$\text{Sr}_{2.8}\text{Ba}_{0.2}\text{Al}_{0.25}\text{Ga}_{0.75}\text{O}_4\text{F}$	0.1689(1)	0.1468(5)	0.6433(5)	17.97(6)
$\text{Sr}_{2.8}\text{Ba}_{0.2}\text{Al}_{0.5}\text{Ga}_{0.5}\text{O}_4\text{F}$	0.1691(2)	0.1481(7)	0.6463(7)	17.93(7)
$\text{Sr}_{2.8}\text{Ba}_{0.2}\text{Al}_{0.75}\text{Ga}_{0.25}\text{O}_4\text{F}$	0.1690(2)	0.1529(7)	0.6495(8)	17.96(7)

In $\text{Sr}_3\text{MO}_4\text{F}$ type materials, the Glazer notation for the tilt systems is $a^0a^0c^-$, where adjacent FSr_6 octahedra reveal alternate clockwise and counterclockwise rotations along the c axis¹⁶⁻¹⁷. The angle at which these adjacent octahedra rotate is known as the tilt angle. The tilt angles for $\text{Sr}_{3-x}\text{Ba}_x\text{Al}_y\text{Ga}_{1-y}\text{O}_4\text{F}$ materials were all found to be near 18° and increase slightly with increasing Ga^{3+} content, which is consistent with what was

observed in $\text{Sr}_{3-x}\text{A}_x\text{AlO}_4\text{F}$ and $\text{Sr}_{3-x}\text{A}_x\text{GaO}_4\text{F}$ materials⁸⁻⁹. According to data provided by Prodjosantoso *et al.*, Green and Vogt, and Sullivan *et al.*⁸⁻¹⁰, the tilt angles in $\text{Sr}_{3-x}\text{A}_x\text{GaO}_4\text{F}$ materials are slightly larger than in $\text{Sr}_{3-x}\text{A}_x\text{AlO}_4\text{F}$ materials and positively correlate with the ion size. (Ga^{3+} : $r = 0.47\text{\AA}$, Al^{3+} : $r = 0.36\text{\AA}$)¹⁸.

Photoluminescence of $\text{Sr}_{3-x}\text{Ba}_x\text{Al}_y\text{Ga}_{1-y}\text{O}_4\text{F}$

$\text{Sr}_{3-x}\text{Ba}_x\text{Al}_y\text{Ga}_{1-y}\text{O}_4\text{F}$ materials were synthesized in order to study the PL emission when having both Al^{3+} and Ga^{3+} at the *M* site within the anti-Perovskite structure.

$\text{Sr}_{3-x}\text{Ba}_x\text{Al}_y\text{Ga}_{1-y}\text{O}_4\text{F}$ materials exhibit a characteristic broad-band emission when excited by 254 nm light after tempering in a 5% H_2 /95% Ar atmosphere; however no

photoluminescence is observed when excited with 365 nm light. Figure 3a-c shows the

PL excitation and emission spectra of $\text{Sr}_{3-x}\text{Ba}_x\text{Al}_y\text{Ga}_{1-y}\text{O}_4\text{F}$ materials. The maximum PL intensity occurs when $x = 0.2$ in $\text{Sr}_{3-x}\text{Ba}_x\text{Al}_{0.5}\text{Ga}_{0.5}\text{O}_4\text{F}$ materials and $x = 0.4$ in

$\text{Sr}_{3-x}\text{Ba}_x\text{Al}_{0.25}\text{Ga}_{0.75}\text{O}_4\text{F}$ and $\text{Sr}_{3-x}\text{Ba}_x\text{Al}_{0.75}\text{Ga}_{0.25}\text{O}_4\text{F}$, while the minimum PL intensity

occurs when $x = 0.8$ in all $\text{Sr}_{3-x}\text{Ba}_x\text{Al}_y\text{Ga}_{1-y}\text{O}_4\text{F}$ materials. $\text{Sr}_{3-x}\text{Ba}_x\text{Al}_{0.75}\text{Ga}_{0.25}\text{O}_4\text{F}$, which is higher in Al^{3+} content, exhibits superior photoluminescence intensity compared to

$\text{Sr}_{3-x}\text{Ba}_x\text{Al}_{0.5}\text{Ga}_{0.5}\text{O}_4\text{F}$ and $\text{Sr}_{3-x}\text{Ba}_x\text{Al}_{0.25}\text{Ga}_{0.75}\text{O}_4\text{F}$. The PL emission data of

$\text{Sr}_{3-x}\text{Ba}_x\text{Al}_y\text{Ga}_{1-y}\text{O}_4\text{F}$ materials are converted into CIE coordinates and plotted on the CIE chromaticity diagram (1931). These chromaticity coordinates are normalized *x* and *y*

values that are widely used as a standard to compare the colors of materials. The CIE

chromaticity coordinate values ($\lambda_{\text{ex}} = 254\text{ nm}$) for all $\text{Sr}_{3-x}\text{Ba}_x\text{Al}_y\text{Ga}_{1-y}\text{O}_4\text{F}$ materials are

listed in Table 2, while Figure 4.4 shows a plot of these coordinates. For each

concentration of Ba^{2+} in $\text{Sr}_{3-x}\text{Ba}_x\text{Al}_y\text{Ga}_{1-y}\text{O}_4\text{F}$ materials there is a gradual blue shift of the

photoluminescence emission from the blue-green region towards the blue region as the Al^{3+} content is increased from $x = 0.25$ to $x = 0.75$.

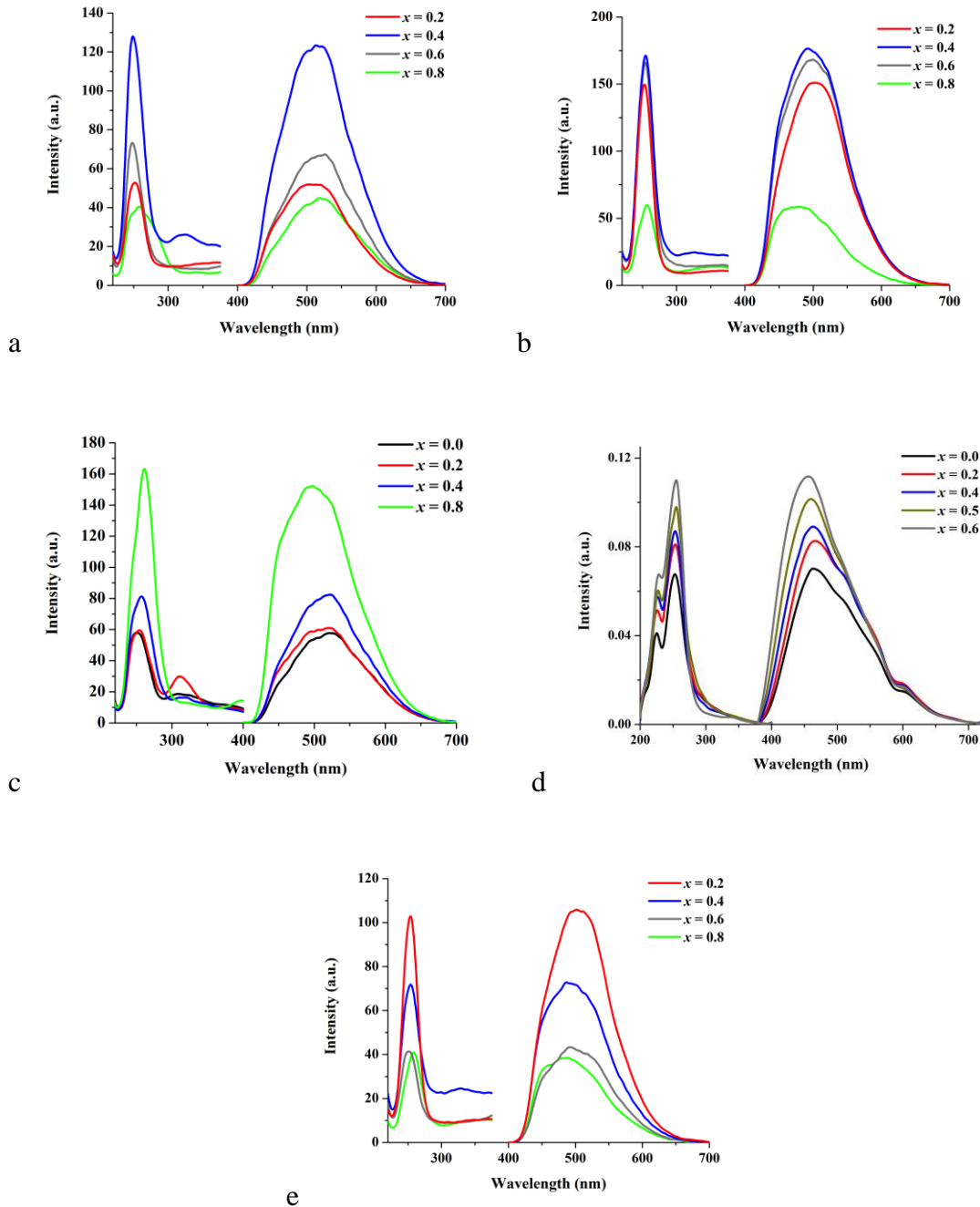


Figure 4.3: Plot of PL excitation and emission spectra of (a) $\text{Sr}_{3-x}\text{Ba}_x\text{Al}_{0.25}\text{Ga}_{0.75}\text{O}_4\text{F}$, (b) $\text{Sr}_{3-x}\text{Ba}_x\text{Al}_{0.5}\text{Ga}_{0.5}\text{O}_4\text{F}$, and (c) $\text{Sr}_{3-x}\text{Ba}_x\text{Al}_{0.75}\text{Ga}_{0.25}\text{O}_4\text{F}$ ($\lambda_{\text{ex}} = 254\text{nm}$). Emission spectra of $\text{Sr}_3\text{MO}_4\text{F}$ type materials under $\lambda_{\text{ex}} = 254\text{nm}$ where (d) $\text{Sr}_{3-x}\text{Ba}_x\text{AlO}_4\text{F}$ taken from Park and Vogt⁷ and (e) $\text{Sr}_{3-x}\text{Ba}_x\text{GaO}_4\text{F}$ ⁸.

Table 4.2: Chromaticity coordinates of Selected $\text{Sr}_{3-x}\text{Ba}_x\text{MO}_4\text{F}$ phosphors

		x	y
1	$\text{Sr}_{2.2}\text{Ba}_{0.8}\text{Al}_{0.25}\text{Ga}_{0.75}\text{O}_4\text{F}$	0.2674	0.4363
2	$\text{Sr}_{2.2}\text{Ba}_{0.8}\text{Al}_{0.5}\text{Ga}_{0.5}\text{O}_4\text{F}$	0.2029	0.3181
3	$\text{Sr}_{2.2}\text{Ba}_{0.8}\text{Al}_{0.75}\text{Ga}_{0.25}\text{O}_4\text{F}$	0.1896	0.2964
4	$\text{Sr}_{2.4}\text{Ba}_{0.6}\text{Al}_{0.25}\text{Ga}_{0.75}\text{O}_4\text{F}$	0.2536	0.4275
5	$\text{Sr}_{2.4}\text{Ba}_{0.6}\text{Al}_{0.5}\text{Ga}_{0.5}\text{O}_4\text{F}$	0.2172	0.3675
6	$\text{Sr}_{2.4}\text{Ba}_{0.6}\text{Al}_{0.75}\text{Ga}_{0.25}\text{O}_4\text{F}$	0.2072	0.3598
7	$\text{Sr}_{2.6}\text{Ba}_{0.4}\text{Al}_{0.25}\text{Ga}_{0.75}\text{O}_4\text{F}$	0.2458	0.4160
8	$\text{Sr}_{2.6}\text{Ba}_{0.4}\text{Al}_{0.5}\text{Ga}_{0.5}\text{O}_4\text{F}$	0.2644	0.4357
9	$\text{Sr}_{2.6}\text{Ba}_{0.4}\text{Al}_{0.75}\text{Ga}_{0.25}\text{O}_4\text{F}$	0.2039	0.3519
10	$\text{Sr}_{2.8}\text{Ba}_{0.2}\text{Al}_{0.25}\text{Ga}_{0.75}\text{O}_4\text{F}$	0.2340	0.3982
11	$\text{Sr}_{2.8}\text{Ba}_{0.2}\text{Al}_{0.5}\text{Ga}_{0.5}\text{O}_4\text{F}$	0.2160	0.3869
12	$\text{Sr}_{2.8}\text{Ba}_{0.2}\text{Al}_{0.75}\text{Ga}_{0.25}\text{O}_4\text{F}$	0.2119	0.3835

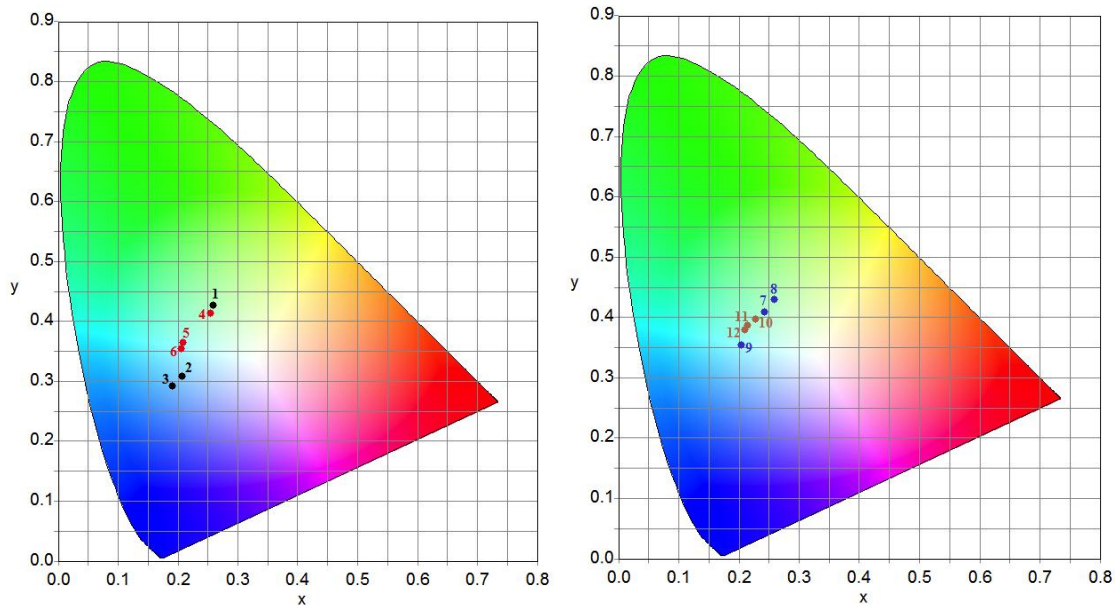


Figure 4.4: CIE chromaticity diagram of $\text{Sr}_{3-x}\text{Ba}_x\text{Al}_y\text{Ga}_{1-y}\text{O}_4\text{F}$ $\lambda_{\text{ex}} = 254 \text{ nm}$. The black dots indicate $x = 0.8$, red dots indicate $x = 0.6$, blue dots indicate $x = 0.4$, and orange dots represent $x = 0.2$ in $\text{Sr}_{3-x}\text{Ba}_x\text{Al}_y\text{Ga}_{1-y}\text{O}_4\text{F}$.

It has been reported by Sullivan *et al*¹⁰, Bin Im *et al*², and Green and Vogt⁸ that substituting Ba^{2+} ions into the A(1) site in $\text{Sr}_3\text{MO}_4\text{F}$ type materials provides an overall increase in their structural stability⁹ as evidenced by a global instability index. The

relationship between structural stability and photoluminescence intensity of $\text{Sr}_{3-x}\text{Ba}_x\text{Al}_y\text{Ga}_{1-y}\text{O}_4\text{F}$ materials at room temperature reveals that the photoluminescence intensity decreases as the Ba^{2+} content $x \geq 0.4$. This decrease in photoluminescence as Ba^{2+} increases is opposite to the one seen in both $\text{Sr}_{3-x}\text{Ba}_x\text{AlO}_4\text{F}$ and $\text{Sr}_{3-x}\text{Ba}_x\text{GaO}_4\text{F}$ materials. Park and Vogt reported that increasing the Ba^{2+} content in $\text{Sr}_{3-x}\text{Ba}_x\text{AlO}_4\text{F}$ materials increases the photoluminescence intensity where $0 \leq x \leq 0.6$ ⁷, while Green and Vogt show a similar trend as x increases from 0.0 to 0.8 in $\text{Sr}_{3-x}\text{Ba}_x\text{GaO}_4\text{F}$. Figure 4.3d-e shows the gradual increase in photoluminescence intensity as Ba^{2+} content increases in $\text{Sr}_{3-x}\text{Ba}_x\text{AlO}_4\text{F}$ materials and $\text{Sr}_{3-x}\text{Ba}_x\text{GaO}_4\text{F}$ materials.

The PL intensity of Ba^{2+} -containing $\text{Sr}_3\text{MO}_4\text{F}$ -type materials, at temperatures ranging from 25°C to 200°C, was studied by Bin Im *et al*, by comparing thermal quenching of PL $\text{Sr}_{2.975}\text{Ce}_{0.025}\text{AlO}_4\text{F}$ and $\text{Sr}_{1.975}\text{BaCe}_{0.025}\text{AlO}_4\text{F}$ to $\text{Y}_3\text{Al}_5\text{O}_{12}:\text{Ce}^{3+}$ ($\text{YAG}:\text{Ce}^{3+}$)². $\text{Sr}_{2.975}\text{Ce}_{0.025}\text{AlO}_4\text{F}$ and $\text{Sr}_{1.975}\text{BaCe}_{0.025}\text{AlO}_4\text{F}$ had similar photoluminescence intensities at room temperature and up to 170°C. As the temperature approaches 200°C, $\text{Sr}_{2.975}\text{Ce}_{0.025}\text{AlO}_4\text{F}$ retained greater photoluminescence intensity² resulting in an apparent trade-off between higher photoluminescence intensity of low Ba^{2+} -containing materials and thermal quenching in high Ba^{2+} -containing $\text{Sr}_3\text{MO}_4\text{F}$ -type materials at LED operating temperatures. Our $\text{Sr}_{3-x}\text{Ba}_x\text{Al}_y\text{Ga}_{1-y}\text{O}_4\text{F}$ materials show that small amounts of Ba^{2+} causes a substantial increase in photoluminescence intensity and may prove to be less prone to thermal quenching due to the presence of F^- ions producing softer phonon modes² than what is observed in $\text{Ce}^{3+}:\text{Y}_3\text{Al}_5\text{O}_{12}$, an industrially employed LED phosphor.

Structural Properties of $\text{Sr}_{2.4}\text{Ba}_{0.6}\text{Al}_y\text{Ga}_{1-y-z}\text{In}_z\text{O}_4\text{F}$

$\text{Sr}_{2.4}\text{Ba}_{0.6}\text{Al}_y\text{Ga}_{1-y-z}\text{In}_z\text{O}_4\text{F}$ materials were synthesized where $z = 0.025, 0.0375, 0.05, 0.0625,$ and 0.075 molar % of In^{3+} . The diffraction patterns of $\text{Sr}_{2.4}\text{Ba}_{0.6}\text{Al}_y\text{Ga}_{1-y-z}\text{In}_z\text{O}_4\text{F}$ materials are shown in Figure 4.5, while the refined lattice parameters of these materials are listed in Table 4.3. The solubility limit for the substitution of In^{3+} is below 0.075 mol% when all three ions are present, however, in $\text{Sr}_{3-x}\text{Ba}_x\text{Al}_{1-c}\text{In}_c\text{O}_{4-\alpha}\text{F}_{1-\delta}$ materials it has been reported that In^{3+} can be substituted up to 20 mol% while varying Ba concentration ⁷. The powder diffraction pattern of these materials reveal no impurities when $z = 0.025, 0.0375, 0.05$ and 0.0625 , however, In_2O_3 impurities begin to appear in the $z = 0.075$ diffraction pattern. The tilt angles of the $\text{Sr}_{2.4}\text{Ba}_{0.6}\text{Al}_{0.1}\text{Ga}_{0.9-z}\text{In}_z\text{O}_4\text{F}$ and $\text{Sr}_{2.4}\text{Ba}_{0.6}\text{Al}_{0.2}\text{Ga}_{0.8-z}\text{In}_z\text{O}_4\text{F}$ materials increase above 18° with increasing In^{3+} content. This can be attributed to the difference in ionic radius between In^{3+} ($r = 0.62\text{\AA}$), Ga^{3+} ($r = 0.47\text{\AA}$) and Al^{3+} ($r = 0.36\text{\AA}$) ¹⁸, where the increased average radius of these ions occupying the M site in $\text{Sr}_{2.4}\text{Ba}_{0.6}\text{Al}_{0.1}\text{Ga}_{0.9-z}\text{In}_z\text{O}_4\text{F}$ materials cause the tilt angles in these anti-Perovskite structure to increase.

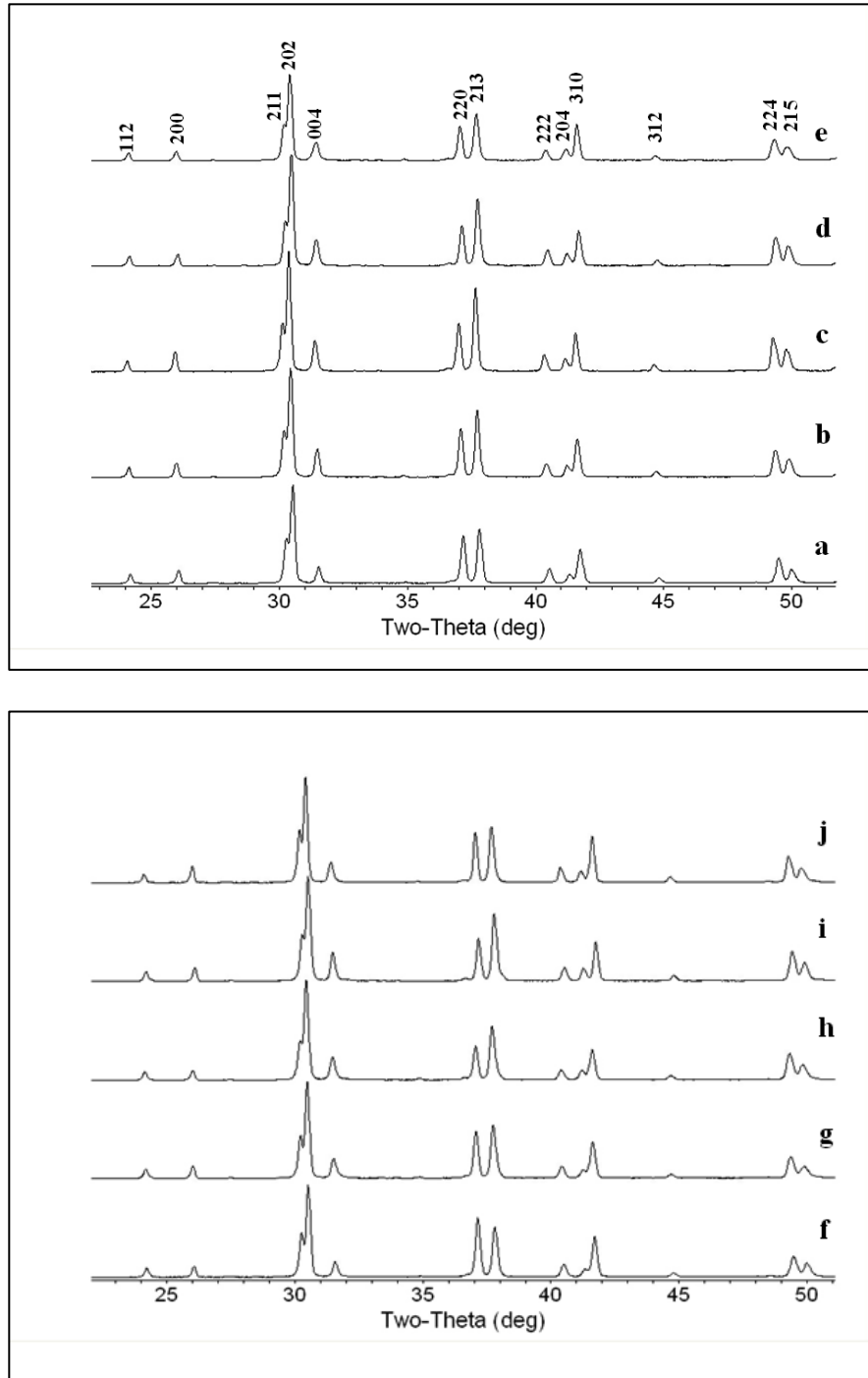


Figure 4.5: Diffraction patterns of $\text{Sr}_{2.4}\text{Ba}_{0.6}\text{Al}_{0.1}\text{Ga}_{0.9-z}\text{In}_z\text{O}_4\text{F}$ materials, where a) $\text{Sr}_{2.4}\text{Ba}_{0.6}\text{Al}_{0.1}\text{Ga}_{0.875}\text{In}_{0.025}\text{O}_4\text{F}$, b) $\text{Sr}_{2.4}\text{Ba}_{0.6}\text{Al}_{0.1}\text{Ga}_{0.8625}\text{In}_{0.0375}\text{O}_4\text{F}$, c) $\text{Sr}_{2.4}\text{Ba}_{0.6}\text{Al}_{0.1}\text{Ga}_{0.85}\text{In}_{0.05}\text{O}_4\text{F}$, d) $\text{Sr}_{2.4}\text{Ba}_{0.6}\text{Al}_{0.1}\text{Ga}_{0.8375}\text{In}_{0.0625}\text{O}_4\text{F}$, e) $\text{Sr}_{2.4}\text{Ba}_{0.6}\text{Al}_{0.1}\text{Ga}_{0.825}\text{In}_{0.075}\text{O}_4\text{F}$, f) $\text{Sr}_{2.4}\text{Ba}_{0.6}\text{Al}_{0.2}\text{Ga}_{0.775}\text{In}_{0.025}\text{O}_4\text{F}$, g) $\text{Sr}_{2.4}\text{Ba}_{0.6}\text{Al}_{0.2}\text{Ga}_{0.7625}\text{In}_{0.0375}\text{O}_4\text{F}$, h) $\text{Sr}_{2.4}\text{Ba}_{0.6}\text{Al}_{0.2}\text{Ga}_{0.75}\text{In}_{0.05}\text{O}_4\text{F}$, i) $\text{Sr}_{2.4}\text{Ba}_{0.6}\text{Al}_{0.2}\text{Ga}_{0.7375}\text{In}_{0.0625}\text{O}_4\text{F}$, and j) $\text{Sr}_{2.4}\text{Ba}_{0.6}\text{Al}_{0.2}\text{Ga}_{0.725}\text{In}_{0.075}\text{O}_4\text{F}$.

Table 4.3: Structural Parameters and tilt angles obtained by Rietveld analysis of X-ray diffraction patterns for $\text{Sr}_{2.4}\text{Ba}_{0.6}\text{Al}_{0.1}\text{Ga}_{0.9-x}\text{In}_x\text{O}_4\text{F}$.

	a (Å)	c (Å)	R_p	R_{wp}
$\text{Sr}_{2.4}\text{Ba}_{0.6}\text{Al}_{0.1}\text{Ga}_{0.875}\text{In}_{0.025}\text{O}_4\text{F}$	6.8699(2)	11.3975(3)	6.83	8.81
$\text{Sr}_{2.4}\text{Ba}_{0.6}\text{Al}_{0.1}\text{Ga}_{0.8625}\text{In}_{0.0375}\text{O}_4\text{F}$	6.8813(1)	11.4074(3)	5.76	7.60
$\text{Sr}_{2.4}\text{Ba}_{0.6}\text{Al}_{0.1}\text{Ga}_{0.85}\text{In}_{0.05}\text{O}_4\text{F}$	6.8810(1)	11.4130(2)	6.12	8.04
$\text{Sr}_{2.4}\text{Ba}_{0.6}\text{Al}_{0.1}\text{Ga}_{0.8375}\text{In}_{0.0625}\text{O}_4\text{F}$	6.8738(1)	11.4237(3)	6.78	9.19
$\text{Sr}_{2.4}\text{Ba}_{0.6}\text{Al}_{0.1}\text{Ga}_{0.825}\text{In}_{0.075}\text{O}_4\text{F}$	6.8804(2)	11.4221(4)	6.74	8.91
$\text{Sr}_{2.4}\text{Ba}_{0.6}\text{Al}_{0.2}\text{Ga}_{0.775}\text{In}_{0.025}\text{O}_4\text{F}$	6.8727(1)	11.3794(5)	6.45	8.40
$\text{Sr}_{2.4}\text{Ba}_{0.6}\text{Al}_{0.2}\text{Ga}_{0.7625}\text{In}_{0.0375}\text{O}_4\text{F}$	6.8806(1)	11.3934(4)	5.75	7.84
$\text{Sr}_{2.4}\text{Ba}_{0.6}\text{Al}_{0.2}\text{Ga}_{0.75}\text{In}_{0.05}\text{O}_4\text{F}$	6.8807(1)	11.4080(3)	5.42	7.19
$\text{Sr}_{2.4}\text{Ba}_{0.6}\text{Al}_{0.2}\text{Ga}_{0.7375}\text{In}_{0.0625}\text{O}_4\text{F}$	6.8683(1)	11.4198(3)	6.66	8.87
$\text{Sr}_{2.4}\text{Ba}_{0.6}\text{Al}_{0.2}\text{Ga}_{0.725}\text{In}_{0.075}\text{O}_4\text{F}$	6.8795(1)	11.4232(3)	6.42	8.56

	$A(2)x$	O_x	O_z	<i>Tilt angle</i>
$\text{Sr}_{2.4}\text{Ba}_{0.6}\text{Al}_{0.1}\text{Ga}_{0.875}\text{In}_{0.025}\text{O}_4\text{F}$	0.1686(1)	0.1529(5)	0.6440(6)	18.04(5)
$\text{Sr}_{2.4}\text{Ba}_{0.6}\text{Al}_{0.1}\text{Ga}_{0.8625}\text{In}_{0.0375}\text{O}_4\text{F}$	0.1680(1)	0.1520(5)	0.6434(5)	18.17(5)
$\text{Sr}_{2.4}\text{Ba}_{0.6}\text{Al}_{0.1}\text{Ga}_{0.85}\text{In}_{0.05}\text{O}_4\text{F}$	0.1679(1)	0.1455(5)	0.6439(4)	18.19(5)
$\text{Sr}_{2.4}\text{Ba}_{0.6}\text{Al}_{0.1}\text{Ga}_{0.8375}\text{In}_{0.0625}\text{O}_4\text{F}$	0.1677(1)	0.1514(6)	0.6435(5)	18.21(6)
$\text{Sr}_{2.4}\text{Ba}_{0.6}\text{Al}_{0.1}\text{Ga}_{0.825}\text{In}_{0.075}\text{O}_4\text{F}$	0.1680(2)	0.1501(6)	0.6392(6)	18.17(6)
$\text{Sr}_{2.4}\text{Ba}_{0.6}\text{Al}_{0.2}\text{Ga}_{0.775}\text{In}_{0.025}\text{O}_4\text{F}$	0.1692(1)	0.1536(5)	0.6446(5)	17.91(5)
$\text{Sr}_{2.4}\text{Ba}_{0.6}\text{Al}_{0.2}\text{Ga}_{0.7625}\text{In}_{0.0375}\text{O}_4\text{F}$	0.1692(1)	0.1511(5)	0.6400(5)	17.91(5)
$\text{Sr}_{2.4}\text{Ba}_{0.6}\text{Al}_{0.2}\text{Ga}_{0.75}\text{In}_{0.05}\text{O}_4\text{F}$	0.1693(1)	0.1490(5)	0.6419(4)	17.88(5)
$\text{Sr}_{2.4}\text{Ba}_{0.6}\text{Al}_{0.2}\text{Ga}_{0.7375}\text{In}_{0.0625}\text{O}_4\text{F}$	0.1677(1)	0.1524(6)	0.6432(5)	18.23(6)
$\text{Sr}_{2.4}\text{Ba}_{0.6}\text{Al}_{0.2}\text{Ga}_{0.725}\text{In}_{0.075}\text{O}_4\text{F}$	0.1683(1)	0.1457(5)	0.6414(5)	18.10(5)

Photoluminescence of $\text{Sr}_{2.4}\text{Ba}_{0.6}\text{Al}_y\text{Ga}_{1-y-z}\text{In}_z\text{O}_4\text{F}$ materials

In this section our primary focus is to report the photoluminescent behavior of $\text{Sr}_{2.4}\text{Ba}_{0.6}\text{Al}_y\text{Ga}_{1-y-z}\text{In}_z\text{O}_4\text{F}$ materials when exposed to a 5% H_2 /95% Ar atmosphere; however these materials also exhibit photoluminescence when annealed in air. In air-annealed samples of $\text{Sr}_{2.4}\text{Ba}_{0.6}\text{Al}_y\text{Ga}_{1-y-z}\text{In}_z\text{O}_4\text{F}$ materials, an electronic trap effect, also seen in $\text{Ga}_{2-x}\text{In}_x\text{O}_3$ ¹⁹⁻²⁰, contributes to the photoluminescence at low to intermediate concentrations of In^{3+} . The difference in electronegativity between Al^{3+} , Ga^{3+} , and In^{3+} creates localized isoelectronic traps, which are energy states within the band gap. These traps attract electrons and holes in close proximity, and subsequent recombination of the electron-hole pair leads to photoluminescence in both air annealed and reduced samples²⁰. The air annealed samples of $\text{Sr}_{2.4}\text{Ba}_{0.6}\text{Al}_y\text{Ga}_{1-y-z}\text{In}_z\text{O}_4\text{F}$ only exhibit photoluminescence at 254 nm excitation, while samples exposed to the 5% H_2 /95% Ar atmosphere exhibit photoluminescence both with 254 nm and 365 nm excitation. Figure 4.6 includes pictures of $\text{Sr}_{2.4}\text{Ba}_{0.6}\text{Al}_{0.2}\text{Ga}_{0.775}\text{In}_{0.025}\text{O}_4\text{F}$ excited by 254 nm light, where the air annealed material exhibits off-white to yellow-white color and a yellow-green color after tempering in a 5% H_2 /95% Ar atmosphere at 1050°C. The corresponding broad-band emission spectra for $\text{Sr}_{2.4}\text{Ba}_{0.6}\text{Al}_{0.2}\text{Ga}_{0.775}\text{In}_{0.025}\text{O}_4\text{F}$ after pre- and post-reduction are shown in Figure 4.7. The air annealed sample has a broad-band photoluminescence spectrum centered near 495 nm and 517 nm, while the sample tempered in a 5% H_2 /95% Ar atmosphere shows a narrower band centered near 557 nm.

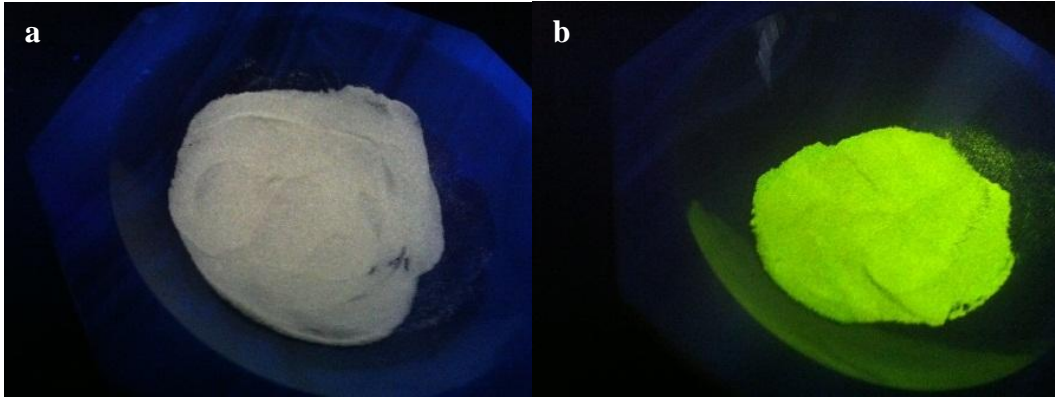


Figure 4.6: Images of $\text{Sr}_{2.4}\text{Ba}_{0.6}\text{Al}_{0.2}\text{Ga}_{0.775}\text{In}_{0.025}\text{O}_4\text{F}$ (a) before and (b) after reduction in 5% H_2 /95% Ar atmosphere $\lambda_{\text{ex}} = 254\text{nm}$

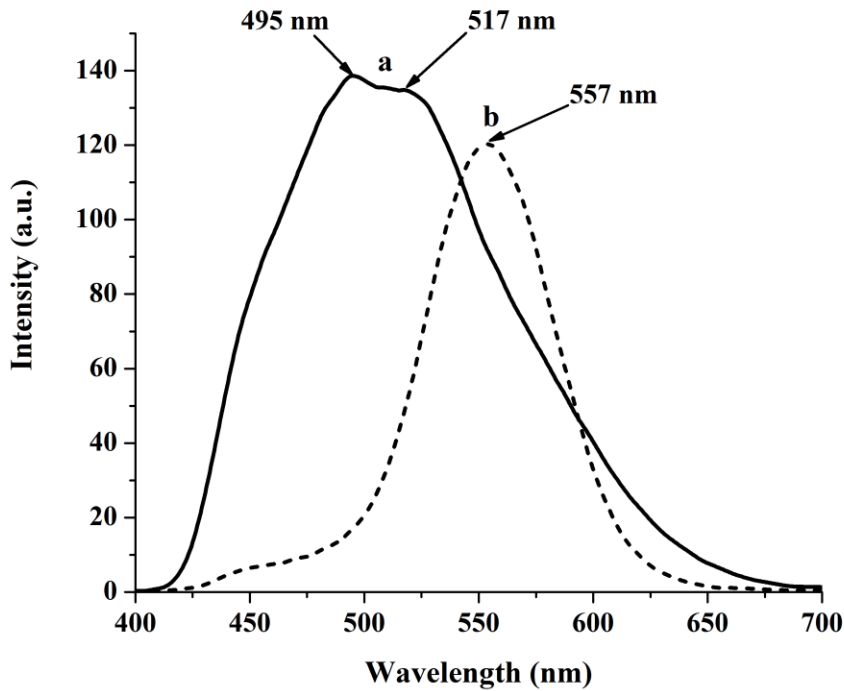


Figure 4.7: Photoluminescence emission spectra of $\text{Sr}_{2.4}\text{Ba}_{0.6}\text{Al}_{0.2}\text{Ga}_{0.775}\text{In}_{0.025}\text{O}_4\text{F}$ under $\lambda_{\text{ex}} = 254\text{nm}$, where (a) is the PL emission spectrum before reduction in 5% H_2 /95% Ar atmosphere and (b) is the PL emission spectrum after reduction.

In order to study the effects that the reducing conditions have on the photoluminescence emissions of $\text{Sr}_{2.4}\text{Ba}_{0.6}\text{Al}_y\text{Ga}_{1-y-z}\text{In}_z\text{O}_4\text{F}$ materials, each sample was tempered for 3 hours in a 5% $\text{H}_2/95\%$ Ar atmosphere at 800°C, 900°C, and 1050°C. The reduced samples of $\text{Sr}_{2.4}\text{Ba}_{0.6}\text{Al}_y\text{Ga}_{1-y-z}\text{In}_z\text{O}_4\text{F}$ now display photoluminescence upon excitation by both 254nm and 365nm light. The excitation spectra for $\text{Sr}_{2.4}\text{Ba}_{0.6}\text{Al}_y\text{Ga}_{1-y-z}\text{In}_z\text{O}_4\text{F}$ materials shown in Figure 4.8A have three distinct peaks located near 258nm, 335nm and 370nm. The broad-band in the excitation spectra located between 300 nm and 400 are a direct result of In^{3+} substitution and is often referred to as the $\text{In}^{3+}-\text{O}^{2-}$ charge transfer band ⁷ also observed in the broad-band excitation spectra for $\text{Sr}_{2.4985}\text{Ca}_{0.5}\text{Pr}_{0.001}\text{Al}_{0.9}\text{In}_{0.1}\text{O}_4\text{F}$ when 10 mol% of Al^{3+} is replaced by In^{3+} ¹³. Figures 4.8B and 4.8C show the photoluminescence emission spectra of $\text{Sr}_{2.4}\text{Ba}_{0.6}\text{Al}_y\text{Ga}_{1-y-z}\text{In}_z\text{O}_4\text{F}$ materials with increasing In^{3+} content under 254nm and 365nm excitation.

In Figure 4.8B, the intensities within the emission spectra of $\text{Sr}_{2.4}\text{Ba}_{0.6}\text{Al}_y\text{Ga}_{1-y-z}\text{In}_z\text{O}_4\text{F}$ materials reveal no obvious pattern with respect to In^{3+} content for the samples tempered at 800°C and 900°C; however the spectral shape is similar for all samples. The emission spectra for $\text{Sr}_{2.4}\text{Ba}_{0.6}\text{Al}_y\text{Ga}_{1-y-z}\text{In}_z\text{O}_4\text{F}$ materials, where $\lambda_{\text{ex}} = 254\text{nm}$, resembles the emission spectrum of the air annealed sample shown in Figure 4.7. The reducing conditions at these temperatures does not yield a significant difference in the emission spectra where the highest intensities occur (λ_{max}) for samples tempered at 800°C and 900°C are all centered near 490 nm. When the temperature of the post synthesis reduction step is increased to 1050°C, a sharp peak centered between at 552 and 554 nm, respectively, dominates the emission spectra for $\text{Sr}_{2.4}\text{Ba}_{0.6}\text{Al}_{0.1}\text{Ga}_{0.9-z}\text{In}_z\text{O}_4\text{F}$ and $\text{Sr}_{2.4}\text{Ba}_{0.6}\text{Al}_{0.2}\text{Ga}_{0.8-z}\text{In}_z\text{O}_4\text{F}$ materials when $\lambda_{\text{ex}} = 254 \text{ nm}$.

The intensity of the peak at 490nm also decreased as the temperature of the reducing step increased to 1050°C.

Figure 4.8C shows the emission spectra of $\text{Sr}_{2.4}\text{Ba}_{0.6}\text{Al}_y\text{Ga}_{1-y-z}\text{In}_z\text{O}_4\text{F}$ materials tempered at 800°C, 900°C, and 1050°C, where $\lambda_{\text{ex}} = 365 \text{ nm}$. The samples of $\text{Sr}_{2.4}\text{Ba}_{0.6}\text{Al}_y\text{Ga}_{1-y-z}\text{In}_z\text{O}_4\text{F}$ materials show two distinct peaks near 450 nm and between 555 and 582 nm. The peaks centered between 555 and 582 are a result of the In^{3+} substitution. Samples of $\text{Sr}_{2.4}\text{Ba}_{0.6}\text{Al}_y\text{Ga}_{1-y-z}\text{In}_z\text{O}_4\text{F}$ materials containing between 0.025 and 0.375 mol% of In^{3+} have greater intensities in the emission spectra when excited by 365 nm light, while $\text{Sr}_{2.4}\text{Ba}_{0.6}\text{Al}_y\text{Ga}_{1-y-z}\text{In}_z\text{O}_4\text{F}$ samples containing 0.075 mol% of In^{3+} exhibit concentration quenching of the photoluminescence emission. In $\text{Sr}_{2.4}\text{Ba}_{0.6}\text{Al}_{0.2}\text{Ga}_{0.8-z}\text{In}_z\text{O}_4\text{F}$ materials there is a dramatic decrease in the photoluminescence intensity accompanied with a noticeable blue shift of the λ_{max} as the temperature of the reduction step increases from 800°C to 900°C. The excitation spectrum (Figure 4.8A) of these materials also shows a similar decrease in intensity of the $\text{In}^{3+}\text{-O}^{2-}$ charge transfer band when the temperature of the reducing step is 900°C. For $\text{Sr}_{2.4}\text{Ba}_{0.6}\text{Al}_{0.1}\text{Ga}_{0.9-z}\text{In}_z\text{O}_4\text{F}$ materials there is a decrease in the intensity of the emission spectra; however there is not a dramatic shift in the λ_{max} for these samples. The change in temperature from the 800-900°C range to 1050°C in the reduction step causes the λ_{max} to blue shift from $\approx 575 \text{ nm}$ to $\approx 558 \text{ nm}$, where the emitted color shifts from orange-yellow to green-yellow under 365nm light. The photoluminescence intensity of these materials also increases with the increasing temperature of the reducing step from 900°C to 1050°C.

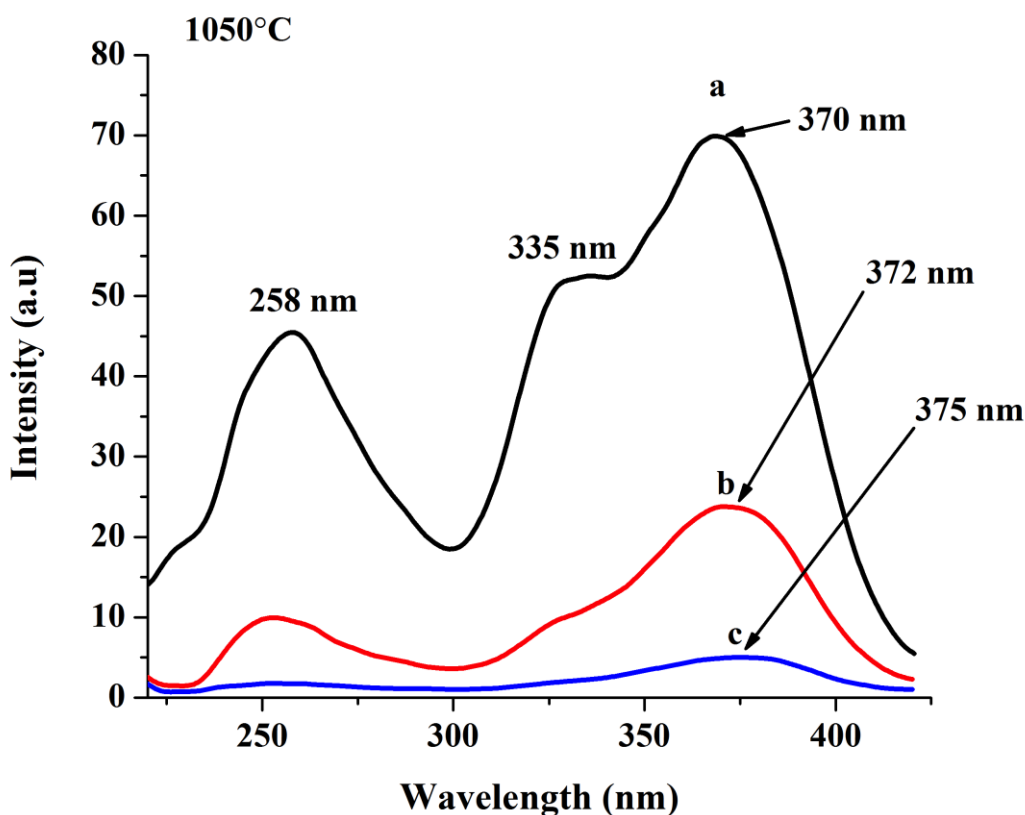


Figure 4.8A: Emission and excitation spectra of $\text{Sr}_{2.4}\text{Ba}_{0.6}\text{Al}_x\text{Ga}_{1-y-z}\text{In}_z\text{O}_4\text{F}$, where a) $\text{Sr}_{2.4}\text{Ba}_{0.6}\text{Al}_{0.10}\text{Ga}_{0.875}\text{In}_{0.025}\text{O}_4\text{F}$ b) $\text{Sr}_{2.4}\text{Ba}_{0.6}\text{Al}_{0.10}\text{Ga}_{0.85}\text{In}_{0.05}\text{O}_4\text{F}$, c) $\text{Sr}_{2.4}\text{Ba}_{0.6}\text{Al}_{0.10}\text{Ga}_{0.825}\text{In}_{0.075}\text{O}_4\text{F}$, d) $\text{Sr}_{2.4}\text{Ba}_{0.6}\text{Al}_{0.20}\text{Ga}_{0.775}\text{In}_{0.025}\text{O}_4\text{F}$, e) $\text{Sr}_{2.4}\text{Ba}_{0.6}\text{Al}_{0.20}\text{Ga}_{0.75}\text{In}_{0.05}\text{O}_4\text{F}$, and f) $\text{Sr}_{2.4}\text{Ba}_{0.6}\text{Al}_{0.20}\text{Ga}_{0.725}\text{In}_{0.075}\text{O}_4\text{F}$ at 1050°C . Other samples include g) $\text{Sr}_{2.4}\text{Ba}_{0.6}\text{Al}_{0.10}\text{Ga}_{0.875}\text{In}_{0.025}\text{O}_4\text{F}$, h) $\text{Sr}_{2.4}\text{Ba}_{0.6}\text{Al}_{0.10}\text{Ga}_{0.8625}\text{In}_{0.0375}\text{O}_4\text{F}$, i) $\text{Sr}_{2.4}\text{Ba}_{0.6}\text{Al}_{0.10}\text{Ga}_{0.8375}\text{In}_{0.0625}\text{O}_4\text{F}$ j) $\text{Sr}_{2.4}\text{Ba}_{0.6}\text{Al}_{0.10}\text{Ga}_{0.825}\text{In}_{0.075}\text{O}_4\text{F}$, k) $\text{Sr}_{2.4}\text{Ba}_{0.6}\text{Al}_{0.20}\text{Ga}_{0.775}\text{In}_{0.025}\text{O}_4\text{F}$, l) $\text{Sr}_{2.4}\text{Ba}_{0.6}\text{Al}_{0.20}\text{Ga}_{0.7625}\text{In}_{0.0375}\text{O}_4\text{F}$, m) $\text{Sr}_{2.4}\text{Ba}_{0.6}\text{Al}_{0.20}\text{Ga}_{0.7375}\text{In}_{0.0625}\text{O}_4\text{F}$, and n) $\text{Sr}_{2.4}\text{Ba}_{0.6}\text{Al}_{0.20}\text{Ga}_{0.725}\text{In}_{0.075}\text{O}_4\text{F}$ measured at 900°C and 800°C . Plot (A) represents the excitation spectrum, plot (B) is the emission spectrum (254nm), and plot (C) is the emission spectra (365nm).

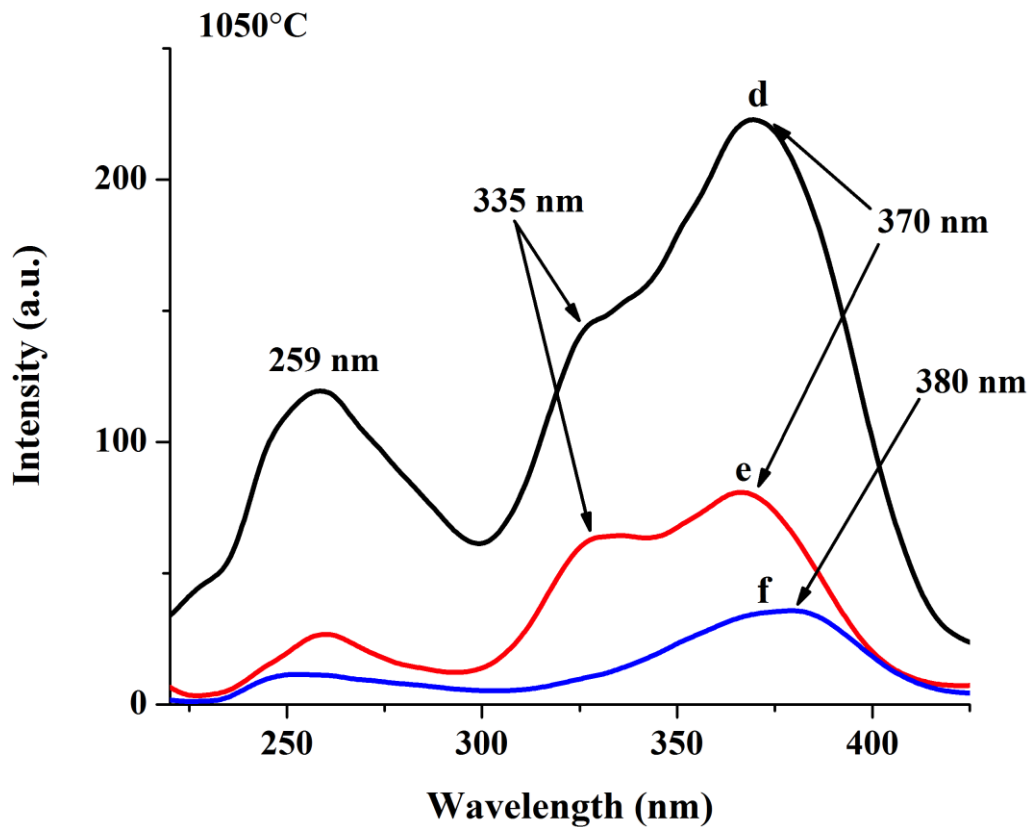


Figure 4.8A: Emission and excitation spectra of $\text{Sr}_{2.4}\text{Ba}_{0.6}\text{Al}_y\text{Ga}_{1-y-z}\text{In}_z\text{O}_4\text{F}$, where a) $\text{Sr}_{2.4}\text{Ba}_{0.6}\text{Al}_{0.10}\text{Ga}_{0.875}\text{In}_{0.025}\text{O}_4\text{F}$ b) $\text{Sr}_{2.4}\text{Ba}_{0.6}\text{Al}_{0.10}\text{Ga}_{0.85}\text{In}_{0.05}\text{O}_4\text{F}$, c) $\text{Sr}_{2.4}\text{Ba}_{0.6}\text{Al}_{0.10}\text{Ga}_{0.825}\text{In}_{0.075}\text{O}_4\text{F}$, d) $\text{Sr}_{2.4}\text{Ba}_{0.6}\text{Al}_{0.20}\text{Ga}_{0.775}\text{In}_{0.025}\text{O}_4\text{F}$, e) $\text{Sr}_{2.4}\text{Ba}_{0.6}\text{Al}_{0.20}\text{Ga}_{0.75}\text{In}_{0.05}\text{O}_4\text{F}$, and f) $\text{Sr}_{2.4}\text{Ba}_{0.6}\text{Al}_{0.20}\text{Ga}_{0.725}\text{In}_{0.075}\text{O}_4\text{F}$ at 1050°C . Other samples include g) $\text{Sr}_{2.4}\text{Ba}_{0.6}\text{Al}_{0.10}\text{Ga}_{0.875}\text{In}_{0.025}\text{O}_4\text{F}$, h) $\text{Sr}_{2.4}\text{Ba}_{0.6}\text{Al}_{0.10}\text{Ga}_{0.8625}\text{In}_{0.0375}\text{O}_4\text{F}$, i) $\text{Sr}_{2.4}\text{Ba}_{0.6}\text{Al}_{0.10}\text{Ga}_{0.8375}\text{In}_{0.0625}\text{O}_4\text{F}$ j) $\text{Sr}_{2.4}\text{Ba}_{0.6}\text{Al}_{0.10}\text{Ga}_{0.825}\text{In}_{0.075}\text{O}_4\text{F}$, k) $\text{Sr}_{2.4}\text{Ba}_{0.6}\text{Al}_{0.20}\text{Ga}_{0.775}\text{In}_{0.025}\text{O}_4\text{F}$, l) $\text{Sr}_{2.4}\text{Ba}_{0.6}\text{Al}_{0.20}\text{Ga}_{0.7625}\text{In}_{0.0375}\text{O}_4\text{F}$, m) $\text{Sr}_{2.4}\text{Ba}_{0.6}\text{Al}_{0.20}\text{Ga}_{0.7375}\text{In}_{0.0625}\text{O}_4\text{F}$, and n) $\text{Sr}_{2.4}\text{Ba}_{0.6}\text{Al}_{0.20}\text{Ga}_{0.725}\text{In}_{0.075}\text{O}_4\text{F}$ measured at 900°C and 800°C . Plot (A) represents the excitation spectrum, plot (B) is the emission spectrum (254nm), and plot (C) is the emission spectra (365nm).

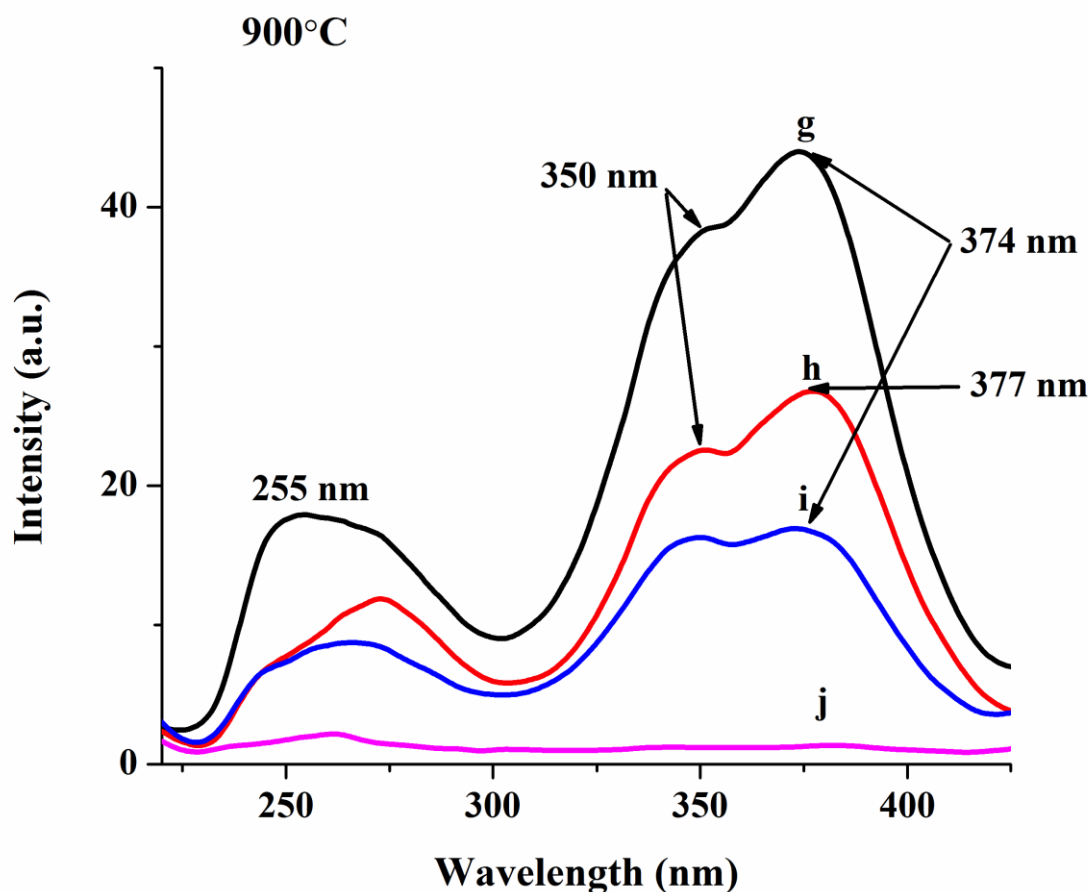


Figure 4.8A: Emission and excitation spectra of $\text{Sr}_{2.4}\text{Ba}_{0.6}\text{Al}_y\text{Ga}_{1-y-z}\text{In}_z\text{O}_4\text{F}$, where a) $\text{Sr}_{2.4}\text{Ba}_{0.6}\text{Al}_{0.10}\text{Ga}_{0.875}\text{In}_{0.025}\text{O}_4\text{F}$ b) $\text{Sr}_{2.4}\text{Ba}_{0.6}\text{Al}_{0.10}\text{Ga}_{0.85}\text{In}_{0.05}\text{O}_4\text{F}$, c) $\text{Sr}_{2.4}\text{Ba}_{0.6}\text{Al}_{0.10}\text{Ga}_{0.825}\text{In}_{0.075}\text{O}_4\text{F}$, d) $\text{Sr}_{2.4}\text{Ba}_{0.6}\text{Al}_{0.20}\text{Ga}_{0.775}\text{In}_{0.025}\text{O}_4\text{F}$, e) $\text{Sr}_{2.4}\text{Ba}_{0.6}\text{Al}_{0.20}\text{Ga}_{0.75}\text{In}_{0.05}\text{O}_4\text{F}$, and f) $\text{Sr}_{2.4}\text{Ba}_{0.6}\text{Al}_{0.20}\text{Ga}_{0.725}\text{In}_{0.075}\text{O}_4\text{F}$ at 1050°C . Other samples include g) $\text{Sr}_{2.4}\text{Ba}_{0.6}\text{Al}_{0.10}\text{Ga}_{0.875}\text{In}_{0.025}\text{O}_4\text{F}$, h) $\text{Sr}_{2.4}\text{Ba}_{0.6}\text{Al}_{0.10}\text{Ga}_{0.8625}\text{In}_{0.0375}\text{O}_4\text{F}$, i) $\text{Sr}_{2.4}\text{Ba}_{0.6}\text{Al}_{0.10}\text{Ga}_{0.8375}\text{In}_{0.0625}\text{O}_4\text{F}$ j) $\text{Sr}_{2.4}\text{Ba}_{0.6}\text{Al}_{0.10}\text{Ga}_{0.825}\text{In}_{0.075}\text{O}_4\text{F}$, k) $\text{Sr}_{2.4}\text{Ba}_{0.6}\text{Al}_{0.20}\text{Ga}_{0.775}\text{In}_{0.025}\text{O}_4\text{F}$, l) $\text{Sr}_{2.4}\text{Ba}_{0.6}\text{Al}_{0.20}\text{Ga}_{0.7625}\text{In}_{0.0375}\text{O}_4\text{F}$, m) $\text{Sr}_{2.4}\text{Ba}_{0.6}\text{Al}_{0.20}\text{Ga}_{0.7375}\text{In}_{0.0625}\text{O}_4\text{F}$, and n) $\text{Sr}_{2.4}\text{Ba}_{0.6}\text{Al}_{0.20}\text{Ga}_{0.725}\text{In}_{0.075}\text{O}_4\text{F}$ measured at 900°C and 800°C . Plot (A) represents the excitation spectrum, plot (B) is the emission spectrum (254nm), and plot (C) is the emission spectra (365nm).

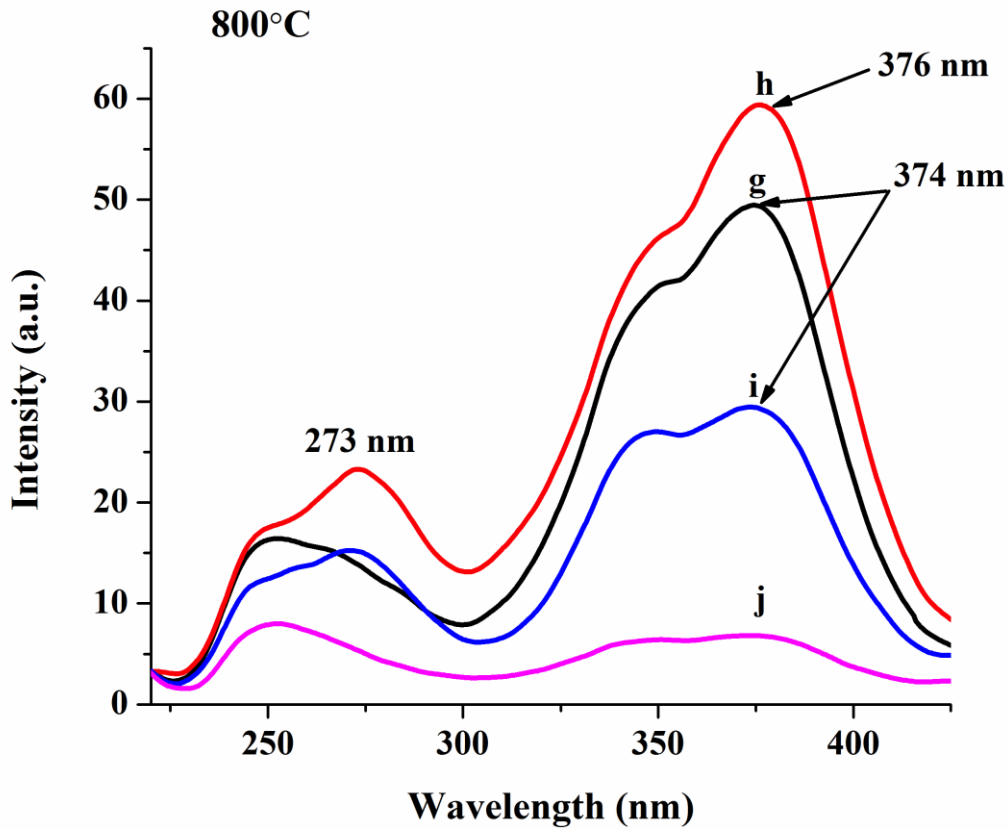


Figure 4.8A: Emission and excitation spectra of $\text{Sr}_{2.4}\text{Ba}_{0.6}\text{Al}_x\text{Ga}_{1-y-z}\text{In}_z\text{O}_4\text{F}$, where a) $\text{Sr}_{2.4}\text{Ba}_{0.6}\text{Al}_{0.10}\text{Ga}_{0.875}\text{In}_{0.025}\text{O}_4\text{F}$ b) $\text{Sr}_{2.4}\text{Ba}_{0.6}\text{Al}_{0.10}\text{Ga}_{0.85}\text{In}_{0.05}\text{O}_4\text{F}$, c) $\text{Sr}_{2.4}\text{Ba}_{0.6}\text{Al}_{0.10}\text{Ga}_{0.825}\text{In}_{0.075}\text{O}_4\text{F}$, d) $\text{Sr}_{2.4}\text{Ba}_{0.6}\text{Al}_{0.20}\text{Ga}_{0.775}\text{In}_{0.025}\text{O}_4\text{F}$, e) $\text{Sr}_{2.4}\text{Ba}_{0.6}\text{Al}_{0.20}\text{Ga}_{0.75}\text{In}_{0.05}\text{O}_4\text{F}$, and f) $\text{Sr}_{2.4}\text{Ba}_{0.6}\text{Al}_{0.20}\text{Ga}_{0.725}\text{In}_{0.075}\text{O}_4\text{F}$ at 1050°C . Other samples include g) $\text{Sr}_{2.4}\text{Ba}_{0.6}\text{Al}_{0.10}\text{Ga}_{0.875}\text{In}_{0.025}\text{O}_4\text{F}$, h) $\text{Sr}_{2.4}\text{Ba}_{0.6}\text{Al}_{0.10}\text{Ga}_{0.8625}\text{In}_{0.0375}\text{O}_4\text{F}$, i) $\text{Sr}_{2.4}\text{Ba}_{0.6}\text{Al}_{0.10}\text{Ga}_{0.8375}\text{In}_{0.0625}\text{O}_4\text{F}$ j) $\text{Sr}_{2.4}\text{Ba}_{0.6}\text{Al}_{0.10}\text{Ga}_{0.825}\text{In}_{0.075}\text{O}_4\text{F}$, k) $\text{Sr}_{2.4}\text{Ba}_{0.6}\text{Al}_{0.20}\text{Ga}_{0.775}\text{In}_{0.025}\text{O}_4\text{F}$, l) $\text{Sr}_{2.4}\text{Ba}_{0.6}\text{Al}_{0.20}\text{Ga}_{0.7625}\text{In}_{0.0375}\text{O}_4\text{F}$, m) $\text{Sr}_{2.4}\text{Ba}_{0.6}\text{Al}_{0.20}\text{Ga}_{0.7375}\text{In}_{0.0625}\text{O}_4\text{F}$, and n) $\text{Sr}_{2.4}\text{Ba}_{0.6}\text{Al}_{0.20}\text{Ga}_{0.725}\text{In}_{0.075}\text{O}_4\text{F}$ measured at 900°C and 800°C . Plot (A) represents the excitation spectrum, plot (B) is the emission spectrum (254nm), and plot (C) is the emission spectra (365nm).

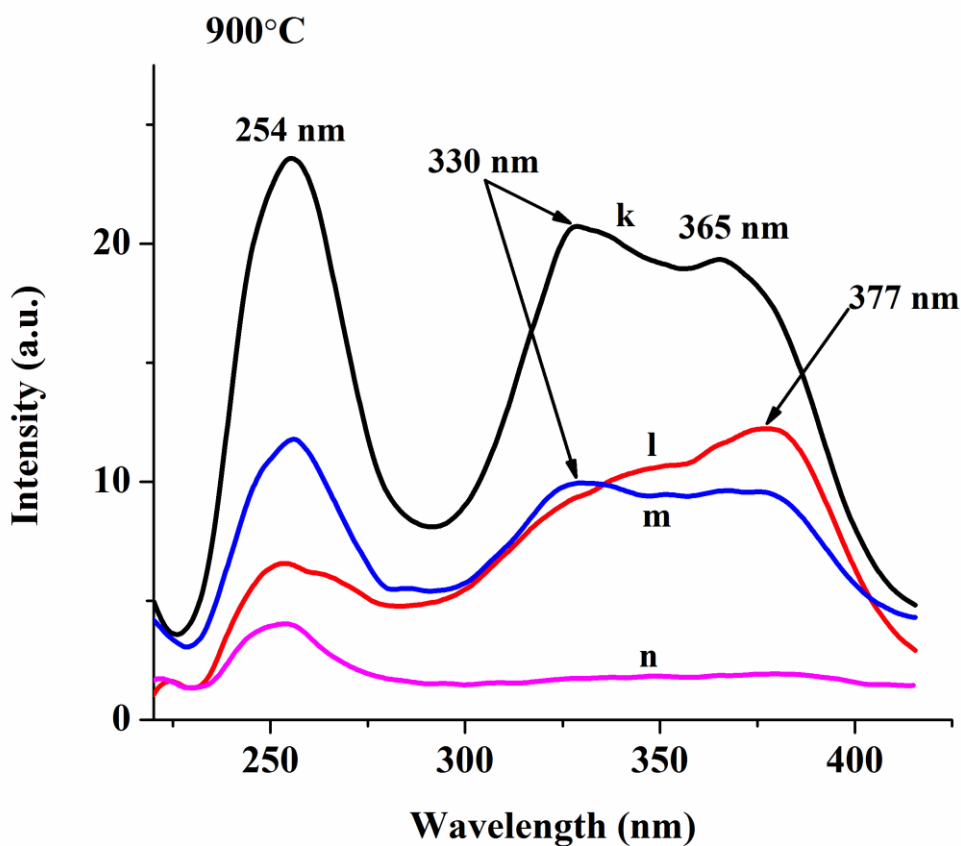


Figure 4.8A: Emission and excitation spectra of $\text{Sr}_{2.4}\text{Ba}_{0.6}\text{Al}_y\text{Ga}_{1-y-z}\text{In}_z\text{O}_4\text{F}$, where a) $\text{Sr}_{2.4}\text{Ba}_{0.6}\text{Al}_{0.10}\text{Ga}_{0.875}\text{In}_{0.025}\text{O}_4\text{F}$ b) $\text{Sr}_{2.4}\text{Ba}_{0.6}\text{Al}_{0.10}\text{Ga}_{0.85}\text{In}_{0.05}\text{O}_4\text{F}$, c) $\text{Sr}_{2.4}\text{Ba}_{0.6}\text{Al}_{0.10}\text{Ga}_{0.825}\text{In}_{0.075}\text{O}_4\text{F}$, d) $\text{Sr}_{2.4}\text{Ba}_{0.6}\text{Al}_{0.20}\text{Ga}_{0.775}\text{In}_{0.025}\text{O}_4\text{F}$, e) $\text{Sr}_{2.4}\text{Ba}_{0.6}\text{Al}_{0.20}\text{Ga}_{0.75}\text{In}_{0.05}\text{O}_4\text{F}$, and f) $\text{Sr}_{2.4}\text{Ba}_{0.6}\text{Al}_{0.20}\text{Ga}_{0.725}\text{In}_{0.075}\text{O}_4\text{F}$ at 1050°C . Other samples include g) $\text{Sr}_{2.4}\text{Ba}_{0.6}\text{Al}_{0.10}\text{Ga}_{0.875}\text{In}_{0.025}\text{O}_4\text{F}$, h) $\text{Sr}_{2.4}\text{Ba}_{0.6}\text{Al}_{0.10}\text{Ga}_{0.8625}\text{In}_{0.0375}\text{O}_4\text{F}$, i) $\text{Sr}_{2.4}\text{Ba}_{0.6}\text{Al}_{0.10}\text{Ga}_{0.8375}\text{In}_{0.0625}\text{O}_4\text{F}$ j) $\text{Sr}_{2.4}\text{Ba}_{0.6}\text{Al}_{0.10}\text{Ga}_{0.825}\text{In}_{0.075}\text{O}_4\text{F}$, k) $\text{Sr}_{2.4}\text{Ba}_{0.6}\text{Al}_{0.20}\text{Ga}_{0.775}\text{In}_{0.025}\text{O}_4\text{F}$, l) $\text{Sr}_{2.4}\text{Ba}_{0.6}\text{Al}_{0.20}\text{Ga}_{0.7625}\text{In}_{0.0375}\text{O}_4\text{F}$, m) $\text{Sr}_{2.4}\text{Ba}_{0.6}\text{Al}_{0.20}\text{Ga}_{0.7375}\text{In}_{0.0625}\text{O}_4\text{F}$, and n) $\text{Sr}_{2.4}\text{Ba}_{0.6}\text{Al}_{0.20}\text{Ga}_{0.725}\text{In}_{0.075}\text{O}_4\text{F}$ measured at 900°C and 800°C . Plot (A) represents the excitation spectrum, plot (B) is the emission spectrum (254nm), and plot (C) is the emission spectra (365nm).

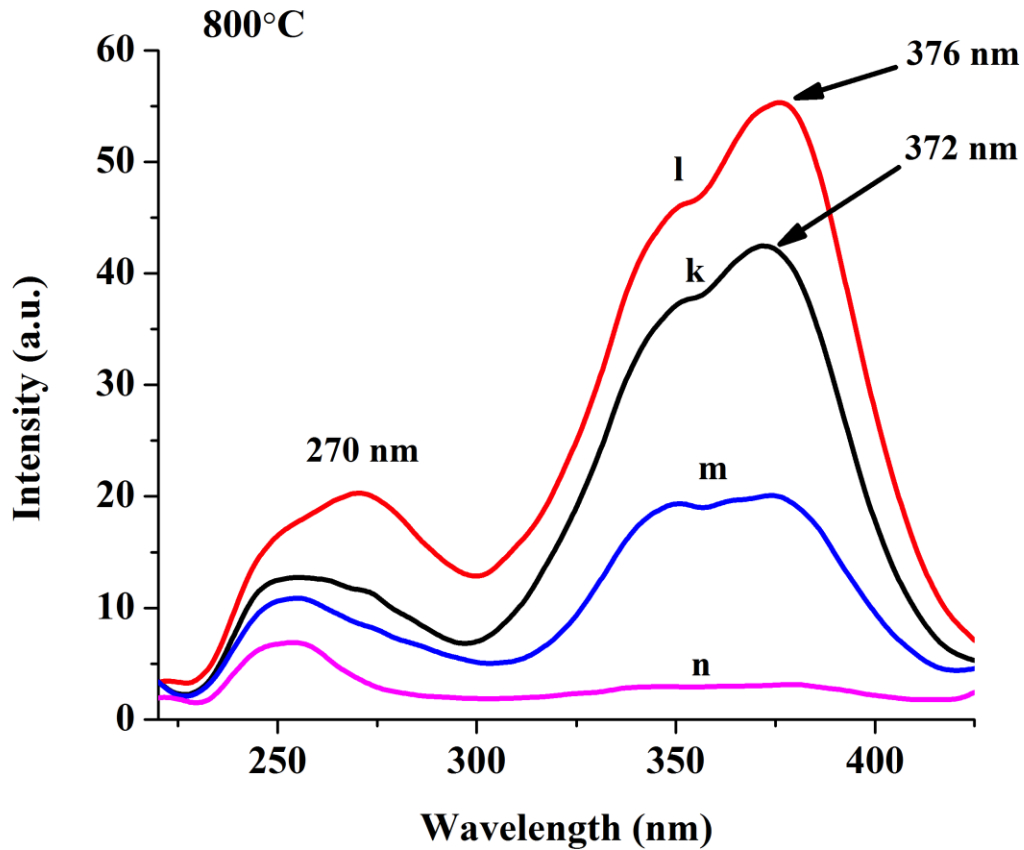


Figure 4.8A: Emission and excitation spectra of $\text{Sr}_{2.4}\text{Ba}_{0.6}\text{Al}_y\text{Ga}_{1-y-z}\text{In}_z\text{O}_4\text{F}$, where a) $\text{Sr}_{2.4}\text{Ba}_{0.6}\text{Al}_{0.10}\text{Ga}_{0.875}\text{In}_{0.025}\text{O}_4\text{F}$ b) $\text{Sr}_{2.4}\text{Ba}_{0.6}\text{Al}_{0.10}\text{Ga}_{0.85}\text{In}_{0.05}\text{O}_4\text{F}$, c) $\text{Sr}_{2.4}\text{Ba}_{0.6}\text{Al}_{0.10}\text{Ga}_{0.825}\text{In}_{0.075}\text{O}_4\text{F}$, d) $\text{Sr}_{2.4}\text{Ba}_{0.6}\text{Al}_{0.20}\text{Ga}_{0.775}\text{In}_{0.025}\text{O}_4\text{F}$, e) $\text{Sr}_{2.4}\text{Ba}_{0.6}\text{Al}_{0.20}\text{Ga}_{0.75}\text{In}_{0.05}\text{O}_4\text{F}$, and f) $\text{Sr}_{2.4}\text{Ba}_{0.6}\text{Al}_{0.20}\text{Ga}_{0.725}\text{In}_{0.075}\text{O}_4\text{F}$ at 1050°C . Other samples include g) $\text{Sr}_{2.4}\text{Ba}_{0.6}\text{Al}_{0.10}\text{Ga}_{0.875}\text{In}_{0.025}\text{O}_4\text{F}$, h) $\text{Sr}_{2.4}\text{Ba}_{0.6}\text{Al}_{0.10}\text{Ga}_{0.8625}\text{In}_{0.0375}\text{O}_4\text{F}$, i) $\text{Sr}_{2.4}\text{Ba}_{0.6}\text{Al}_{0.10}\text{Ga}_{0.8375}\text{In}_{0.0625}\text{O}_4\text{F}$ j) $\text{Sr}_{2.4}\text{Ba}_{0.6}\text{Al}_{0.10}\text{Ga}_{0.825}\text{In}_{0.075}\text{O}_4\text{F}$, k) $\text{Sr}_{2.4}\text{Ba}_{0.6}\text{Al}_{0.20}\text{Ga}_{0.775}\text{In}_{0.025}\text{O}_4\text{F}$, l) $\text{Sr}_{2.4}\text{Ba}_{0.6}\text{Al}_{0.20}\text{Ga}_{0.7625}\text{In}_{0.0375}\text{O}_4\text{F}$, m) $\text{Sr}_{2.4}\text{Ba}_{0.6}\text{Al}_{0.20}\text{Ga}_{0.7375}\text{In}_{0.0625}\text{O}_4\text{F}$, and n) $\text{Sr}_{2.4}\text{Ba}_{0.6}\text{Al}_{0.20}\text{Ga}_{0.725}\text{In}_{0.075}\text{O}_4\text{F}$ measured at 900°C and 800°C . Plot (A) represents the excitation spectrum, plot (B) is the emission spectrum (254nm), and plot (C) is the emission spectra (365nm).

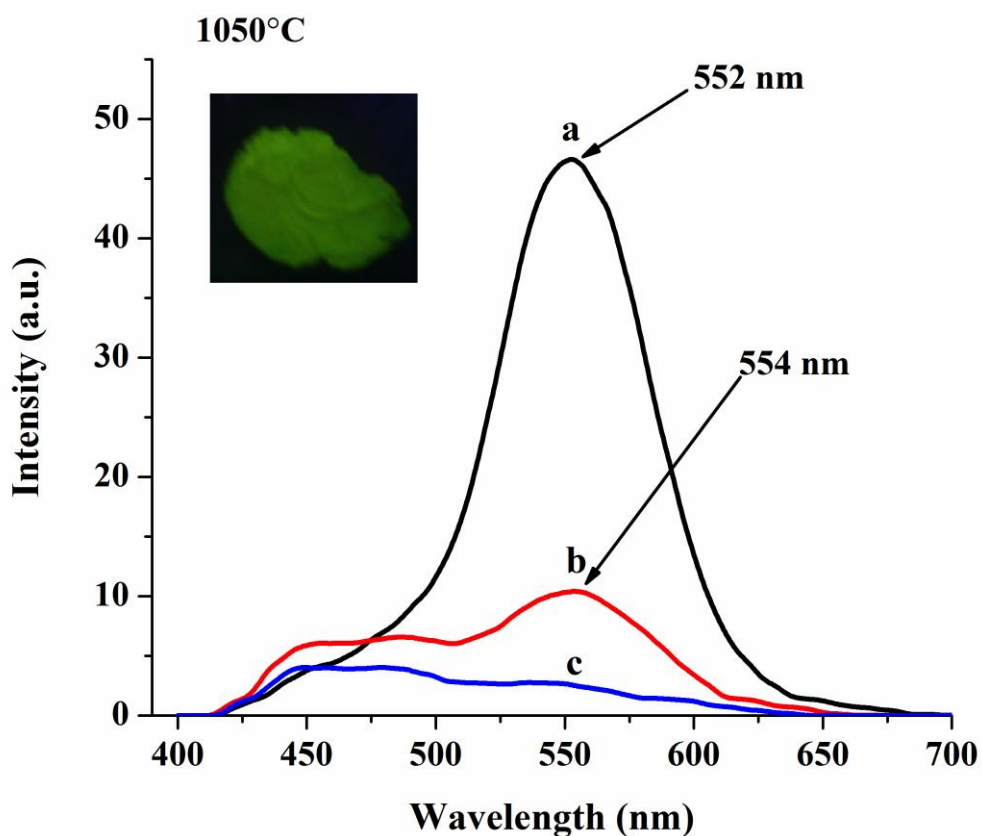


Figure 4.8B: Emission and excitation spectra of $\text{Sr}_{2.4}\text{Ba}_{0.6}\text{Al}_y\text{Ga}_{1-y-z}\text{In}_z\text{O}_4\text{F}$, where a) $\text{Sr}_{2.4}\text{Ba}_{0.6}\text{Al}_{0.10}\text{Ga}_{0.875}\text{In}_{0.025}\text{O}_4\text{F}$ b) $\text{Sr}_{2.4}\text{Ba}_{0.6}\text{Al}_{0.10}\text{Ga}_{0.85}\text{In}_{0.05}\text{O}_4\text{F}$, c) $\text{Sr}_{2.4}\text{Ba}_{0.6}\text{Al}_{0.10}\text{Ga}_{0.825}\text{In}_{0.075}\text{O}_4\text{F}$, d) $\text{Sr}_{2.4}\text{Ba}_{0.6}\text{Al}_{0.20}\text{Ga}_{0.775}\text{In}_{0.025}\text{O}_4\text{F}$, e) $\text{Sr}_{2.4}\text{Ba}_{0.6}\text{Al}_{0.20}\text{Ga}_{0.75}\text{In}_{0.05}\text{O}_4\text{F}$, and f) $\text{Sr}_{2.4}\text{Ba}_{0.6}\text{Al}_{0.20}\text{Ga}_{0.725}\text{In}_{0.075}\text{O}_4\text{F}$ at 1050°C . Other samples include g) $\text{Sr}_{2.4}\text{Ba}_{0.6}\text{Al}_{0.10}\text{Ga}_{0.875}\text{In}_{0.025}\text{O}_4\text{F}$, h) $\text{Sr}_{2.4}\text{Ba}_{0.6}\text{Al}_{0.10}\text{Ga}_{0.8625}\text{In}_{0.0375}\text{O}_4\text{F}$, i) $\text{Sr}_{2.4}\text{Ba}_{0.6}\text{Al}_{0.10}\text{Ga}_{0.8375}\text{In}_{0.0625}\text{O}_4\text{F}$ j) $\text{Sr}_{2.4}\text{Ba}_{0.6}\text{Al}_{0.10}\text{Ga}_{0.825}\text{In}_{0.075}\text{O}_4\text{F}$, k) $\text{Sr}_{2.4}\text{Ba}_{0.6}\text{Al}_{0.20}\text{Ga}_{0.775}\text{In}_{0.025}\text{O}_4\text{F}$, l) $\text{Sr}_{2.4}\text{Ba}_{0.6}\text{Al}_{0.20}\text{Ga}_{0.7625}\text{In}_{0.0375}\text{O}_4\text{F}$, m) $\text{Sr}_{2.4}\text{Ba}_{0.6}\text{Al}_{0.20}\text{Ga}_{0.7375}\text{In}_{0.0625}\text{O}_4\text{F}$, and n) $\text{Sr}_{2.4}\text{Ba}_{0.6}\text{Al}_{0.20}\text{Ga}_{0.725}\text{In}_{0.075}\text{O}_4\text{F}$ measured at 900°C and 800°C . Plot (A) represents the excitation spectrum, plot (B) is the emission spectrum (254nm), and plot (C) is the emission spectra (365nm).

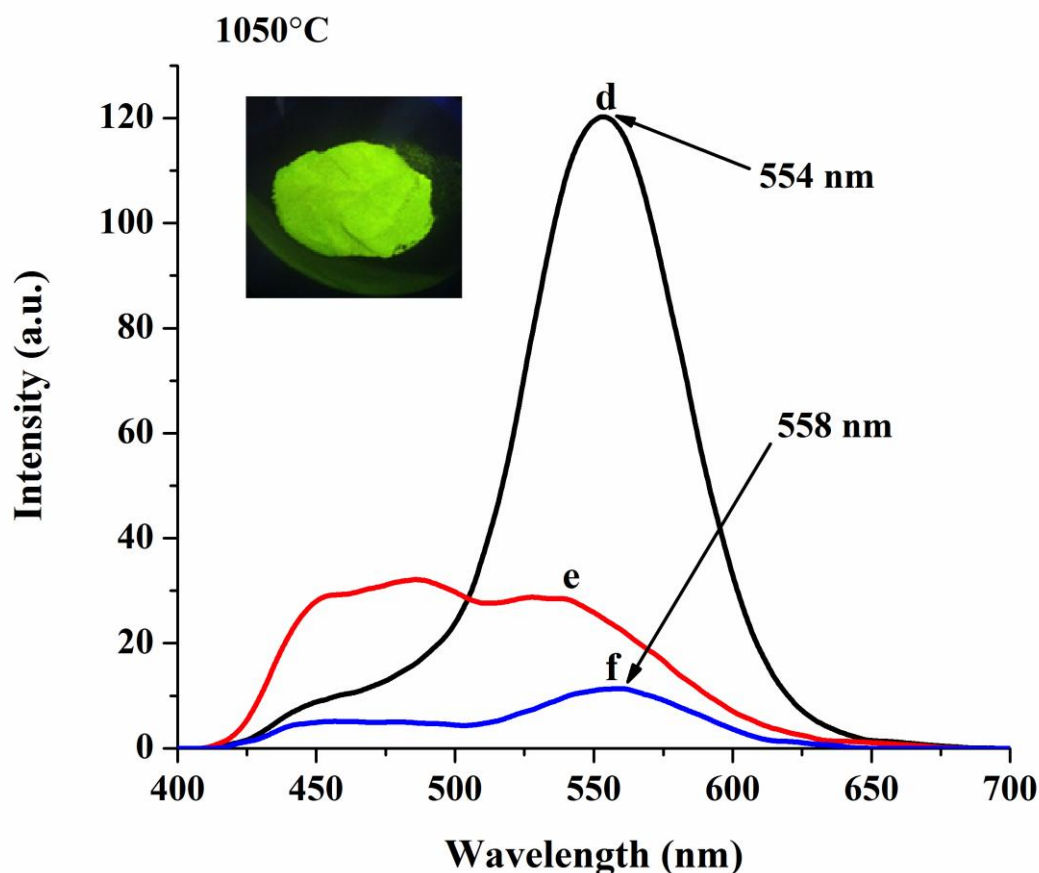


Figure 4.8B: Emission and excitation spectra of $\text{Sr}_{2.4}\text{Ba}_{0.6}\text{Al}_x\text{Ga}_{1-y-z}\text{In}_z\text{O}_4\text{F}$, where a) $\text{Sr}_{2.4}\text{Ba}_{0.6}\text{Al}_{0.10}\text{Ga}_{0.875}\text{In}_{0.025}\text{O}_4\text{F}$ b) $\text{Sr}_{2.4}\text{Ba}_{0.6}\text{Al}_{0.10}\text{Ga}_{0.85}\text{In}_{0.05}\text{O}_4\text{F}$, c) $\text{Sr}_{2.4}\text{Ba}_{0.6}\text{Al}_{0.10}\text{Ga}_{0.825}\text{In}_{0.075}\text{O}_4\text{F}$, d) $\text{Sr}_{2.4}\text{Ba}_{0.6}\text{Al}_{0.20}\text{Ga}_{0.775}\text{In}_{0.025}\text{O}_4\text{F}$, e) $\text{Sr}_{2.4}\text{Ba}_{0.6}\text{Al}_{0.20}\text{Ga}_{0.75}\text{In}_{0.05}\text{O}_4\text{F}$, and f) $\text{Sr}_{2.4}\text{Ba}_{0.6}\text{Al}_{0.20}\text{Ga}_{0.725}\text{In}_{0.075}\text{O}_4\text{F}$ at 1050°C . Other samples include g) $\text{Sr}_{2.4}\text{Ba}_{0.6}\text{Al}_{0.10}\text{Ga}_{0.875}\text{In}_{0.025}\text{O}_4\text{F}$, h) $\text{Sr}_{2.4}\text{Ba}_{0.6}\text{Al}_{0.10}\text{Ga}_{0.8625}\text{In}_{0.0375}\text{O}_4\text{F}$, i) $\text{Sr}_{2.4}\text{Ba}_{0.6}\text{Al}_{0.10}\text{Ga}_{0.8375}\text{In}_{0.0625}\text{O}_4\text{F}$ j) $\text{Sr}_{2.4}\text{Ba}_{0.6}\text{Al}_{0.10}\text{Ga}_{0.825}\text{In}_{0.075}\text{O}_4\text{F}$, k) $\text{Sr}_{2.4}\text{Ba}_{0.6}\text{Al}_{0.20}\text{Ga}_{0.775}\text{In}_{0.025}\text{O}_4\text{F}$, l) $\text{Sr}_{2.4}\text{Ba}_{0.6}\text{Al}_{0.20}\text{Ga}_{0.7625}\text{In}_{0.0375}\text{O}_4\text{F}$, m) $\text{Sr}_{2.4}\text{Ba}_{0.6}\text{Al}_{0.20}\text{Ga}_{0.7375}\text{In}_{0.0625}\text{O}_4\text{F}$, and n) $\text{Sr}_{2.4}\text{Ba}_{0.6}\text{Al}_{0.20}\text{Ga}_{0.725}\text{In}_{0.075}\text{O}_4\text{F}$ measured at 900°C and 800°C . Plot (A) represents the excitation spectrum, plot (B) is the emission spectrum (254nm), and plot (C) is the emission spectra (365nm).

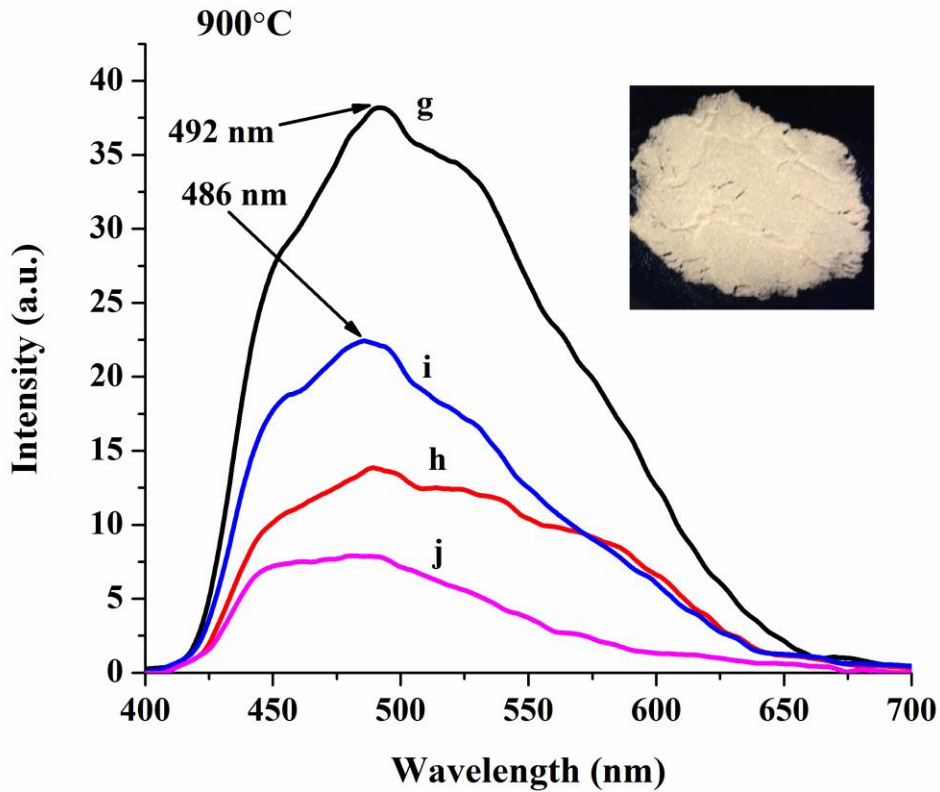


Figure 4.8B: Emission and excitation spectra of $\text{Sr}_{2.4}\text{Ba}_{0.6}\text{Al}_y\text{Ga}_{1-y-z}\text{In}_z\text{O}_4\text{F}$, where a) $\text{Sr}_{2.4}\text{Ba}_{0.6}\text{Al}_{0.10}\text{Ga}_{0.875}\text{In}_{0.025}\text{O}_4\text{F}$ b) $\text{Sr}_{2.4}\text{Ba}_{0.6}\text{Al}_{0.10}\text{Ga}_{0.85}\text{In}_{0.05}\text{O}_4\text{F}$, c) $\text{Sr}_{2.4}\text{Ba}_{0.6}\text{Al}_{0.10}\text{Ga}_{0.825}\text{In}_{0.075}\text{O}_4\text{F}$, d) $\text{Sr}_{2.4}\text{Ba}_{0.6}\text{Al}_{0.20}\text{Ga}_{0.775}\text{In}_{0.025}\text{O}_4\text{F}$, e) $\text{Sr}_{2.4}\text{Ba}_{0.6}\text{Al}_{0.20}\text{Ga}_{0.75}\text{In}_{0.05}\text{O}_4\text{F}$, and f) $\text{Sr}_{2.4}\text{Ba}_{0.6}\text{Al}_{0.20}\text{Ga}_{0.725}\text{In}_{0.075}\text{O}_4\text{F}$ at 1050°C . Other samples include g) $\text{Sr}_{2.4}\text{Ba}_{0.6}\text{Al}_{0.10}\text{Ga}_{0.875}\text{In}_{0.025}\text{O}_4\text{F}$, h) $\text{Sr}_{2.4}\text{Ba}_{0.6}\text{Al}_{0.10}\text{Ga}_{0.8625}\text{In}_{0.0375}\text{O}_4\text{F}$, i) $\text{Sr}_{2.4}\text{Ba}_{0.6}\text{Al}_{0.10}\text{Ga}_{0.8375}\text{In}_{0.0625}\text{O}_4\text{F}$ j) $\text{Sr}_{2.4}\text{Ba}_{0.6}\text{Al}_{0.10}\text{Ga}_{0.825}\text{In}_{0.075}\text{O}_4\text{F}$, k) $\text{Sr}_{2.4}\text{Ba}_{0.6}\text{Al}_{0.20}\text{Ga}_{0.775}\text{In}_{0.025}\text{O}_4\text{F}$, l) $\text{Sr}_{2.4}\text{Ba}_{0.6}\text{Al}_{0.20}\text{Ga}_{0.7625}\text{In}_{0.0375}\text{O}_4\text{F}$, m) $\text{Sr}_{2.4}\text{Ba}_{0.6}\text{Al}_{0.20}\text{Ga}_{0.7375}\text{In}_{0.0625}\text{O}_4\text{F}$, and n) $\text{Sr}_{2.4}\text{Ba}_{0.6}\text{Al}_{0.20}\text{Ga}_{0.725}\text{In}_{0.075}\text{O}_4\text{F}$ measured at 900°C and 800°C . Plot (A) represents the excitation spectrum, plot (B) is the emission spectrum (254nm), and plot (C) is the emission spectra (365nm).

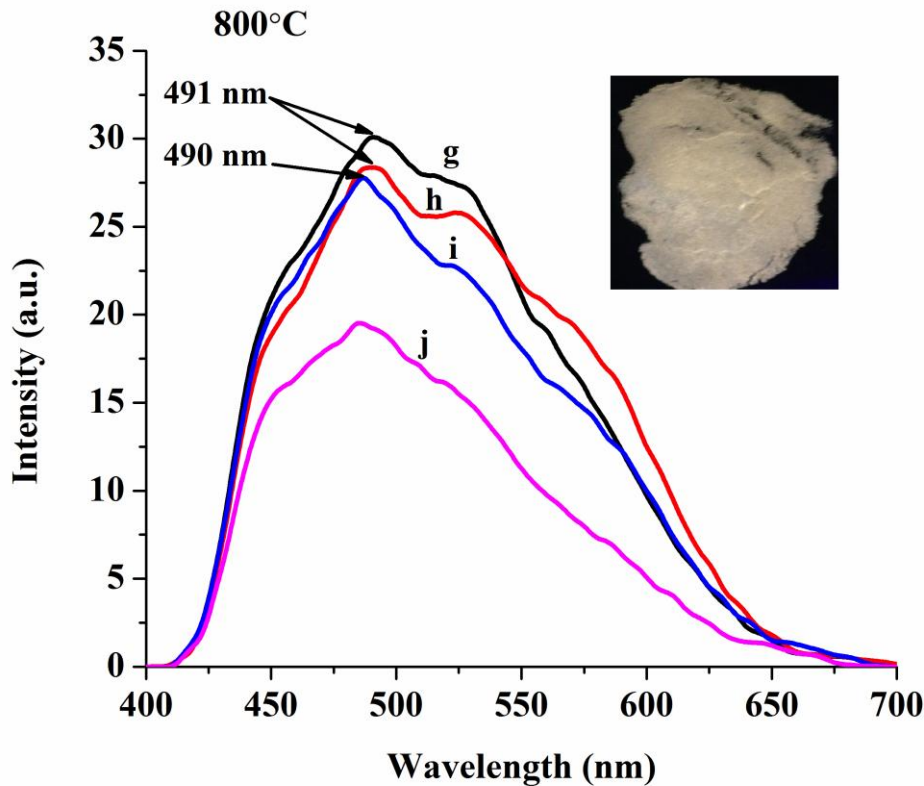


Figure 4.8B: Emission and excitation spectra of $\text{Sr}_{2.4}\text{Ba}_{0.6}\text{Al}_x\text{Ga}_{1-y-z}\text{In}_z\text{O}_4\text{F}$, where a) $\text{Sr}_{2.4}\text{Ba}_{0.6}\text{Al}_{0.10}\text{Ga}_{0.875}\text{In}_{0.025}\text{O}_4\text{F}$ b) $\text{Sr}_{2.4}\text{Ba}_{0.6}\text{Al}_{0.10}\text{Ga}_{0.85}\text{In}_{0.05}\text{O}_4\text{F}$, c) $\text{Sr}_{2.4}\text{Ba}_{0.6}\text{Al}_{0.10}\text{Ga}_{0.825}\text{In}_{0.075}\text{O}_4\text{F}$, d) $\text{Sr}_{2.4}\text{Ba}_{0.6}\text{Al}_{0.20}\text{Ga}_{0.775}\text{In}_{0.025}\text{O}_4\text{F}$, e) $\text{Sr}_{2.4}\text{Ba}_{0.6}\text{Al}_{0.20}\text{Ga}_{0.75}\text{In}_{0.05}\text{O}_4\text{F}$, and f) $\text{Sr}_{2.4}\text{Ba}_{0.6}\text{Al}_{0.20}\text{Ga}_{0.725}\text{In}_{0.075}\text{O}_4\text{F}$ at 1050°C . Other samples include g) $\text{Sr}_{2.4}\text{Ba}_{0.6}\text{Al}_{0.10}\text{Ga}_{0.875}\text{In}_{0.025}\text{O}_4\text{F}$, h) $\text{Sr}_{2.4}\text{Ba}_{0.6}\text{Al}_{0.10}\text{Ga}_{0.8625}\text{In}_{0.0375}\text{O}_4\text{F}$, i) $\text{Sr}_{2.4}\text{Ba}_{0.6}\text{Al}_{0.10}\text{Ga}_{0.8375}\text{In}_{0.0625}\text{O}_4\text{F}$ j) $\text{Sr}_{2.4}\text{Ba}_{0.6}\text{Al}_{0.10}\text{Ga}_{0.825}\text{In}_{0.075}\text{O}_4\text{F}$, k) $\text{Sr}_{2.4}\text{Ba}_{0.6}\text{Al}_{0.20}\text{Ga}_{0.775}\text{In}_{0.025}\text{O}_4\text{F}$, l) $\text{Sr}_{2.4}\text{Ba}_{0.6}\text{Al}_{0.20}\text{Ga}_{0.7625}\text{In}_{0.0375}\text{O}_4\text{F}$, m) $\text{Sr}_{2.4}\text{Ba}_{0.6}\text{Al}_{0.20}\text{Ga}_{0.7375}\text{In}_{0.0625}\text{O}_4\text{F}$, and n) $\text{Sr}_{2.4}\text{Ba}_{0.6}\text{Al}_{0.20}\text{Ga}_{0.725}\text{In}_{0.075}\text{O}_4\text{F}$ measured at 900°C and 800°C . Plot (A) represents the excitation spectrum, plot (B) is the emission spectrum (254nm), and plot (C) is the emission spectra (365nm).

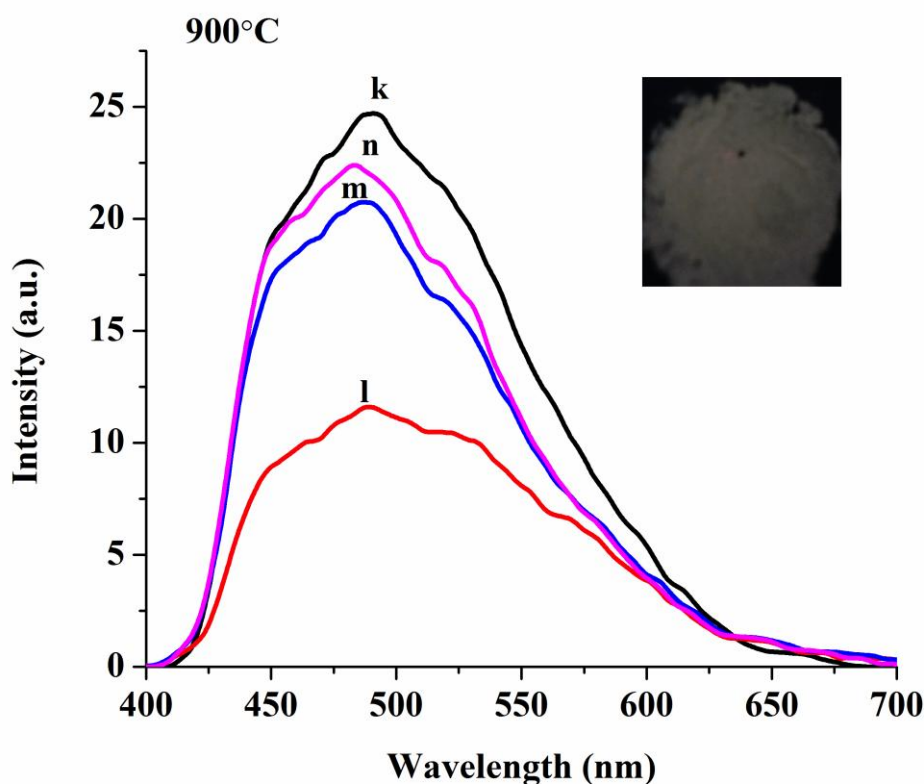


Figure 4.8B: Emission and excitation spectra of $\text{Sr}_{2.4}\text{Ba}_{0.6}\text{Al}_x\text{Ga}_{1-y-z}\text{In}_z\text{O}_4\text{F}$, where a) $\text{Sr}_{2.4}\text{Ba}_{0.6}\text{Al}_{0.10}\text{Ga}_{0.875}\text{In}_{0.025}\text{O}_4\text{F}$ b) $\text{Sr}_{2.4}\text{Ba}_{0.6}\text{Al}_{0.10}\text{Ga}_{0.85}\text{In}_{0.05}\text{O}_4\text{F}$, c) $\text{Sr}_{2.4}\text{Ba}_{0.6}\text{Al}_{0.10}\text{Ga}_{0.825}\text{In}_{0.075}\text{O}_4\text{F}$, d) $\text{Sr}_{2.4}\text{Ba}_{0.6}\text{Al}_{0.20}\text{Ga}_{0.775}\text{In}_{0.025}\text{O}_4\text{F}$, e) $\text{Sr}_{2.4}\text{Ba}_{0.6}\text{Al}_{0.20}\text{Ga}_{0.75}\text{In}_{0.05}\text{O}_4\text{F}$, and f) $\text{Sr}_{2.4}\text{Ba}_{0.6}\text{Al}_{0.20}\text{Ga}_{0.725}\text{In}_{0.075}\text{O}_4\text{F}$ at 1050°C . Other samples include g) $\text{Sr}_{2.4}\text{Ba}_{0.6}\text{Al}_{0.10}\text{Ga}_{0.875}\text{In}_{0.025}\text{O}_4\text{F}$, h) $\text{Sr}_{2.4}\text{Ba}_{0.6}\text{Al}_{0.10}\text{Ga}_{0.8625}\text{In}_{0.0375}\text{O}_4\text{F}$, i) $\text{Sr}_{2.4}\text{Ba}_{0.6}\text{Al}_{0.10}\text{Ga}_{0.8375}\text{In}_{0.0625}\text{O}_4\text{F}$ j) $\text{Sr}_{2.4}\text{Ba}_{0.6}\text{Al}_{0.10}\text{Ga}_{0.825}\text{In}_{0.075}\text{O}_4\text{F}$, k) $\text{Sr}_{2.4}\text{Ba}_{0.6}\text{Al}_{0.20}\text{Ga}_{0.775}\text{In}_{0.025}\text{O}_4\text{F}$, l) $\text{Sr}_{2.4}\text{Ba}_{0.6}\text{Al}_{0.20}\text{Ga}_{0.7625}\text{In}_{0.0375}\text{O}_4\text{F}$, m) $\text{Sr}_{2.4}\text{Ba}_{0.6}\text{Al}_{0.20}\text{Ga}_{0.7375}\text{In}_{0.0625}\text{O}_4\text{F}$, and n) $\text{Sr}_{2.4}\text{Ba}_{0.6}\text{Al}_{0.20}\text{Ga}_{0.725}\text{In}_{0.075}\text{O}_4\text{F}$ measured at 900°C and 800°C . Plot (A) represents the excitation spectrum, plot (B) is the emission spectrum (254nm), and plot (C) is the emission spectra (365nm).

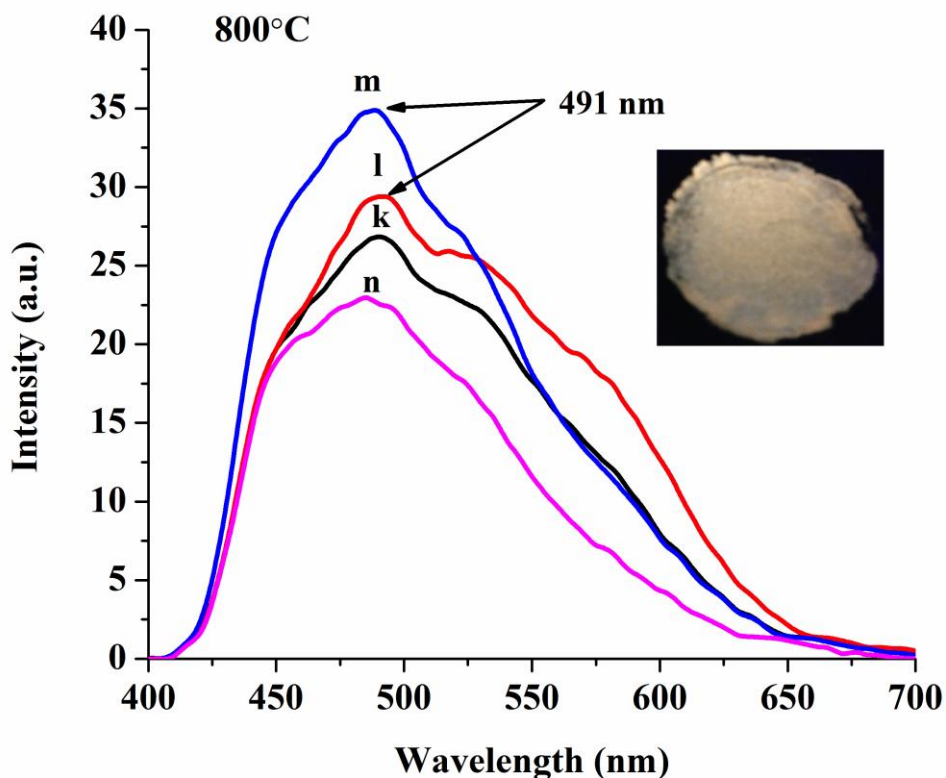


Figure 4.8B: Emission and excitation spectra of $\text{Sr}_{2.4}\text{Ba}_{0.6}\text{Al}_y\text{Ga}_{1-y-z}\text{In}_z\text{O}_4\text{F}$, where a) $\text{Sr}_{2.4}\text{Ba}_{0.6}\text{Al}_{0.10}\text{Ga}_{0.875}\text{In}_{0.025}\text{O}_4\text{F}$ b) $\text{Sr}_{2.4}\text{Ba}_{0.6}\text{Al}_{0.10}\text{Ga}_{0.85}\text{In}_{0.05}\text{O}_4\text{F}$, c) $\text{Sr}_{2.4}\text{Ba}_{0.6}\text{Al}_{0.10}\text{Ga}_{0.825}\text{In}_{0.075}\text{O}_4\text{F}$, d) $\text{Sr}_{2.4}\text{Ba}_{0.6}\text{Al}_{0.20}\text{Ga}_{0.775}\text{In}_{0.025}\text{O}_4\text{F}$, e) $\text{Sr}_{2.4}\text{Ba}_{0.6}\text{Al}_{0.20}\text{Ga}_{0.75}\text{In}_{0.05}\text{O}_4\text{F}$, and f) $\text{Sr}_{2.4}\text{Ba}_{0.6}\text{Al}_{0.20}\text{Ga}_{0.725}\text{In}_{0.075}\text{O}_4\text{F}$ at 1050°C . Other samples include g) $\text{Sr}_{2.4}\text{Ba}_{0.6}\text{Al}_{0.10}\text{Ga}_{0.875}\text{In}_{0.025}\text{O}_4\text{F}$, h) $\text{Sr}_{2.4}\text{Ba}_{0.6}\text{Al}_{0.10}\text{Ga}_{0.8625}\text{In}_{0.0375}\text{O}_4\text{F}$, i) $\text{Sr}_{2.4}\text{Ba}_{0.6}\text{Al}_{0.10}\text{Ga}_{0.8375}\text{In}_{0.0625}\text{O}_4\text{F}$ j) $\text{Sr}_{2.4}\text{Ba}_{0.6}\text{Al}_{0.10}\text{Ga}_{0.825}\text{In}_{0.075}\text{O}_4\text{F}$, k) $\text{Sr}_{2.4}\text{Ba}_{0.6}\text{Al}_{0.20}\text{Ga}_{0.775}\text{In}_{0.025}\text{O}_4\text{F}$, l) $\text{Sr}_{2.4}\text{Ba}_{0.6}\text{Al}_{0.20}\text{Ga}_{0.7625}\text{In}_{0.0375}\text{O}_4\text{F}$, m) $\text{Sr}_{2.4}\text{Ba}_{0.6}\text{Al}_{0.20}\text{Ga}_{0.7375}\text{In}_{0.0625}\text{O}_4\text{F}$, and n) $\text{Sr}_{2.4}\text{Ba}_{0.6}\text{Al}_{0.20}\text{Ga}_{0.725}\text{In}_{0.075}\text{O}_4\text{F}$ measured at 900°C and 800°C . Plot (A) represents the excitation spectrum, plot (B) is the emission spectrum (254nm), and plot (C) is the emission spectra (365nm).

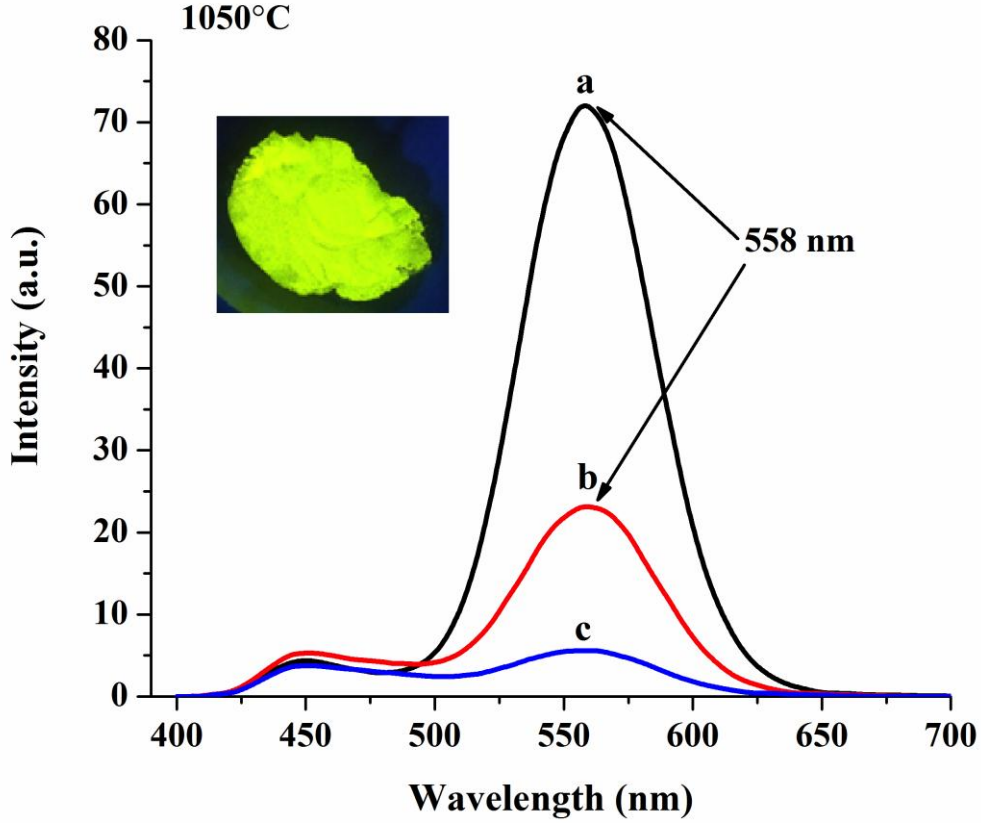


Figure 4.8C: Emission and excitation spectra of $\text{Sr}_{2.4}\text{Ba}_{0.6}\text{Al}_x\text{Ga}_{1-y-z}\text{In}_z\text{O}_4\text{F}$, where a) $\text{Sr}_{2.4}\text{Ba}_{0.6}\text{Al}_{0.10}\text{Ga}_{0.875}\text{In}_{0.025}\text{O}_4\text{F}$ b) $\text{Sr}_{2.4}\text{Ba}_{0.6}\text{Al}_{0.10}\text{Ga}_{0.85}\text{In}_{0.05}\text{O}_4\text{F}$, c) $\text{Sr}_{2.4}\text{Ba}_{0.6}\text{Al}_{0.10}\text{Ga}_{0.825}\text{In}_{0.075}\text{O}_4\text{F}$, d) $\text{Sr}_{2.4}\text{Ba}_{0.6}\text{Al}_{0.20}\text{Ga}_{0.775}\text{In}_{0.025}\text{O}_4\text{F}$, e) $\text{Sr}_{2.4}\text{Ba}_{0.6}\text{Al}_{0.20}\text{Ga}_{0.75}\text{In}_{0.05}\text{O}_4\text{F}$, and f) $\text{Sr}_{2.4}\text{Ba}_{0.6}\text{Al}_{0.20}\text{Ga}_{0.725}\text{In}_{0.075}\text{O}_4\text{F}$ at 1050°C . Other samples include g) $\text{Sr}_{2.4}\text{Ba}_{0.6}\text{Al}_{0.10}\text{Ga}_{0.875}\text{In}_{0.025}\text{O}_4\text{F}$, h) $\text{Sr}_{2.4}\text{Ba}_{0.6}\text{Al}_{0.10}\text{Ga}_{0.8625}\text{In}_{0.0375}\text{O}_4\text{F}$, i) $\text{Sr}_{2.4}\text{Ba}_{0.6}\text{Al}_{0.10}\text{Ga}_{0.8375}\text{In}_{0.0625}\text{O}_4\text{F}$ j) $\text{Sr}_{2.4}\text{Ba}_{0.6}\text{Al}_{0.10}\text{Ga}_{0.825}\text{In}_{0.075}\text{O}_4\text{F}$, k) $\text{Sr}_{2.4}\text{Ba}_{0.6}\text{Al}_{0.20}\text{Ga}_{0.775}\text{In}_{0.025}\text{O}_4\text{F}$, l) $\text{Sr}_{2.4}\text{Ba}_{0.6}\text{Al}_{0.20}\text{Ga}_{0.7625}\text{In}_{0.0375}\text{O}_4\text{F}$, m) $\text{Sr}_{2.4}\text{Ba}_{0.6}\text{Al}_{0.20}\text{Ga}_{0.7375}\text{In}_{0.0625}\text{O}_4\text{F}$, and n) $\text{Sr}_{2.4}\text{Ba}_{0.6}\text{Al}_{0.20}\text{Ga}_{0.725}\text{In}_{0.075}\text{O}_4\text{F}$ measured at 900°C and 800°C . Plot (A) represents the excitation spectrum, plot (B) is the emission spectrum (254nm), and plot (C) is the emission spectra (365nm).

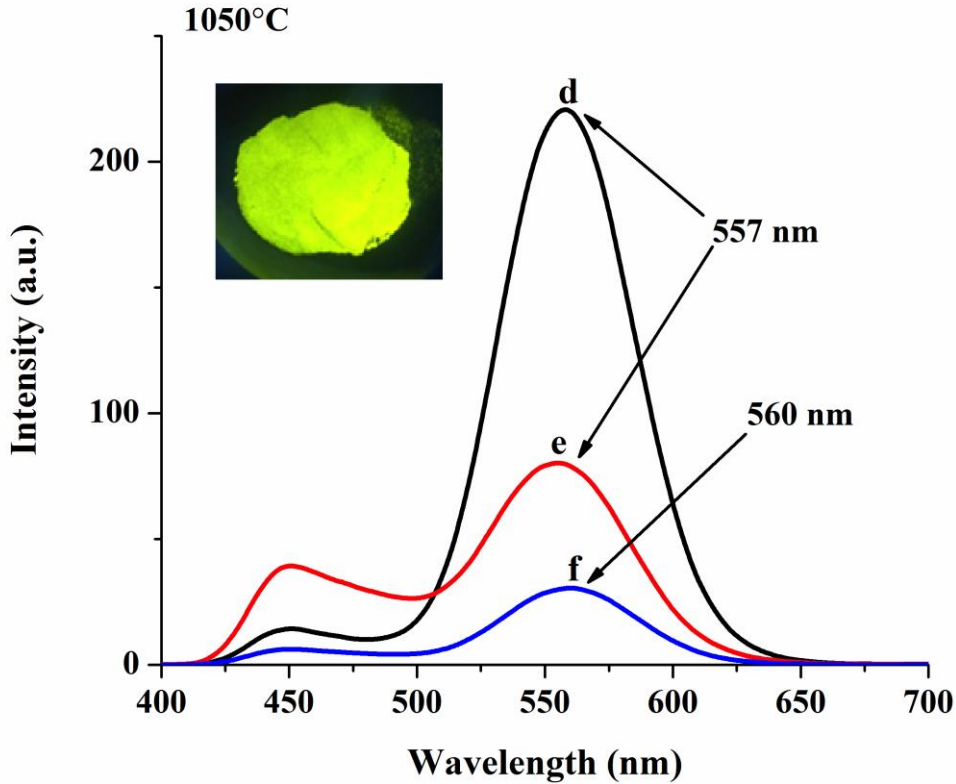


Figure 4.8C: Emission and excitation spectra of $\text{Sr}_{2.4}\text{Ba}_{0.6}\text{Al}_y\text{Ga}_{1-y-z}\text{In}_z\text{O}_4\text{F}$, where a) $\text{Sr}_{2.4}\text{Ba}_{0.6}\text{Al}_{0.10}\text{Ga}_{0.875}\text{In}_{0.025}\text{O}_4\text{F}$ b) $\text{Sr}_{2.4}\text{Ba}_{0.6}\text{Al}_{0.10}\text{Ga}_{0.85}\text{In}_{0.05}\text{O}_4\text{F}$, c) $\text{Sr}_{2.4}\text{Ba}_{0.6}\text{Al}_{0.10}\text{Ga}_{0.825}\text{In}_{0.075}\text{O}_4\text{F}$, d) $\text{Sr}_{2.4}\text{Ba}_{0.6}\text{Al}_{0.20}\text{Ga}_{0.775}\text{In}_{0.025}\text{O}_4\text{F}$, e) $\text{Sr}_{2.4}\text{Ba}_{0.6}\text{Al}_{0.20}\text{Ga}_{0.75}\text{In}_{0.05}\text{O}_4\text{F}$, and f) $\text{Sr}_{2.4}\text{Ba}_{0.6}\text{Al}_{0.20}\text{Ga}_{0.725}\text{In}_{0.075}\text{O}_4\text{F}$ at 1050°C . Other samples include g) $\text{Sr}_{2.4}\text{Ba}_{0.6}\text{Al}_{0.10}\text{Ga}_{0.875}\text{In}_{0.025}\text{O}_4\text{F}$, h) $\text{Sr}_{2.4}\text{Ba}_{0.6}\text{Al}_{0.10}\text{Ga}_{0.8625}\text{In}_{0.0375}\text{O}_4\text{F}$, i) $\text{Sr}_{2.4}\text{Ba}_{0.6}\text{Al}_{0.10}\text{Ga}_{0.8375}\text{In}_{0.0625}\text{O}_4\text{F}$ j) $\text{Sr}_{2.4}\text{Ba}_{0.6}\text{Al}_{0.10}\text{Ga}_{0.825}\text{In}_{0.075}\text{O}_4\text{F}$, k) $\text{Sr}_{2.4}\text{Ba}_{0.6}\text{Al}_{0.20}\text{Ga}_{0.775}\text{In}_{0.025}\text{O}_4\text{F}$, l) $\text{Sr}_{2.4}\text{Ba}_{0.6}\text{Al}_{0.20}\text{Ga}_{0.7625}\text{In}_{0.0375}\text{O}_4\text{F}$, m) $\text{Sr}_{2.4}\text{Ba}_{0.6}\text{Al}_{0.20}\text{Ga}_{0.7375}\text{In}_{0.0625}\text{O}_4\text{F}$, and n) $\text{Sr}_{2.4}\text{Ba}_{0.6}\text{Al}_{0.20}\text{Ga}_{0.725}\text{In}_{0.075}\text{O}_4\text{F}$ measured at 900°C and 800°C . Plot (A) represents the excitation spectrum, plot (B) is the emission spectrum (254nm), and plot (C) is the emission spectra (365nm).

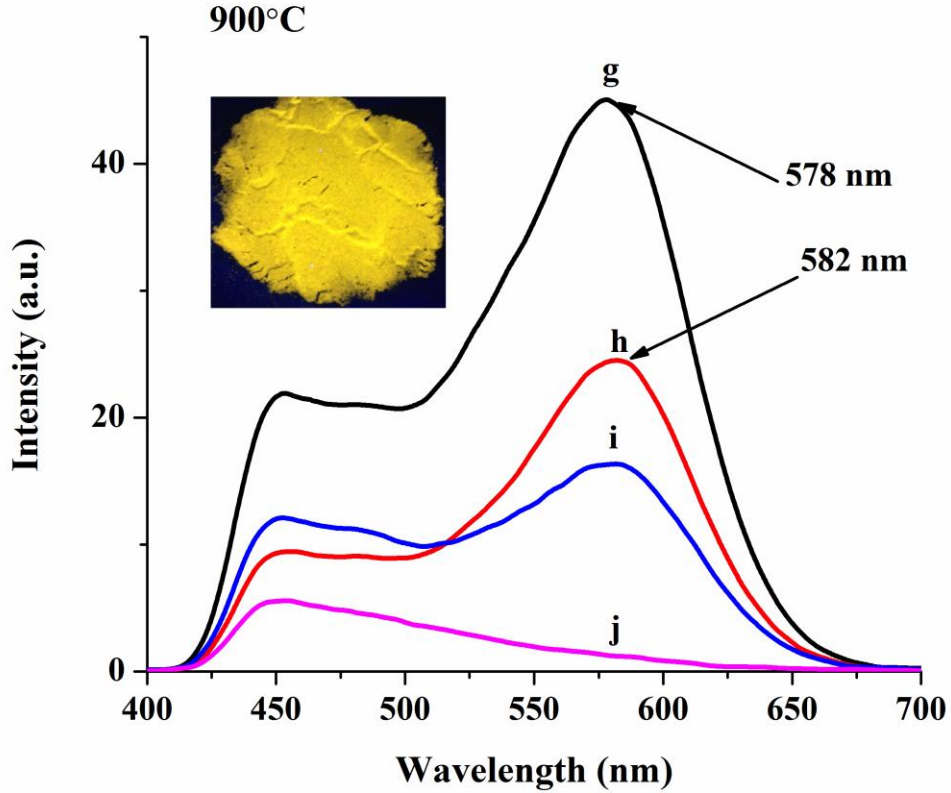


Figure 4.8C: Emission and excitation spectra of $\text{Sr}_{2.4}\text{Ba}_{0.6}\text{Al}_y\text{Ga}_{1-y-z}\text{In}_z\text{O}_4\text{F}$, where a) $\text{Sr}_{2.4}\text{Ba}_{0.6}\text{Al}_{0.10}\text{Ga}_{0.875}\text{In}_{0.025}\text{O}_4\text{F}$ b) $\text{Sr}_{2.4}\text{Ba}_{0.6}\text{Al}_{0.10}\text{Ga}_{0.85}\text{In}_{0.05}\text{O}_4\text{F}$, c) $\text{Sr}_{2.4}\text{Ba}_{0.6}\text{Al}_{0.10}\text{Ga}_{0.825}\text{In}_{0.075}\text{O}_4\text{F}$, d) $\text{Sr}_{2.4}\text{Ba}_{0.6}\text{Al}_{0.20}\text{Ga}_{0.775}\text{In}_{0.025}\text{O}_4\text{F}$, e) $\text{Sr}_{2.4}\text{Ba}_{0.6}\text{Al}_{0.20}\text{Ga}_{0.75}\text{In}_{0.05}\text{O}_4\text{F}$, and f) $\text{Sr}_{2.4}\text{Ba}_{0.6}\text{Al}_{0.20}\text{Ga}_{0.725}\text{In}_{0.075}\text{O}_4\text{F}$ at 1050°C . Other samples include g) $\text{Sr}_{2.4}\text{Ba}_{0.6}\text{Al}_{0.10}\text{Ga}_{0.875}\text{In}_{0.025}\text{O}_4\text{F}$, h) $\text{Sr}_{2.4}\text{Ba}_{0.6}\text{Al}_{0.10}\text{Ga}_{0.8625}\text{In}_{0.0375}\text{O}_4\text{F}$, i) $\text{Sr}_{2.4}\text{Ba}_{0.6}\text{Al}_{0.10}\text{Ga}_{0.8375}\text{In}_{0.0625}\text{O}_4\text{F}$ j) $\text{Sr}_{2.4}\text{Ba}_{0.6}\text{Al}_{0.10}\text{Ga}_{0.825}\text{In}_{0.075}\text{O}_4\text{F}$, k) $\text{Sr}_{2.4}\text{Ba}_{0.6}\text{Al}_{0.20}\text{Ga}_{0.775}\text{In}_{0.025}\text{O}_4\text{F}$, l) $\text{Sr}_{2.4}\text{Ba}_{0.6}\text{Al}_{0.20}\text{Ga}_{0.7625}\text{In}_{0.0375}\text{O}_4\text{F}$, m) $\text{Sr}_{2.4}\text{Ba}_{0.6}\text{Al}_{0.20}\text{Ga}_{0.7375}\text{In}_{0.0625}\text{O}_4\text{F}$, and n) $\text{Sr}_{2.4}\text{Ba}_{0.6}\text{Al}_{0.20}\text{Ga}_{0.725}\text{In}_{0.075}\text{O}_4\text{F}$ measured at 900°C and 800°C . Plot (A) represents the excitation spectrum, plot (B) is the emission spectrum (254nm), and plot (C) is the emission spectra (365nm).

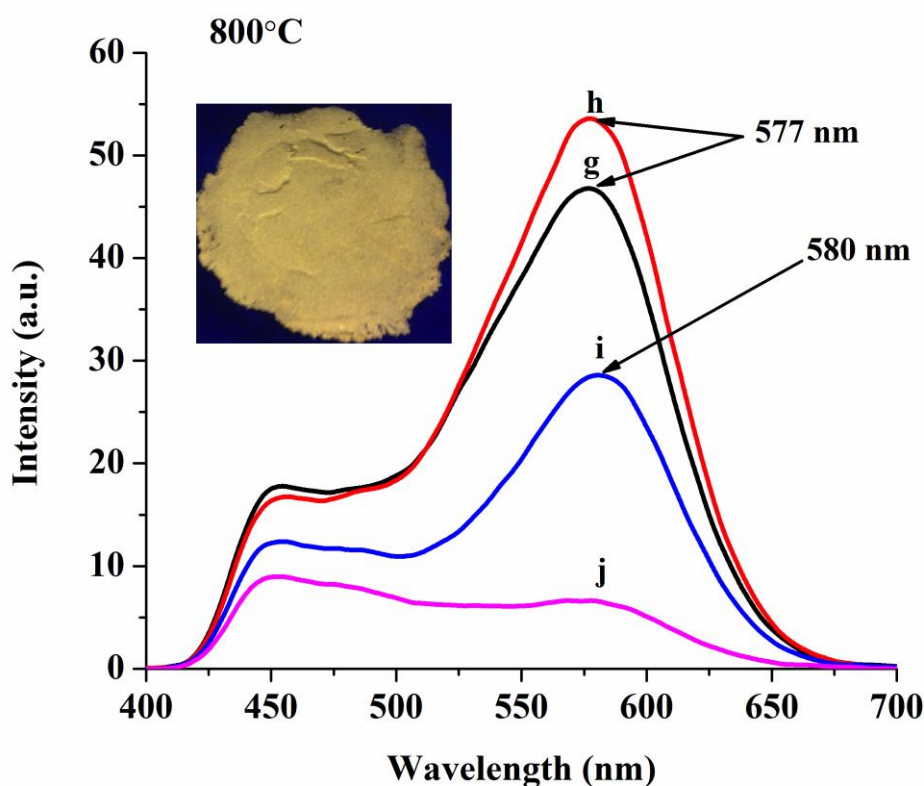


Figure 4.8C: Emission and excitation spectra of $\text{Sr}_{2.4}\text{Ba}_{0.6}\text{Al}_x\text{Ga}_{1-y-z}\text{In}_z\text{O}_4\text{F}$, where a) $\text{Sr}_{2.4}\text{Ba}_{0.6}\text{Al}_{0.10}\text{Ga}_{0.875}\text{In}_{0.025}\text{O}_4\text{F}$ b) $\text{Sr}_{2.4}\text{Ba}_{0.6}\text{Al}_{0.10}\text{Ga}_{0.85}\text{In}_{0.05}\text{O}_4\text{F}$, c) $\text{Sr}_{2.4}\text{Ba}_{0.6}\text{Al}_{0.10}\text{Ga}_{0.825}\text{In}_{0.075}\text{O}_4\text{F}$, d) $\text{Sr}_{2.4}\text{Ba}_{0.6}\text{Al}_{0.20}\text{Ga}_{0.775}\text{In}_{0.025}\text{O}_4\text{F}$, e) $\text{Sr}_{2.4}\text{Ba}_{0.6}\text{Al}_{0.20}\text{Ga}_{0.75}\text{In}_{0.05}\text{O}_4\text{F}$, and f) $\text{Sr}_{2.4}\text{Ba}_{0.6}\text{Al}_{0.20}\text{Ga}_{0.725}\text{In}_{0.075}\text{O}_4\text{F}$ at 1050°C . Other samples include g) $\text{Sr}_{2.4}\text{Ba}_{0.6}\text{Al}_{0.10}\text{Ga}_{0.875}\text{In}_{0.025}\text{O}_4\text{F}$, h) $\text{Sr}_{2.4}\text{Ba}_{0.6}\text{Al}_{0.10}\text{Ga}_{0.8625}\text{In}_{0.0375}\text{O}_4\text{F}$, i) $\text{Sr}_{2.4}\text{Ba}_{0.6}\text{Al}_{0.10}\text{Ga}_{0.8375}\text{In}_{0.0625}\text{O}_4\text{F}$ j) $\text{Sr}_{2.4}\text{Ba}_{0.6}\text{Al}_{0.10}\text{Ga}_{0.825}\text{In}_{0.075}\text{O}_4\text{F}$, k) $\text{Sr}_{2.4}\text{Ba}_{0.6}\text{Al}_{0.20}\text{Ga}_{0.775}\text{In}_{0.025}\text{O}_4\text{F}$, l) $\text{Sr}_{2.4}\text{Ba}_{0.6}\text{Al}_{0.20}\text{Ga}_{0.7625}\text{In}_{0.0375}\text{O}_4\text{F}$, m) $\text{Sr}_{2.4}\text{Ba}_{0.6}\text{Al}_{0.20}\text{Ga}_{0.7375}\text{In}_{0.0625}\text{O}_4\text{F}$, and n) $\text{Sr}_{2.4}\text{Ba}_{0.6}\text{Al}_{0.20}\text{Ga}_{0.725}\text{In}_{0.075}\text{O}_4\text{F}$ measured at 900°C and 800°C . Plot (A) represents the excitation spectrum, plot (B) is the emission spectrum (254nm), and plot (C) is the emission spectra (365nm).

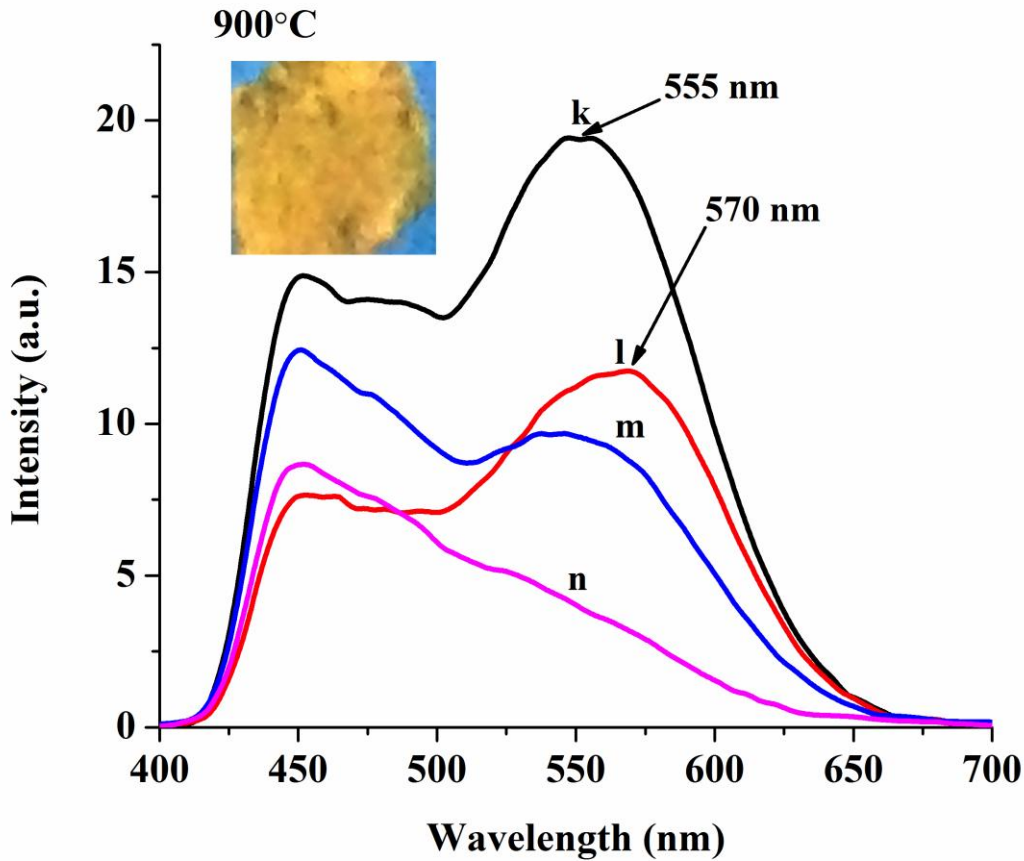


Figure 4.8C: Emission and excitation spectra of $\text{Sr}_{2.4}\text{Ba}_{0.6}\text{Al}_y\text{Ga}_{1-y-z}\text{In}_z\text{O}_4\text{F}$, where a) $\text{Sr}_{2.4}\text{Ba}_{0.6}\text{Al}_{0.10}\text{Ga}_{0.875}\text{In}_{0.025}\text{O}_4\text{F}$ b) $\text{Sr}_{2.4}\text{Ba}_{0.6}\text{Al}_{0.10}\text{Ga}_{0.85}\text{In}_{0.05}\text{O}_4\text{F}$, c) $\text{Sr}_{2.4}\text{Ba}_{0.6}\text{Al}_{0.10}\text{Ga}_{0.825}\text{In}_{0.075}\text{O}_4\text{F}$, d) $\text{Sr}_{2.4}\text{Ba}_{0.6}\text{Al}_{0.20}\text{Ga}_{0.775}\text{In}_{0.025}\text{O}_4\text{F}$, e) $\text{Sr}_{2.4}\text{Ba}_{0.6}\text{Al}_{0.20}\text{Ga}_{0.75}\text{In}_{0.05}\text{O}_4\text{F}$, and f) $\text{Sr}_{2.4}\text{Ba}_{0.6}\text{Al}_{0.20}\text{Ga}_{0.725}\text{In}_{0.075}\text{O}_4\text{F}$ at 1050°C . Other samples include g) $\text{Sr}_{2.4}\text{Ba}_{0.6}\text{Al}_{0.10}\text{Ga}_{0.875}\text{In}_{0.025}\text{O}_4\text{F}$, h) $\text{Sr}_{2.4}\text{Ba}_{0.6}\text{Al}_{0.10}\text{Ga}_{0.8625}\text{In}_{0.0375}\text{O}_4\text{F}$, i) $\text{Sr}_{2.4}\text{Ba}_{0.6}\text{Al}_{0.10}\text{Ga}_{0.8375}\text{In}_{0.0625}\text{O}_4\text{F}$ j) $\text{Sr}_{2.4}\text{Ba}_{0.6}\text{Al}_{0.10}\text{Ga}_{0.825}\text{In}_{0.075}\text{O}_4\text{F}$, k) $\text{Sr}_{2.4}\text{Ba}_{0.6}\text{Al}_{0.20}\text{Ga}_{0.775}\text{In}_{0.025}\text{O}_4\text{F}$, l) $\text{Sr}_{2.4}\text{Ba}_{0.6}\text{Al}_{0.20}\text{Ga}_{0.7625}\text{In}_{0.0375}\text{O}_4\text{F}$, m) $\text{Sr}_{2.4}\text{Ba}_{0.6}\text{Al}_{0.20}\text{Ga}_{0.7375}\text{In}_{0.0625}\text{O}_4\text{F}$, and n) $\text{Sr}_{2.4}\text{Ba}_{0.6}\text{Al}_{0.20}\text{Ga}_{0.725}\text{In}_{0.075}\text{O}_4\text{F}$ measured at 900°C and 800°C . Plot (A) represents the excitation spectrum, plot (B) is the emission spectrum (254nm), and plot (C) is the emission spectra (365nm).

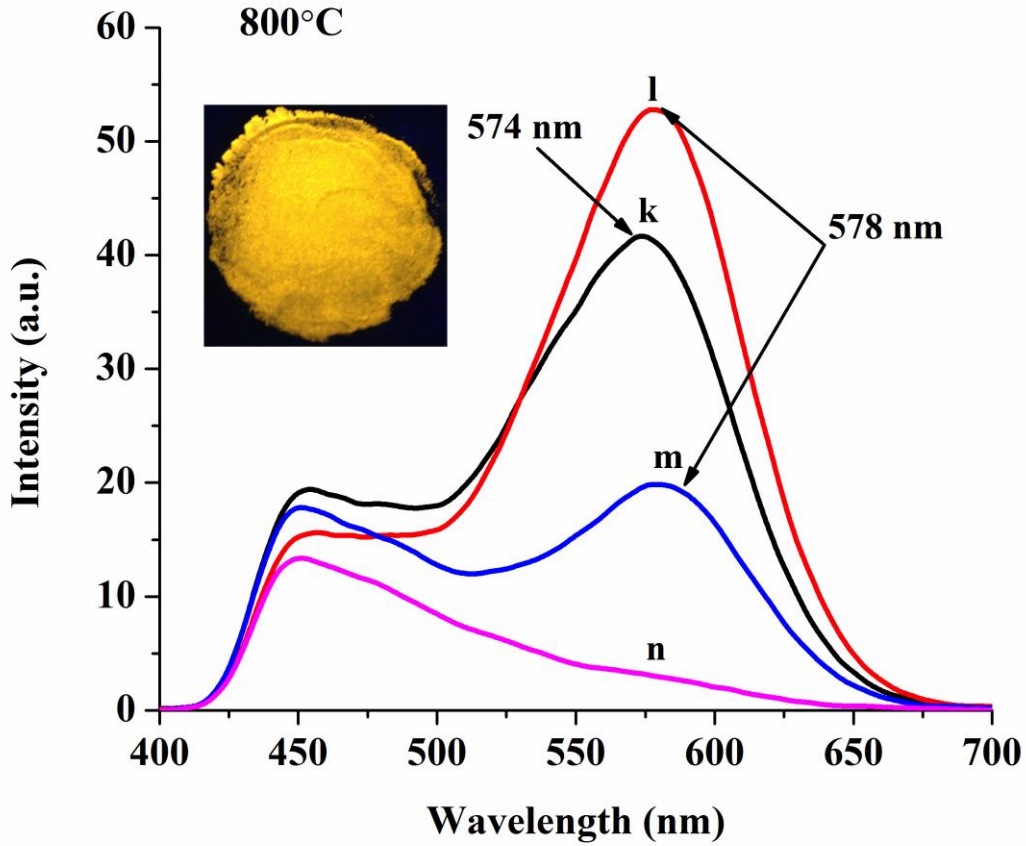


Figure 4.8C: Emission and excitation spectra of $\text{Sr}_{2.4}\text{Ba}_{0.6}\text{Al}_y\text{Ga}_{1-y-z}\text{In}_z\text{O}_4\text{F}$, where a) $\text{Sr}_{2.4}\text{Ba}_{0.6}\text{Al}_{0.10}\text{Ga}_{0.875}\text{In}_{0.025}\text{O}_4\text{F}$ b) $\text{Sr}_{2.4}\text{Ba}_{0.6}\text{Al}_{0.10}\text{Ga}_{0.85}\text{In}_{0.05}\text{O}_4\text{F}$, c) $\text{Sr}_{2.4}\text{Ba}_{0.6}\text{Al}_{0.10}\text{Ga}_{0.825}\text{In}_{0.075}\text{O}_4\text{F}$, d) $\text{Sr}_{2.4}\text{Ba}_{0.6}\text{Al}_{0.20}\text{Ga}_{0.775}\text{In}_{0.025}\text{O}_4\text{F}$, e) $\text{Sr}_{2.4}\text{Ba}_{0.6}\text{Al}_{0.20}\text{Ga}_{0.75}\text{In}_{0.05}\text{O}_4\text{F}$, and f) $\text{Sr}_{2.4}\text{Ba}_{0.6}\text{Al}_{0.20}\text{Ga}_{0.725}\text{In}_{0.075}\text{O}_4\text{F}$ at 1050°C . Other samples include g) $\text{Sr}_{2.4}\text{Ba}_{0.6}\text{Al}_{0.10}\text{Ga}_{0.875}\text{In}_{0.025}\text{O}_4\text{F}$, h) $\text{Sr}_{2.4}\text{Ba}_{0.6}\text{Al}_{0.10}\text{Ga}_{0.8625}\text{In}_{0.0375}\text{O}_4\text{F}$, i) $\text{Sr}_{2.4}\text{Ba}_{0.6}\text{Al}_{0.10}\text{Ga}_{0.8375}\text{In}_{0.0625}\text{O}_4\text{F}$ j) $\text{Sr}_{2.4}\text{Ba}_{0.6}\text{Al}_{0.10}\text{Ga}_{0.825}\text{In}_{0.075}\text{O}_4\text{F}$, k) $\text{Sr}_{2.4}\text{Ba}_{0.6}\text{Al}_{0.20}\text{Ga}_{0.775}\text{In}_{0.025}\text{O}_4\text{F}$, l) $\text{Sr}_{2.4}\text{Ba}_{0.6}\text{Al}_{0.20}\text{Ga}_{0.7625}\text{In}_{0.0375}\text{O}_4\text{F}$, m) $\text{Sr}_{2.4}\text{Ba}_{0.6}\text{Al}_{0.20}\text{Ga}_{0.7375}\text{In}_{0.0625}\text{O}_4\text{F}$, and n) $\text{Sr}_{2.4}\text{Ba}_{0.6}\text{Al}_{0.20}\text{Ga}_{0.725}\text{In}_{0.075}\text{O}_4\text{F}$ measured at 900°C and 800°C . Plot (A) represents the excitation spectrum, plot (B) is the emission spectrum (254nm), and plot (C) is the emission spectra (365nm).

The CIE chromaticity coordinates for the $\text{Sr}_{2.4}\text{Ba}_{0.6}\text{Al}_y\text{Ga}_{1-y-z}\text{In}_z\text{O}_4\text{F}$ materials under 254nm and 365nm excitation are given in Table 4 and are plotted in Figure 4.9. There is a clear shift in the chromaticity coordinates correlating to a red shift in the emission spectra for $\text{Sr}_{2.4}\text{Ba}_{0.6}\text{Al}_y\text{Ga}_{1-y-z}\text{In}_z\text{O}_4\text{F}$ materials when λ_{ex} changes from 254nm to 365nm. It is also evident that there is a gradual blue shift in these materials as the In^{3+} content is increased in the host structure, which correlates with the decreasing emission intensities. The yellow, orange-yellow, and green-yellow emission of $\text{Sr}_{2.4}\text{Ba}_{0.6}\text{Al}_y\text{Ga}_{1-y-z}\text{In}_z\text{O}_4\text{F}$ materials that arise from the varied reducing conditions combined with the $\text{In}_x\text{Ga}_{1-x}\text{N}$ emission near 370 nm could be used in a near UV-LED device. Modifying the reducing conditions in addition to making substitutions to the A(1) and M-sites in $\text{Sr}_{2.4}\text{Ba}_{0.6}\text{Al}_y\text{Ga}_{1-y-z}\text{In}_z\text{O}_4\text{F}$ materials are effective ways to tailor the photoluminescence emission. These rare-earth free phosphor materials might have the potential to decrease the costs of LED phosphors.

Table 4.4: CIE chromaticity coordinates for reduced $\text{Sr}_{2.4}\text{Ba}_{0.6}\text{Al}_y\text{Ga}_{1-y-z}\text{In}_z\text{O}_4\text{F}$ materials. Samples 1-6 are tempered in a 5% H_2 /95% Ar atmosphere at 1050°C. Samples 7-10 and 15-18 are tempered in a 5% H_2 /95% Ar atmosphere at 900°C. Samples 11-14 and 19-22 are tempered in a 5% H_2 /95% Ar atmosphere at 800°C.

		x (254nm)	y (254nm)	x (365nm)	y (365nm)	$\lambda_{\text{ex max}}$ (nm)
1	$\text{Sr}_{2.4}\text{Ba}_{0.6}\text{Al}_{0.10}\text{Ga}_{0.875}\text{In}_{0.025}\text{O}_4\text{F}$	0.3492	0.5581	0.3818	0.5629	370
2	$\text{Sr}_{2.4}\text{Ba}_{0.6}\text{Al}_{0.10}\text{Ga}_{0.85}\text{In}_{0.05}\text{O}_4\text{F}$	0.2833	0.4158	0.3482	0.4949	372
3	$\text{Sr}_{2.4}\text{Ba}_{0.6}\text{Al}_{0.10}\text{Ga}_{0.825}\text{In}_{0.075}\text{O}_4\text{F}$	0.2265	0.3039	0.2887	0.3955	375
4	$\text{Sr}_{2.4}\text{Ba}_{0.6}\text{Al}_{0.20}\text{Ga}_{0.775}\text{In}_{0.025}\text{O}_4\text{F}$	0.3492	0.5581	0.3818	0.5629	370
5	$\text{Sr}_{2.4}\text{Ba}_{0.6}\text{Al}_{0.20}\text{Ga}_{0.75}\text{In}_{0.05}\text{O}_4\text{F}$	0.2833	0.4158	0.3482	0.4949	370
6	$\text{Sr}_{2.4}\text{Ba}_{0.6}\text{Al}_{0.20}\text{Ga}_{0.725}\text{In}_{0.075}\text{O}_4\text{F}$	0.2265	0.3039	0.2887	0.3955	380
7	$\text{Sr}_{2.4}\text{Ba}_{0.6}\text{Al}_{0.10}\text{Ga}_{0.875}\text{In}_{0.025}\text{O}_4\text{F}$	0.2516	0.3762	0.3770	0.4336	374
8	$\text{Sr}_{2.4}\text{Ba}_{0.6}\text{Al}_{0.10}\text{Ga}_{0.8625}\text{In}_{0.0375}\text{O}_4\text{F}$	0.2665	0.3702	0.3763	0.4179	377
9	$\text{Sr}_{2.4}\text{Ba}_{0.6}\text{Al}_{0.10}\text{Ga}_{0.8375}\text{In}_{0.0625}\text{O}_4\text{F}$	0.2247	0.3224	0.3243	0.3667	374
10	$\text{Sr}_{2.4}\text{Ba}_{0.6}\text{Al}_{0.10}\text{Ga}_{0.825}\text{In}_{0.075}\text{O}_4\text{F}$	0.2059	0.2934	0.2005	0.2516	374
11	$\text{Sr}_{2.4}\text{Ba}_{0.6}\text{Al}_{0.10}\text{Ga}_{0.875}\text{In}_{0.025}\text{O}_4\text{F}$	0.2482	0.3734	0.3736	0.4356	374
12	$\text{Sr}_{2.4}\text{Ba}_{0.6}\text{Al}_{0.10}\text{Ga}_{0.8625}\text{In}_{0.0375}\text{O}_4\text{F}$	0.2696	0.3834	0.3889	0.4437	377
13	$\text{Sr}_{2.4}\text{Ba}_{0.6}\text{Al}_{0.10}\text{Ga}_{0.8375}\text{In}_{0.0625}\text{O}_4\text{F}$	0.2514	0.3563	0.3785	0.4109	374
14	$\text{Sr}_{2.4}\text{Ba}_{0.6}\text{Al}_{0.10}\text{Ga}_{0.825}\text{In}_{0.075}\text{O}_4\text{F}$	0.2288	0.3372	0.2801	0.3285	374
15	$\text{Sr}_{2.4}\text{Ba}_{0.6}\text{Al}_{0.20}\text{Ga}_{0.775}\text{In}_{0.025}\text{O}_4\text{F}$	0.2170	0.3405	0.2913	0.3933	365
16	$\text{Sr}_{2.4}\text{Ba}_{0.6}\text{Al}_{0.20}\text{Ga}_{0.7625}\text{In}_{0.0375}\text{O}_4\text{F}$	0.2443	0.3570	0.3238	0.4041	377
17	$\text{Sr}_{2.4}\text{Ba}_{0.6}\text{Al}_{0.20}\text{Ga}_{0.7375}\text{In}_{0.0625}\text{O}_4\text{F}$	0.2130	0.3158	0.2607	0.3329	377
18	$\text{Sr}_{2.4}\text{Ba}_{0.6}\text{Al}_{0.20}\text{Ga}_{0.725}\text{In}_{0.075}\text{O}_4\text{F}$	0.2064	0.3114	0.2110	0.2757	377
19	$\text{Sr}_{2.4}\text{Ba}_{0.6}\text{Al}_{0.20}\text{Ga}_{0.775}\text{In}_{0.025}\text{O}_4\text{F}$	0.2412	0.3568	0.3583	0.4232	374
20	$\text{Sr}_{2.4}\text{Ba}_{0.6}\text{Al}_{0.20}\text{Ga}_{0.7625}\text{In}_{0.0375}\text{O}_4\text{F}$	0.2673	0.3770	0.3976	0.4426	377
21	$\text{Sr}_{2.4}\text{Ba}_{0.6}\text{Al}_{0.20}\text{Ga}_{0.7375}\text{In}_{0.0625}\text{O}_4\text{F}$	0.2194	0.3271	0.3247	0.3525	373
22	$\text{Sr}_{2.4}\text{Ba}_{0.6}\text{Al}_{0.20}\text{Ga}_{0.725}\text{In}_{0.075}\text{O}_4\text{F}$	0.2092	0.3162	0.2004	0.2389	373

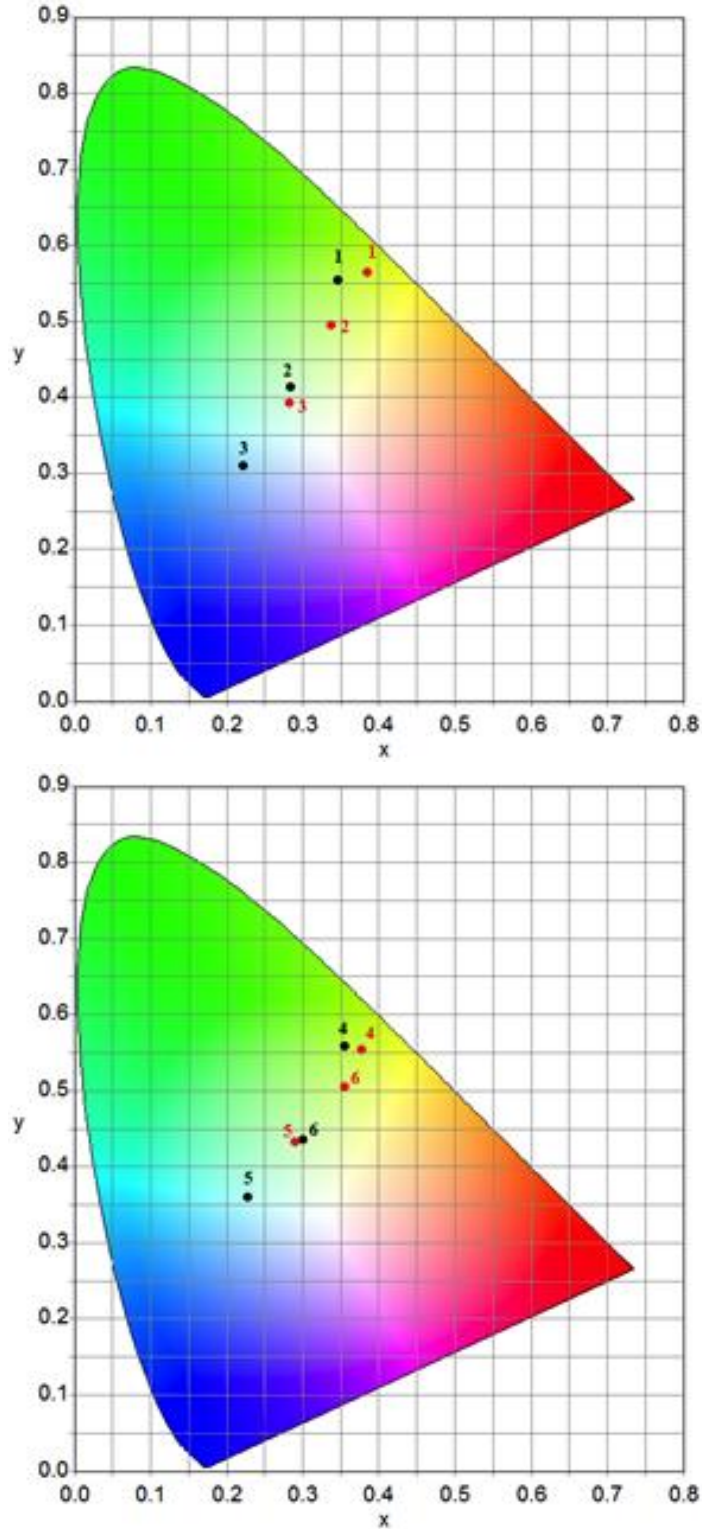


Figure 4.9: CIE chromaticity diagram for $\text{Sr}_{2.4}\text{Ba}_{0.6}\text{Al}_y\text{Ga}_{1-y-z}\text{In}_z\text{O}_4\text{F}$ materials. The arrows indicate shifts in CIE coordinates from 254nm (black dots) to 365nm excitation (red dots)

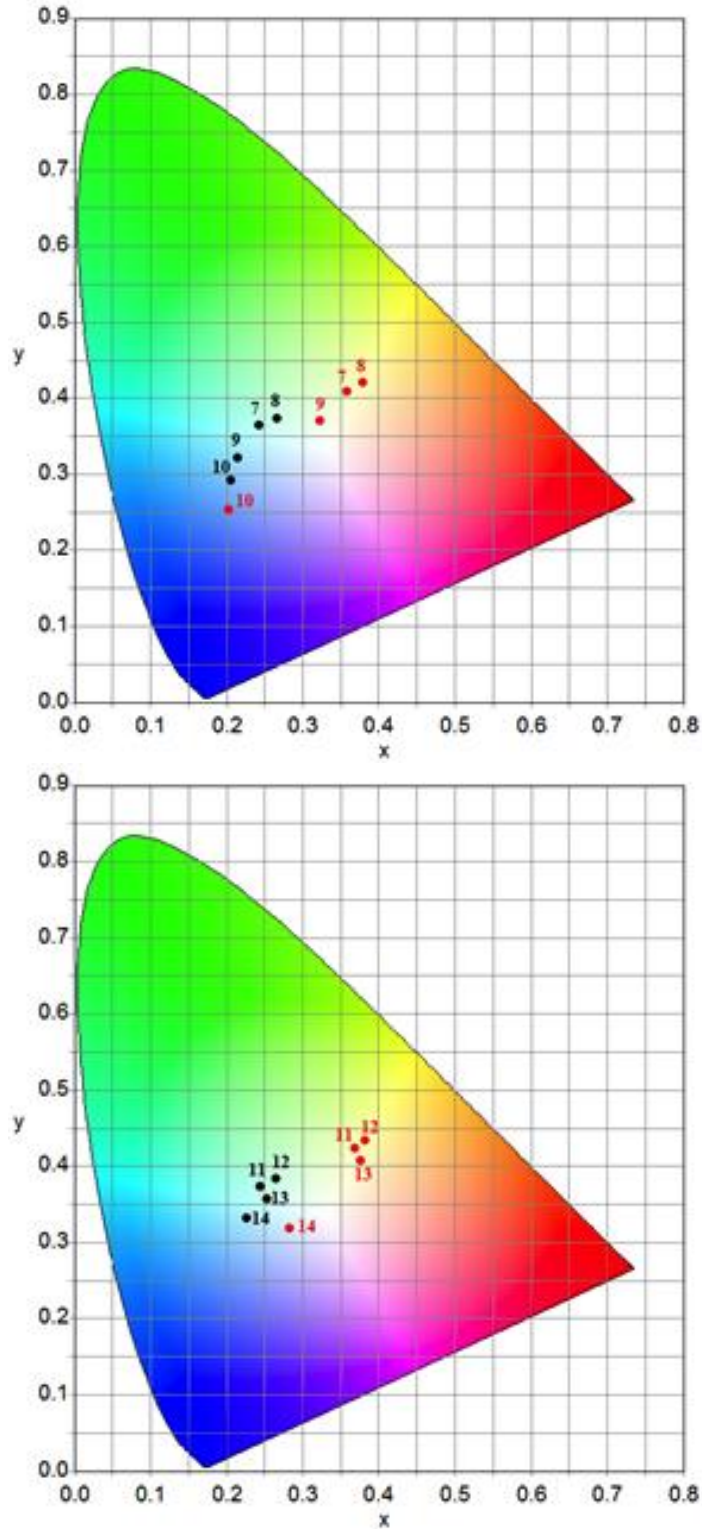


Figure 4.9 (cont'd): CIE chromaticity diagram for $\text{Sr}_{2.4}\text{Ba}_{0.6}\text{Al}_y\text{Ga}_{1-y-z}\text{In}_z\text{O}_4\text{F}$ materials. The arrows indicate shifts in CIE coordinates from 254nm (black dots) to 365nm excitation (red dots)

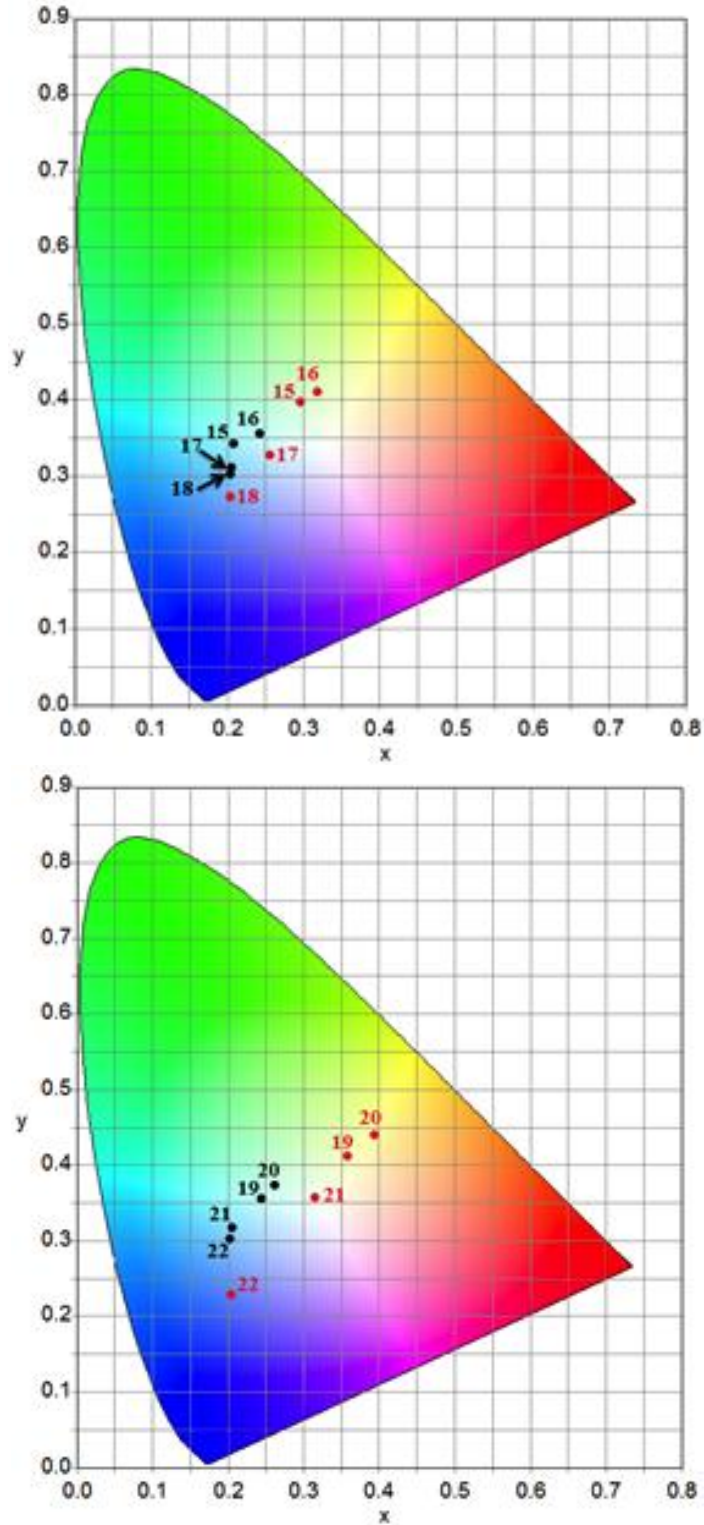


Figure 4.9 (cont'd): CIE chromaticity diagram for $\text{Sr}_{2.4}\text{Ba}_{0.6}\text{Al}_y\text{Ga}_{1-y-z}\text{In}_z\text{O}_4\text{F}$ materials. The arrows indicate shifts in CIE coordinates from 254nm (black dots) to 365nm excitation (red dots)

Conclusions

We have shown that the photoluminescence of single phase $\text{Sr}_{3-x}\text{Ba}_x\text{Al}_y\text{Ga}_{1-y}\text{O}_4\text{F}$ materials can be tailored via substitutions on both the A(1) and M sites. The 254nm excitation wavelength allows for these materials to have potential use as phosphors in CFL bulbs. Furthermore, these materials require lower Ba^{2+} substitution to exhibit substantial photoluminescence intensity, which may potentially reduce thermal quenching in these materials at higher temperatures.

Novel $\text{Sr}_{2.4}\text{Ba}_{0.6}\text{Al}_y\text{Ga}_{1-y-z}\text{In}_z\text{O}_4\text{F}$ materials might have potential use as phosphors for LED lights, since where the incorporation of In^{3+} and tempering in a reducing atmosphere causes the λ_{max} in the excitation spectrum to shift near 375nm. We have shown that the photoluminescence of $\text{Sr}_{2.4}\text{Ba}_{0.6}\text{Al}_y\text{Ga}_{1-y-z}\text{In}_z\text{O}_4\text{F}$ materials can be tailored by varying the temperature of the post-synthesis reduction step. When the temperature of the reducing step is 800°C or 900°C and $\lambda_{\text{ex}} = 254\text{nm}$, the emission spectra in these materials do not show a significant change from the air annealed materials. As the temperature of the reducing step increases to 1050°C, a dramatic shift of the λ_{max} occurs. This corresponds to a strongly green-yellow emitting material. Under 365 nm excitation, these $\text{Sr}_{2.4}\text{Ba}_{0.6}\text{Al}_y\text{Ga}_{1-y-z}\text{In}_z\text{O}_4\text{F}$ materials appear yellow to yellow-orange when the temperature of the reducing step is 800°C and 900°C. As the temperature of the reducing step increases to 1050°C, the color of $\text{Sr}_{2.4}\text{Ba}_{0.6}\text{Al}_y\text{Ga}_{1-y-z}\text{In}_z\text{O}_4\text{F}$ materials changes from orange-yellow to green-yellow.

This study shows that by making the appropriate substitutions and reducing conditions in both $\text{Sr}_{3-x}\text{Ba}_x\text{Al}_y\text{Ga}_{1-y}\text{O}_4\text{F}$ and $\text{Sr}_{2.4}\text{Ba}_{0.6}\text{Al}_y\text{Ga}_{1-y-z}\text{In}_z\text{O}_4\text{F}$ materials, potential

rare-earth free phosphor materials for both CFL and LED lighting applications can be made.

References

- (1) Park, S.; Vogt, T. *Journal of Luminescence* **2009**, *129*, 952-957.
- (2) Im, W. B.; Brinkley, S.; Hu, J.; Mikhailovsky, A.; DenBaars, S. P.; Seshadri, R. *Chemistry of Materials* **2010**, *22*, 2842-2849.
- (3) Setlur, A. A.; Radkov, E. V.; Henderson, C. S.; Her, J.-H.; Srivastava, A. M.; Karkada, N.; Kishore, M. S.; Kumar, N. P.; Aesram, D.; Deshpande, A. *Chemistry of Materials* **2010**, *22*, 4076-4082.
- (4) Fang, Y.; Li, Y. Q.; Qiu, T.; Delsing, A. C. A.; Hintzen, H. T. *Journal of Alloys and Compounds* **2010**, *496*, 614-619.
- (5) Shang, M.; Li, G.; Kang, X.; Yang, D.; Geng, D.; Lin, J. *ACS applied materials & interfaces* **2011**, *3*, 2738-2746.
- (6) Chen, W. *Journal of Alloys and Compounds* **2013**, *550*, 320-325.
- (7) Park, S.; Vogt, T. *Journal of Physical Chemistry C* **2010**, *114*, 11576-11583.
- (8) Green, R.; Vogt, T. *Journal of Solid State Chemistry* **2012**, *194*, 375-384.
- (9) Prodjosantoso, A. K.; Kennedy, B. J.; Vogt, T.; Woodward, P. M. *Journal of Solid State Chemistry* **2003**, *172*, 89-94.
- (10) Sullivan, E.; Avdeev, M.; Vogt, T. *Journal of Solid State Chemistry* **2012**, *194*, 297-306.
- (11) Sullivan, E.; Vogt, T. *ECS Journal of Solid State Science and Technology* **2013**, *2*, R3088-R3099.
- (12) Park, S. *Journal of Solid State Chemistry* **2012**, *186*, 204-207.
- (13) Park, S. *Optical Materials* **2013**, *35*, 516-519.
- (14) Larson, A. C.; Von Dreele, R. B. *General Structure Analysis System*. Los Alamos National Laboratory Report LAUR 860-748 (2000)

- (15) Vogt, T.; Woodward, P. M.; Hunter, B. A.; Prodjosantoso, A. K.; Kennedy, B. J. *Journal of Solid State Chemistry* **1999**, *144*, 228-231.
- (16) Woodward, P. M. *Acta Crystallographica Section B* **1997**, *53*, 32-43.
- (17) Woodward, P. M. *Acta Crystallographica Section B* **1997**, *53*, 44-66.
- (18) Farvid, S. S.; Wang, T.; Radovanovic, P. V. *Journal of the American Chemical Society* **2011**, *133*, 6711-6719.
- (19) Shionoya, S.; Yen, W. M.; Yamamoto, H. *Phosphor Handbook*; CRC Press: 2006; pp 1080.

CHAPTER 5

SYNTHESIS AND CHARACTERIZATION OF STRUCTURAL AND PHOTOLUMINESCENT PROPERTIES OF $\text{Sr}_{2.98-x/2}\text{Na}_{0.01}\text{Ce}_{0.01}\text{Ga}_{1-x}\text{M}_x\text{O}_4\text{F}$ MATERIALS

Introduction

The self-activating photoluminescent properties of $\text{Sr}_3\text{MO}_4\text{F}$ host materials that are investigated in Chapters 2, 3, and 4, where the excitation wavelengths are near 254nm or 365nm, have potential use as phosphors for compact fluorescent lamps (CFLs) and near UV-LEDs. There are environmental implications associated with the use of CFLs due to the presence of small amounts of mercury vapor required for its 254nm emission of UV light when excited in an electrical field. This 254 nm excitation causes down-conversion in phosphors. One way for $\text{Sr}_3\text{MO}_4\text{F}$ -type phosphors to be suitable LED phosphors is to incorporate Ce^{3+} into the structure. Currently, the most commonly used material in LED lights is Ce^{3+} -doped yttrium aluminum garnet ($\text{Y}_3\text{Al}_5\text{O}_{12}:\text{Ce}^{3+}$), where the excitation energy generated by a blue emitting $\text{In}_{1-x}\text{Ga}_x\text{N}$ LED ($\lambda = 450\text{nm}$) is efficiently down-converted by Ce^{3+} . The emission of $\text{In}_{1-x}\text{Ga}_x\text{N}$ is tunable between 370 and 450 nm when $0.0 \leq x \leq 0.3$. Therefore, the excitation wavelengths of Ce^{3+} containing host materials need to be in this range (which correlates to the blue emitting regions). The absorption of blue light excites allowed $4f^1-5d^1$ electronic transitions in Ce^{3+}

activators and subsequent light emissions in the yellow range of the spectrum occur due to $5d^1-4f^1$ transitions are observed. The $4f^1$ ground states are split due to spin-orbit coupling and lead to a broad-band emission³. As mentioned in Chapter 1, the combination of light from blue emitting semiconductors and yellow emitting phosphor materials in LED lighting assemblies yields cold white light.

Two disadvantages of $Y_3Al_5O_{12}: Ce^{3+}$ are the decrease in the color rendering index (CRI) at elevated temperatures due to the lack of a red spectral component⁴ and thermal quenching⁵. In order to compensate for the lack of the red component, Gd^{3+} , Eu^{3+} or a combination of Mg^{2+} and Si^{4+} substitutions are made to cause a red-shift of the photoluminescence emission of $Y_3Al_5O_{12}: Ce^{3+}$ as well as other types of phosphor materials (Ronda, Yen). In $Y_3Al_5O_{12}: Ce^{3+}$ thermal quenching remains an issue that needs to be addressed. The configurational coordinate diagram in Chapter 1 illustrates that non-radiative emission mechanism occur when there is thermal population of vibrational states in the excited state parabola. A way to reduce thermal quenching in LED phosphors is the use of oxyfluoride materials, where additional fluoride ions with lower phonon energies are present. These lower phonon energies reduce the amount of lattice vibrations due to the increasing bond strength provided by fluorine, which has higher electronegativity than oxygen. This increase in bond strength reduces the amount of lattice vibrations and subsequent heat generated by oscillating atoms.

It was reported by Im *et al.* that the lower thermal quenching behavior of the RE^{3+} doped oxyfluoride $Sr_{2.975-x}Ba_xCe_{0.025}AlO_4F$ resulted in a higher PL intensity than observed in $Y_3Al_5O_{12}:Ce^{3+}$ phosphors at temperatures above $170^\circ C$ ⁶. Ma *et al.* also concluded that the Sr_3AlO_4F lattice reveals less thermal quenching than Sr_3SiO_5 when

substituted with similar concentrations of Ce^{3+} ⁷, which is significant due to their structural similarity. Setlur and collaborators have also used this ordered oxyfluoride structure to synthesize the yellow-green emitting phosphor $(\text{Sr,Ca})_3(\text{Al,Si})\text{O}_4(\text{O,F})\text{:Ce}^{3+}$. When combined with $\text{K}_2\text{TiF}_6\text{:Mn}^{4+}$, a red emitting phosphor, a competitive phosphor mixture can be made that rivals the aforementioned $\text{Y}_3\text{Al}_5\text{O}_{12}\text{:Ce}^{3+}$, but more importantly meets the efficacy and color quality goals/standards ⁸.

Recent work on this family of ordered oxyfluorides by Shang *et al.* focuses on the tunable luminescence and energy transfer properties of the Al analogue doped with the rare-earth ions Tm^{3+} , Eu^{3+} , Tb^{3+} and Ce^{3+} ⁹. Chen *et al.* studied the photoluminescence and cathodoluminescence (low-voltage electron beam excitation) of Ce^{3+} -doped $\text{Sr}_3\text{GaO}_4\text{F}$ at liquid helium temperature while increasing the concentration of Ce^{3+} in the host ¹⁰. In this study it was found that Ce^{3+} ions substitute into both the Sr(1) and Sr(2) sites. At 405nm excitation the photoluminescence emission red-shifts with increasing Ce^{3+} concentration. The emission stemming from cathodoluminescence (250 μA and 4 kV excitation) reveals a shift from a bluish-green to green-yellow emission with increased Ce^{3+} doping.

Recently, Im *et al.* examined the phosphor $\text{Sr}_{2.975}\text{Ce}_{0.025}\text{Al}_{1-x}\text{Si}_x\text{O}_{4+x}\text{F}_{1-x}$ using solid-state ^{19}F NMR, and showed that F^- resides in a single crystallographic site in this structure. The photoluminescence (PL) data of this phosphor (emission and excitation) for $x = 0.0, 0.1, 0.3, 0.5, 0.7, 0.9$, and 1.0 and a commercial $\text{Y}_3\text{Al}_5\text{O}_{12}\text{:Ce}^{3+}$ ($\text{Y}_3\text{Al}_5\text{O}_{12}\text{:Ce}^{3+}$) sample were compared using excitation wavelengths of 390, 400, 430, and 450 nm respectively ¹¹. Excitation at these wavelengths resulted in characteristic green emissions arising from electronic transitions of Ce^{3+} from its 5d ($^2\text{D}_{3/2}$, $^2\text{D}_{5/2}$) excited states to the 4f

($^2F_{5/2}$, $^2F_{7/2}$) ground state. With increasing Si^{4+} content, the emission peak positions gradually move towards longer wavelengths, from 474 nm for $Sr_3AlO_4F:Ce^{3+}$ ($x = 0$) to 537 nm for $Sr_3SiO_5:Ce^{3+}$ ($x = 1.0$) revealing that the emissions of these phosphors are tunable. The quantum efficiency at room temperature of $Sr_{2.975}Ce_{0.025}Al_{1-x}Si_xO_{4+x}F_{1-x}$ was 83% when $x = 0.0$ phosphor material. $Sr_{2.975}Ce_{0.025}Al_{0.5}Si_{0.5}O_{4.5}F_{0.5}$ ($x = 0.5$) had the highest PL intensity ($\lambda_{ex} = 430$ or 450 nm) and the highest quantum efficiency (85%) of all $Sr_{2.975}Ce_{0.025}Al_{1-x}Si_xO_{4+x}F_{1-x}$ materials¹¹. Both materials exhibit efficiencies close to that of commercial $Y_3Al_5O_{12}:Ce^{3+}$, which was determined to be 81%. A similar study by Denault *et al.* exploring the substitution of Si^{4+} in $Sr_2Ba(AlO_4F)_{1-x}(SiO_5)_x:Ce^{3+}$ also shows the tunability of these phosphors, using Sr_3AlO_4F and Sr_3SiO_5 as the end members¹². Lee *et al.*, using a similar series of $(Sr_3SiO_5)_{1-x}(Sr_3AlO_4F)_x:Ce^{3+}, Li^+, Tb^{3+}$ phosphor materials, focus on the energy transfer mechanism between Ce^{3+} and Tb^{3+} ¹³ which is based on an electric dipole-quadrupole interaction. The thermal stability of $(Sr_3SiO_5)_{1-x}(Sr_3AlO_4F)_x:Ce^{3+}, Li^+, Tb^{3+}$ also rivals commercial phosphors.

The Sr_3AlO_4F structure adopts the $I4/mcm$ space group and is closely related to the Sr_3SiO_5 structure, which has a $P4/ncc$ space group. The lattice parameters for the Sr_3SiO_5 structure are $a = 6.734\text{\AA}$ and $c = 10.72\text{\AA}$ ^{14 15}. The Sr_3SiO_5 structure studied by Glasser *et al.*¹⁴ has Si atoms at the corners of the unit cell, which are 4-coordinated by O forming SiO_4 tetrahedra. OSr_6 octahedra are also present in Sr_3SiO_5 and exhibits tilting similar to the FSr_6 octahedra described previously in Sr_3AlO_4F . One major difference between the two structures is the arrangement of the MO_4 tetrahedra. The AlO_4 tetrahedra in Sr_3AlO_4F have upper and lower edges parallel to the face diagonal of the

(001) plane, while the SiO_4 tetrahedra are staggered/tilted in alternating layers, which result in a lower symmetry¹¹⁻¹³.

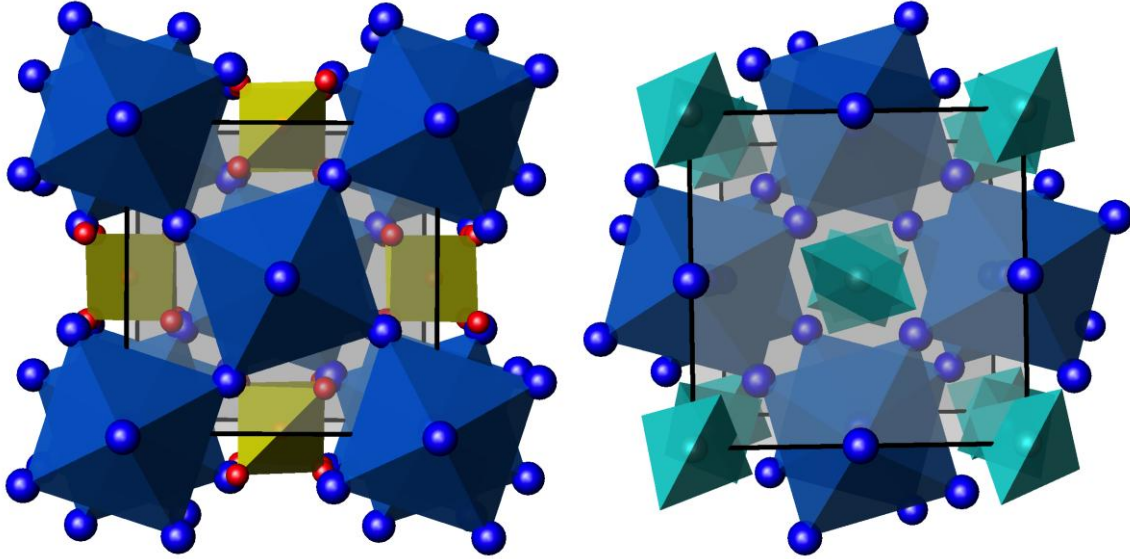


Figure 5.1: Structure of $\text{Sr}_3\text{MO}_4\text{F}$ (left) and Sr_3SiO_5 (right) viewed along the 001 axis. The blue spheres represent Sr, while the red spheres represent O. The yellow and teal octahedral represent AlO_4 and SiO_4 , respectively.

This chapter investigates the aliovalent substitution of Si^{4+} , and Ge^{4+} for Ga^{3+} in the $\text{Sr}_{2.98-x/2}\text{Na}_{0.01}\text{Ce}_{0.01}\text{Ga}_{1-x}\text{M}_x\text{O}_4\text{F}$ framework. This substitution of the GaO_4^{5-} tetrahedra could provide phosphor materials for LED lighting assemblies as well as other applications. I will focus on the changes in structural properties and photoluminescence properties stemming from the substitution at this site. Changes in the photoluminescence emission as a result of varying during synthesis temperatures in the reducing step will also be studied.

Experimental

The $\text{Sr}_{2.98-x/2}\text{Na}_{0.01}\text{Ce}_{0.01}\text{Ga}_{1-x}\text{M}_x\text{O}_4\text{F}$ materials, where M denotes $\text{Si}^{4+}/\text{Ge}^{4+}$ substitution, and $x = 0.05, 0.10, 0.15, 0.20$ are synthesized using the standard solid-state

method by thoroughly mixing the appropriate stoichiometric amounts of SrCO₃ (Aldrich 99.995%), Al₂O₃ (Aldrich 99.95%), SrF₂ (Aldrich 99.995%), CeO₂ (Aldrich 99.95%), Na₂CO₃ (Alfa-Aesar 99.5%), SiO₂ (Aldrich 99.5%), and GeO₂ (Aldrich 99%) using an agate mortar and pestle. The starting materials were heated for 24 hours at 700°C, 800°C, 900°C, and 1100°C in air at a ramp rate of 3 deg/min. To observe photoluminescence, the samples were reduced in a 5% H₂/95% Ar atmosphere for 3 hours at 800°C, 900°C, and 1050°C.

X-ray diffraction data was collected using a Rigaku MiniFlexTM diffractometer producing Cu-K α radiation ($\lambda = 1.54059 \text{ \AA}$) over the range $3^\circ \leq 2\theta \leq 120^\circ$ at 0.02 degrees intervals and a rate of 0.25 (deg/min). The unit cell parameters were refined using the Rietveld method within the least squares refinement program GSAS¹⁶.

Photoluminescence measurements were performed using the LS55 fluorescence spectrometer by Perkin-Elmer equipped with a fiber optic cable and a sample holder and xenon lamp source.

Results and Discussion

In order to determine the appropriate level of charge compensated substitution of Sr²⁺ by Na⁺ and Ce³⁺ in the Sr₃GaO₄F host lattice, 1.0, 1.5, 2.0, and 2.5 molar% of Na⁺ and Ce³⁺ was substituted into the host lattice and the materials was subsequently exposed to a reducing atmosphere for photoluminescence to occur. The powder x-ray diffraction data shown in Figure 5.2 did not reveal any second phase present in these samples. The results of the PL data shown in Figure 5.3 reveal that both the 1.0 and 1.5 molar % substituted Ce³⁺ samples yielded the highest photoluminescence intensities. As the Ce³⁺

concentration increases to 2.0 and 2.5 molar%, the photoluminescence intensities decrease due to concentration quenching. This trend is also seen by Choi and Park¹⁷ and Setlur in Ce³⁺-substituted Sr₃AlO₄F¹⁸. Setlur determined that at low levels of Ce³⁺ substitution, Sr₃AlO₄F experiences minor thermal quenching when T ≈ 200°C. Thermal quenching in these materials were significantly increased when the Ce³⁺ content increases as well as when F⁻ is substituted by O²⁻ ions at the center of the FSr₆ octahedra (Wychoff site 4c), and the photoluminescence emission is also red-shifted¹⁸ as a consequence. Since it is advantageous to have phosphor materials with small amounts of substituted rare-earth ions, the Ce³⁺ concentration used in this chapter will be 1.0 molar %.

The amount of Ce³⁺ needed to produce significant photoluminescence intensities in Sr₃AlO₄F can be controlled based on the isovalent substitution of Ca²⁺ and Ba²⁺. The substitution of Sr²⁺ by Ca²⁺ causes the volume of the Sr₃AlO₄F host structure to decrease, which subsequently leads to concentration quenching of Ce³⁺ to occur at lower substitution levels. Conversely, the substitution of Sr²⁺ by Ba²⁺ causes the expansion of the Sr₃AlO₄F host lattice, and therefore causes the concentration quenching of Ce³⁺ to occur at higher concentrations¹⁷. Sullivan *et al.* studied the structural distortions of charge and non-charge compensated Sr₃AlO₄F and found that there are only minute changes in the lattice parameters of Sr_{2.95}Na_{0.025}Ce_{0.025}AlO₄F and Sr_{2.975}Ce_{0.025}AlO₄F, where the substitution of Na⁺ is used for charge compensation¹⁹. Chen studied the effect that the substitution of other alkali metal ions (Li⁺, K⁺, and Cs⁺) have in Sr_{2.96}Ce_{0.03}M_{0.03}AlO₄F, and found that the emission and excitation showed little or no change²⁰. Kelsey and Brown reported increased photoluminescence intensity with charge compensation²¹ in Ba_{1-x}Sr_xSiO₃ and Ba_{1-x}Sr_xSiO₄ materials co-doped with Ce³⁺ and Li⁺.

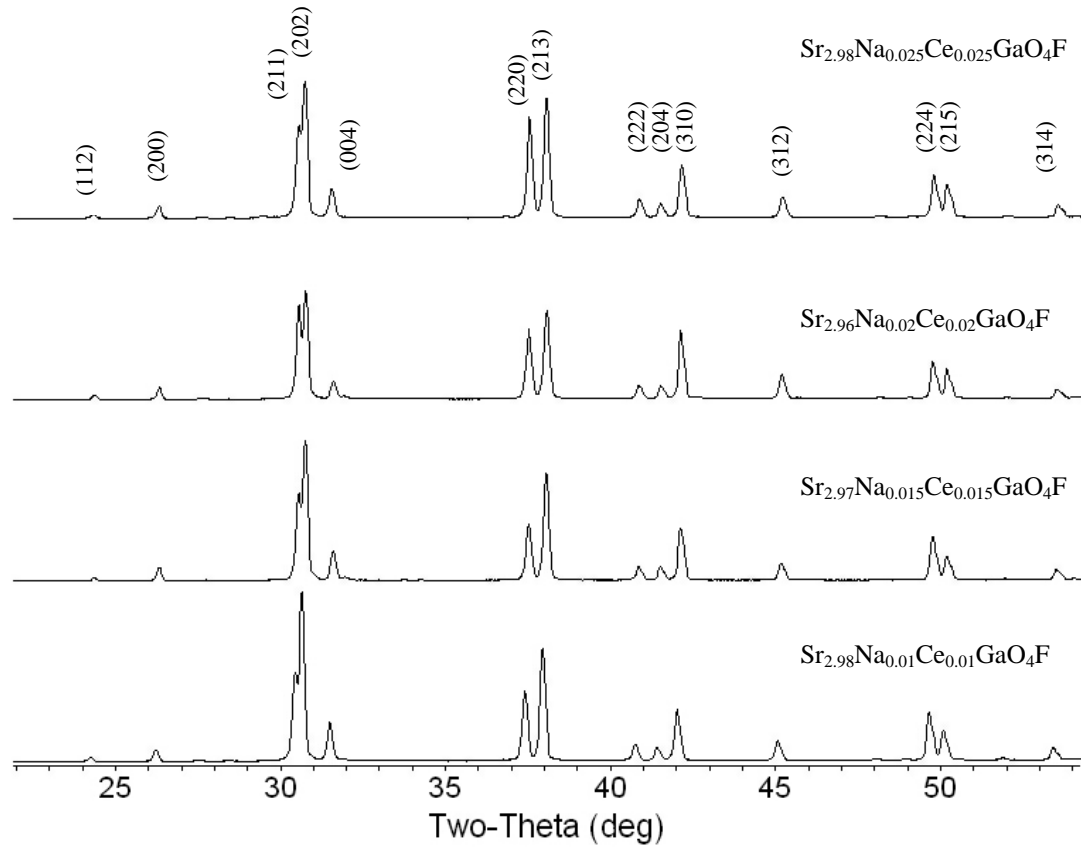


Figure 5.2: X-ray diffraction patterns of $\text{Sr}_{3-2x}\text{Na}_x\text{Ce}_x\text{GaO}_4\text{F}$, where $x = 0.01, 0.015, 0.02,$ and 0.025

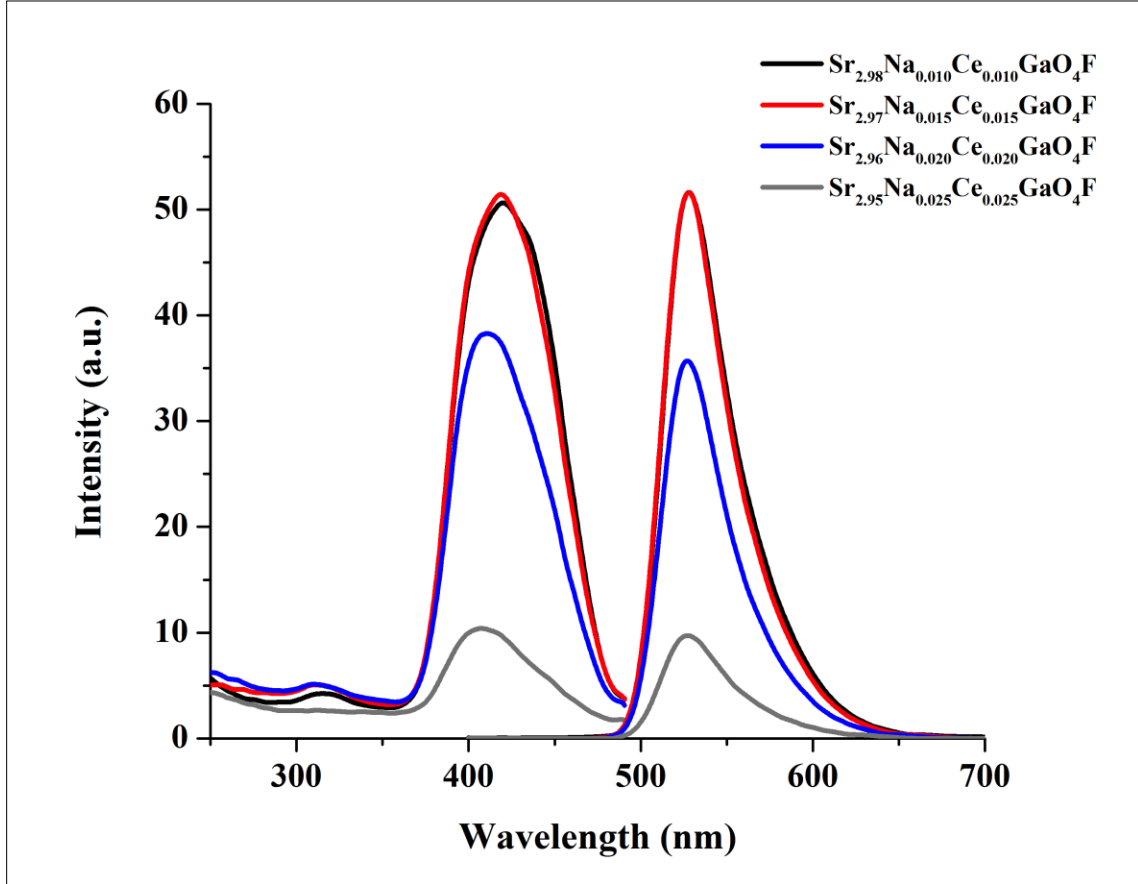


Figure 5.3: Photoluminescence emission and excitation spectra of $\text{Sr}_{3-2x}\text{Na}_x\text{Ce}_x\text{GaO}_4\text{F}$, where $x = 0.01, 0.015, 0.02, \text{ and } 0.025$.

The powder diffraction patterns of Si^{4+} and Ge^{4+} substituted $\text{Sr}_{2.98}\text{Na}_{0.01}\text{Ce}_{0.01}\text{GaO}_4\text{F}$ phosphors are shown in Figures 5.4 and 5.5 and their structures are refined based on the $\text{Sr}_3\text{GaO}_4\text{F}$ structure (space group $I4/mcm$; no 140)²². The diffraction patterns do not reveal any impurities for either the Si^{4+} or Ge^{4+} substituted materials. There is a systematic shifting to higher 2θ angles for many peaks in the diffraction pattern, indicating a decrease in the lattice parameters for either Si^{4+} or Ge^{4+} substitution. This is due to the smaller ionic radii of Si^{4+} and Ge^{4+} compared to the Ga^{3+} ion, which are 0.26\AA , 0.39\AA and 0.47\AA , respectively²³. Closer inspection of the

diffraction pattern indicates that, furthermore, there are structural distortions within the lattice.

Substitutions of Ga^{3+} by Si^{4+} and Ge^{4+} were also made in $\text{Sr}_{2.98-x/2}\text{Na}_{0.01}\text{Ce}_{0.01}\text{Ga}_{1-x}\text{Si}_x\text{O}_4\text{F}$, where $x = 0.25$ and 0.30 , however these samples cannot be refined to a satisfactory degree using the $I4/mcm$ space group with data from a standard laboratory x-ray diffractometer. Setlur *et al.* and Denault *et al.* address this difficulty of the refinement and use both synchrotron or neutron diffraction since these methods provide higher resolution data to help determine the space group of these materials. Setlur *et al.* does provide specific information regarding the structure of $\text{Sr}_{1.7775}\text{Ca}_{1.2}\text{Ce}_{0.0225}\text{Al}_{0.6}\text{Si}_{0.4}\text{O}_{4.4225}\text{F}_{0.5775}$, in which synchrotron data is refined using the higher symmetry $I4/mcm$ space group instead of the $P4/ncc$ space group. Denault *et al.* and Lee *et al.* both describe a change of the $I4/mcm$ space group with increased Si^{4+} substitution in $\text{Sr}_3\text{AlO}_4\text{F}$ -type materials to $P4/ncc$, which is found in Sr_3SiO_5 -type structures.

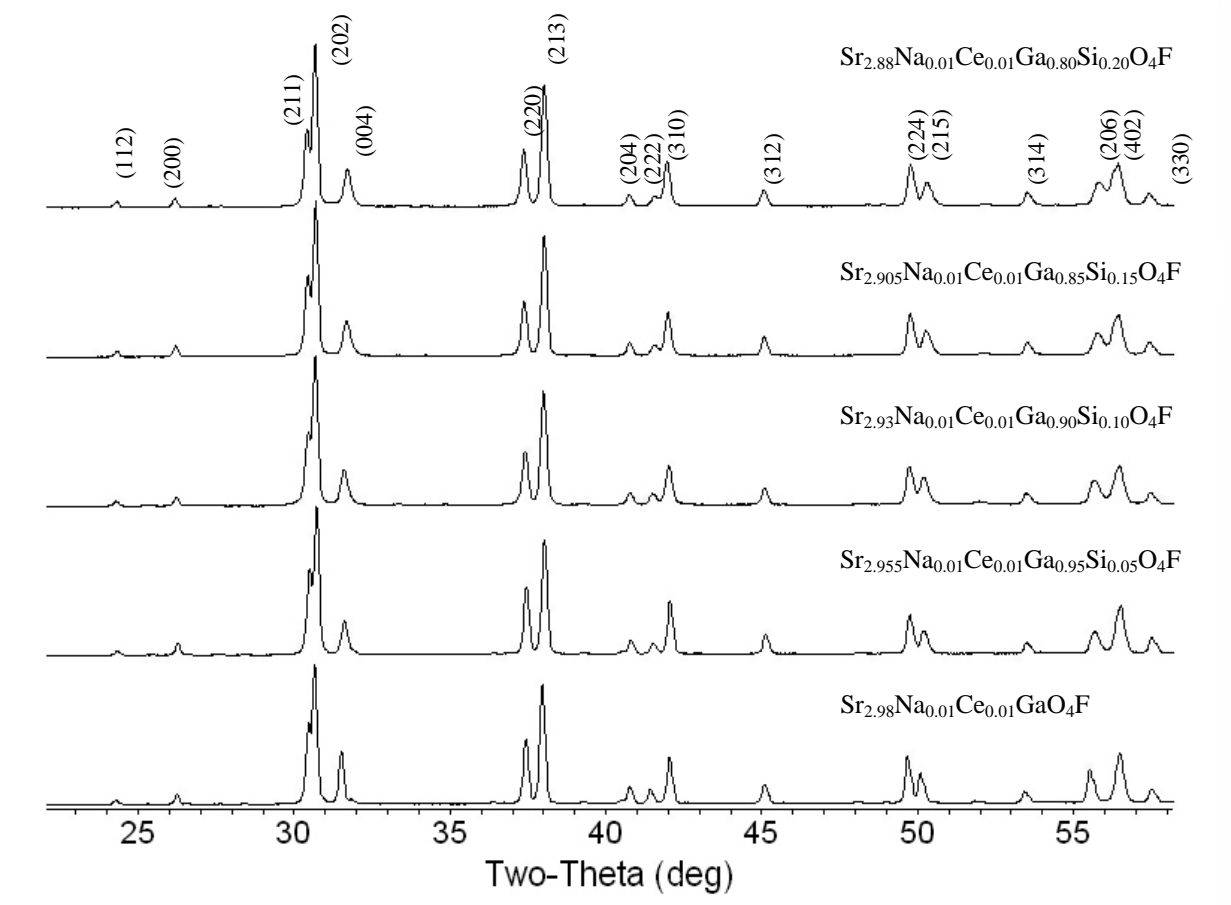


Figure 5.4: XRD patterns of Ge substituted $\text{Sr}_{2.98-x/2}\text{Na}_{0.01}\text{Ce}_{0.01}\text{Ga}_{1-x}\text{Si}_x\text{O}_4\text{F}$, where $0 \leq x \leq 0.20$

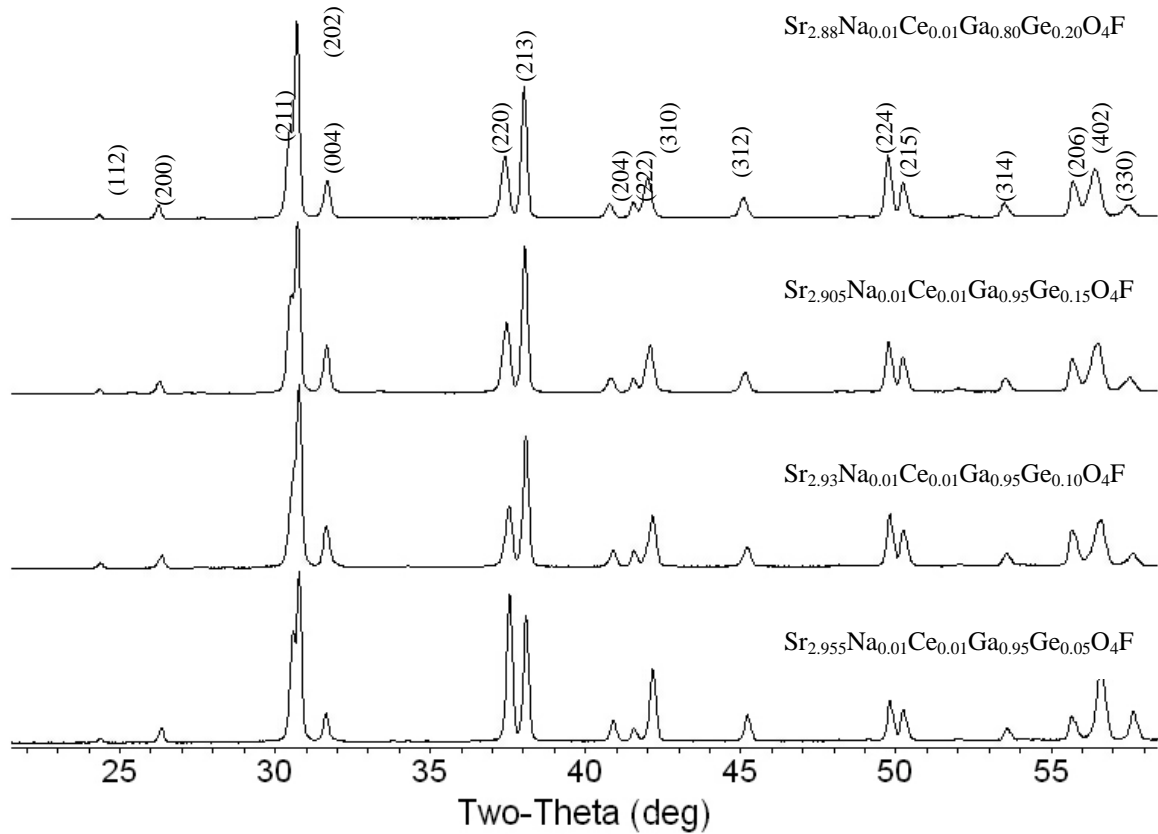


Figure 5.5: XRD patterns of Ge substituted $\text{Sr}_{2.98-x/2}\text{Na}_{0.01}\text{Ce}_{0.01}\text{Ga}_{1-x}\text{Ge}_x\text{O}_4\text{F}$, where $0 \leq x \leq 0.20$

The diffraction pattern and Rietveld refinement of Si^{4+} and Ge^{4+} -substituted $\text{Sr}_{2.98-x/2}\text{Na}_{0.01}\text{Ce}_{0.01}\text{Ga}_{1-x}\text{M}_x\text{O}_4\text{F}$ reveal that it is single phase when $0 \leq x \leq 0.20$. The phosphors are charge compensated by requiring 0.5% mol less Sr^{2+} in the synthesis for each additional charge given by Si^{4+} and Ge^{4+} for the substitution of Ga^{3+} . When 2 Ga^{3+} ions are replaced by either 2 Si^{4+} or 2 Ge^{4+} , a net 2+ charge is created within the host lattice. In order to compensate for this increase in charge, one Sr^{2+} ion is removed from the host, which creates a vacancy. As Si^{4+} is substituted for Ga^{3+} in $\text{Sr}_{2.98-x/2}\text{Na}_{0.01}\text{Ce}_{0.01}\text{Ga}_{1-x}\text{M}_x\text{O}_4\text{F}$, the a -parameter increases, while the c -parameter

decreases, which results in the overall decrease of the unit cell volume. This trend differs from the substitution of Ge^{4+} in $\text{Sr}_{2.98-x/2}\text{Na}_{0.01}\text{Ce}_{0.01}\text{Ga}_{1-x}\text{M}_x\text{O}_4\text{F}$, where the a -parameter increases, while the c -parameter decreases. However, the unit cell volume increases with Ge^{4+} concentration. Lattice parameters and site coordinates are listed in Table 5.1 for both the Si^{4+} and Ge^{4+} substituted $\text{Sr}_{2.98-x/2}\text{Na}_{0.01}\text{Ce}_{0.01}\text{Ga}_{1-x}\text{M}_x\text{O}_4\text{F}$ materials. The a -parameter increases approximately 0.11% when x increases from 0.0 to 0.20 in $\text{Sr}_{2.98-x/2}\text{Na}_{0.01}\text{Ce}_{0.01}\text{Ga}_{1-x}\text{Si}_x\text{O}_4\text{F}$ materials, while the c -parameter decreases by $\approx 0.69\%$. The contraction of the c -parameter correlates directly with the decreased Sr(1)-F bond lengths shown in Table 5.2. The M -O bond, where M is Ga^{3+} and Si^{4+} occupying the same position in $\text{Sr}_{2.98-x/2}\text{Na}_{0.01}\text{Ce}_{0.01}\text{Ga}_{1-x}\text{Si}_x\text{O}_4\text{F}$, decreases as x increases. A similar trend occurs in $\text{Sr}_{2.98-x/2}\text{Na}_{0.01}\text{Ce}_{0.01}\text{Ga}_{1-x}\text{Ge}_x\text{O}_4\text{F}$ materials, where the a -parameter expands by $\approx 0.24\%$, while the c -parameter decreases by $\approx 0.31\%$, which can also be attributed to the decreasing Sr(1)-F bonds. These materials also experience a decrease in the M -O bonds with increasing substitution of both Si^{4+} and Ge^{4+} . The tilt angles in both $\text{Sr}_{2.98-x/2}\text{Na}_{0.01}\text{Ce}_{0.01}\text{Ga}_{1-x}\text{Si}_x\text{O}_4\text{F}$ and $\text{Sr}_{2.98-x/2}\text{Na}_{0.01}\text{Ce}_{0.01}\text{Ga}_{1-x}\text{Ge}_x\text{O}_4\text{F}$ materials increase to $18.10(4)^\circ$ where $x = 0.05$ from $18.01(4)^\circ$ in $\text{Sr}_{2.98}\text{Na}_{0.01}\text{Ce}_{0.01}\text{GaO}_4\text{F}$. When $x \geq 0.05$ the tilt angles gradually decrease to $17.85(5)^\circ$ in $\text{Sr}_{2.98-x/2}\text{Na}_{0.01}\text{Ce}_{0.01}\text{Ga}_{1-x}\text{Si}_x\text{O}_4\text{F}$ and $17.65(5)^\circ$ in $\text{Sr}_{2.98-x/2}\text{Na}_{0.01}\text{Ce}_{0.01}\text{Ga}_{1-x}\text{Ge}_x\text{O}_4\text{F}$.

Table 5.1: Lattice Parameters of Substituted $\text{Sr}_{3-x/2}\text{Na}_{0.01}\text{Ce}_{0.01}\text{Ga}_{1-x}\text{M}_x\text{O}_4\text{F}$. All materials are refined using the $I4/mcm$ space group.

Sample	a (Å)	c (Å)	R_p	R_{wp}
$\text{Sr}_{2.98}\text{Na}_{0.01}\text{Ce}_{0.01}\text{GaO}_4\text{F}$	6.8060(1)	11.3744(2)	5.72	7.53
$\text{Sr}_{2.955}\text{Na}_{0.01}\text{Ce}_{0.01}\text{Ga}_{0.95}\text{Si}_{0.05}\text{O}_{4+\alpha}\text{F}_{1-\alpha}$	6.8047(2)	11.3455(4)	5.21	7.00
$\text{Sr}_{2.930}\text{Na}_{0.01}\text{Ce}_{0.01}\text{Ga}_{0.90}\text{Si}_{0.10}\text{O}_{4+\alpha}\text{F}_{1-\alpha}$	6.8082(1)	11.3369(3)	5.61	7.35
$\text{Sr}_{2.905}\text{Na}_{0.01}\text{Ce}_{0.01}\text{Ga}_{0.85}\text{Si}_{0.15}\text{O}_{4+\alpha}\text{F}_{1-\alpha}$	6.8127(1)	11.3092(3)	6.07	8.06
$\text{Sr}_{2.880}\text{Na}_{0.01}\text{Ce}_{0.01}\text{Ga}_{0.80}\text{Si}_{0.20}\text{O}_{4+\alpha}\text{F}_{1-\alpha}$	6.8135(1)	11.2954(3)	5.68	7.53
$\text{Sr}_{2.955}\text{Na}_{0.01}\text{Ce}_{0.01}\text{Ga}_{0.95}\text{Ge}_{0.05}\text{O}_{4+\alpha}\text{F}_{1-\alpha}$	6.8057(1)	11.3638(2)	5.29	6.94
$\text{Sr}_{2.930}\text{Na}_{0.01}\text{Ce}_{0.01}\text{Ga}_{0.90}\text{Ge}_{0.10}\text{O}_{4+\alpha}\text{F}_{1-\alpha}$	6.8079(1)	11.3618(4)	6.45	8.76
$\text{Sr}_{2.905}\text{Na}_{0.01}\text{Ce}_{0.01}\text{Ga}_{0.85}\text{Ge}_{0.15}\text{O}_{4+\alpha}\text{F}_{1-\alpha}$	6.8159(2)	11.3490(4)	6.68	9.09
$\text{Sr}_{2.880}\text{Na}_{0.01}\text{Ce}_{0.01}\text{Ga}_{0.80}\text{Ge}_{0.20}\text{O}_{4+\alpha}\text{F}_{1-\alpha}$	6.8219(2)	11.3396(4)	6.41	8.33

Sample	$A(2)x$	O_x	O_z	Vol (Å ³)
$\text{Sr}_{2.98}\text{Na}_{0.01}\text{Ce}_{0.01}\text{GaO}_4\text{F}$	0.1688(1)	0.1537(4)	0.6433(4)	526.89(1)
$\text{Sr}_{2.955}\text{Na}_{0.01}\text{Ce}_{0.01}\text{Ga}_{0.95}\text{Si}_{0.05}\text{O}_{4+\alpha}\text{F}_{1-\alpha}$	0.1681(1)	0.1544(4)	0.6465(4)	525.34(2)
$\text{Sr}_{2.930}\text{Na}_{0.01}\text{Ce}_{0.01}\text{Ga}_{0.90}\text{Si}_{0.10}\text{O}_{4+\alpha}\text{F}_{1-\alpha}$	0.1683(1)	0.1508(4)	0.6454(4)	525.48(3)
$\text{Sr}_{2.905}\text{Na}_{0.01}\text{Ce}_{0.01}\text{Ga}_{0.85}\text{Si}_{0.15}\text{O}_{4+\alpha}\text{F}_{1-\alpha}$	0.1688(1)	0.1487(5)	0.6473(4)	524.88(3)
$\text{Sr}_{2.880}\text{Na}_{0.01}\text{Ce}_{0.01}\text{Ga}_{0.80}\text{Si}_{0.20}\text{O}_{4+\alpha}\text{F}_{1-\alpha}$	0.1695(1)	0.1474(4)	0.6482(4)	524.38(3)
$\text{Sr}_{2.955}\text{Na}_{0.01}\text{Ce}_{0.01}\text{Ga}_{0.95}\text{Ge}_{0.05}\text{O}_{4+\alpha}\text{F}_{1-\alpha}$	0.1683(1)	0.1520(4)	0.6440(5)	526.34(2)
$\text{Sr}_{2.930}\text{Na}_{0.01}\text{Ce}_{0.01}\text{Ga}_{0.90}\text{Ge}_{0.10}\text{O}_{4+\alpha}\text{F}_{1-\alpha}$	0.1683(2)	0.1501(6)	0.6418(5)	526.59(4)
$\text{Sr}_{2.905}\text{Na}_{0.01}\text{Ce}_{0.01}\text{Ga}_{0.85}\text{Ge}_{0.15}\text{O}_{4+\alpha}\text{F}_{1-\alpha}$	0.1686(2)	0.1548(6)	0.6488(5)	527.23(4)
$\text{Sr}_{2.880}\text{Na}_{0.01}\text{Ce}_{0.01}\text{Ga}_{0.80}\text{Ge}_{0.20}\text{O}_{4+\alpha}\text{F}_{1-\alpha}$	0.1704(1)	0.1502(5)	0.6448(5)	527.73(3)

Table 5.2: Bond distances and angles for $\text{Sr}_{3-x/2}\text{Na}_{0.01}\text{Ce}_{0.01}\text{Ga}_{1-x}\text{M}_x\text{O}_4\text{F}$ materials

$\text{Sr}_{3-x/2}\text{Na}_{0.01}\text{Ce}_{0.01}\text{Ga}_{1-x}\text{Si}_x\text{O}_4\text{F}$	$x = 0.0$	$x = 0.05$	$x = 0.10$	$x = 0.15$	$x = 0.20$
A(1)-O (x8)	2.850(2)	2.831(2)	2.848(2)	2.847(2)	2.847(2)
A(1)-F (x2)	2.8436 (1)	2.8364 (1)	2.8342 (1)	2.8273(1)	2.8239(1)
A(2)-O (x2)	2.362 (4)	2.383(4)	2.397(4)	2.422(5)	2.432(4)
A(2)-O (x4)	2.735 (3)	2.755(3)	2.730 (4)	2.733(4)	2.736(4)
A(2)-F (x2)	2.5302 (3)	2.5314(3)	2.5231(3)	2.5325(4)	2.5307(3)
M-O (x4)	1.913(4)	1.894(4)	1.875 (4)	1.845(5)	1.828(4)
O-Ga-O	113.7 (1)	112.6(1)	113.6(1)	113.4(2)	113.3(1)
O-Ga-O	101.3(3)	103.4(3)	101.5(3)	101.9(3)	102.0(3)
Tilt Angle	18.01(4)	18.10(4)	18.09(5)	18.00(5)	17.85(5)

$\text{Sr}_{3-x/2}\text{Na}_{0.01}\text{Ce}_{0.01}\text{Ga}_{1-x}\text{Ge}_x\text{O}_4\text{F}$	$x = 0.05$	$x = 0.10$	$x = 0.15$	$x = 0.20$
A(1)-O (x8)	2.851(2)	2.868(3)	2.823(3)	2.858(3)
A(1)-F (x2)	2.8410(1)	2.8405(1)	2.8372(1)	2.8349(1)
A(2)-O (x2)	2.381 (4)	2.378(4)	2.398(6)	2.386(5)
A(2)-O (x4)	2.728 (3)	2.703(3)	2.778 (5)	2.739(4)
A(2)-F (x2)	2.5314 (3)	2.5322(4)	2.5344(4)	2.5311(4)
M-O (x4)	1.895(4)	1.897(4)	1.883 (6)	1.877(5)
O-Ga-O	113.8(1)	114.8(2)	111.8(2)	113.8(2)
O-Ga-O	101.1(3)	99.2(3)	104.8(4)	101.1(3)
Tilt Angle	18.10(4)	18.06(6)	18.04(6)	17.65(5)

The BVS values for the ions in Sr₃GaO₄F published by Vogt *et al.* are compared to the analysis of the bond valence model for Sr_{2.98-x/2}Na_{0.01}Ce_{0.01}Ga_{1-x}M_xO₄F materials. The BVS values of Sr(1) for all samples are near 1.30, which is close to the value published in Vogt *et al.* The BVS values for the F⁻ ion are consistently near 1.15 in each of the Sr_{2.98-x/2}Na_{0.01}Ce_{0.01}Ga_{1-x}Si_xO₄F and Sr_{2.98-x/2}Na_{0.01}Ce_{0.01}Ga_{1-x}Ge_xO₄F samples. The O BVS values range from 1.78 to 1.85 in both Sr_{2.98-x/2}Na_{0.01}Ce_{0.01}Ga_{1-x}Si_xO₄F and Sr_{2.98-x/2}Na_{0.01}Ce_{0.01}Ga_{1-x}Ge_xO₄F, which is comparable to the value of 1.86 generated from the synchrotron data given in Vogt *et al.*²². The most significant change in BVS is in the M site, where Ga³⁺ is substituted by either Si⁴⁺ or Ge⁴⁺ ions. The BVS values increase from 2.49 to 3.08 as Si⁴⁺ is substituted within the host structure, while the increase is from 2.49 to 2.81 with Ge⁴⁺ substitution. The BVS value at the M site in Sr_{2.98-x/2}Na_{0.01}Ce_{0.01}GaO₄F indicates that Ga³⁺ is slightly under-bonded and that ions with greater formal charges can be readily substituted into the host lattice. This rationale is similar to the one given for the iso- and aliovalent substitutions at the Sr(1) site, which is also underbonded in Sr₃AlO₄F.

The discrepancy factors (d_i) are generated by subtracting BVS values of ions from their formal valences. However, for these materials the formal charge of the Mⁿ⁺ ion must be changed to a weighted average based on the formal charges of Ga³⁺ and either Si⁴⁺ and Ge⁴⁺. For example, the discrepancy factor for M in Sr_{2.98-x/2}Na_{0.01}Ce_{0.01}Ga_{0.80}Si_{0.20}O₄F is calculated by first weighting the formal charge by using the equation

$$\text{Formal Charge (weighted)} = [(3 \times 0.80) + (4 \times 0.20)] = 3.20, \quad (5.1)$$

then subtract this value from the calculated BVS value (3.08) to the calculated d_i value of -0.12.

The global instability index (G) is still calculated by the equation

$$G = (\Sigma_i/N)^{1/2}, \quad (5.2)$$

where N represents the total number of atoms in the formula unit. For the $\text{Sr}_{2.98-x/2}\text{Na}_{0.01}\text{Ce}_{0.01}\text{Ga}_{1-x}\text{Si}_x\text{O}_4\text{F}$ materials, the substitution leads to increased stability of the $\text{Sr}_3\text{MO}_4\text{F}$ -type structure as G decreases from 0.3126 in $\text{Sr}_{2.98-x/2}\text{Na}_{0.01}\text{Ce}_{0.01}\text{GaO}_4\text{F}$ to 0.2426 in $\text{Sr}_{2.98-x/2}\text{Na}_{0.01}\text{Ce}_{0.01}\text{Ga}_{0.80}\text{Si}_{0.20}\text{O}_4\text{F}$. The increased substitution of Ge^{4+} in $\text{Sr}_{2.98-x/2}\text{Na}_{0.01}\text{Ce}_{0.01}\text{Ga}_{1-x}\text{Ge}_x\text{O}_4\text{F}$ does not yield similar results as the values for G fluctuate randomly between 0.2599 and 0.3177. This is due to the greater amount of distortion caused by the substitution of the larger Ge^{4+} ion compared to the Si^{4+} ion. This trend in $\text{Sr}_{2.98-x/2}\text{Na}_{0.01}\text{Ce}_{0.01}\text{Ga}_{1-x}\text{Ge}_x\text{O}_4\text{F}$ materials provides evidence that these structures are slightly strained.

Table 5.3: Bond Valence Sums (BVS) of ions in $\text{Sr}_{3-x/2}\text{Na}_{0.01}\text{Ce}_{0.01}\text{Ga}_{1-x}\text{Si}_x\text{O}_4\text{F}$

Ion	$x = 0.0$	$x = 0.05$	$x = 0.10$	$x = 0.15$	$x = 0.20$
Sr(1)	1.30	1.37	1.31	1.32	1.32
Sr(2)	2.25	2.15	2.17	2.10	2.07
M	2.49	2.61	2.74	2.95	3.08
F	1.15	1.15	1.15	1.15	1.16
O	1.79	1.78	1.81	1.83	1.85

Table 5.4: Discrepancy factors and Global Instability Indices in $\text{Sr}_{3-x/2}\text{Na}_{0.01}\text{Ce}_{0.01}\text{Ga}_{1-x}\text{Si}_x\text{O}_4\text{F}$

Ion	$x = 0.0$	$x = 0.05$	$x = 0.10$	$x = 0.15$	$x = 0.20$
Sr(1)	-0.70	-0.63	-0.69	-0.68	-0.68
Sr(2)	0.25	0.15	0.17	0.10	0.07
<i>M</i>	-0.51	-0.44	-0.36	-0.20	-0.12
F	0.15	0.15	0.15	0.15	0.16
O	-0.21	-0.22	-0.19	-0.17	-0.15
<i>Global Instability Index</i>	0.3126	0.2757	0.2775	0.2503	0.2426

Table 5.5: Bond Valence Sums (BVS) of ions in $\text{Sr}_{3-x/2}\text{Na}_{0.01}\text{Ce}_{0.01}\text{Ga}_{1-x}\text{Ge}_x\text{O}_4\text{F}$

Ion	$x = 0.05$	$x = 0.10$	$x = 0.15$	$x = 0.20$
Sr(1)	1.30	1.25	1.39	1.29
Sr(2)	2.21	2.27	2.07	2.18
<i>M</i>	2.63	2.63	2.75	2.81
F	1.14	1.14	1.15	1.15
O	1.80	1.82	1.78	1.83

Table 5.6: Discrepancy factors and Global Instability Indices in $\text{Sr}_{3-x/2}\text{Na}_{0.01}\text{Ce}_{0.01}\text{Ga}_{1-x}\text{Ge}_x\text{O}_4\text{F}$

Ion	$x = 0.05$	$x = 0.10$	$x = 0.15$	$x = 0.20$
Sr(1)	-0.70	-0.75	-0.61	-0.71
Sr(2)	0.21	0.27	0.07	0.18
<i>M</i>	-0.42	-0.47	-0.40	-0.39
F	0.14	0.14	0.15	0.15
O	-0.20	-0.18	-0.22	-0.17
<i>Global Instability Index</i>	0.2925	0.3177	0.2599	0.2867

Photoluminescence

The photoluminescence of both $\text{Sr}_{2.98-x/2}\text{Na}_{0.01}\text{Ce}_{0.01}\text{Ga}_{1-x}\text{Si}_x\text{O}_4\text{F}$ and $\text{Sr}_{2.98-x/2}\text{Na}_{0.01}\text{Ce}_{0.01}\text{Ga}_{1-x}\text{Ge}_x\text{O}_4\text{F}$ materials exhibit broad-band emission spectra when excited near 420 nm. These photoluminescence spectra are shown in Figure 5.6 and 5.7. A critical distance (R_c) defined as the distance between Ce^{3+} ions is calculated using Blasse's equation^{13, 24}

$$R_c \approx 2 \left(\frac{3V}{4\pi\chi_c N} \right)^{1/3} \quad (5.3)$$

, where V is the volume of the unit cell, N is the number of available cation sites in the unit cell, and χ_c denotes the critical concentration of Ce^{3+} ions, where the average separation of nearest activator ions is equal to the critical distance. In the $\text{Sr}_3\text{MO}_4\text{F}$ host lattice, it is assumed that the Ce^{3+} ions occupy the 8-coordinated Sr(2) site (Wyckoff site $8h$, multiplicity of 8), thus giving a total of 8 ions in the unit cell. The occupation of Ce^{3+} in $\text{Sr}_3\text{GaO}_4\text{F}$ was studied by Chen at liquid helium temperatures, where $x = 0.01, 0.15,$ and 0.30 . In this study, when $x = 0.01$, the photoluminescence spectra confirmed that the majority of the Ce^{3+} ions occupies the Sr(2) site. As the Ce^{3+} content increases to $x = 0.15$, it is clear that Ce^{3+} occupies both the Sr(1) and Sr(2) sites in the host lattice. When $x = 0.30$, the photoluminescence emission spectra shows that the dominant peak corresponds to the 10-coordinated Sr(1) site¹⁰. In $\text{Sr}_{3-2x}\text{Na}_x\text{Ce}_x\text{GaO}_4\text{F}$ materials the critical concentration is 2.5 mol%, as shown in Figure 5.2. Based on the small amount of Ce^{3+} ions substituted, the critical distance (R_c) is 23.3\AA based on the assumption that the majority of these ions occupy the Sr(2) site. This gives us reason to believe that the quenching mechanism sustained by exchange interaction is not the dominant mechanism,

but a non-radiative energy transfer between Ce^{3+} activator ions. The separation needed for the exchange interaction is about 5\AA and is deemed insignificant beyond 10\AA ^{13,25-26}.

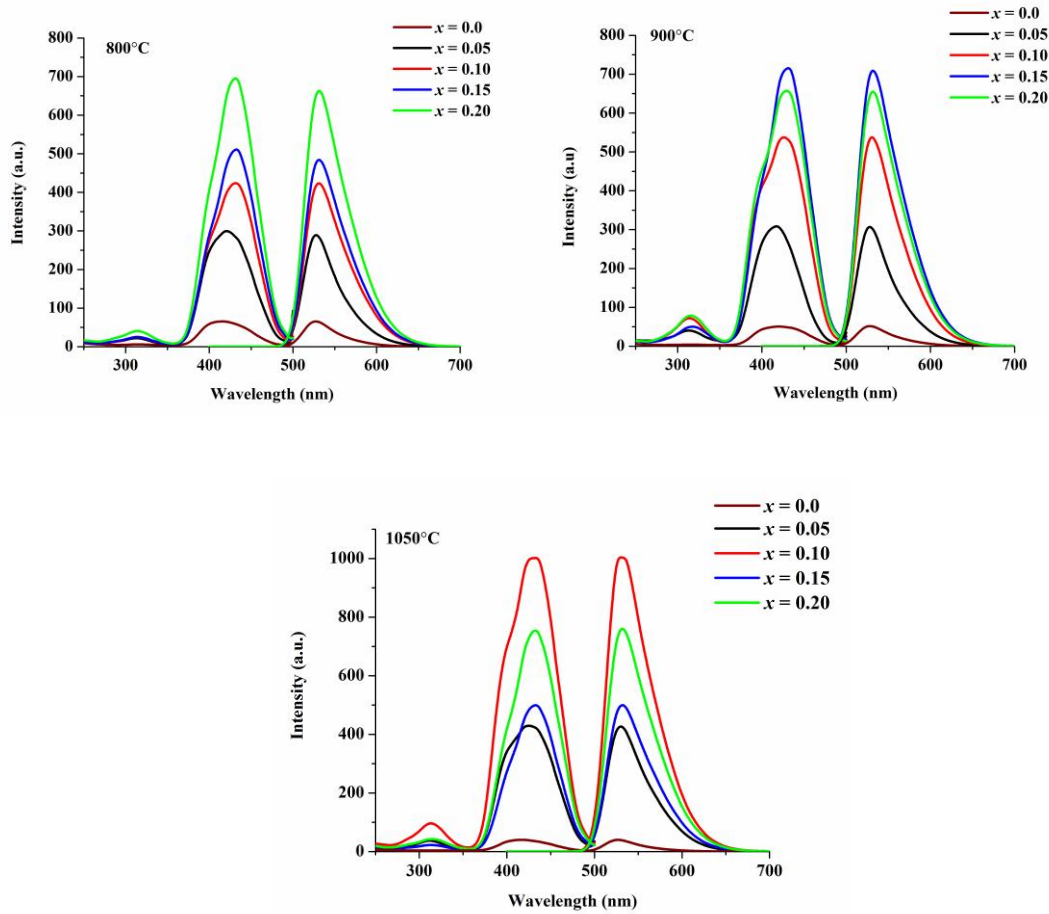


Figure 5.6: Photoluminescence spectra of $Sr_{3-x/2}Na_{0.01}Ce_{0.01}Ga_{1-x}Si_xO_4F$ with a post-synthesis reduction temperature of 800°C, 900°C and 1050°C.

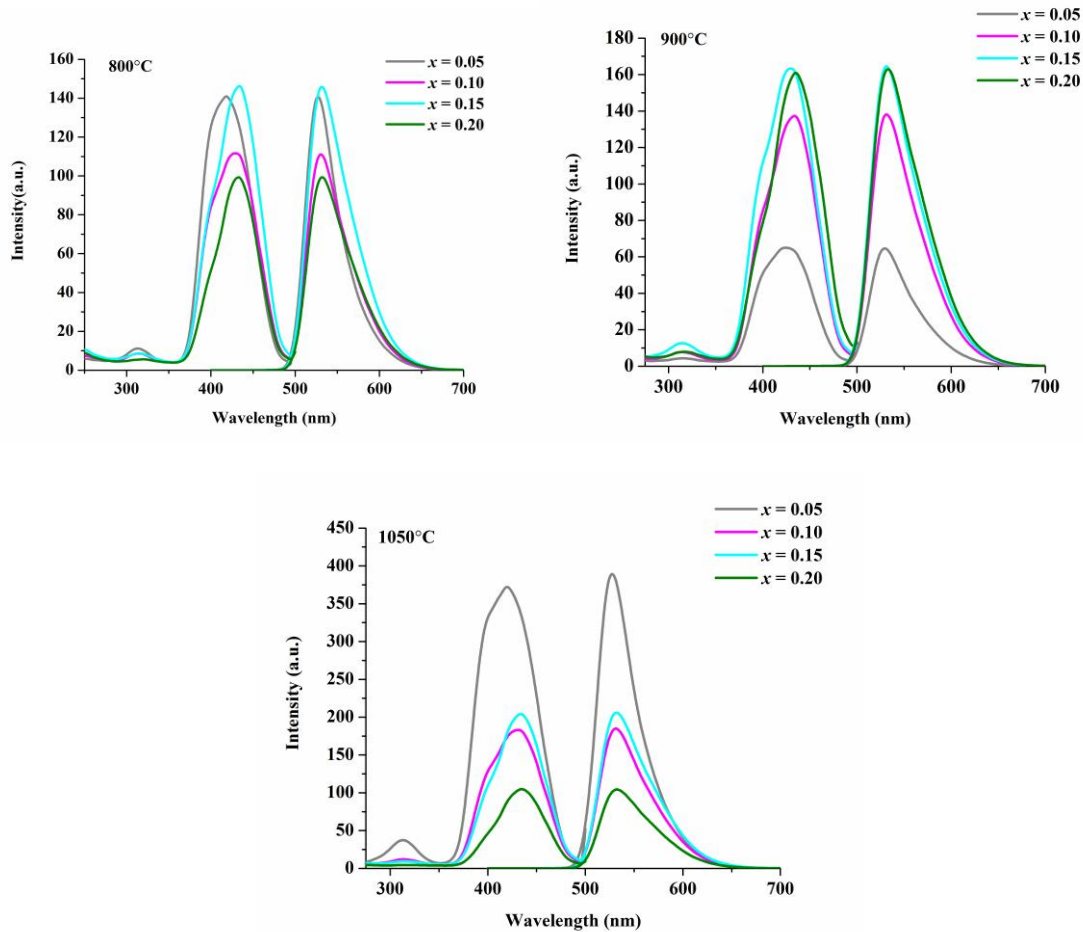


Figure 5.7: Photoluminescence spectra of $\text{Sr}_{3-x/2}\text{Na}_{0.01}\text{Ce}_{0.01}\text{Ga}_{1-x}\text{Ge}_x\text{O}_4\text{F}$ with a post-synthesis reduction temperature of 800°C, 900°C and 1050°C.

Research has been conducted involving the substitution of Si^{4+} into the $\text{Sr}_3\text{AlO}_4\text{F}$ -type lattice by Im *et al*, Lee *et al*¹³, Denault *et al*¹², and Ma *et al*⁷, where the substitution ranges from $0 \leq x \leq 1$. Even though the photoluminescence is studied for the Si^{4+} substituted materials, there is limited information describing the structural details of the substitutions over the entire series of materials. The substitution of 1.0 molar% Ce^{3+} in $\text{Sr}_3\text{MO}_4\text{F}$ -type structures causes these materials to exhibit an intense blue-green light when tempered in a 5% H_2 /95% Ar atmosphere. The increased substitution of Si^{4+} and

Ge⁴⁺ into the host-lattice, causes the maximum emission and excitation intensity (λ_{max}) to shift to longer wavelengths.

In the excitation spectra of the Si⁴⁺ and Ge⁴⁺ substituted Sr_{2.98-x/2}Na_{0.01}Ce_{0.01}Ga_{1-x}M_xO₄F materials, the $\lambda_{\text{excitmax}}$ ranges from ≈ 415 nm to 433 nm where the reducing temperature of the materials are 800°C, 900°C and 1050°C, while in the emission spectra the λ_{emmax} ranges from ≈ 527 nm to 532 nm at 800°C, 900°C and 1050°C. It appears that the amount of Si⁴⁺ and Ge⁴⁺ substituted into the host is responsible for the tuning of the emission in these materials. The temperature of the reducing step has little effect on the range of the red shift in the Si⁴⁺ and Ge⁴⁺ substituted materials. Denault *et al*¹² showed that the maximum excitation wavelength varies from 398 to 409, while the maximum emission wavelength ranges from 523 to 552 nm in Sr₂Ba(AlO₄F)_{1-x}(SiO₅)_x materials. Xiaole *et al*⁷ showed a range of 518-541nm in the emission spectrum for Sr_{2.95}(Al_xSi_{1-x})O_{5-x}F_x 0.1 \leq x \leq 0.9. Im *et al*⁶ also reports a 63 nm difference between the Ce³⁺-substituted Sr₃AlO₄F and Sr₃SiO₅ end members. Furthermore, Denault *et al*¹² and Im *et al*⁶ both report a decrease in the emission intensity as the Si⁴⁺ content increases in their respective hosts. The additional substitution of Si⁴⁺ and Ge⁴⁺ ions within the Sr_{2.98-x/2}Na_{0.01}Ce_{0.01}Ga_{1-x}M_xO₄F host will most likely cause the emission spectra of these materials to continue to be red-shifted, however the materials are not likely to be a single phase. Furthermore, the increased substitution of Si⁴⁺ and Ge⁴⁺ will also cause these materials to exhibit “oxide-type” behavior by becoming more susceptible to thermal quenching.

Although the maximum intensity of the excitation spectrum is between 415 nm and 433 nm in Si⁴⁺ and Ge⁴⁺ substituted Sr_{2.98-x/2}Na_{0.01}Ce_{0.01}Ga_{1-x}M_xO₄F materials, there is

an appreciable amount of intensity near 450nm, which is a clear indication that these materials can show significant photoluminescence emission when excited by light stemming from blue LED chips. Figure 5.8 shows the difference between the photoluminescence intensity at the material's λ_{\max} and at the LED excitation wavelength.

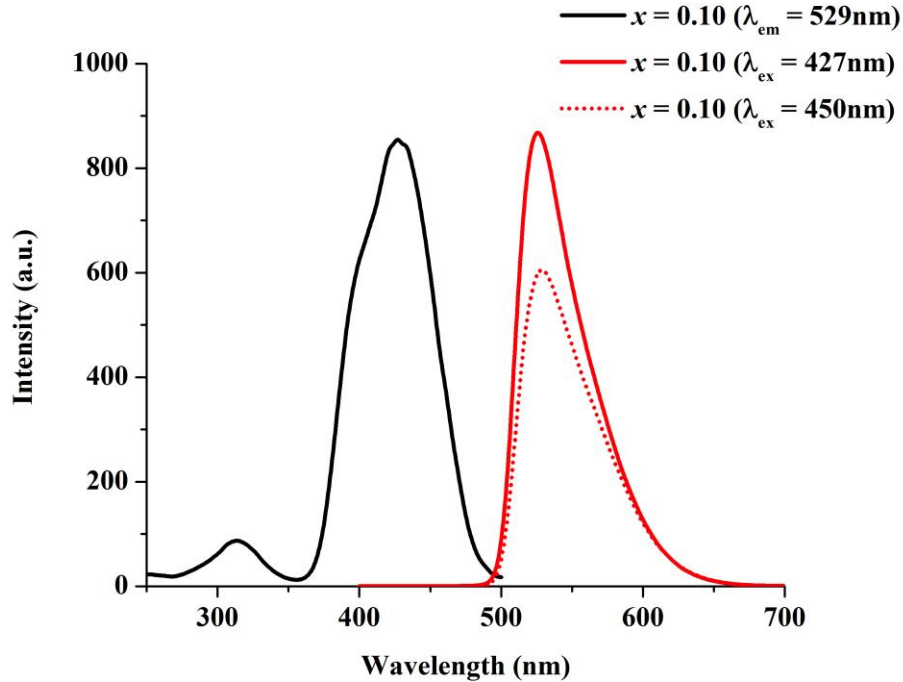


Figure 5.8: Comparison of the photoluminescence intensities of $\text{Sr}_{2.93}\text{Na}_{0.01}\text{Ce}_{0.01}\text{Ga}_{0.90}\text{Si}_{0.10}\text{O}_4\text{F}$ reduced at 1050°C under $\lambda_{\text{ex}} = 427\text{nm}$ and $\lambda_{\text{ex}} = 450\text{nm}$, where 450nm indicates blue excitation for LED devices.

The increased substitution of Si^{4+} from 0.0 to 0.20 in $\text{Sr}_{2.98-x/2}\text{Na}_{0.01}\text{Ce}_{0.01}\text{Ga}_{1-x}\text{Si}_x\text{O}_4\text{F}$ when the reducing temperature is 800°C and 900°C shows an increase of the maximum PL intensity in Figure 5.9a. When the reducing temperature is 1050°C the PL is increasing, however there is a dramatic increase in the intensity in $\text{Sr}_{2.98-x/2}\text{Na}_{0.01}\text{Ce}_{0.01}\text{Ga}_{0.90}\text{Si}_{0.10}\text{O}_4\text{F}$. In Figure 5.9b, where the maximum PL

intensities are plotted against substitution in $\text{Sr}_{2.98-x/2}\text{Na}_{0.01}\text{Ce}_{0.01}\text{Ga}_{1-x}\text{Ge}_x\text{O}_4\text{F}$ materials, this trend is not as noticeable.

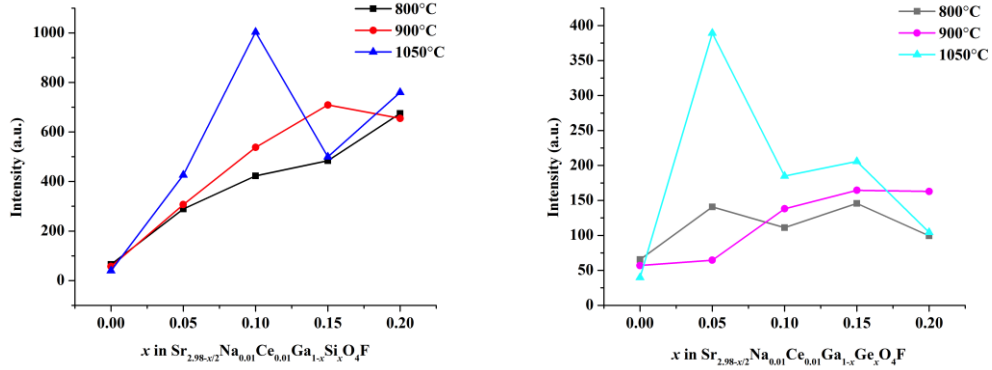


Figure 5.9: Comparison of the maximum photoluminescence intensities at 800°C, 900°C and 1050°C of $\text{Sr}_{3-x/2}\text{Na}_{0.01}\text{Ce}_{0.01}\text{Ga}_{1-x}\text{Si}_x\text{O}_4\text{F}$ and $\text{Sr}_{3-x/2}\text{Na}_{0.01}\text{Ce}_{0.01}\text{Ga}_{1-x}\text{Ge}_x\text{O}_4\text{F}$

Under $\lambda_{\text{ex}} = 415\text{nm}$ light, the increase of Si^{4+} and Ge^{4+} substitutions in $\text{Sr}_{3-x/2}\text{Na}_{0.01}\text{Ce}_{0.01}\text{Ga}_{1-x}\text{M}_x\text{O}_4\text{F}$ materials causes the emitted color to shift from blue-green to a green-yellow color. These values are listed in Table 5.7 and are plotted on the CIE chromaticity diagram in Figure 5.10. The increase in temperature (from 800°C, 900°C, to 1050°C) of the post-synthesis reduction step for each material causes minimal changes in the chromaticity coordinates, however it is obvious that these $\text{Sr}_{3-x/2}\text{Na}_{0.01}\text{Ce}_{0.01}\text{Ga}_{1-x}\text{M}_x\text{O}_4\text{F}$ materials are tunable with the increasing substitution of Si^{4+} and Ge^{4+} .

Table 5.7: CIE Chromaticity Coordinates (415nm excitation)

Sample	800°C		900°C		1050°C	
	x	y	x	y	x	y
$\lambda_{ex} = 415\text{nm}$ 1 Sr_{2.98}Na_{0.01}Ce_{0.01}GaO₄F	0.1524	0.3014	0.1565	0.3425	0.1623	0.3962
2 Sr_{2.955}Na_{0.01}Ce_{0.01}Ga_{0.95}Si_{0.05}O_{4+a}F_{1-a}	0.1664	0.3959	0.1887	0.4274	0.1741	0.4310
3 Sr_{2.930}Na_{0.01}Ce_{0.01}Ga_{0.90}Si_{0.10}O_{4+a}F_{1-a}	0.1846	0.4432	0.1983	0.4588	0.1996	0.4895
4 Sr_{2.905}Na_{0.01}Ce_{0.01}Ga_{0.85}Si_{0.15}O_{4+a}F_{1-a}	0.1867	0.4098	0.2054	0.4760	0.2012	0.4819
5 Sr_{2.880}Na_{0.01}Ce_{0.01}Ga_{0.80}Si_{0.20}O_{4+a}F_{1-a}	0.1997	0.4695	0.2041	0.4798	0.2138	0.5132
6 Sr_{2.955}Na_{0.01}Ce_{0.01}Ga_{0.95}Ge_{0.05}O_{4+a}F_{1-a}	0.1619	0.3215	0.1742	0.3978	0.1606	0.3899
7 Sr_{2.930}Na_{0.01}Ce_{0.01}Ga_{0.90}Ge_{0.10}O_{4+a}F_{1-a}	0.1822	0.4338	0.1869	0.4407	0.1853	0.4456
8 Sr_{2.905}Na_{0.01}Ce_{0.01}Ga_{0.85}Ge_{0.15}O_{4+a}F_{1-a}	0.1947	0.4645	0.1984	0.4537	0.1983	0.4727
9 Sr_{2.880}Na_{0.01}Ce_{0.01}Ga_{0.95}Ge_{0.20}O_{4+a}F_{1-a}	0.2050	0.4640	0.2231	0.5115	0.2106	0.4875

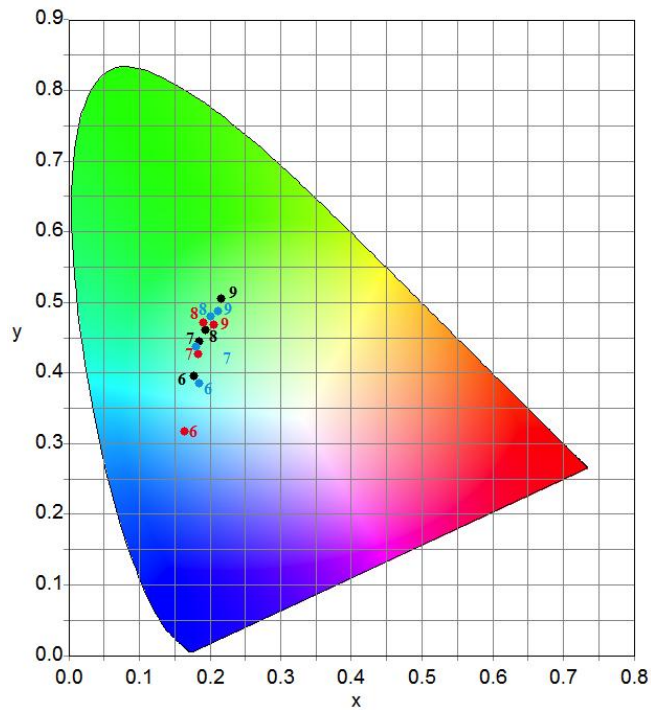
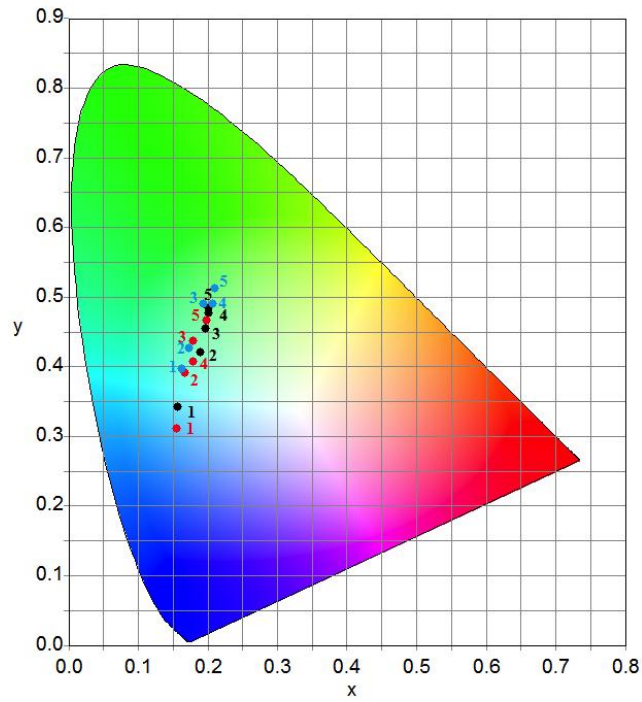


Figure 5.10: Dependence of Si^{4+} and Ge^{4+} substituted $\text{Sr}_{3-x/2}\text{Na}_{0.01}\text{Ce}_{0.01}\text{Ga}_{1-x}\text{M}_x\text{O}_4\text{F}$ on chromaticity coordinates. The red, black and blue dots represent the reducing temperature at 800°C , 900°C and 1050°C , respectively.

Conclusion

In this chapter, the structural and photoluminescent properties of Si and Ge substituted $\text{Sr}_{2.98-x/2}\text{Na}_{0.01}\text{Ce}_{0.01}\text{Ga}_{1-x}\text{M}_x\text{O}_4\text{F}$ materials are studied. Based on the Rietveld refinements of Si^{4+} and Ge^{4+} substitutions made in $\text{Sr}_{2.98-x/2}\text{Na}_{0.01}\text{Ce}_{0.01}\text{Ga}_{1-x}\text{M}_x\text{O}_4\text{F}$, it is apparent that they form a single phase. Structurally, the increased substitution of Ge^{4+} in $\text{Sr}_{2.98-x/2}\text{Na}_{0.01}\text{Ce}_{0.01}\text{Ga}_{1-x}\text{M}_x\text{O}_4\text{F}$ causes the global instability indices to vary inconsistently, while the values for Si substituted materials gradually decrease, indicating that they are becoming more stable with increasing substitution. This increased stability also translates into consistently higher PL intensities, with the Si-substituted $\text{Sr}_{2.98-x/2}\text{Na}_{0.01}\text{Ce}_{0.01}\text{Ga}_{1-x}\text{M}_x\text{O}_4\text{F}$ materials showing an increase in PL intensity at 800°C and 900°C with decreasing G , while Ge-substituted $\text{Sr}_{2.98-x/2}\text{Na}_{0.01}\text{Ce}_{0.01}\text{Ga}_{1-x}\text{M}_x\text{O}_4\text{F}$ materials do not show this trend. It is also shown that there is a significant amount of photoluminescence intensity in these materials where $\lambda_{\text{ex}} = 450\text{nm}$ when compared to the λ_{max} . Based on the current data shown in this chapter, Si^{4+} -substituted $\text{Sr}_{2.98-x/2}\text{Na}_{0.01}\text{Ce}_{0.01}\text{Ga}_{1-x}\text{M}_x\text{O}_4\text{F}$ materials seem to be the more promising potential phosphors than the Ge^{4+} substituted ones due to the increased PL intensities.

References

- (1) Nakamura, S. *Materials Research Society Symposium Proceedings* **1994**, 339, 173-173.
- (2) Nakamura, S.; Mukai, T.; Senoh, M. *Applied Physics Letters* **1994**, 64, 1687-1689.
- (3) Setlur, A. *The Electrochemical Society Interface* **2009**, 16, 32-36.
- (4) Li, Y. Q.; Van Steen, J. E. J.; Van Krevel, J. W. H.; Botty, G.; Delsing, A. C. A.; DiSalvo, F. J.; Hintzen, H. T. *Journal of alloys and compounds* **2006**, 417, 273-279.
- (5) Lakshmanan, A.; Satheesh Kumar, R.; Sivakumar, V.; Thomas, P. C.; Jose, M. T. *Indian Journal of Pure and Applied Physics* **2011**, 49, 303-307.
- (6) Im, W. B.; Brinkley, S.; Hu, J.; Mikhailovsky, A.; DenBaars, S. P.; Seshadri, R. *Chemistry of Materials* **2010**, 22, 2842-2849.
- (7) Ma, X.; Zhuang, W.; Guo, H.; Liu, R.; Liu, Y.; He, H.; Peng, P.; Chen, L. *Journal of Rare Earths*. **2013**, 31, 665-668.
- (8) Setlur, A. A.; Radkov, E. V.; Henderson, C. S.; Her, J.-H.; Srivastava, A. M.; Karkada, N.; Kishore, M. S.; Kumar, N. P.; Aesram, D.; Deshpande, A. *Chemistry of Materials* **2010**, 22, 4076-4082.
- (9) Shang, M.; Li, G.; Kang, X.; Yang, D.; Geng, D.; Lin, J. *ACS applied materials & interfaces* **2011**, 3, 2738-2746.
- (10) Chen, W.; Liang, H.; Han, B.; Zhong, J.; Su, Q. *The Journal of Physical Chemistry C* **2009**, 113, 17194-17199.
- (11) Im, W. B.; George, N.; Kurzman, J.; Brinkley, S.; Mikhailovsky, A.; Hu, J.; Chmelka, B. F.; DenBaars, S. P.; Seshadri, R. *Advanced Materials* **2011**, 23, 2300-2305.
- (12) Denault, K. A.; George, N. C.; Paden, S. R.; Brinkley, S.; Mikhailovsky, A. A.; Neufeind, J.; DenBaars, S. P.; Seshadri, R. *Journal of Materials Chemistry* **2012**, 22, 18204-18213.
- (13) Lee, J.; Unithrattil, S.; and Bin Im, W. *Journal of Alloys and Compounds* **555**, 297-303.

- (14) Glasser, L. S. D.; Glasser, F. P. *Acta Crystallographica* **1965**, *18*, 453-454.
- (15) Skakle, J. M. S.; Fletcher, J. G.; West, A. R. *Journal of the Chemical Society, Dalton Transactions* **1996**, 2497-2501.
- (16) Larson, A. C.; Von Dreele, R. B. *General Structure Analysis System*. Los Alamos National Laboratory Report LAUR 860-748 (2000)
- (17) Choi, H.-M.; Park, S. *Journal of Luminescence* **2012**, *132*, 2213-2216.
- (18) Setlur, A. A.; Porob, D. G.; Happek, U.; Brik, M. G. *Journal of Luminescence* **2013**, *133*, 66-68.
- (19) Sullivan, E.; Avdeev, M.; Vogt, T. *Journal of Solid State Chemistry* **2012**, *194*, 297-306.
- (20) Chen, W. *Journal of Alloys and Compounds* **2013**, *550*, 320-325.
- (21) Kelsey, P. V.; Brown, J. J. *Journal of The Electrochemical Society* **1976**, *123*, 1384-1388.
- (22) Vogt, T.; Woodward, P. M.; Hunter, B. A.; Prodjosantoso, A. K.; Kennedy, B. J. *Journal of Solid State Chemistry* **1999**, *144*, 228-231.
- (23) Shannon, R. D. *Acta Crystallographica Section A: Crystal Physics, Diffraction, Theoretical and General Crystallography* **1976**, *32*, 751-767.
- (24) Blasse, G. *Physics Letters A* **1968**, *28*, 444-445.
- (25) Won, Y.-H.; Jang, H. S.; Jeon, D. Y. *Journal of The Electrochemical Society* **2011**, *158*, J276-J281.
- (26) Ronda, C. R. *Luminescence*; Wiley-VCH: 2007; pp 276.

CHAPTER 6

CONCLUSIONS AND FUTURE WORK

In this dissertation, the structural and PL properties of potential phosphor materials are investigated. The potential phosphor materials without RE rely on self activation, while the PL emission in RE containing materials is caused by electronic transitions characteristic of the RE ions. Chapter 2 contains the images of unsubstituted $\text{Sr}_3\text{AlO}_4\text{F}_{(\text{air})}$ and $\text{Sr}_3\text{AlO}_4\text{F}_{(\text{r})}$, where exposure to a 5% $\text{H}_2/95\%$ Ar atmosphere induces photoluminescence. The broad-band PL emission seen when excited by 254 nm light make this material a potential phosphor for compact fluorescent lamps. Overall these materials have the potential to be used as single phosphor and might cause the costs of production to decrease since the starting materials are inexpensive.

It has also been shown that the emission of these materials can be tuned based on the substitutions made at the A(1), A(2) and *M* sites as well as changing the temperature of the reducing gas. In chapter 3, the isovalent substitution of Ba^{2+} and Ca^{2+} in $\text{Sr}_3\text{GaO}_4\text{F}$ yield different results that comparable substitutions made in $\text{Sr}_3\text{AlO}_4\text{F}$, where substitution of Ba^{2+} caused the $\text{Sr}_3\text{GaO}_4\text{F}$ structure to become more stable as well as increased the PL intensity overall. The substitution of Ca^{2+} caused the opposite to occur in these materials. In chapter 4 the PL of $\text{Sr}_{3-x}\text{Ba}_x\text{GaO}_4\text{F}$ materials were tuned by varying both the Ba^{2+} content as well as the Al-Ga ratio. It was determined that increased Al content caused a blue-shift in the PL emission.

The substitution of In^{3+} at the M site in these materials causes the excitation band to shift near 400 nm, which causes these materials to be used as potential LED phosphors without the use of rare earth ions. The ions Al^{3+} , Ga^{3+} , and In^{3+} occupy the M site simultaneously, which is a remarkable feat. The increased substitution of In^{3+} causes the PL emission to be quenched, therefore substitutions where $x \leq 0.025$ are ideal for phosphor material with an appreciable PL intensity. The increase in the temperature of the reducing atmosphere causes the PL emission to change from orange-yellow to a green-yellow color. This information is important since it is known that the combination of a blue emitting $\text{In}_x\text{Ga}_{1-x}\text{N}$ semiconductor combined with a yellow emitting phosphor will yield a cold white light emitting LED.

Chapter 5 includes the substitution of Ce^{3+} ions within the $\text{Sr}_3\text{GaO}_4\text{F}$ host with Na^+ used for charge compensation. It was determined that the critical concentration of Ce^{3+} is 1.0 molar%, where the critical distance near 23.3\AA was calculated. The additional substitution of Si^{4+} and Ge^{4+} caused the PL intensity to increase, however, the intensity increase is greater in the Si^{4+} substituted materials. The $\text{Sr}_{2.98-x/2}\text{Na}_{0.01}\text{Ce}_{0.01}\text{Ga}_{1-x}\text{Si}_x\text{O}_4\text{F}$ materials show the greatest PL intensity when excited between 415nm and 433nm. Additionally, there is a considerable amount of PL intensity when excited by 450nm light, which is comparable to $\text{Y}_3\text{Al}_5\text{O}_{12}:\text{Ce}^{3+}$.

Future Work

It has been determined that ordered oxyfluoride materials discussed within this work adopt the $A_3\text{MO}_4\text{F}$ host structure, which has the $I4/mcm$ space group. These

materials are slightly hygroscopic and will decompose if left in air for 1-2 weeks. This will undoubtedly affect the PL of these materials. These structural and photoluminescent studies contained within are preliminary and have not gone through the rigorous testing protocols employed by industries.








In order to incorporate these potential phosphor materials into devices the materials should be competitive with known materials currently on the market in terms of luminous efficacy, color rendering index (CRI) and correlated color temperature (CCT). Luminous efficacy is known as the luminescent output as a function of the electrical input and is measured in lumens per watt (lm W^{-1}). The color-rendering index (R_a) compares a light source to natural light, while correlated color temperature refers to the temperature that a black-body radiator emits a comparable color (in K).

In the further development of potential phosphors using the $\text{Sr}_3\text{MO}_4\text{F}$ host structure, the next step will be to test the stability of these materials over time. It will be interesting to study the substitution of known rare-earth ions into the host lattice and the longevity of these materials both pre and post packaged. This includes studying the potential breakdown of the structure and the effect that this breakdown has on the photoluminescence emission. Eventually this will lead to the testing of the most promising phosphor materials in LED lighting assemblies. Once these processes are optimized, a chain of custody procedure will be developed for the manufacturing of these materials.

APPENDIX A

COPYRIGHT PERMISSION

Authors can use either their **accepted author manuscript** or **final published article** for:

	Use at a conference, meeting or for teaching purposes
	Internal training by their company
	Sharing individual articles with colleagues for their research use* (also known as 'scholarly sharing')
	Use in a subsequent compilation of the author's works
	inclusion in a thesis or dissertation
	Reuse of portions or extracts from the article in other works
	Preparation of derivative works (other than for commercial purposes)

*Please note this excludes any **systematic or organized distribution** of published articles.